12-3-2019 10:00 AM

Raman-scatter Lidar measurements of Water Vapor determined using an integrated Microwave Radiometer-Lidar retrieval

Jeffrey VanKerkhove, *The University of Western Ontario*

Supervisor: Sica, Robert J., *The University of Western Ontario*

A thesis submitted in partial fulfillment of the requirements for the Doctor of Philosophy degree in Astronomy

Abstract

Water vapor plays a crucially important role in many atmospheric processes. However, it is poorly characterized in much of the atmosphere. Vibrational Raman-scattering Lidar has excellent spatial and temporal resolution, but requires an external calibration to correct for instrumental biases. Microwave Radiometers have poorer resolution, but can be calibrated absolutely and can be used to calibrate the Lidar system.

I have implemented a new technique, incorporating both instruments to generate a calibrated water vapor mixing ratio profile. This integrated retrieval uses an inverse method which includes a combined forward model, integrating radiative transfer equations (Schroeder and Westwater 1991) and lidar equations (Sica and Haefele 2016) to account for both radiometer and lidar components. The retrieval uses lidar signal measurements from the RAman Lidar for Meteorological Observations (RALMO) and brightness temperatures from a RPG-HATPRO-G2 microwave radiometer, both located at the MeteoSwiss station in Payerne, Switzerland.

The integrated retrieval is tested on synthetically-generated measurements, as well as real measurements from Payerne for clear day and nighttime observations. The performance of this retrieval is compared to the radiosonde-calibrated lidar retrieval technique of Sica and Haefele 2016 and Hicks-Jalali et al 2019, in which lidar constants are determined through a radiosonde-derived calibration factor. The integrated retrieval retrieves this factor directly, which is determined to be within 10% of the radiosonde-derived value for most nighttime retrievals. Additionally, the uncertainties associated with the integrated method-retrieved factors are around 1.5%, as opposed to approximately 5% for the radiosonde-calibrated method. Integrated retrievals over 24-hour periods show diurnal shifts in the calibration factor, which are shown to vary seasonally in parallel with high background count rates in the daytime. For the retrieval of water vapor mixing ratio, the results from the two methods are similar, with retrieved humidity profiles determined with confidence extending into the upper troposphere for clear nights. The integrated retrieval also has the advantage of a lower total systematic uncertainty over the entire effective range of the retrieval, particularly in the lower troposphere. This method is thereby demonstrated to be a viable alternative to water vapor retrievals via radiosonde-calibrated lidar, with the potential to be incorporated into routine operation at the Payerne meteorological site.

Keywords: water vapor, Raman Lidar, Microwave Radiometer, Optimal Estimation Method

Summary for Lay Audience

Water vapor plays an essential role in many atmospheric processes. However, it is difficult to measure it precisely, particularly at the level of clouds in the atmosphere. One instrument for measuring atmospheric water vapor is lidar, which emits laser pulses into the sky, with the returning pulses indicating the abundance of atmospheric constituents, such as water vapor, at various heights. Although they sample the atmosphere on very fine time and height scales, they need to be calibrated against another instrument in order for the result to be physically meaningful. Most commonly, this other instrument is a radiosonde (a weather balloon equipped with sensors for measuring temperature and humidity as it rises) which is launched while the lidar is measuring.

In this thesis, I use an alternative instrument, a microwave radiometer measuring the intensity of radiation in the atmosphere, to calibrate the lidar. Although they operate with a poorer height scale than lidars, radiometers can be calibrated internally.

This thesis introduces a technique which takes in raw measurements from the two instruments and uses them to simultaneously find the amount of water vapor at different altitudes in the atmosphere. It uses measurements from the RAman Lidar for Meteorological Observations (RALMO) and a RPG-HATPRO (Humidity And Temperature PROfiler), both located at the MeteoSwiss weather station in Payerne, Switzerland.

Compared to the atmospheric water vapor determined by the radiosonde-corrected lidar, my method shows similar results for nighttime observations and with better accuracy. This new method is shown to be a viable alternative to water vapor retrievals via radiosonde-calibrated lidar, with the potential to be incorporated into routine operation at the Payerne meteorological site as well as other sites in the future.

Co-Authorship statement

This thesis is written under the supervision of Dr. Robert J. Sica. For the Integrated retrieval project, Dr. Alexander Haefele of MeteoSwiss was instrumental in advising me and helping to get the retrieval working. Dr. Domenico Cimini of IMAA-CNR provided us with the forward model used for retrieving humidity from radiometer, this thesis refers to this radiative transfer adaption as the "Cimini Implementation". Dr. Maxime Hervo of MeteoSwiss provided the necessary HATPRO radiometer data, as well as the bias corrections. Dr. Shannon Hicks-Jalali extended the functionality of the lidar retrieval code documented in Sica & Haefele 2016, and provided me with GRUAN-corrected radiosonde data.

Acknowledgements

First, I would like to thank my supervisor, Dr. Robert Sica. This thesis would not be possible without his advise and guidance over these years.

I would also like to thank my colleagues, past and present, from the Purple Crow Lidar group: Emily McCullough, Robin Wing, Steve Argall, Ali Jalali, Ghazal Farhani, Shannon Hicks-Jalali, Sham Gamage, Achini Abayakoon, and Venu Wadehra. They have provided much needed assistance, in everything from helping with bugs in my code to cleaning bugs on the mirror.

Work on the integrated retrieval project would not be what it is today without the support of those at MeteoSwiss Payerne. In particular, Alexander Haefele, Francisco Navas Guzmn, and Maxime Hervo were there to answer my many, many questions.

I am also indebted to Beth Grzenia, for her efforts in proofreading this thesis and providing invaluable suggestions for its improvement.

And finally, I am eternally grateful for the support from my friends and family. In particular, I owe innumerable thanks to Yuanjun, T-Rex, and Cashew, for their patience and for keeping me somewhat sane during this process.

Contents

List of Figures

List of Tables

Chapter 1

Introduction

Water vapor's ubiquitous role in global atmospheric processes cannot be overstated. Despite its importance, it has proven difficult to accurately monitor water vapor due to its high spatio-temporal variability and extremely low abundance in certain parts of the atmosphere. Limitations in our capacity to effectively characterize it throughout the entire atmosphere constrain our potential to fully understand the atmosphere holistically. Although many systems have been designed to measure atmospheric water vapor, each has its own set of inherent drawbacks.

Due to the inherent advantages and limitations of any meteorological instrument, it is impossible to investigate atmospheric water vapor comprehensively using a single instrument, prompting numerous efforts over the years to integrate sensors for improved analyses of atmospheric quantities such as water vapor. Instrument synergy has provided a viable means for addressing such concerns by using multiple instruments to not only complement each other, but also provide a more comprehensive picture of the atmosphere. Raman lidars are ideally suited for monitoring the high spatio-temporal variations in atmospheric water vapor, but they require external calibration in order for their measurements to be physically meaningful. Commonly, this calibration is carried out by comparing to humidity measurements from a coincidental radiosonde, which has a number of shortcomings. Another instrument, microwave radiometer, performs an absolute calibration internally, but has much coarser vertical resolution than lidar. The use of radiometer to calibrate a lidar may avoid some of the shortcomings of radiosonde calibration, ultimately providing a more accurate determination of atmospheric water vapor.

Three relatively recent papers have worked toward this goal, with the retrieval of atmospheric water vapor using observations from Raman lidar and passive remote sensors. Barrera-Verdejo et al. 2016 and Foth & Pospichal 2017 both used data from a HATPRO radiometer as well as lidar during the HOPE campaign in spring 2013 to carry out a retrieval of atmospheric water vapor, while using different lidars (BASIL and Polly^{XT}, respectively) and retrieval approaches [1][2]. The work of Turner & Blumberg 2019 also carries out a retrieval of humidity, but instead uses spectra from an atmospheric emitted radiance interferometer (AERI) and observations from the ARM lidar [3]. Each of these studies show improvement when lidar observations are added to the retrieval. However, these approaches use measurement states comprised of the passive measurement and lidar water vapor mixing ratio profiles instead of the raw lidar measurement.

The fundamental objective of this project is to develop a method for retrieving profiles of atmospheric water vapor using simultaneous raw measurements from lidar and microwave radiometer, thereby eliminating the need for radiosonde calibration. This objective will be carried out through the employment of an integrated retrieval, based around a first principles forward model characterizing the lidar and radiometer systems in order to more effectively derive an accurate water vapor product. It is the intention that this work will contribute another block to our foundational understanding of the atmosphere through the implmentation of a novel technique for retrieving water vapor through the integration of two unique sensors in order to produce something which is greater than the sum of its two components.

In Chapter 2, the importance of water vapor is discussed in terms of atmospheric processes, as well as means of quantifying and measuring it, with a focus on observations via lidar. Chapter 3 introduces the instruments used in the retrieval method, the RALMO lidar and a HATPRO microwave radiometer, with coincidental radiosondes as a comparative metric. Chapter 4 provides an overview of some of the existing techniques for calibrating Raman water vapor lidars. Chapter 5 then dives right in to the foundations for the Integrated retrieval, first providing an overview of the Optimal Estimation Method, the framework around which this retrieval is

built. The elements needed for carrying out a successful water vapor mixing ratio retrieval are discussed, along with how such elements are determined, as well as an explanation of the implementation for 3 different retrieval schemes: radiosonde-calibrated Lidar, Radiometer-only, and Integrated (radiometer-calibrated Lidar). Chapter 6 then tests these retrievals with inputs of measurements simulated from radiosonde data. Chapter 7 then looks at retrievals based on real measurements, including clear night and day observations. Finally, Chapter 8 provides a final summary of the findings, along with some suggestions for future efforts.

Bibliography

[1] Barrera-Verdejo, M., Crewell, S., Löhnert, U., Orlandi, E., and Di Girolamo, P.: Ground-based lidar and microwave radiometry synergy for high vertical resolution absolute humidity profiling, Atmospheric Measurement Techniques, 9, 4013–4028, doi:10.5194/amt-9-4013-2016, 2016.

[2] Foth, A. and Pospichal, B.: Optimal estimation of water vapour profiles using a combination of Raman lidar and microwave radiometer, Atmospheric Measurement Techniques, 10, 3325–3344, doi:10.5194/amt-10-3325-2017, 2017.

[3] Turner, D. D. and Blumberg, W. G.: Improvements to the AERIoe thermodynamic profile retrieval algorithm, IEEE Journal of Selected Topics in Applied Earth Observations and Remote Sensing, 12, 1339–1354, doi:10.1109/JSTARS.2018.2874968, 2019.

Chapter 2

A Review of Atmospheric Water Vapor

2.1 Importance of Atmospheric Water Vapor

Water vapor plays vital roles in many atmospheric phenomena. Most obvious is its presence in the hydrological cycle, which circulates water below, on, and above the Earth's surface, serving as a primary element in the development of weather patterns and climate systems. Despite having the shortest atmospheric lifetime among all greenhouse gases (averaging only 9 days [75]), water vapor plays a major role in Earth's radiative budget. Due to its ability to efficiently absorb infrared radiation, water vapor is dominant greenhouse gas [32]. However, increases in water vapor leads to more cloud formation, increasing planetary albedo and promoting cooling. The competition between these effects is difficult to quantify effectively, with estimates of roughly 50% contribution to the effect [61]. A more conclusive understanding of the net greenhouse forcing of water vapor could be achieved through more precise measurements of water vapor throughout the atmosphere [64]. Water vapor also affects atmospheric chemistry, notably in its interaction with ozone. When injected into the lower stratosphere, water vapor provides hydroxyl radicals, shifting available chlorine into catalytically-active free-radicals of ClO, resulting in greater ozone destruction [5]. The condensation of atmospheric water vapor converts substantial amounts of latent heat into sensible heat, enhancing thermally-driven

circulation [84]. This circulation facilitates the transport of aerosols, ozone, and other trace chemical species [76].

2.2 Circulation of Atmospheric Water vapor

The concentration of water vapor varies substantially, as a function of geographic location, season, and altitude. On the Earth's surface, water vapor comprises 0-4% of the atmosphere's composition, with the greatest and smallest concentrations in tropical and polar regions, respectively [4]. Above the surface, water vapor concentrations decrease quickly such that 99% of all water vapor is within the troposphere, the lowest layer of the atmosphere [53]. Water vapor enters the atmosphere via evaporation from bodies of water or transpiration from plants. Air parcels laden with water vapor are transported by winds and rise until the water vapor condenses, where it may precipitate out of the atmosphere. Such phase transitions release large quantities of latent heat into the surrounding environment, providing energy for the transport of atmospheric constituents and the development of storms.

2.2.1 Brewer-Dobson circulation

Early sounding measurements showed very little water vapor in the lower stratosphere, with concentrations less than 1 mg/m^3 above 15 km [23]. Brewer attributed the lack of stratospheric water vapor to an upper tropospheric "cold trap", where the cold temperatures cause the air to dry by condensation such that only a tiny fraction of water enters the stratosphere. These traces of water vapor enter the stratosphere in tropical regions, drifting poleward and descending into the extratropical troposphere [11]. This process, known as *Brewer-Dobson circulation*, transports trace species poleward via planetary waves and also helps explain the high ozone concentrations observed at high latitudes [23]. However, this model is purely conceptual, only providing a rudimentary understanding for this circulation mechanism.

2.2.2 Upper Troposphere-Lower Stratosphere exchange

Although extratropical stratospheric water vapor concentrations are small, they are larger than what would be supplied by the slow mean motion hypothesized by Brewer and Dobson. The primary source of stratospheric water vapor would instead be large, tropical cumulonimbus clouds. Massive storm cells can develop above land masses with dominant maritime tropical air masses such as Indonesia or India, where strong updrafts can cause these clouds to overshoot their neutral buoyancy, penetrating the tropopause and injecting some water vapor into the stratosphere [7] .

In order to understand the role of the UTLS (Upper Troposphere-Lower Stratosphere) in global circulation, it is necessary to understand the tropopause. The tropopause is a transition between the atmospheric instability of the troposphere and stability of the stratosphere. The World Meteorological Organization (WMO) defines the tropopause to be where the environmental lapse rate is less than 2° K/km, causing the height of the tropopause to vary greatly between the equator and poles. Thus, the tropopause height varies from around 7 km at the poles up to 20 km at the Equator. However, the lapse rate is not conservative, with atmospheric dynamics being better understood through potential vorticity. Under frictionless conditions with diabatic heating, potential vorticity is conserved, allowing it to act as a tracer of fluid motion [6]. Potential temperature, or the temperature if an air parcel is adiabatically moved to a 1000 mb pressure, is also conservative, serving as a tracer. The tropical tropopause is an isentropic (constant potential temperature) surface of 380 K, while the extratropical tropopause is a surface of constant potential vorticity [4]. Since the extratropical tropopause intersects isentropic lines, adiabatic eddy motions can push air and chemical constituents from the tropical upper troposphere to the extratropical stratosphere along isentropic surfaces [34] (See Figure 2.1). As a consequence, the UTLS exchange provides an important mechanism for transporting tropical water vapor poleward.

This picture of the UTLS region also shows a profound degree of coupling between constituents and conditions found in the troposphere and stratosphere. Since saturation vapor

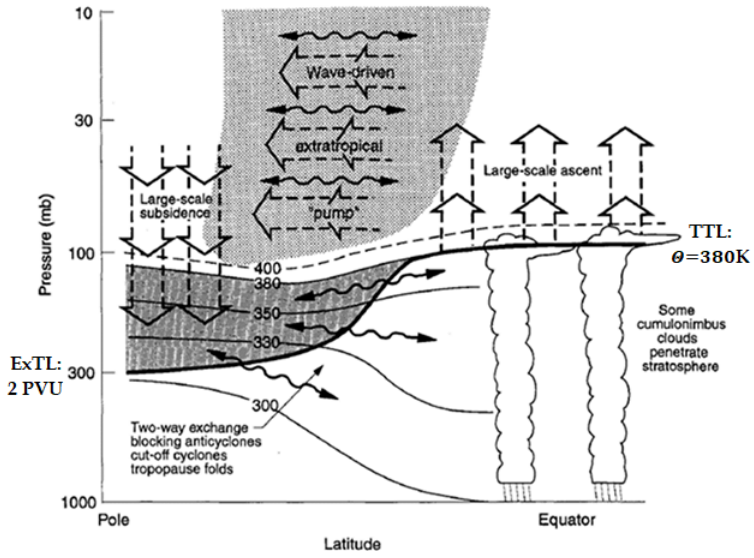

Figure 2.1: UTLS exchange. Moist equatorial air that rises above the Tropical Troposphere Layer (TTL) at the 380 K isentrope. Air is then pumped poleward, subsiding into the dark grey region (the *middle world*) above the Extra-Tropical Troposphere Layer (ExTL), where it can enter the troposphere. (Adapted from Holton et al. 1995 [34].)

pressure increases with temperature, the concentration of atmospheric water vapor is directly related to temperature. However, this relation is not restricted to one layer of the atmosphere. The abundance of water vapor in the stratosphere decreased by approximately 10% in the first decade of the 21st century, resulting in the slowing of surface temperature warming by 25% between 2000-2009 [70]. It is projected that atmospheric water vapor abundances will increase with a warming climate. Over the last 4 decades, a 3.5% increase in tropospheric water vapor have been observed, which is consistent with a 0.5° C increase in surface temperature [72]. Climate model projections indicate upper tropospheric water vapor will continue to increase, by at least 1% annually over the next century [68]. A recent study shows that reanalyses overestimate upper tropospheric water vapor by 150%, when compared to Microwave Limb Sounder observations [37].

Although lower tropospheric water vapor is important for many atmospheric processes, UTLS water vapor is of particular interest currently, due to its minuscule concentrations and the complicated nature of atmospheric processes in this region. The ability to more accurately retrieve water vapor in this region would be instrumental in better understanding this region

and the atmosphere as a whole.

2.3 Measuring Atmospheric Water Vapor

2.3.1 Quantities

There are a number of metrics used by the atmospheric and meteorological communities to quantify water in the atmosphere.

Absolute humidity is the density of water vapor in an air parcel, expressed as:

$$AH = \frac{m_{wv}}{V_{air}} \ [\mathrm{g/m^3}] \tag{2.1}$$

where m_{wv} is the mass of water vapor and V_{air} is the volume of the air parcel. However, changes in temperature and pressure will affect the volume of the air parcel and thus the absolute humidity, making this a poor means of measuring humidity under changing atmospheric conditions [4].

A more familiar quantity is relative humidity, defined as the ratio of water vapor content to the capacity of the parcel:

$$RH \simeq 100\frac{e}{e_s} \ [\%] \tag{2.2}$$

where e is the vapor pressure, or the pressure exerted by molecules on the air parcel, and e_s is saturation vapor pressure, which tells how much water vapor is needed to saturate the air at a certain temperature. When the air's vapor pressure equals the saturation vapor pressure, the relative humidity is 100% and the air is saturated with water vapor. Saturation vapor pressure increases exponentially with temperature. As a result, relative humidity greatly varies with diurnal changes in temperature (possibly changing by 50% over the course of a day [84]), which may not be indicative of the total water vapor content.

Mixing ratio is the ratio of the atmospheric constituents content to the dry air content. In the case of water vapor, the volume mixing ratio is the ratio of the water vapor density to the

to the density of dry air in an air parcel:

$$w_V = \frac{n_{wv}}{n_{dry}} \text{ [ppmv]} \tag{2.3}$$

where n_{wv} and n_{dry} are the water vapor and dry air density, respectively. Depending on the abundance of the quantities, it may be expressed as moles per mole (mol/mol), or parts per million/billion/trillion by volume (ppmv/ppbv/pptv) for trace species. It can also be expressed as the ratio of the mass of water vapor to dry air (mass mixing ratio):

$$w_m = \frac{m_{wv}}{m_{dry}} = \frac{n_{wv}}{n_{dry}} \frac{M_{wv}}{M_{dry}} = \frac{M_{wv}}{M_{dry}} \cdot w_V \text{ [g/kg]} \tag{2.4}$$

where M is the molecular weight. Unlike relative humidity, mixing ratio is conserved under dynamic conditions where the phase is unchanged, serving as an indicator of air motion [87]. Mass mixing ratio is preferred for thermodynamic studies and investigations of tropospheric radiative transfer, while volume mixing ratio is generally used in stratospheric investigations involving chemical reactions where mass is not conserved but volume is (such as ozone destruction or creation) [7]. Closely related to mixing ratio is the specific humidity, which is expressed in terms of mixing ratio, as:

$$q = \frac{w_m}{1 + w_m} \tag{2.5}$$

While mixing ratio is a ratio relating the water vapor mass to the mass of dry air in a parcel, specific humidity is proportion of water vapor mass to the total parcel mass. Thus, these quantities can be quite similar for tiny concentrations, but deviate with increased water vapor.

The aforementioned quantities can be measured at a single position (such as a surface measurement) or as height profile by certain in situ or remote sensing instruments. However, some passive remote sensing instruments can monitor the water vapor content in a vertical

column. This quantity, known as integrated water vapor (IWV), is expressed as:

$$IWV = \int_{z_0}^{z} \rho_{dry} w_m dz \ \ [\mathrm{kg/m^2}] \tag{2.6}$$

where ρ_{dry} is the density of dry air. This term is closely related to the total precipitable water, or precipitable water vapor, which gives the height of the water in a column if all of the water precipitates as rain. It is determined by replacing the dry air density with the density of liquid water. Similarly, liquid water path is a measure of the total liquid water content in a column, and has a formulation similar to integrated water vapor, but requires the liquid water mixing ratio instead of the water vapor mixing ratio.

2.3.2 Instruments

Early Instruments

It has been known for centuries that certain materials respond to changes in humidity. Materials such as hair, whale bone, and goldbeater's skin (parchment-like sheet composed of animal intestine, on which goldsmiths would beat gold into flat leaves [15]) will contract under drier conditions and expand or extend in more humid conditions. The degree of contraction or expansion can be measured and used to empirically determine relative humidity via an instrument called a *hygrometer*. In the case of human hair, an increase from 0 to 100% relative humidity will increase the length of hair by 2.5% [4]. More recently, electric hygrometers have been used, which employ a flat plate coated with a carbon film, in which the resistance changes with moisture.

Radiosondes

Radiosondes are in situ meteorological instruments carried by weather balloon. Due to their mobility and ease of use, they are commonly used during field campaigns as well as routine measurements at weather stations. These balloons are generally equipped with a modern

hygrometer, which uses a substrate covered with a hydrophilic polymer coating, which acts as the dielectric in a capacitor. Water molecules are caught by the polymer, causing the current across the thin-film capacitor to increase directly with the number of molecules [49]. In addition to measuring relative humidity via this capacitive hygrometer, temperature, pressure, and wind speed/direction from the surface and into the stratosphere may also be measure. However, radiosondes are primarily intended for measurements in the troposphere, suffering from complications in the extremely cold and dry conditions of the upper troposphere and lower stratosphere. That is, when temperatures drop below -40° C, the hygrometer's response time can be delayed by more than 20 s, approximately 40 times longer than the response time for temperatures near +20° C [2]. Additionally, relative humidity values of less than 5% can yield uncertainties greater than 10% [49].

Balloon-Borne Cryogenic Frostpoint hygrometer (CFH)

CFHs (Cryogenic Frost-point Hygrometers) are an alternative balloon-borne measurement technique addressing some of the concerns regarding the accuracy of UTLS water vapor measurements. Developed by a team at the University of Colorado, a CFH determines water content by maintaining a near-constant condensate layer on a mirror. The thickness of this layer is held stable by a heating element as well as a cryogenic coolant. When the mirror is in equilibrium with its surroundings, its temperature is also the frost-point temperature, which can then be used to calculate a relative humidity. One advantage of this technique is lesser uncertainties than conventional radiosondes, which do not exceed 10% for altitudes below 25 km. One drawback of CFHs is that cloudy weather complicates their ability to measure water vapor, as the cloud droplets may not be in thermal equilibrium [81]. As these droplets are generally cooler than the ambient air, a frost-point hygrometer passing through a cloud would measure a lower temperature and consequently, a larger relative humidity, possibly resulting in a relative humidity greater than 100% [82].

Microwave Radiometers (MWR)

This passive remote sensing instrument detects the radiance, the radiation power per unit area per unit frequency per unit sold angle ($W/m^2/Hz/sr$), emitted by atmospheric gases on the wings of pressure-broadened rotational lines at specific microwave frequencies [69]. Since the radiance values are tiny in the microwave region, they are generally converted to brightness temperature, or the physical temperature at which an ideal blackbody would emit [30]. The combination of intensity measurements at different frequencies can be used to compute a total column measurement, or the mass of water vapor in a column of air [33]. The oxygen complex at 60 GHz allows for temperature profiling [20], whereas the intense water vapor line at 183 GHz as well as a weaker line at 22 GHz contain information for humidity profiling [43]. Although the 183 GHz line is much more sensitive to water vapor than the 22 GHz, the atmosphere is also much more opaque at this frequency [58]. Therefore, measurements using the 183 GHz line are possible for space-based, high-altitude, or low-humidity observations, while 22 GHz measurements are appropriate for ground-based observations. Although the temporal resolution is generally on the order of hours to days, spatial resolution increases with height, giving high sensitivity in the upper stratosphere and mesosphere up to 80 km [38]. Despite the high sensitivity in the upper atmosphere, the spatial resolution is poorer than active remote sensors like lidar in the lower atmosphere due to their smooth weighting functions [29]. Despite their relatively poor vertical resolution, radiometers have the distinct advantage of being able to carry out an absolute calibration.

Lidar

Unlike microwave radiometers, lidar (LIght Detection And Ranging) is an active remote sensing technique, in which a narrow-band laser is pulsed into the sky where the photons are scattered by atmospheric constituents. A small fraction of these photons are backscattered and collected by a receiver system, where the backscatter is detected as photocounts. The time between the laser pulse and photocount detection is directly related to the height of

the backscatterer, allowing one to generate altitude-dependent profiles of the backscattering species' density. Despite the complicated nature of their set up, lidars do have the advantage of high spatial and temporal resolution, making them ideal for monitoring the variability of atmospheric water vapor [57]. Although they have the ability to sample the atmosphere with excellent vertical resolution, calibration against an external source is required for determining atmospheric water vapor content via Raman lidar. More details regarding the Raman lidar technique and instrumentation will be provided in Section 2.4. Another lidar capable of determining water vapor is Differential-absorption lidar (DIAL), where two laser pulses (one on and one off the water vapor absorption line) are emitted. As the molecular scattering is virtually equivalent if the wavelengths are close enough, the change in the backscattered signal for each wavelength is related to the absorption by molecules of water vapor at each wavelength. DIAL is not as dependent on calibration as Raman lidars, but is a more complicated than Raman lidar systems due to the need to tune the laser to the desired spectral line [80].

Other instruments

Fourier Transform Infrared Spectrometry is another technique for determining atmospheric water vapor content, using an interferometer to determine the infrared absorption of water vapor [21]. Like the microwave radiometer, it is a passive remote sensing instrument which can retrieve highly accurate total column measurements, but with poor vertical resolution.

Satellites can also be equipped with instruments capable of measuring water vapor. For example, the Atmospheric Chemistry Experiment mission uses solar occultation to measure various atmospheric species, including water vapor [14]. Although such satellites provide excellent coverage on global scales, profiles of water vapor generally very coarse vertical resolution as well.

Aside from ground-based sensors and radiosondes, in situ measurements can also be made via aircraft. MOZAIC, for example, is an airplane which has been equipped with various meteorological instruments [44]. As with radiosondes, its measurements are limited to when

the aircraft is in flight.

2.3.3 Difficulties in comparing instruments

Intercomparisons between instruments are essential for validating the accuracy of measurements. However, some issues arise when comparing instruments that employ different techniques to retrieve humidity measurements.

Comparisons between lidar and radiosonde water vapor measurements can sometimes be problematic. The fundamental difference between a lidar and radiosonde measurement is that lidar is stationary, while the radiosonde is balloon-borne. The lidar is constrained to sampling the atmosphere at a single location, while the radiosonde can drift, generally drifting about 50 km from their starting point by the time they reach the lower stratosphere [62]. Additionally, radiosondes collect data continuously during its ascent, while lidar counts are usually summed or averaged over a certain time interval.

Another complication comes from the conversion between mixing ratio and relative humidity. The hygrometer on a radiosonde measures relative humidity while mixing ratio comes out naturally when measuring lidar photocounts from nitrogen and water vapor backscatter. These, in order to compare measurements from the two instruments and calibrate the lidar, it is necessary to convert radiosonde relative humidity into mixing ratio. The relation between these two quantities is:

$$RH = 100 \cdot \frac{w}{w_s} \simeq 100 \cdot \frac{e}{e_s} \tag{2.7}$$

where w_s is the saturation mixing ratio, or the ratio of mass of saturated water vapor to the mass of dry air. It can be written as [52]:

$$w_s = \frac{M_w}{M_d} \frac{e_s}{p_{dry}} = \frac{M_w}{M_d} \frac{e_s}{p - e_s} \tag{2.8}$$

where e_s is the saturation vapor pressure. The saturation vapor pressure is derived from the Clausius-Clapeyron equation, which requires latent heat. Thus, the saturation vapor pressure

over ice differs from the pressure over liquid water. Supercooled water has a greater Gibbs energy and therefore greater vapor pressure than ice, which gives a maximum difference between the vapor pressures of liquid water and ice at 261.3 K [50]. Furthermore, water can also exist in a supercooled liquid phase down to 230 K [84]. As a result, there are a number of models used to calculate saturation vapor pressure, many of which diverge at lower temperatures.

Although microwave radiometers do not require the same level of corrections as radiosondes do under cold and dry conditions, comparisons with lidar can still be challenging. In order to convert the lidar's mixing ratio into a total column measurement, the mixing ratio needs to be integrated over the range of altitudes covered by the radiometer [27]. However, due to the geometric overlap of these active remote sensors (more discussion on the topic in Section A.2.3), many lidars cannot effectively measure returns from the lowermost altitudes of the atmosphere. This starting point varies between instruments, but lidars with water vapor-retrieving capabilities generally cannot use measurements from the first few hundred meters above the surface. Thus, mixing ratio values for the bottom of the atmosphere must be assumed or incorporated from other measurements, introducing additional uncertainty.

2.4 Introduction to Atmospheric Lidar

Figure 2.2 shows the set up for a Raman lidar system capable of detecting water vapor. The laser is pulsed into the sky, where it is scattered by atmospheric constituents (Rayleigh and Raman scattering is discussed in Section 2.4.2). The backscatter is collected by a receiver, and then directed into the detection unit.

2.4.1 Historical Overview

A 1930 paper first suggested the use of light beam scattering to determine atmospheric density, in which hundreds of searchlights would be pointed at a patch of sky and the backscatter collected in a large mirror and photo-cell receiver [74]. A few years later, Tuve suggested using

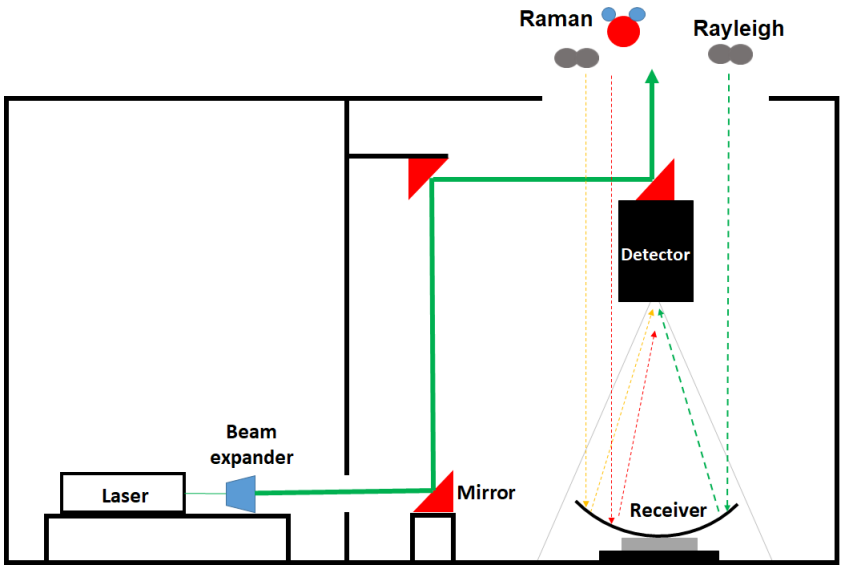

Figure 2.2: Simple schematic of a lidar system. The laser beam is directed into the sky, where it interacts with atmospheric molecules. Note that Rayleigh scattering is inelastic, and Raman scattering is inelastic (causing a change in the wavelength of the scattered light). For example, if the laser pulses are emitted at 532 nm, the Rayleigh backscattered light will also be at 532 nm, while the Raman backscatter from nitrogen and water vapor will be at 607 nm and 660 nm, respectively. The backscattered laser light is collected in a receiver and sent to the detectors.

a modulated searchlight instead, so that the background would only be a Fourier component of sky light, increasing the possible range of observation [77]. The searchlight remote sensing method was put into practice in the early 1950s, when Elterman set up a modulated searchlight transmitter and 60 inch mirror receiver placed 20 km apart on separate peaks in the Sandia mountains of New Mexico, generating rudimentary density profiles up to 67 km [26]. The invention and early developments of the laser in the early 1960s, providing extremely narrow, nearly monochromatic light, would profoundly improve our ability to carry out active remote sensing of the atmosphere. The laser replaced the white searchlight, where the laser radar is used to hear 'echoes' from the atmosphere under clear conditions [28][17]. In the early 1960s, Clemesha used a Q-spoiled ruby laser with a rapidly-moving shutter to reduce laser-induced fluorescence from the lowest-altitude returns [16].

To avoid complications from aerosol backscatter at the laser wavelengths, Cooney used a 694.3 nm laser to measure the Raman-shifted backscatter of molecular nitrogen at 828.5 nm

[18]. Soon after, Melfi used the Raman-shifted backscatter approach to detect atmospheric water vapor up to 2 km via a frequency-doubled, Q-switched ruby laser [48]. Calibration was carried out by comparing lidar water vapor measurements to humidity sensors mounted on a weather tower [73] and balloon sondes [47]. By the late 1980s, instrumentation had improved so that water vapor observations could be made up to the tropopause [78], with detection of lower stratospheric water vapor by the late 1990s [13][25].

2.4.2 Scattering

Lidars can detect interactions between laser light and atmospheric particulates via Mie, Rayleigh, or Raman scattering events. For particles much larger than the wavelength of emitted light, such as many aerosol species, Mie scattering occurs. Rayleigh scattering, on the other hand, occurs when light interacts with particles smaller than its wavelength. Rayleigh scattering can therefore be used to detect atmospheric species such as molecular nitrogen and oxygen. As it is also an elastic process, energy is neither released or absorbed during the scattering process, causing the backscatter to be at the same wavelength as the incident beam. Due to their intense backscatter in the middle and upper atmosphere, Rayleigh lidars can measure density and temperature to more than 100 km [40].

Raman scattering, on the other hand, is inelastic, resulting in the release or absorption of energy. The change in energy causes a frequency shift due to transitions in the molecular rotational and vibrational energy levels. Depending on whether energy is gained or lost, the transition is either referred to as an *Anti-Stokes* or *Stokes* shift, respectively. However, most Raman lidar systems are designed to monitor the Stokes frequency, as the Anti-Stokes vibrational shift is rarely observed beyond first order states since there is not enough collisional energy for excitation to vibrational states at atmospheric temperatures [41]. The Stokes shift band can be further categorized into branches. Of the 3 branches, the Q-branch has the largest intensity and cross section, while the surrounding branches (O and S) have lesser intensities, resulting from changes in the rotational quantum number, J. The Raman shifts for water va-

por are 3651.7 cm^{-1} and 2330.7 cm^{-1} respectively [8]. For light at 532 nm, the resulting bands for Raman water vapor and nitrogen would be centered near 660 nm and 607 nm, respectively. Rayleigh backscatter is much more intense than Raman backscatter, with the nitrogen Raman scattering cross section being nearly 1150 times smaller than the Rayleigh scattering cross section [8]. However, Raman scattering has the distinct advantage of ensuring backscatter from only one type of molecule [42]. For this reason, Raman lidar is used for detecting specific molecular species, including nitrogen, oxygen, or water vapor.

2.4.3 Lidar Equation

The lidar equation provides an estimate of the signal that should be received, accounting for the ways by which light first emitted by the laser is lost before reaching the detectors. In order to make the equation practical, a number of assumptions are made [41]:

1. Single and independent scattering events only (not good for opaque or cloudy conditions) [86].

2. Atmospheric parameters are constant over the spatial range of the laser pulse. These pulses are generally a few nanoseconds, a spatial range of a few meters.

3. The total range of observation should be much greater than the laser pulse range.

4. The optical depth of the range is small, within the lidar operating range.

5. The field-of-view (FOV) of the optics is larger than the laser beam divergence.

The Raman-scattering lidar equation for molecular species X in terms of laser power can be written as [88]:

$$P(\lambda_X, z) = P_0(\lambda_L) \cdot \frac{A}{z^2} \cdot n_X(z) \cdot \frac{d\sigma_X(\lambda_L, \pi)}{d\Omega} \cdot \xi(\lambda_X) \cdot O_X(z) \cdot \Gamma(\lambda_L, z) \cdot \Gamma(\lambda_X, z) + P_B \qquad (2.9)$$

where:

$P(\lambda_X, z)$ = Height-dependent received backscatter power [W]

$P_0(\lambda_L)$ = Output power of the laser $[W]$

A = Area of the telescope's primary mirror $[m^2]$

n_X = Number density of the species $[m^{-3}]$

$\frac{d\sigma_X(\lambda_L,\pi)}{d\Omega}$ = Differential backscattering cross section $[m^2 sr^{-1}]$

ξ = Instrument efficiency

O_X = Overlap function

$\Gamma(\lambda_L, z)$ = Atmospheric transmission function (before scattering)

$\Gamma(\lambda_X, z)$ = Atmospheric transmission function (after scattering)

P_B = Background power $[W]$

The height dependence of the received power is actually a function of the relay time, $z = \frac{c\cdot\tau}{2}$, where c is the speed of light, τ is the laser pulse duration. The total transmission is determined by combining the upward and downward transmission functions: $\Gamma(\lambda_L, z) \cdot \Gamma(\lambda_X, z) = \exp(-\int_0^z [\alpha(\lambda_L, z') + \alpha(\lambda_X, z')]dz')$, where α is the extinction coefficient $[m^{-1}]$, which accounts for the absorption and scattering of other atmospheric constituents. The extinction coefficient is written as: $\alpha = \sum_i \sigma_{ext,i} \cdot n_i(z)$, where σ_{ext} is the sum of scattering and absorption cross sections [46]. Written in terms of signal, or photocount rate, the lidar equation becomes:

$$N(\lambda_X, z) = \frac{P_0(\lambda_L)\cdot\Delta t}{hc/\lambda_L}\cdot\frac{A}{z^2}\cdot n_X(z)\cdot\frac{d\sigma_X(\lambda_L,\pi)}{d\Omega}\cdot\xi(\lambda_X)\cdot O_X(z)\cdot\exp(-\int_0^z[\alpha(\lambda_L,z')+\alpha(\lambda_X,z')]dz')+N_B \tag{2.10}$$

where Δt is the time bin length. A shorthand version of this may be shown as:

$$N_X = N_0 \cdot \frac{A}{z^2} \cdot n_X \cdot \sigma_X \cdot \xi_X \cdot O_X \cdot \Gamma_X + N_{B,X} \tag{2.11}$$

These terms will be discussed in more detail in the following section.

2.4.4 Water Vapor Mixing Ratio equation for Lidar

The water vapor mixing ratio (WVMR) is used extensively to quantify water vapor measured by lidar. The WVMR can be expressed as [89]:

$$w_m = \frac{m_H}{m_{dry}} = \frac{M_H}{M_{dry}}\frac{n_H}{n_{dry}} = \frac{M_H}{M_{dry}} \cdot \frac{n_N}{n_{dry}} \cdot \frac{n_H}{n_N} \approx 0.781\frac{M_H}{M_{dry}} \cdot \frac{n_H}{n_N} \tag{2.12}$$

where the subscripts H and N represent quantities related to water vapor and nitrogen respectively. The nitrogen volume mixing ratio , $\frac{n_N}{n_{dry}}$, is well-determined to be constant up to 80 km, with a value of approximately 0.781 mol/mol [39][63]. Rearranging the shorthand lidar equations for nitrogen and water vapor (Equation 2.11), and substituting them into the above WVMR gives the WVMR equation for lidar:

$$w_m = \frac{M_H}{M_{dry}} \cdot \frac{n_N}{n_{dry}} \cdot \frac{\sigma_N}{\sigma_H} \cdot \frac{\xi_N}{\xi_H} \cdot \frac{O_N}{O_H} \cdot \frac{\Gamma_N}{\Gamma_H} \cdot \frac{N'_H}{N'_N} \tag{2.13}$$

where N'_H and N'_N are the background-subtracted count rates of water vapor and nitrogen, respectively.

The lidar water vapor mass mixing ratio equation can also be written as:

$$w_m(z) = \frac{M_H}{M_{dry}} \cdot \frac{n_N}{n_{dry}} \cdot \frac{\sigma_N(\lambda_N)}{\sigma_H(\lambda_H)} \cdot \frac{\xi_N(\lambda_N)}{\xi_H(\lambda_H)} \cdot \frac{F_N(T,z)}{F_H(T,z)} \cdot \frac{O_N(z)}{O_H(z)} \cdot \frac{\Gamma_N(\lambda_N,z)}{\Gamma_H(\lambda_H,z)} \cdot \frac{N_H(z)}{N_N(z)} \tag{2.14}$$

where the new term $F_X(T,z)$ is a correction accounting for the temperature dependence of the backscattering cross section. It is important to note that $N_H(z)$ and $N_N(z)$ are the corrected count rates for the water vapor and nitrogen channels respectively, which are discussed in Section A.2.1.

Raman backscattering cross section

In the early days of Raman lidar, measured and modelled cross sections for water vapor were poorly constrained. The inverse cross section ratio, $\frac{\sigma_H}{\sigma_N}$, was determined by estimating the

other terms in the WVMR, and rearranging it to solve for the ratio, assuming the other terms in the WVMR were accurate. Some such studies found the ratio to be: 5 [19], 4 [48], 3 [73]. The variability of these ratios required a more sophisticated way of determining the cross section values.

The differential scattering cross section, $\frac{d\sigma_X}{d\Omega}$ or sometimes integrated over the entire solid angle to give σ_X for channel X, is an important quantity to measure, as it determines the degree of backscatter. The differential cross section for Rayleigh scattering from a molecule subject to a beam of unpolarized light is:

$$\frac{d\sigma_m(\phi)}{d\Omega} = \frac{\pi^2(n^2-1)^2}{N^2\lambda^4}(1+cos^2\phi) \tag{2.15}$$

where n is the index of refraction, and N is the number density of scatterers [46].
The Raman backscatter differential cross section is more complicated, as it deals with vibrational (Δv) and rotational (ΔJ) transitions. The total cross section from a diatomic nitrogen molecule is:

$$\left(\frac{d\sigma_j}{d\Omega}\right)_{tot} = \left(\frac{2\pi}{c}\right)^4 \frac{b_j^2(\nu_0-\nu_j)^4}{[1-exp(-h\nu_j/kT)]} g_j\left(\alpha_j'^2 + \frac{7}{45}\gamma_j'^2\right) \tag{2.16}$$

where ν_j is the Raman shift, $b_j = \sqrt{h/8\pi^2\nu_j}$ is the zero point vibrational amplitude of the mode, g is the degree of degeneracy of the nth vibrational mode, and α and γ are isotropic and anisotropic polarizability coefficients [36]. Although the total cross section is composed of many transition lines, it can be well-approximated by the 3 strongest branches: Q ($\Delta J = 0$), S (ΔJ=-2), and O (ΔJ=2) [42]. The Q-branch is:

$$\left(\frac{d\sigma_j}{d\Omega}\right)_{Q} = \left(\frac{2\pi}{c}\right)^4 \frac{b_j^2(\nu_0-\nu_j)^4}{[1-exp(-h\nu_j/kT)]} g_j\left(\alpha_j'^2 + \frac{7}{180}\gamma_j'^2\right) \tag{2.17}$$

and the S and O-branches [35] are both equivalent to:

$$\left(\frac{d\sigma_j}{d\Omega}\right)_{S,O} = \left(\frac{2\pi}{c}\right)^4 \frac{b_j^2(\nu_0-\nu_j)^4}{[1-exp(-h\nu_j/kT)]} g_j\frac{7}{60}\gamma_j'^2 \tag{2.18}$$

Adam [3] gives an excellent overview of how the nitrogen cross section is derived and calculated.

As water is not a diatomic molecule, modeling its cross section is more challenging. The cross section was estimated experimentally by Penney and Lapp [54]. As the cross section of molecular nitrogen was already well-defined by this time [55], the cross section ratio was estimated to be $\frac{\sigma_H}{\sigma_N} = 2.5$, with an uncertainty of 10 % [54] A later experiment was carried out by [59], giving a ratio of 3.1 with an uncertainty of 0.6 %, though the details of the investigation are not provided. Unfortunately, little experimentation regarding the water vapor cross section has been carried out since.

Avila et al. 1999 [9] developed a model for the OH-stretching spectrum of water vapor, considering both anisotropic and isotropic components. The Raman cross section is given by:

$$\left(\frac{\partial\sigma}{\partial\Omega}\right) = (\nu_\circ - \nu)^4 \frac{e^{-\frac{E_\circ}{kT}}}{Z(T)} \left(A^{XX} + A^{XY}\right) \tag{2.19}$$

where ν_o is the laser wavenumber, E_o is initial energy level, Z is the partition function, and A^{XX} and A^{XY} are coefficients of energy level transitions for parallel and perpendicular polarization, respectively. These coefficients were adapted in Avila et al. 2004 [10] to consider experimental and theoretical upgrades. Currently, this is the best estimate for the water vapor cross section.

Instrument efficiency

The instrument efficiency factor, $\xi_X(\lambda_X)$, accounts for the performance and efficiency of the instruments and optics through which the laser beam and backscattered signal travel. This includes transmittance through optics such as lens, interference filters, or beam splitters, reflectance off of mirrors or beam splitters, attenuation by neutral density filters, and quantum efficiency of PMTs (photomultiplier tubes). A detailed discussion of determining the instrument efficiency for a lidar system (the Purple Crow Lidar) is provided in Appendix A.2.3.

The performance of PMTs decays over time due to light exposure. Additionally, depending

on the design of the PMT, it may also be subjected to degradation caused by a slow, gradual outgassing [67]. Not only could PMTs degrade at different rates depending on the design and amount of light exposure, but the active surface of the PMT could also degrade differentially. This was tested by Simeonov, where a green LED was used to scan across the PMT surface, finding that the sensitivity varied between 0.2 and 2.8 times the average value [66].

Often, the optical manufacturers will provide specifications of these properties with the product. However, in the case of PMTs and coated optics such as interference filters, these properties may change over time. PMTs suffer from fatigue over time, due to stresses imposed by persistent light exposure and temperature fluctuations, causing the quantum efficiency to degrade over time [67]. The coating on interference filters also degrades over time (particularly for sharp-edged filters), reducing the transmittance and gradually shifting the peak wavelength over time [22]. Thus, the manufacturer's specifications can not always be trusted for aging instruments, and even if the instruments are identical in design, being exposed to different frequencies and intensities will differentially degrade the optics. Regular measurement of the efficiencies for the individual instruments is key for ensuring the overall instrument efficiency is accurate.

Temperature Dependence Function

As temperature increases, transitions further from the Q-branch ($\Delta J = 0$) become more likely [88]. As a result, changes in atmospheric temperature with altitude will affect the Raman cross section spectra for water vapor and nitrogen. Since a spectrum analyzer, such as an interference filter or grating polychromator, is carefully chosen for an optimal signal-to-noise ratio at the specific Raman wavelength, changes in the spectrum due to atmospheric temperature variations with height could result in signal loss. For very wide filters covering the full Raman spectrum, there is no temperature sensitivity, since most molecules would already be in the vibrational ground state at temperatures normally found in Earth's atmosphere [12].

The temperature dependence function is defined for channel X as [88]:

$$F_X(T) = \frac{\int_{\Delta\lambda_X} \frac{d\sigma_X(\lambda,\pi,T)}{d\Omega}\xi(\lambda)d\lambda}{\frac{d\sigma_X(\pi)}{d\Omega}\xi(\lambda_X)} \tag{2.20}$$

where $\frac{d\sigma_X(\lambda,\pi,T)}{d\Omega}$ is the wavelength and temperature-dependent cross section and $\xi(\lambda)$ is the instrument efficiency, which are integrated over the filter's passband, $\Delta\lambda_X$. It is normalized by $\frac{d\sigma_X(\pi)}{d\Omega}$, the total cross section as well as the instrumental efficiency, $\xi(\lambda_X)$, at the laser wavelength. Since only the interference filter's transmission varies with temperature (assuming the PMTs are kept in a temperature-controlled environment), the instrument function here can be approximated as the interference filter's transmission [60]. The terms integrated in the numerator could instead be summed or convolved, as the individual Raman transition lines are much more narrow than the transmission curve of the interference filter [79][63]. Since this function is dependent on the shape of the interference filter's transmission curve, the factor varies largely with the filter's peak wavelength and bandwidth [88].

Calculating $\frac{F_N}{F_H}$ gives a temperature-dependent correction factor. In order to apply it to the water vapor mixing ratio, $\frac{F_N}{F_H}$ must then be converted to an altitude-dependent correction by means of a temperature profile, such as a radiosonde profile or a US Standard Atmosphere Model profile, introducing additional sources of uncertainties.

Geometric Overlap

The overlap function, or geometric compression, accounts for the possibility of light lost at the lowest altitudes due to the transmitted laser beam not being completely contained within the receiver's field-of-view [31]. The function is unity if the laser beam divergence angle is

less than the telescope's opening angle [46], and can be written as [71]:

$$O(z) = \begin{cases} 0 & \nu(z) \geq (s + e(z))/2 \\ \frac{\{\psi_1(z) - \sin\psi_1(z)\}s^2 + \{\psi_2(z) - \sin\psi_2(z)\}e^2(z)}{2\pi e^2(z)} & |s - e(z)|/2 < \nu(z) < s + e(z)/2 \\ s^2/e^2(z) & \nu(z) < [e(z) - s]/2, e(z) > s \\ 1 & \nu(z) < [s - e(z)]/2, e(z) \leq s \end{cases} \tag{2.21}$$

where $\psi_1(z) = 2\arccos\frac{s^2+4\nu^2(z)-e^2(z)}{4\nu(z)s}$, $\psi_2(z) = 2\arccos\frac{e^2(z)+4\nu^2(z)-s^2}{4\nu(z)e(z)}$, the area illuminated by the beam is $e(z) = f(\delta + \frac{b_0+D}{z})$, and $\nu(z) = |f\frac{d_0-\Theta z}{z}|$ is the offset between the illumination area and telescope's field of view.[1] The fundamental input parameters are then:

D = Telescope's primary mirror diameter

f = Telescope's focal length

s = Receiver aperture

b_0 = Initial beam diameter

δ = Initial beam divergence

d_0 = Lateral displacement between the laser beam and telescope axis

Θ = Laser beam angle with respect to the telescope axis

However, since this relation is wavelength-independent, and since lidars generally employ reflective telescopes which are virtually free from chromatic aberrations, the overlap functions for the water vapor and nitrogen channels should cancel [22]. Despite the unity of the aforementioned overlap equation, differential overlap may still be an issue. This overlap effect can be directly estimated in the same manner as the empirical calculation of the cross section ratio. Assuming the other terms in the WVMR are correct, it can be rearranged to solve for the overlap ratio [85]. Alternately, it can also be gauged by replacing the water vapor interference filter with one identical to the nitrogen channel filter, and finding the resulting signal ratio [78][89].

[1] The first conditional expression in the overlap function has been altered from the original text of Stelmaszczyk et al. 2005, which gives it as $\nu(z) \geq s + e(z)/2$.

Atmospheric Transmission

The atmospheric transmission function accounts for laser beam attenuation in the atmosphere due to aerosol extinction, ozone absorption, and additional molecular scatterings [63]. The transmission function for each channel must consider the transmission going up into the atmosphere at the laser's wavelength, and the transmission coming back at the Raman-shifted wavelength. The Raman transmission can be expressed as:

$$\Gamma_X(z) = e^{-\tau_X} \tag{2.22}$$

where the optical depth, τ, takes molecular and aerosol extinction into consideration:

$$\tau_X(z) = \tau_{mole} + \tau_{aer,X} = \int_0^z \sigma_{ray} n_{air} dz + \tau_{aer}(\lambda_L)(\frac{\lambda_X}{\lambda_L})^{-a} \tag{2.23}$$

in which a is the Angstrom exponent, used for empirically finding the aerosol optical depth [65].

Corrected Count rates

The WVMR equation (Equation 2.14) requires the corrected count rates from Raman water vapor, N'_H, and nitrogen, N'_N, backscatter.

Dark counts, or a tiny, non-zero count rates detected in the absence of visible light, should be accounted for when processing raw signal. It can originate from infrared photons (*thermionic* emission), or other electronic effects, such as an analog floating voltage, stray background noise, or signal-induced noise [1]. The current associated with such counts is generally between 10^{-17}-10^{-13} A at room temperature, depending on the detector's design [46]. In the case of the CANDAC Rayleigh-Mie-Raman lidar in Eureka, Nunavut, dark profiles can be measured and consequently subtracted by acquiring data with all detector apertures blocked as well as the trigger and flash lamps on, but the laser not firing [45]. The dark counts can be minimized

by cooling the detectors to below room temperature, and by replacing or updating the PMTs as they get noisy with age [1].

In addition to preliminary dark count subtraction, counts from the ambient background while the system is running must also be subtracted. Background photocounts originate from ambient light such as the Sun or Moon, as well as from the opto-electronics and potential leaks in the detectors [45]. It is generally defined as the region in the uppermost portion of the profile, above which the signal drops to the noise level, where the signal-to-noise ratio approaches 1. In general, the background can be considered a height-independent white light, making a scalar subtraction across the whole profile sufficient. However, it may instead be height-dependent, requiring the background counts to be interpolated and then subtracted accordingly. As a rule of thumb, if the slope of the background trend is larger than the slope's uncertainty, then a linear background removal is needed [13].

For photon counting (PC) detection, applying a nonlinearity (dead time) correction for high count rates is essential. Also referred to as pulse pileup, this saturation effect results in fewer measured counts than actual counts. The sampling detection rate is inversely related to the dead time, the time when the system cannot differentiate between adjacent pulses. Depending on the detection system used, there are 2 possible modes of correcting for the pulse pileup: non-paralyzable and paralyzable. For a non-paralyzable system, the dead time is not extended by successive photons, whereas a paralyzable system can become temporarily paralyzed, as any subsequent photons arriving during within the dead time of the first photon pulse will extend the length of the first dead time. The correction for the paralyzable system can be written as:

$$N_O = N_T \cdot \exp(-N_T \cdot \tau_d) \tag{2.24}$$

while the correction for non-paralyzable dead time is:

$$N_O = \frac{N_T}{1 + N_T \cdot \tau_d} \tag{2.25}$$

where N_O is the observed count rate, N_T is the true count rate, and τ_d is the dead time [24].

In addition to a PC detection mode, some detection systems consist of analog detection, in which voltage is measured instead of discrete signal pulses. PC counts provide best sensitivity at higher altitudes, while analog counts are not vulnerable to pulse pileup, make them preferable at lower altitudes. Merging, or gluing, the two channels into a single profile would therefore improve the dynamic range of the retrieval. After fulfilling the previously mentioned processing steps, a linear regression of the PC and analog ordered pair arrays is carried in a region where the PC counts are linear and the analog counts are above the noise threshold [56]. The regression can be used to convert the analog counts to *virtual* PC counts:

$$PC' = a \cdot AD + b \tag{2.26}$$

where PC' is the virtual PC count rate, AD is the analog count rate, and a and b are the slope and intercept of the regression between the PC and analog count arrays, respectively. The merged profile is then constructed such that the virtual PC counts replace the original PC counts, if the PC count rate is above a certain cutoff value. For the US Department of Energy's Raman lidar near Billings, Oklahoma, this cutoff value is 50 MHz [51]. For the Howard University Raman Lidar, it is 10 MHz [83]. One major issue with this approach is the lack of procedural standards for the parameters, such as the ranges of the linear region or the cutoff count rate, making its incorporation into systematic processing difficult. Depending on the system, additional processing steps may be needed. See Appendix A.2 for more details about some the processing specific to the Purple Crow Lidar system.

Bibliography

[1] Photomultiplier Handbook, Tech. rep., Burle Technologies, Inc., 1980.

[2] Vaisala Radiosonde RS92 Data Sheet, Tech. rep., Vaisala, URL www.vaisala.com, 2013.

[3] Adam, M.: Notes on temperature-dependent lidar equations, J. Atm. & Oceanic Tech., 26, 1021, 2009.

[4] Ahrens, C.: Meteorology Today: an introduction to weather, climate, and the environment, Brooks/Cole Publishing, Pacific Grove, CA, 2000.

[5] Anderson, J., Wilmouth, D., and Smith, J.: UV Dosage Levels in Summer: Increased Risk of Ozone Loss from Convectively Injected Water Vapor, Science, 337, 835, 2012.

[6] Andrews, D.: An Introduction to Atmospheric Physics, Cambridge University Press, 2nd edn., 2010.

[7] Andrews, D., Holton, J., and Leovy, C.: Middle Atmosphere Dynamics, Academic Press, 1987.

[8] Argall, S., Sica, R., and Bryant, C.: Calibration of the Purple Crow Lidar vibrational Raman water-vapour mixing ratio and temperature measurements, Can. J. Phys., 85, 119, 2007.

[9] Avila, G., Fernandez, J., and Mate, B.: Ro-vibrational Raman cross sections of water vapor in OH stretching region, J. Mol. Spectrosc., 196, 77, 1999.

[10] Avila, G., Fernandez, J., and Tejeda, G.: The Raman spectra and cross-sections of H2O, D2O, and HDO in the OH/OD stretching regions, J. Mol. Spectrosc., 228, 38, 2004.

[11] Brewer, A.: Evidence for a world circulation provided by the measurements of Helium and water vapour distribution in the Stratosphere, Q. J. R. Meteorol. Soc., 75, 351, 1949.

[12] Bribes, J., Gaufres, R., and Monan, M.: Raman band contours for water water vapour as a function of temperature, Appl. Physics Lett., 28, 336, 1976.

[13] Bryant, C.: First measurements of the upper tropospheric and lower stratospheric water vapour mixing ratios using the Purple Crow Lidar raman-scatter lidar, Master's thesis, University of Western Ontario, 1999.

[14] Carleer, M. R., Boone, C. D., Walker, K. A., Bernath, P. F., Strong, K., Sica, R. J., Rand all, C. E., Vömel, H., Kar, J., Höpfner, M., Milz, M., von Clarmann, T., Kivi, R., Valverde-Canossa, J., Sioris, C. E., Izawa, M. R. M., Dupuy, E., McElroy, C. T., Drummond, J. R., Nowlan, C. R., Zou, J., Nichitiu, F., Lossow, S., Urban, J., Murtagh, D., and Dufour, D. G.: Validation of water vapour profiles from the Atmospheric Chemistry Experiment (ACE), Atmospheric Chemistry & Physics Discussions, 8, 4499–4559, 2008.

[15] Chollet, L.: Balloon fabrics made of Goldbeater's skins, Tech. rep., Technical Section of Aeronautics (S. T. Ae.), 1922.

[16] Clemesha, R., Kent, G., and Wright, R.: Laser Probing the Lower Atmosphere, Nature, 209, 184, 1966.

[17] Collis, R. and Ligda, M.: Laser Radar Echoes from the Clear Atmosphere, Nature, 203, 1964.

[18] Cooney, J.: Measurements on the Raman Component of Laser Atmospheric Backscatter, Appl. Physics Lett., 12, 40, 1968.

[19] Cooney, J.: Remote Measurements of Atmospheric Water Vapor Profiles Using the Raman Component of Laser Backscatter, J. Appl. Met., 9, 182, 1970.

[20] Crewell, S. and Lohnert, U.: Accuracy of Boundary Layer Temperature Profiles Retrieved With Multifrequency Multiangle Microwave Radiometry, IEEE Transactions on

Geoscience and Remote Sensing, 45, 2195–2201, doi:10.1109/tgrs.2006.888434, URL https://doi.org/10.1109/tgrs.2006.888434, 2007.

[21] Davis, S.: Fourier transfer spectrometry, Academic Press, 2001.

[22] Dinoev, T., Simeonov, V., and Arshinov, Y.: Raman Lidar for Meteorological Observations, RALMO – Part 1: Instrument description, Atmos. Meas. Tech., 6, 1329, 2013.

[23] Dobson, G.: Origin and distribution of the polyatomic molecules in the atmosphere, Proc. Royal Soc. London, 236, 187, 1956.

[24] Donovan, D., Whiteway, J., and Carswell, A.: Correction for nonlinear photon-counting effects in lidar systems, Appl. Opt., 32, 6742, 1993.

[25] Ehret, G., Hoinka, K., and Stein, J.: Low stratospheric water vapor measured by an airborne DIAL, J. Geophys. Res., 104, 31,351, 1999.

[26] Elterman, L.: The measurement of stratospheric density distribution with the searchlight technique, J. Geophys. Res, 56, 1951.

[27] England, M., Ferrare, R., Melfi, S., Whiteman, D., and Clark, T.: Atmospheric Water Vapor Measurements: Comparison of Microwave Radiometry and Lidar, J. Geophys. Res., 97, 899, 1992.

[28] Fiocco, G. and Smullins, L.: Detection of Scattering Layers in the Upper Atmosphere (60–140 km) by Optical Radar, Nature, 199, 1963.

[29] Guldner, J. and Spankuch, D.: Remote Sensing of the Thermodynamic State of the Atmospheric Boundary Layer by Ground-Based Microwave Radiometry, J. Atm. & Oceanic Tech., 18, 926, 2001.

[30] Han, Y. and Westwater, E. R.: Analysis and improvement of tipping calibration for ground-based microwave radiometers, IEEE Transactions on Geoscience and Remote Sensing, 38, 1260–1276, doi:10.1109/36.843018, 2000.

[31] Harms, J.: Lidar return signals for coaxial and noncoaxial systems with central obstruction, Appl. Opt., 18, 1559, 1979.

[32] Held, I. M. and Soden, B. J.: Water Vapor Feedback and Global Warming, Annual Review of Energy and the Environment, 25, 441–475, doi:10.1146/annurev.energy.25.1.441, URL https://doi.org/10.1146/annurev.energy.25.1.441, 2000.

[33] Hogg, D., Guiraud, F., Snider, J., Decker, M., and Westwater, E.: A Steerable Dual-Channel Microwave Radiometer for Measurement of Water Vapor and Liquid in the Troposphere, J. Climate & Appl. Met., 22, 789, 1983.

[34] Holton, J., Haynes, P., and McIntyre, M.: Stratosphere-troposphere exchange, Revs. Geophys., 33, 405, 1995.

[35] Inaba, H.: Detection of atoms and molecules by Raman scattering and resonance fluorescence, Springer-Verlag, 1976.

[36] Inaba, H. and Kobayasi, T.: Laser-Raman Radar: Laser-Raman scattering methods for remote detection and analysis of atmospheric pollution, Opto-electronics, 4, 101, 1972.

[37] Jiang, J. H., Su, H., Zhai, C., Wu, L., Minschwaner, K., Molod, A., and Tompkins, A.: An assessment of upper troposphere and lower stratosphere water vapor in MERRA, MERRA2, and ECMWF reanalyses using Aura MLS observations, Journal of Geophysical Research: Atmosphere, 120, 11 468–11 485, 2015.

[38] Kampfer, N., Nedoluha, G., Haefele, A., and DeWachter, E.: Monitoring Atmospheric Water Vapour: Ground-Based Remote Sensing and In-situ Methods, chap. 5: Microwave Radiometry, Springer Science, 2013.

[39] Kent, G. and Wright, R.: A Review of Laser Radar Measurements of Atmospheric Properties, J. Atm. & Terrest. Phys., 32, 917, 1970.

[40] Khanna, J., Bandoro, J., and Sica, R.: New technique for retrieval of atmospheric temperature profiles from Rayleigh-scatter lidar measurements using nonlinear inversion, Appl. Opt., 51, 7945, 2012.

[41] Kovalev, V. and Eichinger, W.: Elastic Lidar: Theory, Practice, and Analysis Methods, John Wiley & Sons, Inc., 2004.

[42] Leblanc, T., Trickl, T., and Vogelmann, H.: Monitoring Atmospheric Water Vapour: Ground-Based Remote Sensing and In-situ Methods, chap. 7: Lidar, Springer Science, 2013.

[43] Löhnert, U., Crewell, S., and Simmer, C.: An integrated approach toward retrieving physically consistent profiles of temperature, humidity, and cloud liquid water, Journal of Applied Meteorology, 43, 1295–1307, doi:10.1175/1520-0450(2004)043⟨1295:AIATRP⟩2.0.CO;2, 2004.

[44] Marenco, A., Thouret, V., NéDéLec, P., Smit, H., Helten, M., Kley, D., Karcher, F., Simon, P., Law, K., Pyle, J., Poschmann, G., von Wrede, R., Hume, C., and Cook, T.: Measurement of ozone and water vapor by Airbus in-service aircraft: The MOZAIC airborne program, An overview, Journal of Geophysical Research, 103, 25,631–25,642, doi:10.1029/98JD00977, 1998.

[45] McCullough, E.: A new technique for interpreting depolarization measurements using the CRL atmospheric lidar in the Canadian High Arctic, Ph.D. thesis, University of Western Ontario, 2015.

[46] Measures, R.: Laser Remote Sensing: Fundamentals and Applications, Krieger Publishing Company, 1984.

[47] Melfi, S.: Remote Measurements of the Atmosphere using Raman Scatteing, Appl. Opt., 11, 1605, 1972.

[48] Melfi, S., Lawrence, J., and McCormick, M.: Observation of Raman Scattering by Water Vapor in the Atmosphere, Appl. Physics Lett., 15, 295, 1969.

[49] Miloshevich, L., Vomel, H., and Whiteman, D.: Accuracy assessment and correction of Vaisala RS92 radiosonde water vapour measurements, J. Geophys. Res., 114, 11 305, 2009.

[50] Murphy, D. and Koop, T.: Review of the vapour pressures of ice and supercooled water for atmospheric applications, Q. J. R. Meteorol. Soc., 131, 1539, 2005.

[51] Newsom, R., Turner, D., and Mielke, B.: Simultaneous analog and photon counting detection for Raman lidar, Appl. Opt., 48, 20, 2009.

[52] North and Erukhimova: Atmospheric Thermodynamics: Elementary Physics and Chemistry, Cambridge University Press, 2009.

[53] Parker: Concise Encyclopedia of Science & Technology, McGraw Hill, 1984.

[54] Penney, C. and Lapp, M.: Raman-scattering cross sections for water vapor, J. Opt. Soc. Am., 66, 422, 1976.

[55] Penney, C., Goldman, L., and Lapp, M.: Raman Scattering Cross Sections, Nature Physical Science, 235, 110, 1972.

[56] Petty, D. and Turner, D.: Combined analog-to-digital and photon counting detection utilized for continuous Raman lidar measurements, in: 23rd International Laser Radar Conference, Nara, Japan, 2006.

[57] Pourney, J., Renault, D., and Orszag, A.: Raman-lidar humidity sounding of the atmospheric boundary layer, Appl. Opt., 18, 1141, 1979.

[58] Racette, P. E., Westwater, E. R., Han, Y., Gasiewski, A. J., Klein, M., Cimini, D., Jones, D. C., Manning, W., Kim, E. J., Wang, J. R., Leuski, V., and Kiedron, P.: Measure-

ment of Low Amounts of Precipitable Water Vapor Using Ground-Based Millimeter-wave Radiometry, Journal of Atmospheric and Oceanic Technology, 22, 317–337, doi: 10.1175/JTECH1711.1, 2005.

[59] Renault, D., Pourny, J., and Capitini, R.: Daytime Raman-lidar measurements of water vapor, Opt. Lett., 5, 233, 1980.

[60] Sakai, T., Nagai, T., and Nakazato, M.: Comparisons of Raman Lidar Measurements of Tropospheric Water Vapor Profiles with Radiosondes, Hygrometers on the Meteorological Observation Tower, and GPS at Tsukuba, Japan, J. Atm. & Oceanic Tech., 24, 1407, 2007.

[61] Schmidt, G. A., Ruedy, R. A., Miller, R. L., and Lacis, A. A.: Attribution of the present-day total greenhouse effect, Journal of Geophysical Research Atmospheres, 115, 1–6, doi:10.1029/2010JD014287, 2010.

[62] Seidel, D. J., Sun, B., Pettey, M., and Reale, A.: Global radiosonde balloon drift statistics, Journal of Geophysical Research: Atmospheres, 116, doi: 10.1029/2010JD014891, URL https://agupubs.onlinelibrary.wiley.com/doi/abs/10.1029/2010JD014891, 2011.

[63] Sherlock, V., Garnier, A., and Hauchecorne, A.: Implementation and validation of a Raman lidar measurement of middle and upper tropospheric water vapour, Appl. Opt., 38, 5838, 1999.

[64] Sherwood, S., Roca, R., Weckwert, T., and Andronova, N.: Tropospheric Water Vapor, Convection, and Climate, Reviews of Geophysics, 48, 2010.

[65] Sica, R. and Haefele, A.: Retrieval of water vapor mixing ratio from a multiple channel Raman-scatter lidar using an optimal estimation method, Appl. Opt., 55, 763, 2016.

[66] Simeonov, V., Larcheveque, G., and Quaglia, P.: Influence of the photomultiplier tube spatial uniformity on lidar signals, Appl. Opt., 38, 5186, 1999.

[67] Simeonov, V., Fastig, S., and Haefele, A.: Instrumental correction of the uneven PMT aging effect on the calibration constant of a water vapor Raman lidar, Proc. of SPIE, 9246, 2014.

[68] Soden, B. J., Jackson, D. L., Ramaswamy, V., Schwarzkopf, M. D., and Huang, X.: The Radiative Signature of Upper Tropospheric Moistening, Science, 310, 841–844, doi: 10.1126/science.1115602, URL https://science.sciencemag.org/content/310/5749/841, 2005.

[69] Solheim, F. and Godwin, J. R.: Passive ground-based remote sensing of atmospheric temperature, water vapor, and cloud liquid water profiles by a frequency synthesized microwave radiometerPassive bodengebundene atmosphärische Fernerkundung von Temperatur-, Wasserdampf- und Wolkenwasserprofilen mit eine frequenzsynthetisierten Mikrowellen-Radiometer, Meteorologische Zeitschrift, 7, 370–376, doi:10.1127/metz/7/1998/370, 1998.

[70] Solomon, S., Rosenlof, K. H., Portmann, R. W., Daniel, J. S., Davis, S. M., Sanford, T. J., and Plattner, G.-K.: Contributions of Stratospheric Water Vapor to Decadal Changes in the Rate of Global Warming, Science, 327, 1219–1223, doi:10.1126/science.1182488, URL https://science.sciencemag.org/content/327/5970/1219, 2010.

[71] Stelmaszczyk, K., Dell'Aglio, M., and Chudzynski, S.: nalytical function for lidar geometrical compression form-factor calculations, Appl. Opt., 44, 1323, 2005.

[72] Stocker, T. and Qin, D., eds.: Climate Change 2013: The Physical Science Basis (IPCC Report 2013), Cambridge University Press, 2013.

[73] Strauch, R., Derr, V., and Cupp, R.: Atmospheric Water Vapor Measurement by Raman Lidar, Remote Sensing of Environment, 2, 101, 1972.

[74] Synge, E.: A method of investigating the higher atmosphere, Phil. Mag., 9, 1014, 1930.

[75] Trenberth, K. E.: Atmospheric Moisture Residence Times and Cycling: Implications for Rainfall Rates and Climate Change, Climate Change, 39, 667–694, 1998.

[76] Trickl, T., Cooper, O. R., Eisele, H., James, P., Mücke, R., and Stohl, A.: Intercontinental transport and its influence on the ozone concentrations over central Europe: Three case studies, Journal of Geophysical Research (Atmospheres), 108, 8530, doi: 10.1029/2002JD002735, 2003.

[77] Tuve, M., Johnson, E., and Wulf, O.: A New Experimental Method for Study of the Upper Atmosphere, J. Geophys. Res., 40, 1935.

[78] Vaughan, G., Wareing, D., and Thomas, L.: Humidity measurements in the free troposphere using Raman backscatter, Q. J. R. Meteorol. Soc., 114, 1471, 1988.

[79] Venable, D., Whiteman, D., and Calhoun, M.: Lamp mapping technique for independent determination of the water vapour mixing ratio calibration factor for a Raman lidar system, Appl. Opt., 50, 2011.

[80] Vogelmann, H. and Trickl, T.: Wide-range sounding of free-tropospheric water vapor with a differential-absorption lidar (DIAL) at a high-altitude station, Appl. Opt., 47, 2116–2132, doi:10.1364/AO.47.002116, URL http://ao.osa.org/abstract.cfm?URI=ao-47-12-2116, 2008.

[81] Vomel, H. and Jeannet, P.: Monitoring Atmospheric Water Vapour: Ground-Based Remote Sensing and In-situ Methods, chap. 3: Balloon-Borne Frostpoint Hygrometry, Springer Science, 2013.

[82] Vomel, H., David, D., and Smith, K.: Accuracy of tropospheric and stratospheric water vapour measurements by the cryogenic frost point hygrometer: Instrumental details and observations, J. Geophys. Res., 112, 8305, 2007.

[83] Walker, M., Venable, D., and Whiteman, D.: Gluing for Raman Lidar systems using the lamp mapping technique, Appl. Opt., 53, 8535, 2014.

[84] Wallace and Hobbs: Atmospheric Science: an introductory survey, Academic Press, New York, 2006.

[85] Wandinger, U. and Ansmann, A.: Experimental determination of the lidar overlap profile with Raman lidar, Appl. Opt., 41, 511, 2002.

[86] Weitkamp, C., ed.: Lidar: Range-Resolved Optical Remote Sensing of the Atmosphere, Springer Science, 2005.

[87] Whiteman, D.: Examination of the traditional raman lidar technique, II: Evaluating the ratios for water vapour and aerosols, Appl. Opt., 42, 2593, 2003.

[88] Whiteman, D.: Examination of the Traditional Raman lidar technique. I. Evaluating the temperature- dependent lidar equations, Appl. Opt., 42, 2003.

[89] Whiteman, D., Melfi, S., and Ferrare, R.: Raman lidar system for the measurement of water vapor and aerosols in the Earth's atmosphere, Appl. Opt., 31, 3068, 1992.

Chapter 3

Instrumentation Used in the Thesis

3.1 Lidar

3.1.1 RALMO

RALMO (RAman Lidar for Meteorological Observations) is located at the aerological station at Payerne (46.81° N, 6.95° E, 491 m elevation), operated by the Federal Office of Meteorology and Climatology (hereafter referred to as MeteoSwiss). This lidar was designed and built by the Swiss Federal Institute of Technology, in collaboration with MeteoSwiss. It was set up in July 2007 and has been in operation since August 2008.

The transmitter is a Nd:YAG frequency-tripled (354.7 nm) laser with an energy up to 400 mJ/pulse at a 30 Hz repetition rate (12 W power). However, the normal operational energy is set to 300 mJ/pulse (9 W) to prolong the lifetime of the flash lamps and optical elements. The receiver is an assembly of four 30 cm mirrors, with fibers collecting signal and sending it to a grating polychromator [5]. An additional, off-axis fiber allows the measurement range to extend down to 75 m above the surface [6]. The narrowband nature of this UV laser allows it to operate during the day as well as night. The system is set up to run autonomously, stopping only for routine maintenance and repairs, as well as certain weather conditions (precipitation, low clouds, and fog) [5]. Between October 2009 and September 2010, data was collected

52.6% of the time, with 25.7% of downtime due to maintenance and technical issues, and the remaining 16.2% due to unfavorable weather [4]. With approximately 50% downtime from 2007-2016, RALMO, has one of the largest continuous lidar data sets available [9]. Examples of the raw measurements from RALMO are shown in Section 5.3.1.

3.2 Microwave Radiometer

3.2.1 RPG-HATPRO

HATPRO (Humidity And Temperature PROfiler) is a radiometer produced commercially by Radiometer Physics GmbH (RPG). A RPG-HATPRO-G2 (generation 2 model) radiometer has been operating at the Payerne site since August 2006 [11]. As shown in Figure 3.2, it measures brightness temperatures in 7 K-band channels (22.24, 23.04, 23.84, 25.44, 26.24, 27.84, 31.4 GHz) and 7 V-band channels (51.26, 52.26, 53.86, 54.94, 56.66, 57.3, 58.0 GHz). The K-band channels are located on the water vapor line centered around 22.24 GHz in order to use the line shape to determine its humidity content. The V-band are located on the oxygen line, allowing for temperature information retrieval [2].

In this setup, radiation is focused into a waveguide consisting of a corrugated feedhorn antenna, boasting wide bandwidth, low cross-polarization, and a rotationally symmetric beam pattern. A scanning paraboloid allows for intensity to be measured at different elevation angles. To ensure a low noise level, the antenna must be insulated for thermally stability [15]. The signal is then amplified, filtered by bandpass filter, and detected by a Schottky diode. The instrument is shielded by a microwave-transparent screen equipped with a blower to prevent the buildup of precipitation and dew [2]. The system uses a direct detection filter bank receiver which allows for high-speed, parallel detection at a temporal resolution down to 1 second. The receiver elements are stabilized thermally to within ±0.02 K, with an absolute radiometric accuracy of 0.3 K [15]. One fundamental advantage of the radiometers is their ability to be self-calibrating. The instrument is calibrated using an external cold load (attaching a liquid

nitrogen target to the receiver) and an internal ambient temperature load [14]. As long as the system is properly insulated, the physical temperature of these loads is equivalent to radiometric temperature [15]. Measurement examples from the MeteoSwiss HATPRO radiometer appear in Section 5.4.1.

Figure 3.1: RPG-HATPRO-G2 radiometer located at the MeteoSwiss field station in Payerne, Switzerland.

Validation of measurements from the HATPRO instrument in Payerne was carried out between 2006 and 2009, where it provided reliable temperature profiles, which agreed to within 0.5 K of radiosondes in the lower boundary layer [11]. The HATPRO was also shown to be in good agreement with the TEMPURA radiometer [13]. Absolute accuracy in the brightness temperature measurement is estimated to be approximately 0.5 K, due largely to uncertainties associated with the calibration [8][2][12].

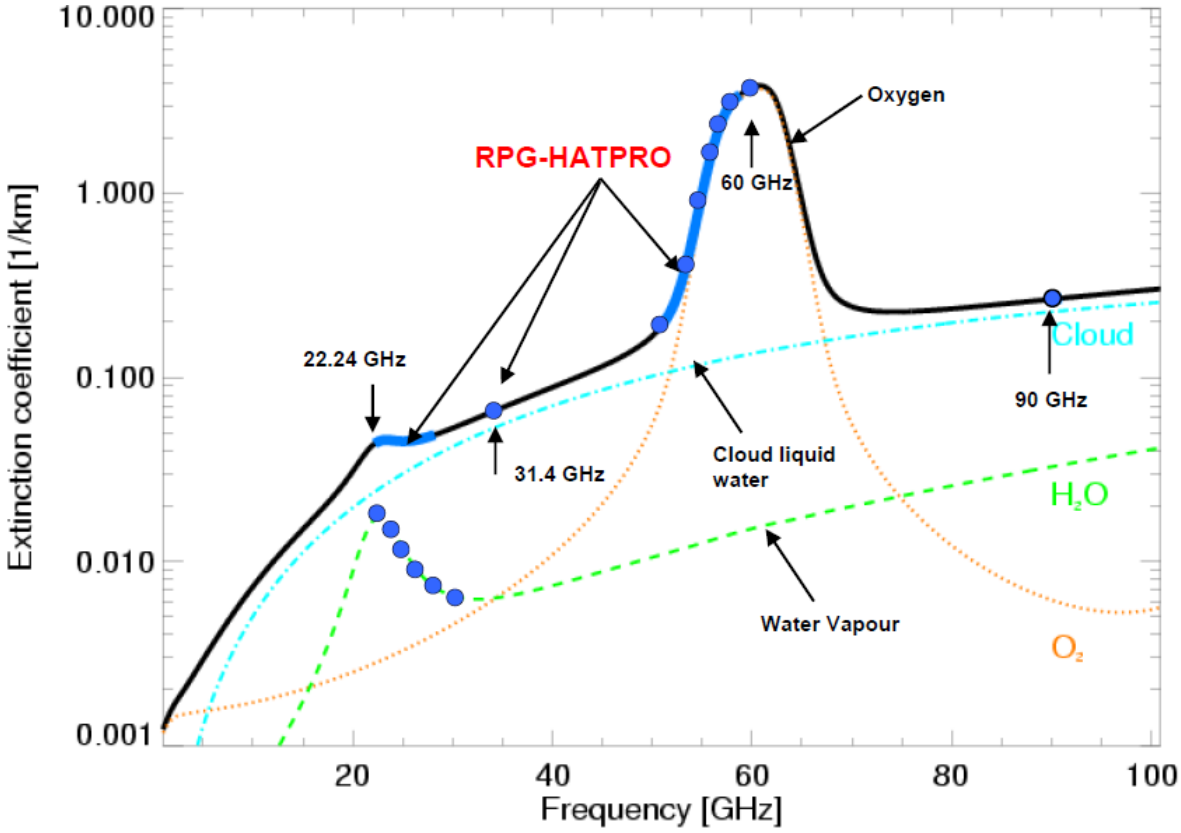

Figure 3.2: Spectrum of the RPG-HATPRO-G2 [2]. The orange, green, cyan, and solid black lines represent the lines due to oxygen, water vapor, liquid water, and total. The blue dots show the positions of the K-band and V-band channels. The first 6 K-band frequencies are located on the water vapor feature, with the 31.4 GHz channel used for liquid water determination. The V-band channels are located on the oxygen feature. The 90 GHz channel is used for other RPG radiometer models, but not for the HATPRO.

3.3 Radiosondes

The Payerne weather station has hosted radiosonde launches since 1941 [10]. Routine radiosonde launches occur twice daily - generally around 11:00 and 23:00 UTC [4].

Radiosondes used for routine monitoring include SRS-C34. Manufactured by MeteoLabor, the SRS-C34 can be equipped with three different humidity sensors: a hygristor, an HC2 sensor, or a SnowWhite hygrometer [17][1]. Since February 2017, the newer MeteoLabor SRS-C50 model, used for routine soundings at Payerne [16], were replaced by Vaisala RS41 soundings in 2018. The popular Vaisala RS92 radiosondes have been used for the validation of the RALMO water vapor measurements [5]. RS92 radiosondes, manufactured by Vaisala since 2003, comprise a substantial share of 30% of the balloon sounding market [7]. Although widely used for meteorological soundings globally, their correction algorithms are proprietary, making it difficult to ascertain the origin of the uncertainty data products.

The GCOS (Global Climate Observing System) Reference Upper-Air Network (GRUAN) processing network has addressed this concern by providing correction algorithms for the instrumental and physical biases of the Vaisala RS92. The corrections are then used for developing a rigorous systematic uncertainty budget, which gives overall humidity uncertainties ranging between 5-15% [7]. The Payerne station is a member of GRUAN, with archived soundings from SRS-C34 (2014-2017), RS92 (2011-2018), and RS41 (2014-Present) [3].

Bibliography

[1] SRS-C34 Digital Radiosonde, Meteolabor AG, Wetzikon, Switzerland, 2010.

[2] HATPRO Technical Instrument Manual: Description of Instrument Technology, Radiometer Physics, https://www.radiometer-physics.de/products/microwave-remote-sensing-instruments/radiometers/humidity-and-temperature-profilers/, 2013.

[3] Radiosondes: Backbone of GRUAN, https://www.gruan.org/instruments/radiosondes/, 2019.

[4] Brocard, E., Jeannet, P., Begert, M., Levrat, G., Philipona, R., Romanens, G., and Scherrer, S. C.: Upper air temperature trends above Switzerland 1959-2011, Journal of Geophysical Research Atmospheres, 118, 4303–4317, doi:10.1002/jgrd.50438, 2013.

[5] Dinoev, T., Simeonov, V., and Arshinov, Y.: Raman Lidar for Meteorological Observations, RALMO – Part 1: Instrument description, Atmos. Meas. Tech., 6, 1329, 2013.

[6] Dinoev, T., Hafele, A., Martucci, G., Simeonov, V. B., Calpini, B., Serikov, I., Bobrovnikov, S., and Leuenbergerd, D.: Raman lidar in operational meteorology, p. 18, doi:10.1117/12.2501987, 2018.

[7] Dirksen, R. J., Sommer, M., Immler, F. J., Hurst, D. F., Kivi, R., and Vömel, H.: Reference quality upper-air measurements: GRUAN data processing for the Vaisala RS92 radiosonde, Atmospheric Measurement Techniques, 7, 4463–4490, doi:10.5194/amt-7-4463-2014, 2014.

[8] Han, Y. and Westwater, E. R.: Analysis and improvement of tipping calibration for ground-based microwave radiometers, IEEE Transactions on Geoscience and Remote Sensing, 38, 1260–1276, doi:10.1109/36.843018, 2000.

[9] Hicks-Jalali, S., Sica, R., Haefele, A., and Martucci, G.: A Calibration of the MeteoSwiss RAman Lidar for Meteorological Observations (RALMO)Water Vapour Mixing

Ratio Measurements using a Radiosonde Trajectory Method, EPJ Web of Conferences, 176, 08 015, doi:10.1051/epjconf/201817608015, URL https://doi.org/10.1051/epjconf/201817608015, 2018.

[10] Jeannet, P.: Swiss Contribution to the Global Climate Observing Systems 2001, Tech. rep., MeteoSwiss, 2001.

[11] Löhnert, U. and Maier, O.: Operational profiling of temperature using ground-based microwave radiometry at Payerne: Prospects and challenges, Atmospheric Measurement Techniques, 5, 1121–1134, doi:10.5194/amt-5-1121-2012, 2012.

[12] Maschwitz, G., Löhnert, U., Crewell, S., Rose, T., and Turner, D. D.: Investigation of ground-based microwave radiometer calibration techniques at 530 hPa, Atmospheric Measurement Techniques, 6, 2641–2658, doi:10.5194/amt-6-2641-2013, 2013.

[13] Navas-Guzmán, F., Kämpfer, N., and Haefele, A.: Validation of brightness and physical temperature from two scanning microwave radiometers in the 60 GHz O2 band using radiosonde measurements, Atmospheric Measurement Techniques, 9, 4587–4600, doi:10.5194/amt-9-4587-2016, 2016.

[14] Rose, T. and Czekala, H.: RPG-HATPRO Operating Manual, Radiometer Physics, 8.04 edn., https://www.radiometer-physics.de/products/microwave-remote-sensing-instruments/radiometers/humidity-and-temperature-profilers/, 2009.

[15] Rose, T., Crewell, S., Löhnert, U., and Simmer, C.: A network suitable microwave radiometer for operational monitoring of the cloudy atmosphere, Atmospheric Research, 75, 183–200, doi:10.1016/j.atmosres.2004.12.005, 2005.

[16] Voirin, J.: Water Vapor Calibration of the Raman LIDAR for meteorological Observation Master Internship Report, Tech. rep., MeteoSwiss, 2017.

[17] Vömel, H., Fujiwara, M., Shiotani, M., Hasebe, F., Oltmans, S. J., and Barnes, J. E.: The behavior of the Snow White chilled-mirror hygrometer in extremely dry conditions, Journal of Atmospheric and Oceanic Technology, 20, 1560–1567, doi:10.1175/1520-0426(2003)020⟨1560:TBOTSW⟩2.0.CO;2, 2003.

Chapter 4

Calibration of Raman Water Vapor Lidar

4.1 Traditional Method for determining WVMR

In an ideal world, we would be able to carry out a "First Principles" characterization of all the terms in the lidar WVMR equation. However, carrying out this characterization can be exceedingly difficult. The instrument efficiency and temperature-dependence function can be monitored, as long as instrument degradation is considered and the efficiencies are measured regularly. Additionally, it is possible to characterize instrumental effects such as signal-induced noise and fluorescence. Although the nitrogen cross section is well-known, the cross section for water vapor is not, with the best estimates coming from models. Furthermore, atmospheric transmission can be ascertained through direct detection of atmospheric properties such as extinction via coincidental instruments. If such measurements are not available, atmospheric transmission terms may be estimated via a model, such as MODTRAN (MODerate resolution atmospheric TRANsmission [4]), where transmission can estimated based on environment (polar/mid-latitude/tropical, maritime/continental, rural/urban), visibility, cloud cover, and operational wavelengths [2]. Lastly, although the conventional overlap is not believed to be an issue in determining the WVMR, the poorly-constrained differential overlap may indeed be a concern.

As a result of these factors, the lidar WVMR equation can be rewritten as:

$$w_m(z) = C \cdot \frac{\Gamma_N(\lambda_N, z)}{\Gamma_H(\lambda_H, z)} \frac{N'_H(z)}{N'_N(z)} \tag{4.1}$$

which is the same as Equation 2.14, with many of those terms consolidated into C, the system calibration factor [20]. Thus, instead of having to determine these individual quantities, the lidar $\frac{\Gamma_N(\lambda_N,z)}{\Gamma_H(\lambda_H,z)} \frac{N'_H(z)}{N'_N(z)}$ can be directly compared to the mixing ratio determined by another instrument, with relation between the two quantities serving as the calibration term.

4.2 Radiosonde

4.2.1 Traditional Calibration Method

Radiosonde comparison is the most common type of calibration for atmospheric lidars. This is particularly convenient for lidars based at meteorological stations where radiosondes are launched regularly. The relative humidity measured by the coincident radiosonde is converted to a mixing ratio via a saturation vapor pressure model and placed on the same altitude grid as the lidar data. A weighted least squares fit between the lidar mixing ratio, as shown in Equation 4.1, and the radiosonde mixing ratio is carried out:

$$min = \Sigma_{i=1}^{n} (Sonde_i - Lidar_i \cdot C_{sys})^2 \tag{4.2}$$

When the minimum sum of squares is reached, C_{sys} becomes the system calibration factor and is used to scale the lidar mixing ratio values [15][20].

The fit is generally calculated from the summation of the first 30 lidar scans following the sonde launch, as this is the average time for the balloon to reach the tropopause for mid-latitudes [9], over a fixed range of altitudes. For early data from RALMO (2009-2010), the calibration fitting range was the first 6 km of the profile [6]. Alternately, instead of using a fixed

range of altitudes, altitude bins with low signal (SNR < 2) could be omitted from the summation [9]. The fit can also be based on defining a calibration window in which the correlation between the lidar mixing ratio and the radiosonde-derived mixing ratio is sufficiently high. For the procedure employed in Hicks-Jalali et al. 2019, a correlation coefficient above 0.75 is required [9].

Some of the possible methods for calibration based on the time and spatial-coincidence of the radiosonde with respect to the lidar are shown in Figure 4.1. Method 1 considers the entire time domain of the lidar dataset up to 10 km, while Method 2 only determines a calibration based on a radiosonde which is spatially and temporally coincident with the lidar. In Method 3, only altitudes at which the lidar's water vapor signal variability is less than 20% are considered. Method 4 only considers the calibration region to be the individual altitude bins at the time the radiosonde passes through them. In this study, the smallest standard deviation in the calibration constant was attributed to Method 3 [13].

4.2.2 Trajectory method

One major shortcoming of the traditional radiosonde calibration method is that it does not take the sonde's movement relative to the lidar into consideration. Radiosondes which drift significantly from the lidar may enter a different air mass, resulting in calibration potentially based on completely different atmospheric circumstances. Recent efforts of Hicks-Jalali et al. 2019 addresses this concern by tracking the path of radiosondes launched at Payerne. A calibration region is defined, with a radius of 3 km around the lidar, within which conditions are assumed to be homogeneous. Thus, in this case, only scans where the radiosonde is within this homogeneous region are considered for calibrating the lidar. The method was shown to reduce the difference between radiosonde and lidar measurements in non-homogeneous air masses [9].

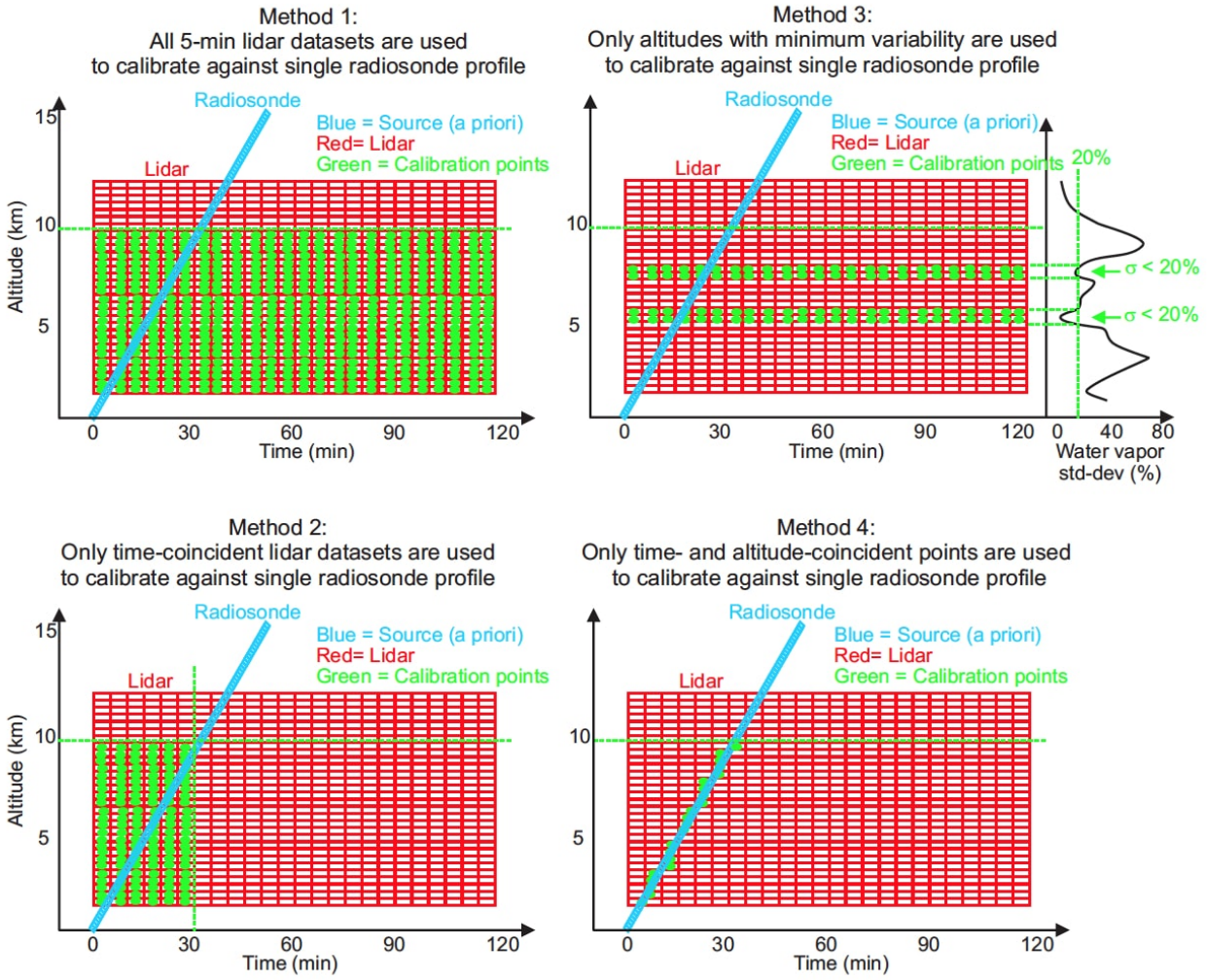

Figure 4.1: Different methods used in the determination of a calibration factor for lidar based on coincidental radiosondes. In each subplot, the blue line indicates the ascent of the radiosonde as a function of time and altitude, the red grid shows the resolution and height domain of the lidar scans, and the green gives the points used for calibration. (Figure credit: Leblanc et al. 2012 [13])

4.3 Radiometer

Microwave radiometers can also be used as a calibration source. Contrary to radiosondes, which produce profiles of humidity, radiometers are passive instruments designed to retrieve column quantities, such as integrated water vapor. Integrated water vapor for the lidar can be determined via Equation 2.6, through the integration of its uncalibrated mixing ratio profile along with a reasonable air density profile over its entire range. As the uncalibrated lidar profile is relative, it may initially yield an unrealistic total column measurement. This lidar quantity can then be scaled to the value derived from the radiometer, with the scaling factor then applied to the uncalibrated water vapor mixing ratio profile [8]. As precipitable water vapor is an integrated quantity, its uncertainty does not vary with altitude as is the case for radiosonde humidity measurements. Recent instrumental retrievals, such as those by G2 HATPRO radiometers, estimate integrated water vapor accuracies of $0.2\,kg/m^2$ [1]. However, the major challenge with this calibration is the lack of lidar measurements at the lowest altitudes of the atmosphere, causing it to significantly underestimate its total column measurement. For example, for a lidar with a profile starting 1000 m above the surface, if the atmospheric water vapor concentration resembles the US Standard Atmosphere Model 1976, the integrated water vapor would be underestimated by 41%, compared to a profile extending all the way to the surface.

4.4 GPS calibration

In order to achieve positioning precision, GPS needs to account for the atmosphere through which it transmits signal. The refraction caused by the atmosphere causes a delay, or excess zenith path length, quantified as:

$$L = \int_0^\infty N dz \tag{4.3}$$

where N is the refractivity:

$$N = 77.6(P_{dry}/T)Z_{dry}^{-1} + 64.8(e/T)Z_{wv}^{-1} + 3.776 \times 10^5(e/T^2)Z_w^{-1} \tag{4.4}$$

and P_{dry} and e are the partial pressure of dry and water vapor, T is temperature, while $Z_w^{-1}(e, T)$ and $Z_{air}^{-1}(P_{dry}, T)$ are inverse compressibility factors for water vapor and dry air [17]. The total path length was later determined to be related to the amount of precipitable water vapor and, assuming hydrostatic equilibrium, was derived as:

$$L = 0.2272 \cdot P_{surf} + 6.277 \cdot V \tag{4.5}$$

where P_{surf} is the surface pressure and V is precipitable water vapor [10]. Bevis et al. 1992 [5] was then able to present an expression relating the wet path length component, the zenith wet delay ΔL_w^0, to the integrated water vapor:

$$IWV \approx \kappa \Delta L_w^0 \tag{4.6}$$

where κ is an empirical term which includes a location-specific mean surface temperature [5]. The Maido atmospheric station on Reunion Island, which also houses a relatively new Raman lidar facility [3], uses a GNSS receiver, yielding tropospheric wet delay as a data product. This delay can then be used to determine the integrated water vapor, which can then be used to calibrate the lidar in the same manner as the radiometer calibration described in the previous section [7].

4.5 Internal/Hybrid Calibration

The Table Mountain Facility pioneered a hybrid approach, using a combination of internal and external sources for lidar calibration. The external calibration is still carried out during occa-

sional campaigns, such as MOHAVE [12]. However, a routine partial calibration, sometimes referred to as a *white light* calibration, is also carried using a laboratory-calibrated lamp with a highly stable output. A calibrated quartz-tungsten halogen lamp is mounted above the mirror and adjacent to the focal point. It then shines on the mirror for 15 minutes before and after regular observation, with the hatch closed and the room darkened. The ratio of water vapor to nitrogen channel signal is then the overall system efficiency convolved with the lamp's irradiance. Thus, any changes in this calibration ratio over time will indicate changes in the system's efficiency, likely due to instrument aging [11][13]. Figure 4.2 shows how the white light calibration is used to monitor changes in the lidar at the Table Mountain Facility. The figure provides the ratio of the nitrogen to water vapor channel intensities as a function of time between October 2007 and August 2008 at 3 different intensity ranges. Although the abrupt changes in the ratios can be attributed to intentional changes or repairs to the system, the gradual drifts in the ratio can be indicative of change in the system efficiency. Calibration via this method has also been attempted for the Purple Crow Lidar system, with more information available in Appendix A.3.

A calibrated lamp which scans the entire aperture of the primary receiver is advantageous over one held at a fixed position, which can only sample a small fraction of the mirror's total aperture. This lamp mapping calibration technique is currently employed by both the Howard University Raman Lidar [18] and ALVICE (Atmospheric Laboratory for Validation, Interagency Collaboration and Education) lidar [21]. This technique can also be used to determine channel merging coefficients in the absence of lidar data, agreeing to within 5 % of the traditional method [19].

4.6 Solar Background calibration

Instead of using a lamp, passive daytime observation of diffuse sunlight may also be used for internal calibration. This method uses the ratio of measured signal from daytime sky radiance

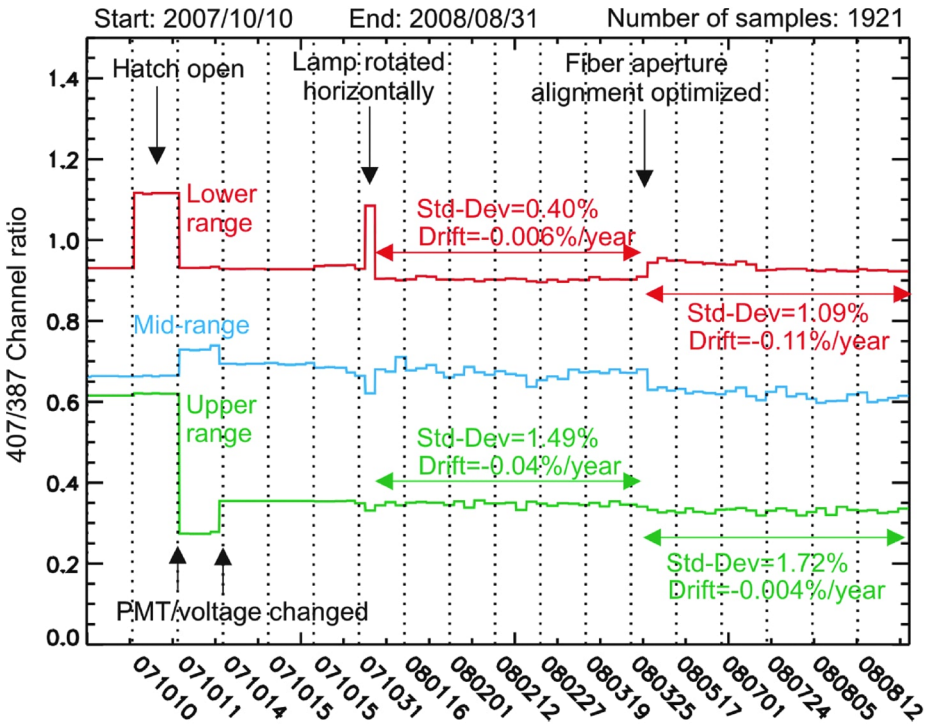

Figure 4.2: White light calibration for the Table Mountain lidar, at different intensities. Note the gradual drift of the calibration ratio in each of the intensity ranges over time. [11]

through the water vapor and nitrogen Raman detector channels.

As opposed to the lamp calibration method, this method does not require a stable, well-characterized lamp. However, it does require thorough characterization of the downwelling radiation as a function of solar zenith angle. Additionally, since the daytime background is far more significant than nighttime values, care must be taken to ensure there is minimal light leakage through the detector filters from outside the Raman wavelength ranges. Baffles should also be added to eliminate sunlight reflections from surface structures [16]. Although this method is not sensitive to temperature fluctuations as the calibration lamp method, it does require clear sky conditions for consistent results. Simulations of diffuse sunlight indicate measurements should occur at solar zenith angles between 50 and 70° to minimize the sensitivity from the aerosol scattering phase function, although it is in recommended to use aerosol properties derived by a collocated instrument, such as a sunphotometer, in order to keep calibration uncertainties under 10% [16].

Lamp and solar background calibrations were both performed for the Observatoire de Haute Provence lidar, with more favorable results from the solar calibration when a simultaneous sunphotometer is used [16]. This calibration technique was carried out during the MALICCA campaign, but results were fixed due to overwhelmingly cloudy conditions during daytime observations [7]. A Solar background calibration was also carried out for the RALMO system by Masters intern Jordan Voirin, as it is does not have the same temperature dependence as the lamp calibration method. Correction ratios were determined during Solar zenith angles of 20°, corresponding to the maximum elevation angle on the winter solstice in Payerne, for dates between 2008 and 2017, resulting in good agreement with radiosonde-derived calibration factors [14].

Bibliography

[1] HATPRO Technical Instrument Manual: Description of Instrument Technology, Radiometer Physics, https://www.radiometer-physics.de/products/microwave-remote-sensing-instruments/radiometers/humidity-and-temperature-profilers/, 2013.

[2] Argall, S., Sica, R., and Bryant, C.: Calibration of the Purple Crow Lidar vibrational Raman water-vapour mixing ratio and temperature measurements, Can. J. Phys., 85, 119, 2007.

[3] Baray, J. L., Courcoux, Y., Keckhut, P., Portafaix, T., Tulet, P., Cammas, J. P., Hauchecorne, A., Godin Beekmann, S., De Mazière, M., Hermans, C., Desmet, F., Sellegri, K., Colomb, A., Ramonet, M., Sciare, J., Vuillemin, C., Hoareau, C., Dionisi, D., Duflot, V., Vérèmes, H., Porteneuve, J., Gabarrot, F., Gaudo, T., Metzger, J. M., Payen, G., Leclair De Bellevue, J., Barthe, C., Posny, F., Ricaud, P., Abchiche, A., and Delmas, R.: Maïdo observatory: A new high-altitude station facility at Reunion Island (21 S, 55 E) for long-term atmospheric remote sensing and in situ measurements, Atmospheric Measurement Techniques, 6, 2865–2877, doi:10.5194/amt-6-2865-2013, 2013.

[4] Berks, A., Bernstein, L., and Robertson, D.: MODTRAN: A moderate resolution model for LOWTRAN 7, Tech. rep., Spectral Sciences, Inc., Burlington, MA, 1989.

[5] Bevis, M., Businger, S., Herring, T. A., Rocken, C., Anthes, R. A., and Ware, R. H.: GPS meteorology: remote sensing of atmospheric water vapor using the global positioning system, Journal of Geophysical Research, 97, 787–801, 1992.

[6] Brocard, E., Jeannet, P., Begert, M., Levrat, G., Philipona, R., Romanens, G., and Scherrer, S. C.: Upper air temperature trends above Switzerland 1959-2011, Journal of Geophysical Research Atmospheres, 118, 4303–4317, doi:10.1002/jgrd.50438, 2013.

[7] Dionisi, D., Keckhut, P., and Courcoux, Y.: Water vapor observations up to the lower

stratosphere through the Raman lidar during the Maïdo Lidar Calibration Campaign, Atmos. Meas. Tech., 8, 1425, 2015.

[8] Han, Y., Snider, J. B., Westwater, E. R., Melfi, S. H., and Ferrare, R. A.: Observations of water vapor by ground-based microwave radiometers and Raman lidar, Journal of Geophysical Research, 99, 18 695, doi:10.1029/94jd01487, 1994.

[9] Hicks-Jalali, S., Sica, R. J., Haefele, A., and Martucci, G.: Calibration of a water vapour Raman lidar using GRUAN-certified radiosondes and a new trajectory method, Atmospheric Measurement Techniques, 12, 3699–3716, doi:10.5194/amt-12-3699-2019, 2019.

[10] Hogg, D. C., Guiraud, F. O., and Decker, M. T.: Measurement of excess radio transmission length on earth-space paths, Astronomy and Astrophysics, 95, 304–307, 1981.

[11] Leblanc, T. and McDermid, I.: Accuracy of raman liar water vapour calibration and its applicability to long-term measurements, Appl. Opt., 47, 5592, 2008.

[12] Leblanc, T., Walsh, T., and McDermid, I.: Measurements of Humidity in the Atmosphere and Validation Experiments (MOHAVE)-2009: overview of campaign operations and results, Atmos. Meas. Tech., 4, 2579, 2011.

[13] Leblanc, T., McDermid, I., and Walsh, T.: Ground-based water vapor raman lidar measurements up to the upper troposphere and lower stratosphere for long-term monitoring, Atmos. Meas. Tech., 5, 17, 2012.

[14] Martucci, G., Voirin, J., Simeonov, V., Renaud, L., and Haefele, A.: A novel automatic calibration system for water vapor Raman LIDAR, EPJ Web of Conferences, 176, 05 008, doi:10.1051/epjconf/201817605008, 2018.

[15] Melfi, S.: Remote Measurements of the Atmosphere using Raman Scatteing, Appl. Opt., 11, 1605, 1972.

[16] Sherlock, V., Hauchecorne, A., and Lenoble, J.: Methodology for the independent calibration of Raman backscatter water-vapor lidar systems, Applied Optics, 38, 5816, doi: 10.1364/ao.38.005816, 1999.

[17] Thayer, G. D.: An improved equation for the radio refractive index of air, Radio Science, 9, 803–807, doi:10.1029/RS009i010p00803, 1974.

[18] Venable, D., Whiteman, D., and Calhoun, M.: Lamp mapping technique for independent determination of the water vapour mixing ratio calibration factor for a Raman lidar system, Appl. Opt., 50, 2011.

[19] Walker, M., Venable, D., and Whiteman, D.: Gluing for Raman Lidar systems using the lamp mapping technique, Appl. Opt., 53, 8535, 2014.

[20] Whiteman, D., Melfi, S., and Ferrare, R.: Raman lidar system for the measurement of water vapor and aerosols in the Earth's atmosphere, Appl. Opt., 31, 3068, 1992.

[21] Whiteman, D., Cadrirola, M., and Venable, D.: Correction technique for Raman water vapor lidar signal-dependent bias and suitability for water vapor trend monitoring in the upper troposphere, Atmos. Meas. Tech., 5, 2893, 2012.

Chapter 5

Implementation of the Integrated Retrieval

As mentioned in the previous chapter, it is often difficult to characterize some of the terms comprising the lidar water vapor mixing ratio equation, requiring some sort of calibration. Each of these methods has their advantages and disadvantages, but one common trait is that they all require the lidar signal to contain corrected count rates. However, in some cases, one may not be entirely sure if the counts are indeed correct. That is, a non-linearity correction requires a dead time value for the system, which may or may not be known. Merging the analog and PC counts requires a region in which to glue the two profiles. However, there is no systematically accepted technique for this task.

In this chapter, we introduce a method which can retrieve water vapor mixing ratio without many of the issues associated with corrected lidar counts. The Optimal Estimation Method (OEM) is a non-linear inverse method which has the fundamental advantage of retrieving parameters of interest using a measurement state comprised of raw data rather than corrected counts. An implementation for an OEM retrieval of water vapor via RALMO lidar measurements and coincidental radiosondes is discussed, as well as a retrieval method using HATPRO radiometer measurements. Then, a novel retrieval method incorporating measurements from

both instruments is introduced, with results shown in the following chapters.

5.1 The Retrieval Framework: Optimal Estimation Method

5.1.1 Forward and inverse modeling

The use of forward modeling, and consequently model inversion, is an essential consideration in physical sciences, where physical phenomena can be modelled mathematically, and inverted in order to retrieve a desirable parameter.

The forward equation is shown below:

$$y = F(x, b) + \epsilon \tag{5.1}$$

It relates the physical considerations of the problem, $F(x, b)$, or the forward model, with a vector of measurements, y, and its associated uncertainty, ϵ. Embedded within the forward model are the state vector, x, and forward model parameter vector, b [39]. The state vector contains the quantities which are to be retrieved. If these desired quantities cannot be observed directly, they can be retrieved through their relationship to a physical measurement via the forward model. The forward model therefore contains the physical and instrumental considerations needed to rigorously model the physical state. Aside from the state vector quantities, the forward model also contains model parameters, or *b-parameters*, which account for the quantities within the model which will not be retrieved. In order to retrieve the state vector quantities, the forward equation must be inverted.

5.1.2 Optimal Estimation Method (OEM)

OEM is a method that provides an efficient way to solve inverse problems. Its power is largely due to its application of Bayes' theorem, where the probability of an outcome may be determined based on contributions from potentially relevant prior knowledge of the system. It

may be expressed as:

$$P(x|y) = \frac{P(y|x)P(x)}{P(y)} \simeq P(y|x)P(x) \tag{5.2}$$

where $P(x|y)$ is the probability density function (PDF) of the state vector given the measurement vector, $P(x)$ and $P(y)$ are the independent PDFs of the prior state and measurement state, respectively, and $P(y|x)$ is the PDF of the measurement state based on the state vector. That is, a prior estimate of the state (or an a priori state vector), x_a, may be incorporated into the method to assist in retrieving the desired state quantities. This prior knowledge of the system may be considered a virtual measurement, weighted by the uncertainties of this prior knowledge [39], providing an estimate of the state to be retrieved. This *a priori* state could be a reference state, or an ideal starting point for the retrieval, but does not need to be. For example, if one wanted to retrieve a WVMR profile, a reference or *a priori* state vector could be the WVMR profile provided in the US Standard Atmosphere Model [1].

If the probability density functions characterizing the measurement and priori state are Gaussian, Bayes' Theorem can be rewritten in a vectorized form representing the cost function for the retrieval:

$$cost = [y - F(x,b)]^T S_\epsilon^{-1}[y - F(x,b)] + [x - x_a]^T S_a^{-1}[x - x_a] \tag{5.3}$$

where S_ϵ is the measurement covariance and S_a is the *a priori* covariance. The form of this function is similar to the conventional least squares solution, with a regularization term to take the *a priori* information content into consideration. Minimizing this cost function and solving for $\hat{x}$ via the Levenberg-Marquardt algorithm will constrain the estimated value, giving the final retrieved state:

$$\hat{x} = x_a + (S_a^{-1} + K^T S_y^{-1} K)^T K^T S_y^{-1}(y - F(x_a)) \tag{5.4}$$

where K is the Jacobian [39].

The retrieval's performance can also be gauged by investigating the Jacobians and Averaging Kernels. The Jacobian, or weighting function matrix, determines how the forward model

changes with respect to the state vector:

$$K = \frac{\partial F}{\partial x} = \frac{\partial y}{\partial x} \tag{5.5}$$

It is an indicator of how insensitive the forward model and measurement state are to the state vector, with a value of 0 inferring complete insensitivity.

The averaging kernel is used to gauge how the retrieval responds to changes in the atmosphere [39]:

$$A = \frac{\partial \hat{x}}{\partial x} = \frac{\partial \hat{x}}{\partial y}\frac{\partial y}{\partial x} = G_y K_X \tag{5.6}$$

where G_y is the Gain matrix, the sensitivity of the retrieval with respect to the measurement, and can be calculated as:

$$G_y = S_a K^T (K S_a K^T + S_\epsilon)^{-1} \tag{5.7}$$

Under ideal conditions, $\hat{x}$ and x would be the same and the averaging kernel matrix would simply be an identity matrix. However, state vectors characterizing real conditions contain noise and may be correlated. Under this consideration, rows of the averaging kernel matrix would ideally be a delta-like function near unity. This expectation is reasonable for active remote sensors such as lidar, while passive remote sensors generally have wider Gaussian-like functions. The averaging kernel matrix also has the use in gauging the information content of the retrieval, by providing the degrees of freedom for the signal, which can be expressed as the trace of A [39].

5.1.3 Uncertainties

The retrieval noise covariance is expressed as:

$$S_m = G_y S_\epsilon G_y^T \tag{5.8}$$

whereas the smoothing error covariance is:

$$S_s = (A - I_n)S_e(A - I_n)^T \tag{5.9}$$

where S_e is the covariance of ensemble of states about the mean [39]. For each *b-parameter* term, the associated error covariance matrix is:

$$S_f = G_y K_b S_b K_b^T G_y^T \tag{5.10}$$

where S_b is the initial *b-parameter* covariance, and $K_b = \frac{\partial y}{\partial b}$ is the sensitivity of the forward model to the forward model *b-paremeter*. The total covariance for the retrieval is then a summation of the above matrices [39]:

$$S_{tot} = S_m + S_s + \Sigma_i S_{f,i} \tag{5.11}$$

5.1.4 Advantages of the OEM

OEM retrievals have a number of advantages over the traditional method for determining lidar WVMR. Since the OEM works with the measurement vector instead of individual profiles, the measurements do not need to be in same altitude range with the same resolution, or even in the same physical units. The retrieval vector can be defined on a grid arbitrarily, such that the grid is ultimately interpolated onto the same grid as the other retrieved state parameters to provide a single, retrieved profile [36]. The forward model should provide a compact, yet comprehensive characterization of the instrumental and physical considerations. If this is performed adequately, the retrieval is much less dependent on some of the assumptions and ad hoc corrections associated with the lidar WVMR traditional method (Section 4.1). It also has the fundamental advantage of the OEM is the ability to not only determine the statistical and smoothing errors associated with the retrieval, but also to quantify uncertainties for each of the *b-parameters* of the forward model, allowing for the creation of a comprehensive uncertainty

budget on a profile-by-profile basis [43]. It is also equipped diagnostic tools, such as Averaging Kernels, for gauging the performance of the retrieval.

5.2 OEM inputs

5.2.1 *A priori* retrieval state (mixing ratio)

As the goal here is to retrieve a water vapor mixing ratio profile, it is reasonable for the *a priori* state to also be a water vapor mixing ratio profile. Figure 5.1 shows the profiles considered. Model humidity profiles come from FASCOD and the US Standard Atmosphere 1976. FASCOD (Fast Atmospheric Signature CODe), supported by the Air Force Geophysics Laboratory, provides temperature and trace gas volume mixing ratios for general geographic locations (tropical, midlatitude, subarctic) during different seasons (winter, summer) [5][2]. This model data was provided in the ARTS package (refer to Section 5.4.2 for more on ARTS). The US Standard Atmosphere 1976 model is the historic standard, providing an idealized model of the Earth's atmosphere, including water vapor in the troposphere and lower stratosphere [1]. Tropospheric water vapor mixing ratio values in the US Standard model come from the database of world-wide radiosonde data (humidity atlas [20]). Stratospheric values are provided by high-altitude soundings [45][33], aircraft-carried frost-point instruments [8], and rocket soundings [41]. In Figure 5.1, "Sonde" is a humidity profile from a single coincidental GRUAN radiosonde launch in Payerne, and "Sonde clim" is a monthly climatological average of Payerne radiosonde launches between 1973 to 2017. The sonde climatological average profile shows a substantial bias above 12 km due to fewer humidity measurements available in this region. When used as the *a priori* profile, where little is data available (less than 70% of the possible measurements), the profile at those heights is replaced by values from the US Standard Atmosphere profile.

For the following analysis, we use the US Standard Model as the *a priori* humidity profile for testing the retrieval, since it is a much smoother profile than that of the radiosonde and

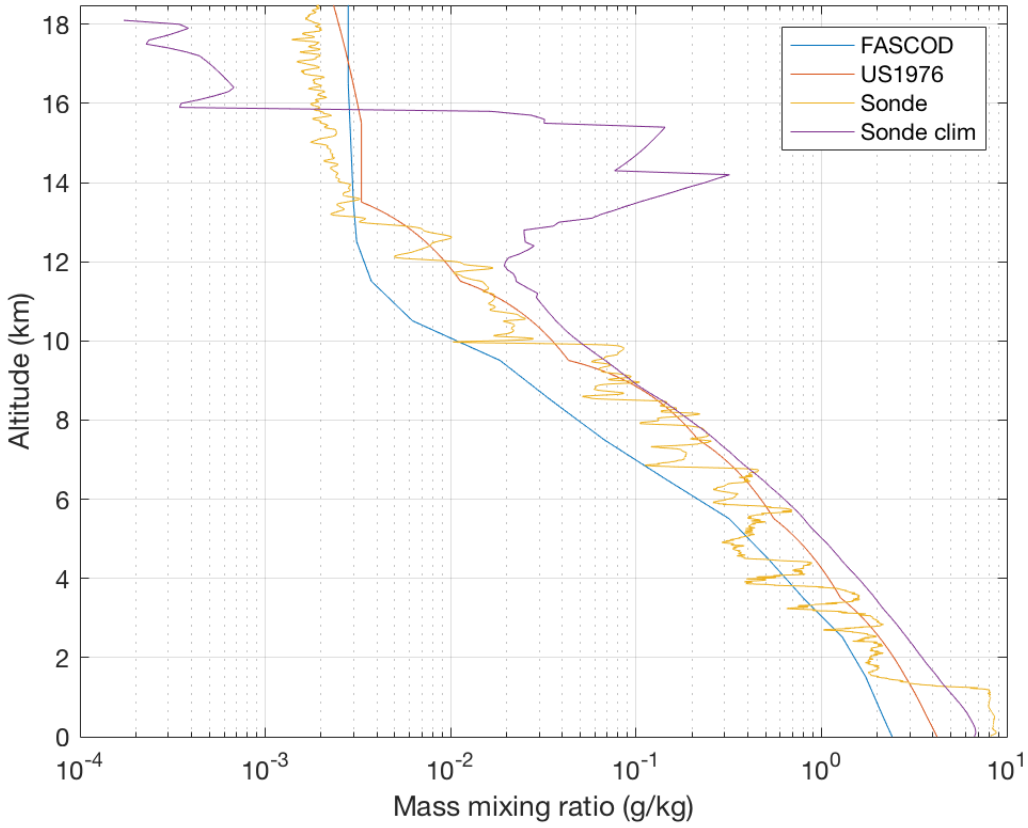

Figure 5.1: Raw mixing ratio profiles considered for the *a priori* state. *Sonde* is a single raw radiosonde profile (GRUAN-corrected sonde from October 5, 2011 at 22:55UT), *Sonde clim* is a monthly (October) climatological average of the radiosondes, *FASCOD* is the winter FASCOD model profile [5][2] and *US1976* is the US 1976 model profile [1]

does not underestimate the tropospheric water vapor content like the FASCOD profile. Since the US Standard provides a single profile for typical Northern mid-latitude humidity over the entire year [1], its mixing ratio will be different from the profiles taken on seasonal (FASCOD), monthly (radiosonde climatology) or daily (radiosonde) timescales at various times of the year. Figure 5.2 shows a more detailed profile of the US Standard mixing ratio.

The choice of the *a priori* state should not affect the outcome of retrieval significantly (shown later, in Figure 6.23). However, use of a dramatically different profile may extend the computation time required for the solution to converge (shown later, in Figure 6.24). The *a priori* profile should also be smoothed, as cusps or other sharp features may result in discontinuities during numerical computations (Figure 6.6).

5.2.2 Additional atmospheric state quantities

In addition to choosing an *a priori* humidity profile, profiles of atmospheric pressure and temperature must also be chosen. These profiles are used as *b-parameter* terms in the radiative transfer part of the radiometer forward model (introduced in Section 5.4.2), and are required for the number density profile used in the lidar forward model (introduced in Section 5.3.2).

Figure 5.3 shows the sample pressure and temperature profiles, as well as the calculated number density profiles from the various sources considered for this analysis. Along with the sources mentioned in the previous sections, additional profiles have been considered here. MSISE Model 1990 is a revised version of the MSIS-86 (Mass-Spectrometer-Incoherent-Scatter) model, initially intended for study of the upper atmosphere, which extends it down into the lower atmosphere [22], with lowermost atmospheric values largely based on analysis of National Meteorological Center Data [47]. Like MSIS, the CIRA-86 (COSPAR International Reference Atmosphere) model is also intended for upper atmospheric study, but does also extend into the lower atmosphere [38]. Both MSIS-90 and CIRA-86 provide temperature data for various times throughout the year, for different latitudes. Both are also provided in the ARTS package (See Section 5.4.2 for more on ARTS). NCEP (National Center for Environ-

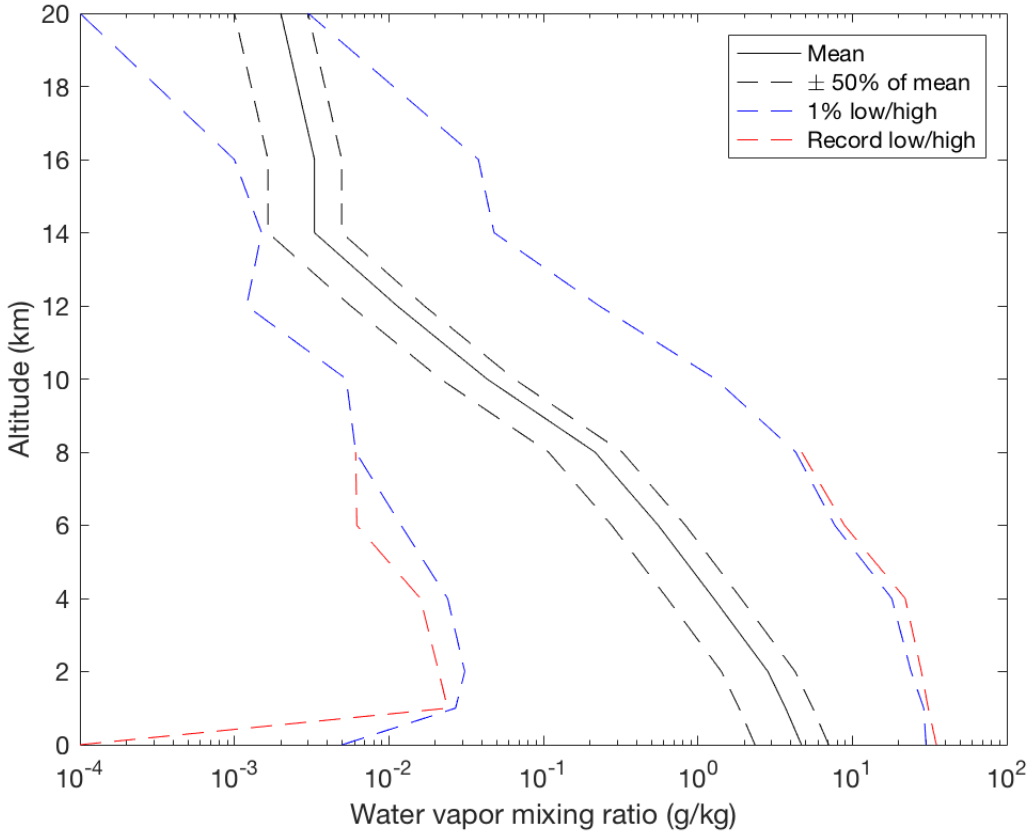

Figure 5.2: Water vapor mixing ratio profile from the US Standard Atmosphere model 1976. The solid black line is the mid-latitude mean, with the dashed black lines showing ±50% of the mean value. The dashed blue lines show the 1% low and high levels, with the dashed red lines showing the extreme low and high values based on global record measurements (Adapted from [1], Table 20).

mental Prediction) is the NCEP/NCAR Reanalysis, which carries out data assimilation from an extensive long-term database comprised of radiosoundings, as well as surface, aircraft, and satellite-based measurements. The reanalysis outputs average quantities 4 times daily (00:00, 06:00, 12:00, 18:00 UTC) [1] [15].

The radiosonde, launched at 22:55 UTC, has a temperature measurement that is more variable during its ascent than the climatological or model-derived profiles. The NCEP profile appears to follow the radiosonde reasonably well, with a temperature difference no greater than 1.5% up to 18 km. This similarity is reasonable, as the NCEP profile is a reanalysis determined by assimilation of data from various sources, including global radiosondes. Since it follows the sonde well, and is a much smoother profile than the raw sonde measurement, it is used for comparing the pressure and temperature from the other profiles. The US1976 and FASCOD temperature profiles show a sharp turn around 10 km, approximately where the mid-latitude tropopause would be. As a result, they show the greatest difference from the NCEP profiles for both pressure and temperature.

5.2.3 Atmospheric State uncertainties

In setting up the OEM retrieval, it is essential to estimate the uncertainties associated with the *a priori* mixing ratio profile, as well as the *b-parameter* pressure and temperature profiles. The profiles shown in Figures 5.1 and 5.3 are mean profiles, which do not indicate how variable these atmospheric state quantities can be over time. To determine this variability, and thus estimate the uncertainties of such *a priori* atmospheric profiles, we have taken the available individual radiosonde profiles between 1973 and 2017 (not just the climatological averages, as shown in the aforementioned figures) and plotted those in Figure 5.4. Fetched from the University of Wyoming radiosonde database[2], these plots represent the available atmospheric

[1] NCEP/NCAR Reanalysis data is available through the NOAA Earth System Research Laboratory: https://www.esrl.noaa.gov/psd/data/gridded/data.ncep.reanalysis.html

[2] The University of Wyoming, Department of Atmospheric Science hosts a database of soundings from around the world. http://weather.uwyo.edu/upperair/sounding.html

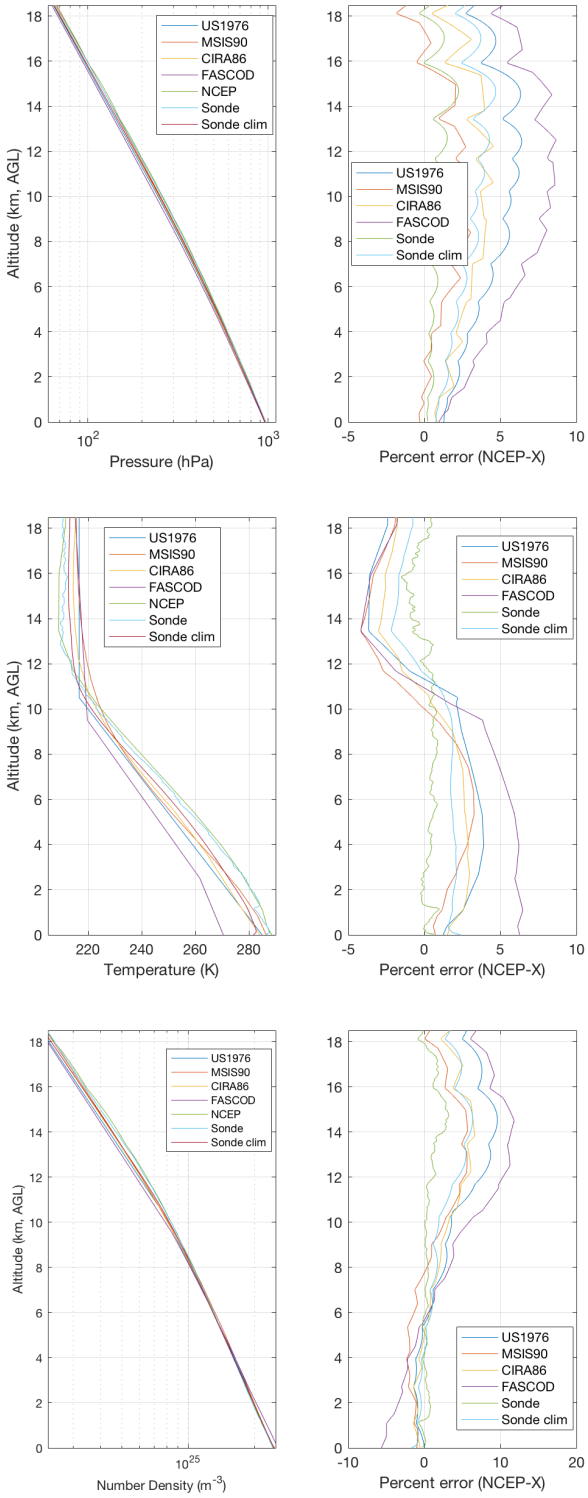

Figure 5.3: Raw pressure (top), temperature (middle), and number density (bottom) profiles considered for the input atmospheric state. *Sonde* is a single raw radiosonde profile on October 5, 2011 at 22:55 UTC, *Sonde clim* is a monthly (October) climatological average of the radiosondes, *NCEP* is a reanalysis, and *US1976*, *MSIS90*, *CIRA86*, and *FASCOD* are profiles provided by their respective atmospheric models.

state data from the nightly radiosondes launched at Payerne between 1973 and 2017 during the month of October, with outliers exceeding 3σ omitted. From the figure, it is evident that the lack of humidity measurements above 12 km, so the uncertainties for humidity determined in this section will go up to this height. Additionally, the data here come from a times series spanning more than 40 years, with the October monthly mean profiles for temperature, pressure, relative humidity, and mixing ratio over this time shown in Figure 5.5. Over this 44 year time series, the pressure profiles show little variation (standard deviation around 7 hPa near the surface), with the standard deviation of temperature around 4 K near the surface. The relative humidity and mixing ratio, on the other hand, vary dramatically from year to year. Such a substantial variation in humidity is due to the natural variability of atmospheric water vapor along with very little data available in the upper troposphere, particularly in the earlier days of observation. The resulting relative standard deviation (the ratio of the standard deviation to the mean, showing variation with respect to the mean) for each atmospheric quantity over varying time scales are shown in Figure 5.6. For each quantity, the relative standard deviation is generally small close to the surface, increasing as the radiosonde reaches the tropopause. For temperature and pressure, the variation is less than 3% at all altitudes, while the relative humidity and mixing ratio show much greater variation above the first 3 km. Time trends in the data do not have a large effect these standard deviations. That is, estimating the standard deviation from a smaller, more recent timespan (2007-2017), as opposed to use of the entire time series (1973-2017), alters the temperature uncertainty by no more than 0.2% and the mixing ratio uncertainty less than 8%. In Section 6.3.1, the effects of these standard deviations will be examined.

5.2.4 *A priori* covariance

As mentioned in Section 5.2.1, the choice of an *a priori* state should not affect the retrieved state. The *a priori* covariance, on the other hand, is essential for a successful retrieval, and must therefore be chosen carefully.

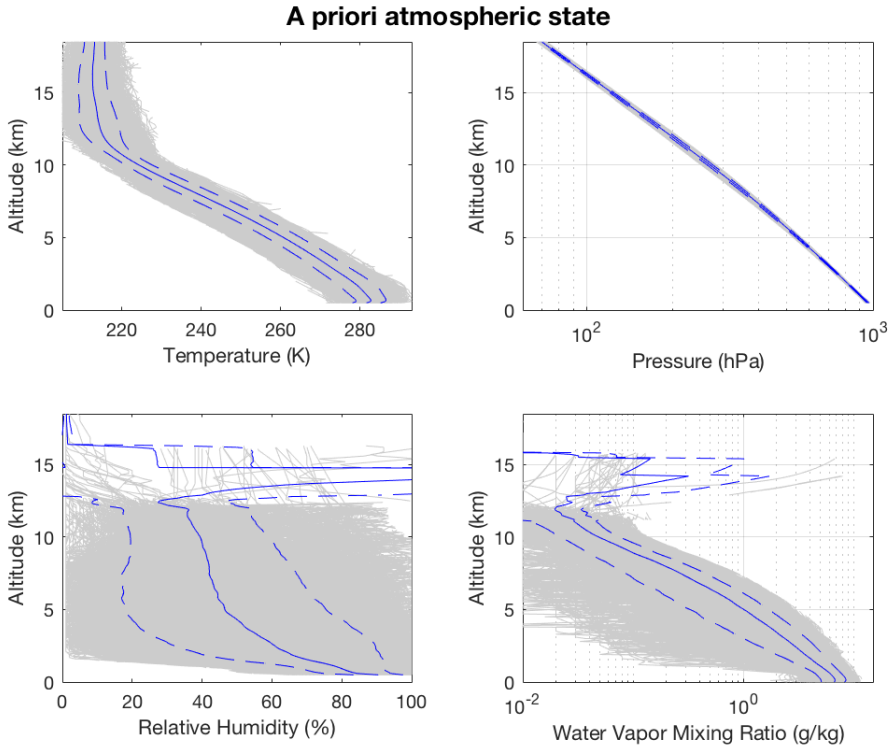

Figure 5.4: Atmospheric states from October nightly Payerne radiosondes, 1973-2017. The solid line is the mean, with the dashed lines being the standard deviation.

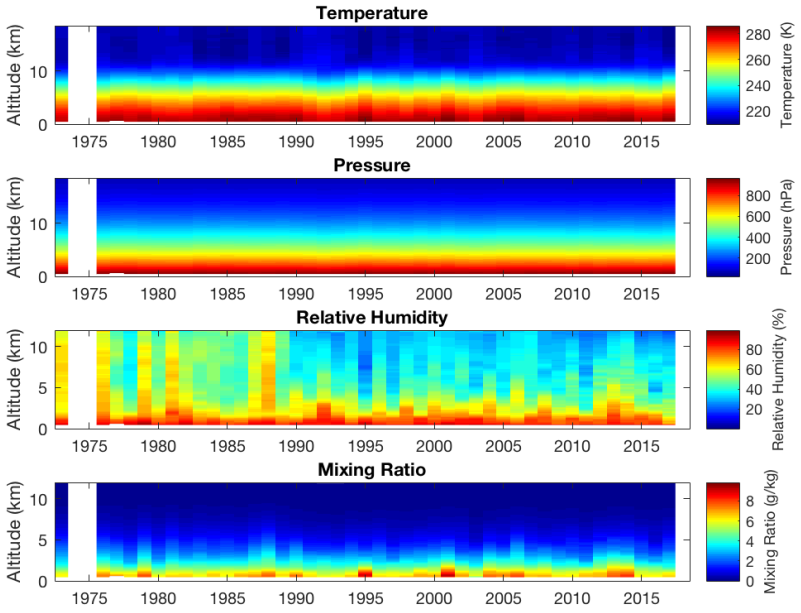

Figure 5.5: Time series (1973-2018) of yearly means for temperature, pressure, and mixing ratio.

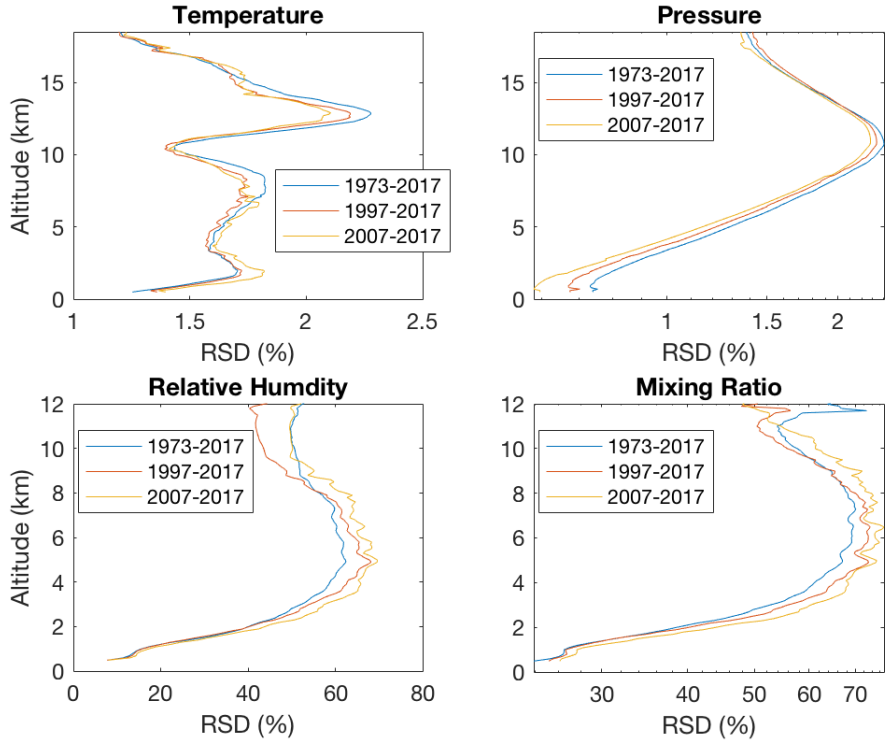

Figure 5.6: Relative standard deviations (RSD) for data across different time ranges.

Although it may be calculated from a atmospheric climatological records, the idealized *a priori* covariance matrix can be expressed as:

$$S_{ij} = \sigma_a^2 \exp(-|i-j|\frac{\delta z}{l_c}) \tag{5.12}$$

where σ_a^2 is the variance, δz is the spacing between grid levels, and l_c is the length scale where the inter-level correlation is 1/e (hereafter referred to as the correlation length) [39]. The covariance matrix can further be specified by choosing from three different correlation functions [17]:

Linear (tent) function

$$S_{ij} = \sigma_i \sigma_j \left[1 - (1 - e^{-1})\frac{2|z_i - z_j|}{l_{c,i} + l_{c,j}}\right] \tag{5.13}$$

Exponential function

$$S_{ij} = \sigma_i \sigma_j \exp\left(\frac{-2|z_i - z_j|}{l_{c,i} + l_{c,j}}\right) \tag{5.14}$$

Gaussian function

$$S_{ij} = \sigma_i \sigma_j \exp\left(-4\left(\frac{z_i - z_j}{l_{c,i} + l_{c,j}}\right)^2\right) \tag{5.15}$$

Variance

In each case, the covariance matrix is dependent on the variance and the correlation length. The variance for the *a priori* covariance matrix comes from estimates of the standard deviation for the mixing ratio. Sica & Haefele 2016 used a constant standard deviation of 50% of the *a priori* mixing ratio, which is a reasonable estimate for the highly variable nature of atmospheric water vapor [44]. The standard deviation from radiosonde climatological data shown in Figure 5.6 gives a profile varying from 20-70%. Both standard deviations will be tested and compared in a simulated retrieval (Chapter 6).

Correlation Length

The correlation length is a metric describing the scale (the range of altitudes in our case) on which atmospheric parameters are assumed to be related, and may therefore be difficult to constrain. In Sica & Haefele 2016 [44], a correlation length of 787.5 m is used for the *a priori* mixing ratio covariance. Correlation lengths have been set for other OEM retrievals, including temperature (l_c = 3000 m [43]), ozone (l_c = 1000 m below 18 km, l_c = 1500 m above 18 km [18]), air density (l_c = 1500 m [18]), and aerosols (l_c = 1 − 2 km [36]).

The aerosol correlation length was determined by generating an autocorrelation matrix from a 10 year set of backscatter sondes. A least squares fit across each row of the matrix is performed on Equation 5.14 to determine a height profile of correlation lengths. Although the calculated correlation length varied between 1 to 2 km, the authors use a much smaller value of 100 m as the correlation length for their analyses, so it would not overconstrain the solution [37].

A similar procedure was carried out for a mixing ratio correlation length, using the climatological radiosonde dataset for Payerne. An autocorrelation matrix is constructed from the sonde dataset by calculating the Pearson correlation coefficient for each point (Figure 5.8). We then assume the covariance is proportional to the correlation, such that the correlation length via the linear function is related to the correlation:

$$Corr_i = \exp\left(\frac{-|z - z_i|}{\bar{l_{c,i}}}\right) \tag{5.16}$$

where i is the index for each row of the matrix. As shown in Figure 5.7, a least squares fit can then be performed across each row of the autocorrelation matrix, finding the correlation length via each correlation function type: Tent (Equation 5.13), Exponential (Equation 5.14), Gaussian (Equation 5.15). The resulting correlation length profile is shown in the right plot of Figure 5.8, with best fitting function at each altitude. The correlation length is determined along the rows of the autocorrelation matrix, while the correlation peak trends along the secondary diagonal of the matrix. Sampling this matrix horizontally may stretch the shape of this peak, giving a false estimate of the correlation length. Sampling of the matrix was also carried out, with slices running along the primary diagonal axis, perpendicular to the correlation peak. Figure 5.9 shows the correlation length determined in this manner, demonstrating significantly reduced correlation lengths. A summary of these values in shown in Table 5.1. The effects of using different correlation lengths will be discussed for simulated retrieval cases in Section 6.3.1.

5.3 Lidar Retrieval

A longtime tool in the passive remote sensing community, the use of OEM has started making an appearance in the retrievals of lidar-derived quantities in recent years. Inverse modelling has previously been used in the retrieval of aerosol parameters [46] and Rayleigh-scatter temperatures [27]. Optimal estimation has also been used to retrieve the Raman channel overlap

Correlation Lengths			
Quantity	Pressure	Temperature	log(mixing ratio)
Minimum $l_c(z)$ (km)	14.5	1.58	2.3
Mean $l_c(z)$ (km)	23.5	5.4	6.9
Maximum $l_c(z)$ (km)	42.4	8.66	9.4
Correlation function	Gaussian	Tent	Exponential
Minimum $l_{c,slice}(z)$ (km)	5.7	-	1.7
Mean $l_{c,slice}(z)$ (km)	9.5	3.5	3.0
Maximum $l_{c,slice}(z)$ (km)	14.6	11.1	3.9
Correlation function	Gaussian	Tent	Gaussian

Table 5.1: Statistics from correlation length height profiles calculated using the method discussed in Section 5.2.4 for October radiosonde climatologies, using least squares fitting horizontally (l_c) and diagonally ($l_{c,slice}$) across the autocorrelation matrix (As in Figure 5.8). The listed correlation functions represent the functions resulting in the best fit for that profile.

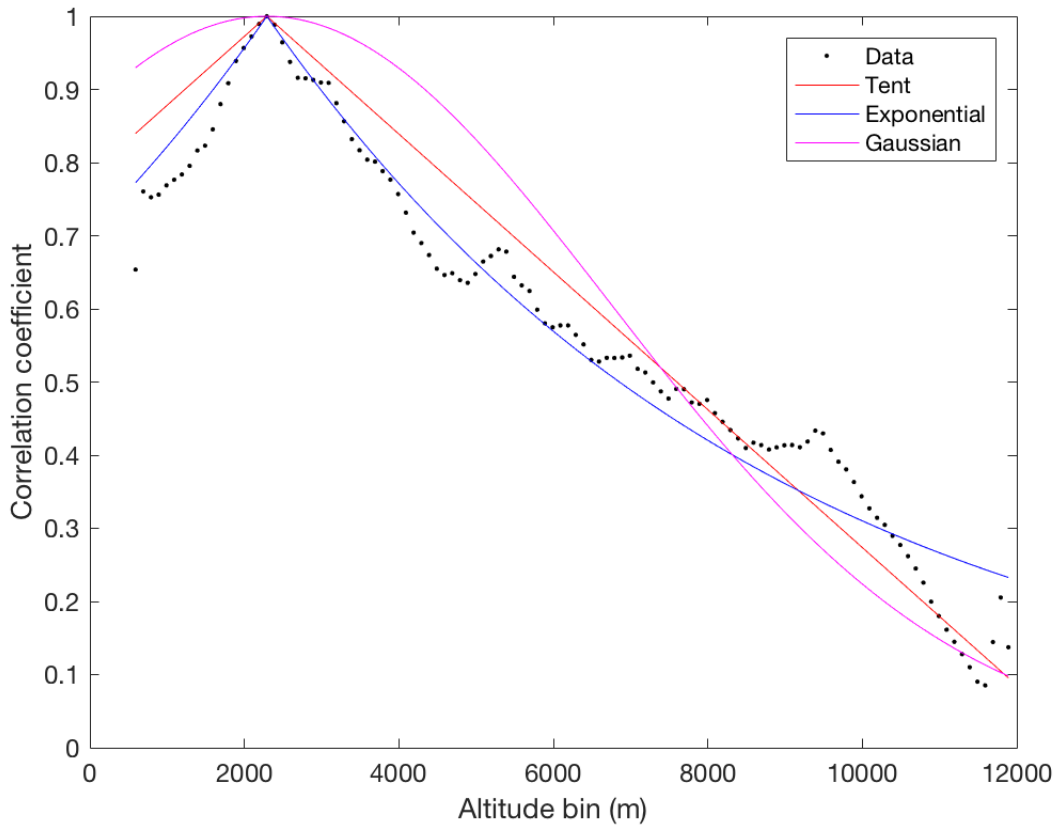

Figure 5.7: Fit of various functions (Tent: Equation 5.13, Exponential: Equation 5.13, Gaussian: Equation 5.15) to the matrix row corresponding to 2.29 km in Figure 5.8.

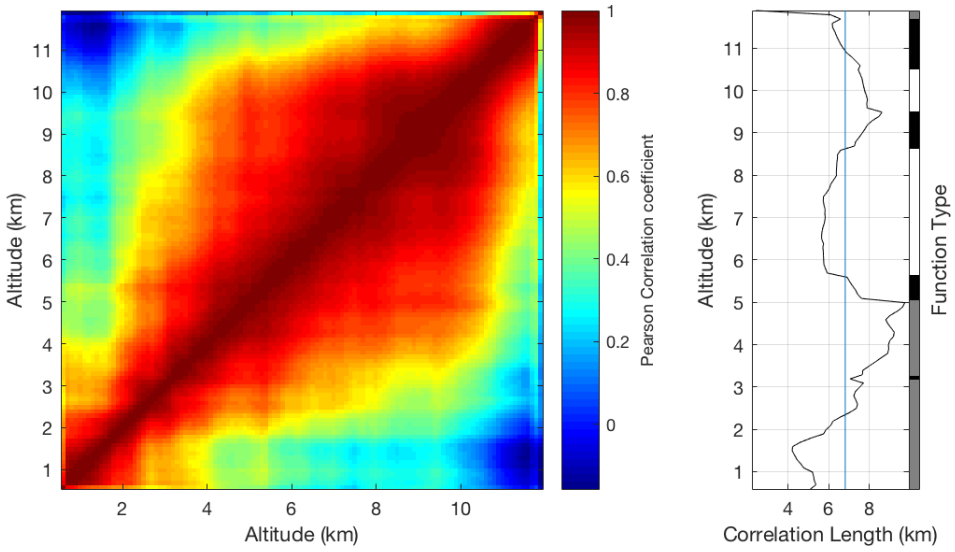

Figure 5.8: (Left) Autocorrelation matrix of the climatological radiosonde-derived mixing ratios. (Right) The correlation length calculated for each row of the matrix, with a color bar showing the function with the best fit at that altitude (Tent=black, Exponential=grey, Gaussian=white).

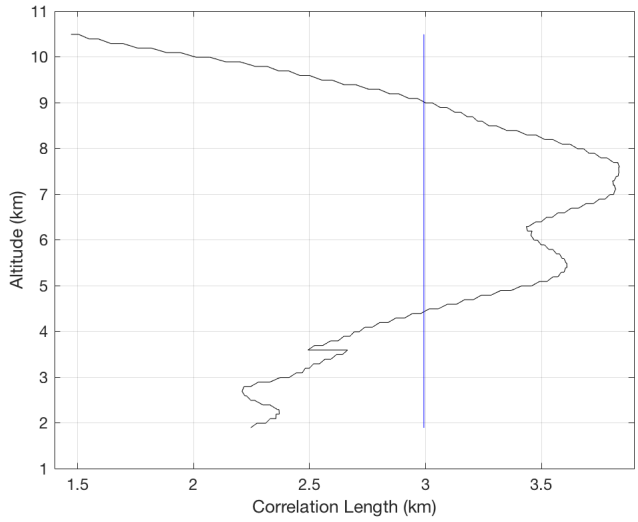

Figure 5.9: Correlation length derived by slicing across the autocorrelation matrix diagonally rather than horizontally.

function [35] and aerosols [36], Rayleigh-scatter [43][25] and Rotational Raman temperature [30], and ozone number density [18] profiles. The following lidar retrieval description comes from the approach presented in Sica & Haefele 2016, with further modifications made by Shannon Hicks-Jalali [23].

5.3.1 Lidar measurement state and covariance

For the retrieval of water vapor mixing ratio via Raman lidar, the measurement state consists of height profiles of backscattered signal from water vapor and nitrogen. The nitrogen and water vapor counts, in both PC and analog counting modes, are binned spatially into 3.75 m altitude bins and temporally into 1 minute "scans". Scans with PC nitrogen SNR<1[3] at 13 km are assumed to have clouds, and are masked and removed from the count array. For night observations, scans with high background in the PC nitrogen channel (>0.01 counts/bin/s) are also omitted [24]. The raw count profiles for the 4 RALMO channels used in water vapor retrievals are shown in Figure 5.10.

The counts are summed over the entire measurement period into single height profiles for each channel. Analog counts below 50 m and PC counts below 500 m above the surface are removed. The profiles are coadded with height, and count rates are then converted to hertz. The measurement variance is piecewise, calculated as:

$$\sigma_y^2 = std(y - y_f)^2 \tag{5.17}$$

where y_f is the fitted measurement. For calculating the PC channel variance, the measurement is corrected for deadtime. The processed data, along with their respective variances, are shown in Figure 5.11. As the measurements are assumed to be uncorrelated, the measurement covariance matrix is simply a matrix where the measurement variances fall along the diagonal, with no off-diagonal elements.

[3]For this work, SNR (signal-to-noise ratio) is defined as the ratio of the background-subtracted lidar signal to the noise (the square root of the lidar signal).

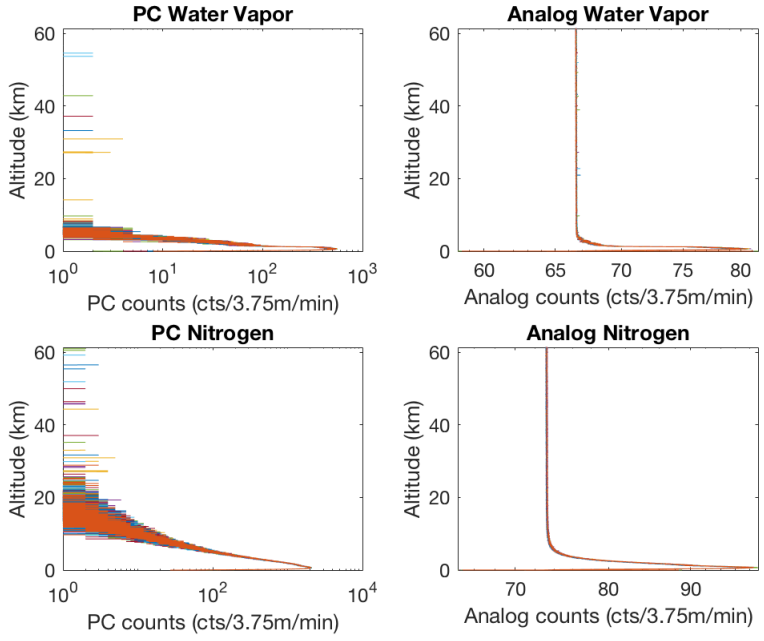

Figure 5.10: 30 minutes of raw count data for water vapor and nitrogen (in PC and analog counting modes), starting at 22:55 UTC on October 5, 2011. Each trend represents a profile of counts averaged over a 1 minute scan.

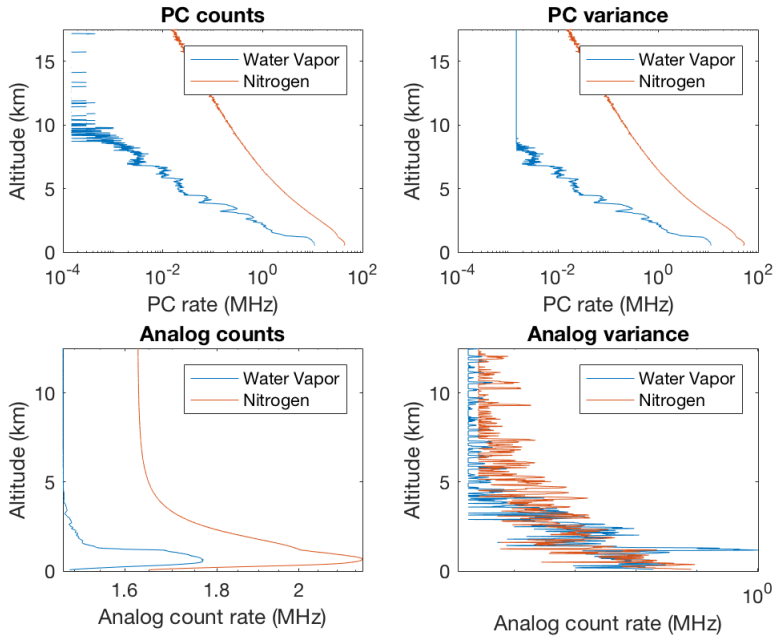

Figure 5.11: Processed measurements of the water vapor and nitrogen channels (left), and their variances (right).

5.3.2 Lidar Forward Model

In the OEM Lidar WVMR retrieval, the forward model is comprised of the lidar equations for each of the 4 data channels (in the form of Equation 2.11):

$$\begin{aligned} N'_{HD}(z) &= \frac{C_{HD}}{z^2} \cdot n_H(z) \cdot O_H(z) \cdot \Gamma_H(z, \lambda_H) + B_{HD}(z) \\ N_{HA}(z) &= \frac{C_{HA}}{z^2} \cdot n_H(z) \cdot O_H(z) \cdot \Gamma_H(z, \lambda_H) + B_{HA}(z) \\ N'_{ND}(z) &= \frac{C_{ND}}{z^2} \cdot n_N(z) \cdot O_N(z) \cdot \Gamma_N(z, \lambda_N) + B_{ND}(z) \\ N_{NA}(z) &= \frac{C_{NA}}{z^2} \cdot n_N(z) \cdot O_N(z) \cdot \Gamma_N(z, \lambda_N) + B_{NA}(z) \end{aligned} \tag{5.18}$$

where the subscripts HD and HA are the water vapor PC and analog channels, and ND and NA are the nitrogen PC and analog channels. Each equation also has a calibration constant term, C_X, absorbing the additional terms from Equation 2.11. As the lidar equation works under the assumption that N_X is the true count rate, the PC channel lidar equations in Equation 5.20 are corrected for count saturation. So, in order to transform the true state into the observed measurement state for these channels, a deadtime correction is required:

$$\begin{aligned} N_{HD}(z) &= \frac{N'_{HD}}{1 + N'_{HD} \cdot \tau_{d,H}} \\ N_{ND}(z) &= \frac{N'_{ND}}{1 + N'_{ND} \cdot \tau_{d,N}} \end{aligned} \tag{5.19}$$

where N_X is the measurement, N'_X is the true state, and $\tau_{d,X}$ is the dead time for each channel.

The mixing ratio can be incorporated into the forward model by rearranging the WVMR (Equation 2.12) and inserting it into the water vapor number density in the water vapor channel lidar equations:

$$\begin{aligned} N'_{HD}(z) &= \frac{C_{HD}}{z^2} \cdot w \cdot \frac{n_N(z)}{w_N} \cdot O_H(z) \cdot \Gamma_H(z, \lambda_H) + B_{HD}(z) \\ N_{HA}(z) &= \frac{C_{HA}}{z^2} \cdot w \cdot \frac{n_N(z)}{w_N} \cdot O_H(z) \cdot \Gamma_H(z, \lambda_H) + B_{HA}(z) \end{aligned} \tag{5.20}$$

where w_N is the nitrogen mixing ratio.

The nitrogen number comes from the input atmosphere state temperature and pressure profiles. As in Sica & Haefele 2016, the overlap function comes from Dinoev et al. 2013 [14]. Atmospheric transmission and optical depth are defined in Equations 2.22 and 2.23 respectively. The Rayleigh extinction cross section, $\sigma_{ray}(\lambda_X)$, is calculated via Nicolet 1984 [34], and the Angstrom exponent is given a value of 1.5 (1.0 in Sica & Haefele 2016). The aerosol optical depth is then:

$$\tau_{aer} = \int_0^z \alpha_{aer} dz \tag{5.21}$$

The aerosol extinction is:

$$\alpha_{aer} = LR \cdot (\beta_{mol} \cdot (\beta - 1)) \tag{5.22}$$

where LR is the lidar ratio, β_{mol} is the molecular backscatter coefficient and β is the aerosol backscatter coefficient. The lidar ratio is chosen based on Ansmann and Muller [6]. β_{mol} is calculated using equations given in Bucholtz 1995 [9]. β is derived from the ratio of the lidar's elastic backscatter signal to its molecular signal.

Aside from the mixing ratio, it is useful to retrieve the other unknown quantities in the forward model. One such quantity is the deadtime. Although counting instruments are generally equipped with specifications including properties such as deadtime, it would be ideal to be able to retrieve it. Additionally, although we can estimate the lidar signal background, this may not be representative of the true background.

The calibration constants for each channel are also not well known, making them an ideal choice of retrieval. To give more physical significance to these constants, only 3 of the 4 calibration constants are retrieved. The fourth constant, C_{HD}, is not retrieved, but is instead scaled from C_{ND} via a calibration factor, η:

$$C_{HD} = \eta \cdot C_{ND}. \tag{5.23}$$

The calibration factors over time for RALMO, determined using a variety of methods, are

shown in Figure 5.12. $C_{trad,1}$ and $C_{trad,0}$ are the factors calculated via the traditional radiosonde calibration method (from Section 4.2.1), using GRUAN-corrected radiosondes (as discussed in Hicks-Jalali et al. 2019 [24]) and operational radiosondes, respectively. C_{traj} are determined using the Trajectory method (Section 4.2.2) for GRUAN-corrected sondes (as discussed in Hicks-Jalali et al. 2019 [24]), while C_{BKG} are calculated using the Solar background calibration (Section 4.6, from [31]).

Originally, Sica & Haefele 2016 also retrieved aerosol optical depth. However, it was replaced by the retrieval of the overlap function, as it is exceedingly difficult to model the function close to the surface due to the presence of a near-field fiber in the receiver system. As the uncertainty in the overlap function is much smaller above 2500 m when complete overlap is reached [44], there is a switch-off, such that below 6 km (for nights), overlap is retrieved, and aerosol extinction is retrieved above this threshold [23].

The remaining terms in the forward model are then set as *b-parameters*. These include the terms that are reasonably well characterized, such as the Rayleigh extinction cross section, air density, calibration factor, Angstrom exponent, aerosol extinction below 6ḱm, and overlap above 6 km. A summary of the retrieved quantities and the forward model *b-parameters* is provided in Table 5.2.

An alternative version of the lidar forward model is also considered. Summarized in Table 5.3, this forward model is not dependent on the radiosonde-dependent calibration factor, but rather retrieves the calibration constants for each channel directly. Retrievals via this forward model are carried out in Chapter 7, where they are compared to the other retrieval methods.

Although both variations of the lidar retrieval are able to retrieve numerous parameters, this work focuses on the retrieval of water vapor mixing ratio exclusively. A more thorough discussion of the additional retrieved parameters is available elsewhere [44][23].

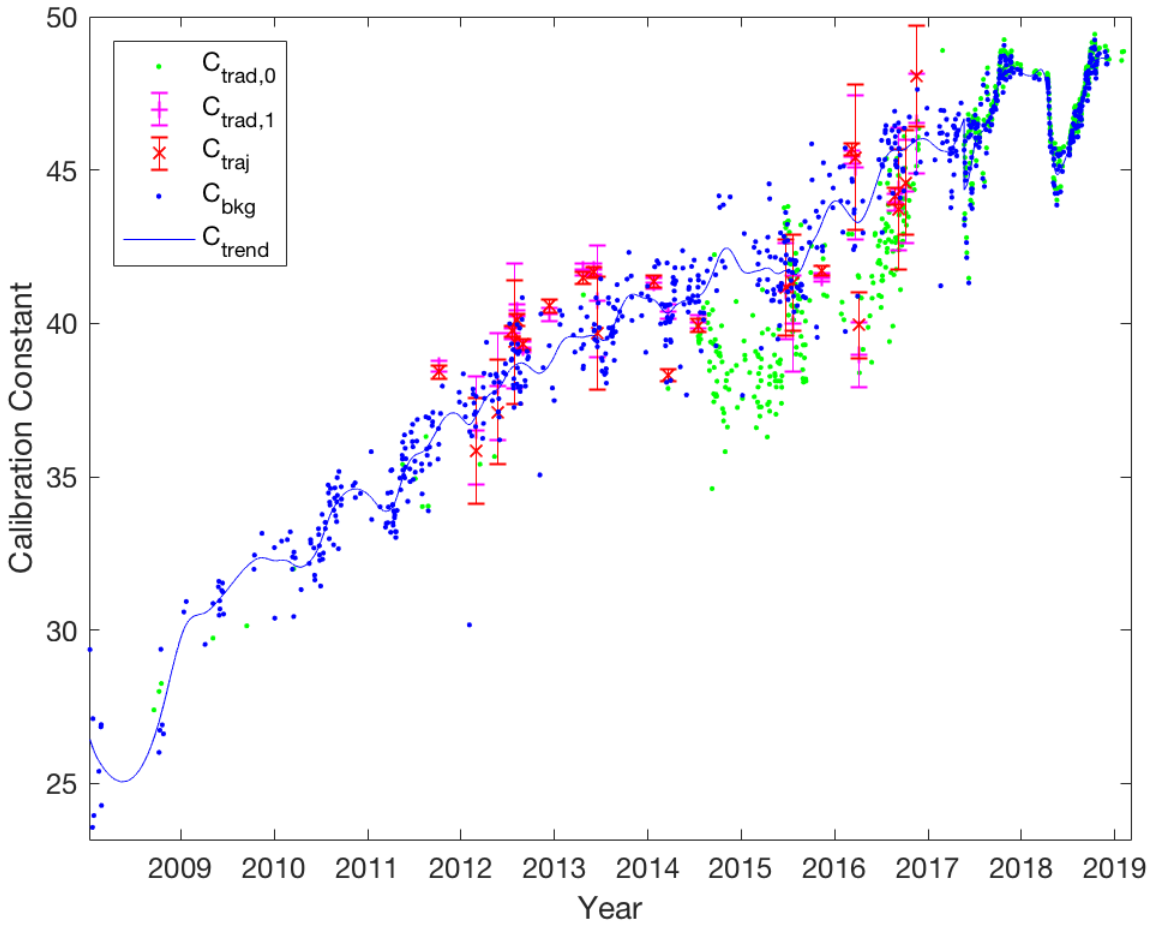

Figure 5.12: Long-term calibration factor trends for RALMO via different methods. $C_{trad,0}$ is the traditionally-determined radiosonde calibration factor, while $C_{trad,1}$ and C_{traj} are the Traditional and Trajectory method values of Hicks-Jalali et al. 2019 [24]. C_{bkg} and C_{trend} are calibration factors determined via the Solar background method [31].

Lidar Forward Model (radiosonde-calibrated retrieval)		
Quantity	State parameters (2m+9)	*a priori* uncertainty, σ_a
Mixing ratio	w [m×1 = $z_0 : z_{top}$]	50% [44]
Overlap	$O(z)$ [m_1×1 = $z_0 : z_{switch}$]	10% [44]
Extinction	$\alpha(z)$ [m_2×1 = $z_{switch} : z_{top}$]	50% [44]
WV analog Lidar Constant (LC)	C_{HA} [1×1]	50% [44]
N_2 analog LC	C_{NA} [1×1]	10% [44]
N_2 PC LC	C_{ND} [1×1]	10% [44]
WV PC dead time	$\tau_{d,H}$ [1×1]	0.2% [44]
N_2 PC dead time	$\tau_{d,H}$ [1×1]	0.2% [44]
WV analog background	B_{HA} [1×1]	Measurement standard deviation
N_2 analog background	B_{NA} [1×1]	Measurement standard deviation
WV PC background	B_{HD} [1×1]	Measurement standard deviation
N_2 PC background	B_{ND} [1×1]	Measurement standard deviation
Quantity	Model *b-parameters*	*b-parameter* uncertainty, σ_b
Rayleigh cross section	$\sigma_R(\lambda)$ [1×1]	0.3% [44]
Air density	n_{air} [m×1 = $z_0 : z_{top}$]	1% [44]
Calibration factor	η [1×1]	5% [44]
Angstrom exponent	a [1×1]	10% [44] 50% [23]
Overlap	$O(z)$ [m_2×1 = $z_{switch} : z_{top}$]	0.01% (Complete overlap) [44]
Extinction	$\alpha(z)$ [m_1×1 = $z_0 : z_{switch}$]	50% [44]

Table 5.2: The input parameters for the Lidar forward model. m is the number of elements in the retrieval grid, an altitude profile ranging from z_0 to z_{top}. m_1 and m_2 are subsets of this retrieval grid, where m_1 is the number of elements from surface up to the hand-off for the overlap/extinction retrieval (6 km [23]), while m_2 is the number of elements from the hand-off to the top of the retrieval.

Lidar Forward Model: Option 2 (no external calibration source)		
Quantity	State parameters (2m+**10**)	*a priori* uncertainty, σ_a
Mixing ratio	w [m×1 = $z_0 : z_{top}$]	50% [44]
Overlap	$O(z)$ [m_1×1 = $z_0 : z_{switch}$]	10% [44]
Extinction	$\alpha(z)$ [m_2×1 = $z_{switch} : z_{top}$]	50% [44]
WV analog Lidar Constant (LC)	C_{HA} [1×1]	50% [44]
N_2 analog LC	C_{NA} [1×1]	10% [44]
WV PC LC	C_{HD} **[1×1]**	**50% [44]**
N_2 PC LC	C_{ND} [1×1]	10% [44]
WV PC dead time	$\tau_{d,H}$ [1×1]	0.2% [44]
N_2 PC dead time	$\tau_{d,H}$ [1×1]	0.2% [44]
WV analog background	B_{HA} [1×1]	Measurement standard deviation
N_2 analog background	B_{NA} [1×1]	Measurement standard deviation
WV PC background	B_{HD} [1×1]	Measurement standard deviation
N_2 PC background	B_{ND} [1×1]	Measurement standard deviation
Quantity	Model *b-parameters*	*b-parameter* uncertainty, σ_b
Rayleigh cross section	$\sigma_R(\lambda)$ [1×1]	0.3% [44]
Air density	n_{air} [m×1 = $z_0 : z_{top}$]	1% [44]
~~Calibration factor~~	~~η [1×1]~~	~~5% [44]~~
Angstrom exponent	a [1×1]	10% [44] 50% [23]
Overlap	$O(z)$ [m_2×1 = $z_{switch} : z_{top}$]	0.01% (Complete overlap) [44]
Extinction	$\alpha(z)$ [m_1×1 = $z_0 : z_{switch}$]	50% [44]

Table 5.3: This forward model option is identical to the Lidar Forward Model (Table 5.2), aside from the additional retrieval of the PC water vapor calibration constant (bolded term), and the removal of the calibration factor as a *b-parameter* (crossed out term).

5.3.3 Lidar retrieval Jacobians

As mentioned in Section 5.1.2, Jacobians are necessary for determining the sensitivity of the forward model, and thus the measurement, to the retrieved state, making them essential for retrieval optimization and the development of parameter uncertainties. The Jacobians for the measurements with respect to the retrieved state are calculated numerically. This is carried out by perturbing one of the state parameters at a certain altitude, running it through the forward model, and finding the difference of the output measurement state relative to that calculated via an unperturbed retrieval state. Although computing Jacobians numerically is conceptually straightforward, it can be computationally intensive, especially for complicated forward models. Luckily, the lidar forward model is relatively simple, allowing for analytic calculation of the forward model sensitivity to model *b-parameters*.

5.4 Microwave Radiometer retrieval

OEM is already a well-established practice in the detection of water vapor using passive sensing instruments, such as radiometers. This section discusses how water vapor mixing ratio can be retrieved from radiometer measurements, based on a radiative transfer forward model.

5.4.1 Radiometer measurement state and covariance

For microwave radiometers, the fundamental measurement is brightness temperature. In the case of the RPG-HATPRO-G2, this consists of brightness temperatures measured in 2 frequency bands: the K-band for profiling the water vapor line and the V-band for profiling the oxygen complex. Under conditions of constant temperature and pressure, the line shape for water vapor can be expressed as a Lorentzian, which can be parameterized by two degrees of freedom: amplitude and bandwidth. However, constant pressure and temperature is not a reasonable assumption for the Earth's atmosphere, requiring additional degrees of freedom. For determining column measurements, such as liquid water path, using the water vapor line at

22.235 GHz, it is ideal to sample using a frequency on the wing of the line and another in the window region. The former is chosen such that the water vapor absorption is more or less independent of altitude, while the latter channel is in a region dominated by liquid water rather than water vapor [29]. The precise choice of channels can be determined by finding the correlation between the brightness temperatures for certain frequency groups. Analysis has shown that sampling at 22.4, 23.9, and 31.4 GHz allows for a complete characterization this water vapor line shape [4]. For the retrieval of a water vapor mixing ratio profile using the HATPRO, we use brightness temperature measurements at 7 K-band frequencies. Although only 3 independent degrees of freedom are required to characterize the water vapor line shape, use of additional channels reduces noise [4].

The radiometer also has 2 scanning modes: zenith and BL-mode. During zenith-mode, the radiometer is zenith-pointing only, measuring brightness temperatures that are used for the retrieval of tropospheric temperature and humidity profiles, liquid water path, and integrated water vapor, at a rate of 1 sample per second. The BL-mode is used for high-resolution profiling of temperature around the boundary layer, scanning across 6 elevation angles: 90°, 42°, 30°, 19.2°, 10.2°, 5.4°. Depending on the user input, BL-scanning can take 2-6 minutes, with a repetition period of 10-20 minutes. The remaining radiometer operating time is devoted to zenith-mode sampling [3]. For our purposes, we only consider zenith-mode measurements. The zenith brightness temperature measurements (Figure 5.13) are then averaged over a certain integration period (for comparison with GRUAN-calibrated lidar retrievals, this is 30 minutes) to produce a single array of frequency-dependent brightness temperatures, as shown in Figure 5.14.

Due to effects such as imperfect calibration and characterization of the radiometer channels, a bias in the raw brightness temperatures may exist. As the offset is nearly constant with time, a scalar correction may be required for the raw brightness temperature data. The difference between brightness temperatures measured by the radiometer, and the expected brightness temperatures (the quantity calculated by inputting radiosonde atmospheric state measurements

into a radiative transfer equation), is shown in Figure 5.15, which uses bias corrections provided by Maxime Hervo, a research scientist at MeteoSwiss Payerne. This brightness temperature bias is determined by the mean, channel-dependent bias over epochs of homogeneous instrument performance. The top plot of this figure shows the bias for each channel over a time series from 2006 to 2018, while the bottom plot shows the resulting brightness temperature difference after the bias is subtracted out. However, as evidenced by the brightness temperatures of Figure 5.14, the bias correction does not always correct the raw measurement, as signal at K-band frequencies is dominated by highly variable water vapor. Additionally, the corrected spectrum looks worse than the raw spectra, due to the high variability in the bias of the 25.44 GHz and 26.24 GHz channels in the region from April to November 2011. The large positive and negative biases of the 26.24 GHz of the 25.44 GHz channels skew their respective mean biases, such that raw measurements with an initially low bias in these channels would be corrected toward an inflated bias.

Radiometric noise can be estimated by:

$$\Delta T_b = \frac{T_{b,atm} + T_r}{\sqrt{\tau \cdot \Delta\nu}} \tag{5.24}$$

where $T_{b,atm}$ is the brightness temperature of the atmosphere, τ is the integration time, $\Delta\nu$ is the channel bandwidth, and T_r is the noise temperature of the receiver ($T_r = \frac{P}{k\Delta\nu}$, where P is the power due to internal noise). The measurement uncertainty is set to 0.1 K for each of the K-band measurements, which is the root-mean-square radiometric resolution, as provided by the HATPRO instrument manual [4]. An uncertainty of 0.1 K is used for testing the retrieval with simulated measurements (Chapter 6). The absolute brightness temperature accuracy of 0.5 K, accounting for noise, short-term stability, and calibration [21][13][32], is used as the measurement uncertainty for retrievals of real measurements (Chapter 7). This may also be determined by monitoring the internal noise of the radiometer over a few hours. The measurement covariance is then derived from the error between the forward model and the measurement [7].

However, here, as in the case of the lidar measurement covariance matrix, the covariance of the radiometer measurement is simply set as a diagonal matrix with the square of the radiometric resolution as the variance. This assumption indicates the measurements are uncorrelated. This is reasonable for simulations, but may not true be for real measurements, as the radiometric channels may be correlated with each other. Despite this, the use of this measurement covariance matrix should not affect the outcome of the retrieval and is therefore used.

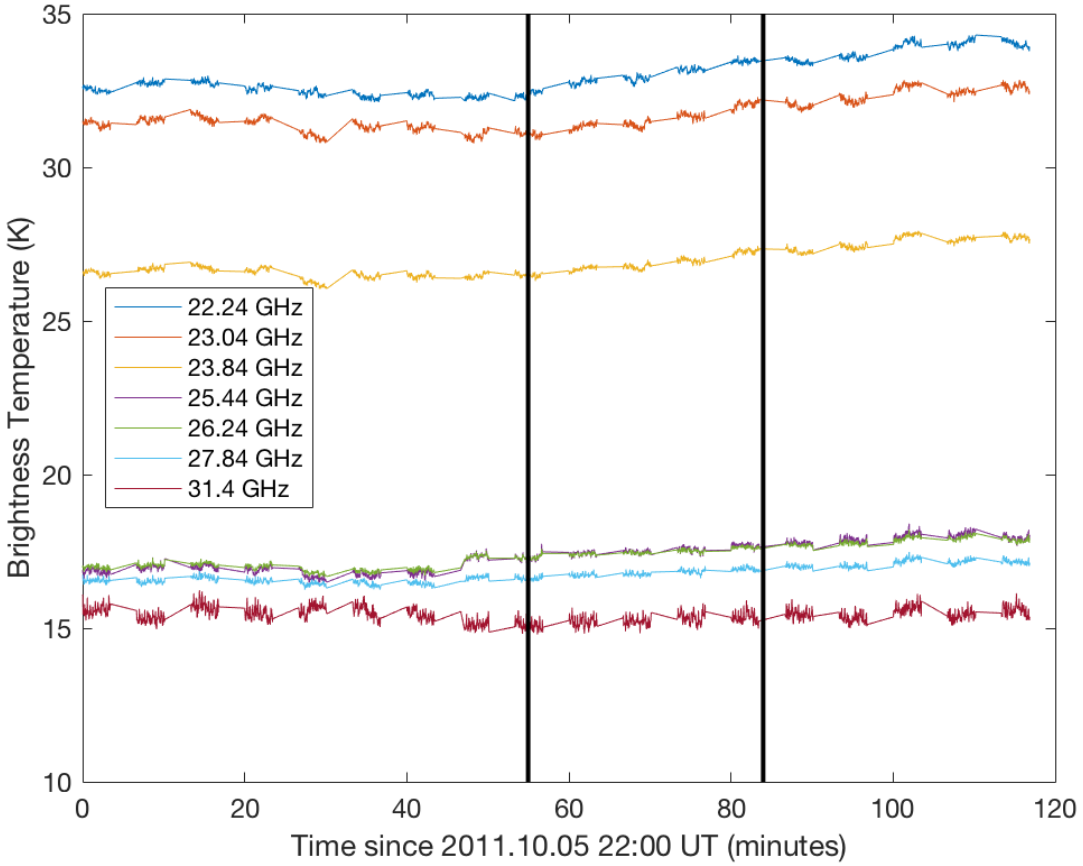

Figure 5.13: Time series of the raw brightness temperatures for the K-band channels between 22:00UT and 23:59UT on October 5, 2011. The vertical black lines indicate the averaging region to produce a single profile (Figure 5.14).

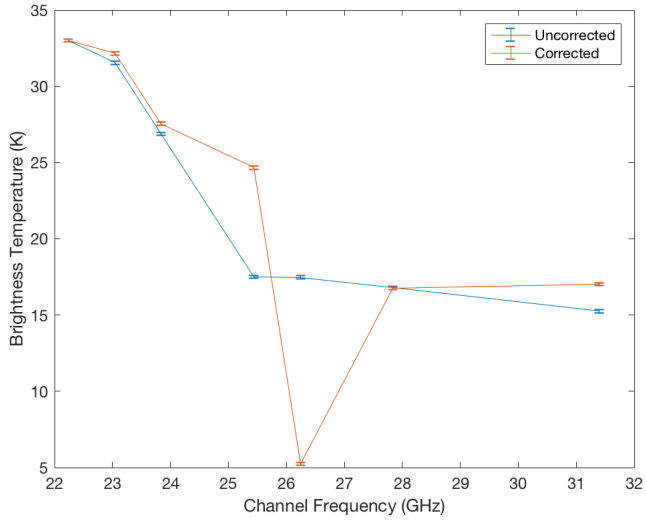

Figure 5.14: Mean K-band brightness temperatures for 22:55-23:25 UTC on October 5, 2011, including the raw and bias-corrected spectra. The error bars represent the radiometric resolution of 0.1 K.

5.4.2 Radiometer Forward Model

The forward model from which atmospheric quantities such as temperature and humidity profiles, as well as integrated quantities such integrated water vapor and liquid water path, can be retrieved from brightness temperature measurements is based on the radiative transfer equation.

The solution for the transfer equation, $\frac{dI_\nu}{ds} = \alpha(B_\nu - I_\nu)$, is:

$$I_\nu(0) = I_\nu(s_0)e^{-\tau(s_0)} + \int_0^{s_0} B_\nu(T)e^{-\tau(s)}\alpha \cdot ds. \tag{5.25}$$

where $I_\nu(s)$ is the intensity as a function of the radiation path length, $B_\nu(T)$ is the Planck function, and τ is optical depth, defined as:

$$\tau(s) = \int_0^{s} \alpha(s') \cdot ds' \tag{5.26}$$

where α is the absorption coefficient. Since $h\nu << kT$ in the microwave region, the Planck function can be approximated as the Rayleigh-Jeans limit. Under this approximation, scattering is also assumed to be negligible, when compared to absorption, in the absence of precipitation

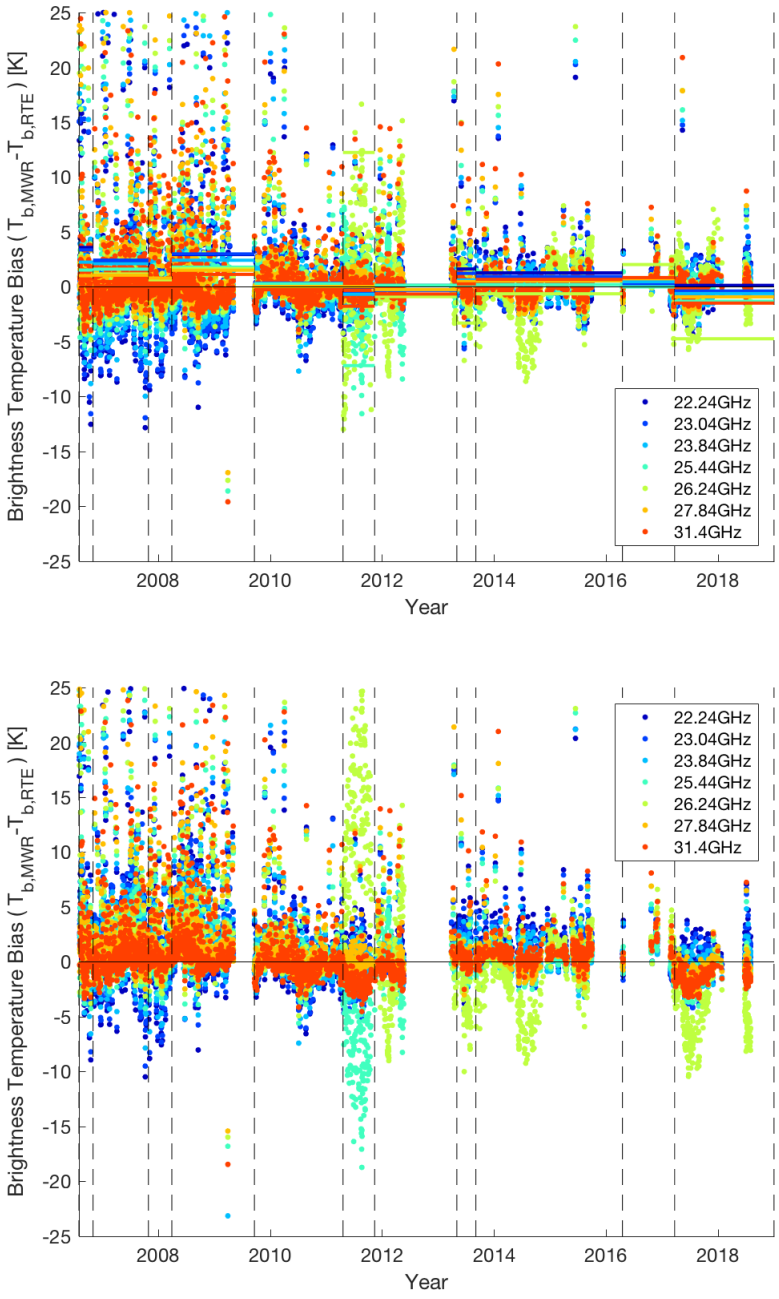

Figure 5.15: (Top) Time series of the radiometer bias, the difference between the radiometer brightness temperature and the simulated brightness temperature from coincidental radiosondes, for each of the K-band channels. The vertical dashed lines show the epochs in which the average bias is used to correct the radiometric brightness temperature. The horizontal lines show this average bias for each channel during each epoch. (Bottom) The difference in brightness temperature after subtracting out the average bias. Data provided by Maxime Hervo, MeteoSwiss.

[42]. Rearranging the Planck function and inserting it into the transfer equation solution gives the monochromatic brightness temperature equation:

$$T_b(\nu) = T_{b,0}(\nu)e^{-\tau(\nu,s_0)} + \int_0^{s_0} T(s) \cdot e^{-\tau(\nu,s)} \cdot \alpha(\nu, s) \cdot ds \tag{5.27}$$

where $T_{b,0}$ is the background brightness temperature, $\tau = \int_{s_0}^{s} \alpha(\nu, s')ds'$ is opacity, and α is the absorption coefficient [26].

The absorption coefficient can then be expressed as:

$$\alpha_{tot}(s) = \alpha_{dry}(s) + \alpha_{wet}(s) + \alpha_{liq}(s) + \alpha_{ice}(s) \tag{5.28}$$

where α_{dry} accounts for the absorption due to nitrogen and oxygen, α_{wet} accounts for water vapor, and the latter two terms on the right are due to liquid water and ice. For clear skies, the latter two terms on the right side of this equation are dropped [42]. The dry and wet absorption coefficients can be dissected further:

$$\alpha = \alpha_l + \alpha_c \tag{5.29}$$

in which the terms on the right are the line and continuum absorption, respectively. The line absorption can be written as:

$$\alpha_l(\nu) = n \cdot S(T) \cdot F(\nu) \tag{5.30}$$

where n is the number density of the absorbing species, $S(T)$ is the line strength, and $F(\nu)$ is the line shape function [19]. In the PWR98 water vapor absorption model, the line absorption uses a Van Vleck-Weisskopf line shape function, which may be thought of as a corrected Lorentzian (pressure-broadened) line shape [40]. The continuum absorption is an empirical formulation, which for the PWR98 water vapor absorption model can be expressed as:

$$\alpha_c = \nu^2 \cdot P_{H_2O} \cdot (C^0_{H_2O} \cdot P_{H_2O} \cdot \Theta^{7.5} + C^0_{dry} \cdot P_{dry} \cdot \Theta^3) \tag{5.31}$$

where P_{H_2O} and P_{dry} are the partial pressure of water vapor and dry air, $\Theta = \frac{300K}{T}$, and $C^0_{H_2O}$ and C^0_{dry} are empirical coefficients.

Both absorption terms are ultimately dependent on pressure, temperature, and vapor pressure, consequently requiring the forward model to take in profiles of pressure, temperature, and humidity. A summary of inputs required by the radiometric forward model is provided in Table 5.4. The state vector of the the radiometer retrieval is the water vapor mixing ratio. The priori estimate of the state is provided by a smoothed US Standard Atmosphere Model water vapor mixing ratio profile, with an *a priori* covariance based on an *a priori* mixing ratio uncertainty of 50%. The forward model also considers *b-parameter* profiles of pressure and temperature. The initial *b-parameter* covariance, S_b, for pressure is built based on an input *b-parameter* pressure uncertainty of 5%. The *b-parameter* covariance for temperature is built via a temperature uncertainty of 5 K.

Radiometer Forward Model		
Quantity	State parameter (m)	*a priori* uncertainty, σ_a
Mixing ratio	w [m×1 = $z_0 : z_{top}$]	50% [44]
Quantity	Model *b-parameters*	*b-parameter* uncertainty, σ_b
Pressure	$P(z)$ [m×1 = $z_0 : z_{top}$]	5% [28]
Temperature	$T(z)$ [m×1 = $z_0 : z_{top}$]	5 K [28]

Table 5.4: Summary of the inputs for the radiometer forward model.

ARTS Implementation

The ARTS (Atmospheric Radiative Transfer Simulator) program, developed by researchers from the University of Bremen in Germany and Chalmers University in Sweden, is a modeling tool intended for 1-dimensional simulations of atmospheric radiative transfer for passive remote sensing in millimeter and sub-millimeter regimes. Absorption coefficients are calculated line-by-line using catalogues such as JPL, HITRAN, or MYTRAN. Its flexibility allows for the user to choose from various observational geometries (zenith, nadir, limb, etc.), as well as options for line shape and absorption model. It is written in C++ for fast computation, and can

calculate the Jacobians for atmospheric species abundances analytically [10]. The ARTS community has also released Qpack, a software package providing a MATLAB shell around the ARTS forward model.[4] This package allows the user to specify parameters via a MATLAB interface, which then calls the ARTS forward model using the Qarts utility. Qpack also allows for the characterization of the sensor, and provides additional useful functions for reducing data, constructing covariance matrices, and performing retrieval inversions [17]. ARTS-2 expands on the capabilities of its predecessor by allowing for 2 and 3-D modelling, includes functionality for handling scattering and polarization, and considers additional observational geometries [16]. The recent stable release of ARTS-2.2 includes a planetary toolbox for simulations of planetary atmospheres [11].

Cimini Implementation

In addition to ARTS, we also considered the NOAA radiative transfer forward model implementation presented in Schroeder & Westwater 1991 [42]. This implementation, originally written in Fortran, was adapted into MATLAB functions by Domenico Cimini, a researcher at the Institute of Methodologies and Environmental Analysis of the National Research Council in Italy. (This forward model implementation is hereafter referred to as the Cimini Implementation.) Although it does not boast the speed and generality of ARTS, its functionality is dependent on significantly fewer functions, making it possible to adapt the forward model for an integrated retrieval.

Due to the complicated nature of the forward model, we set up the retrieval so the Jacobians are calculated numerically, in the same manner as the retrieved parameter Jacobians in the lidar retrieval.

[4] Both ARTS and the Atmlab package (which contains Qpack) are publicly available at the ARTS website: http://www.radiativetransfer.org/

Comparison between the Implementations

Since the ARTS forward model has been used extensively by the atmospheric community, we want to test the performance of the Cimini implementation relative to ARTS. Atmospheric state profiles from the US Standard Model Atmosphere 1976 are fed into the forward models, with the calculated brightness temperatures shown in Figure 5.16. Aside from the 2 most opaque channels, the difference in calculated brightness temperature is less than the radiometric resolution, and all channels are well within in the HATPRO's absolute brightness temperature accuracy of 0.5 K.

Jacobian calculation and retrievals were carried out using both implementations. Comparison plots between the water vapor volume mixing ratio Jacobians calculated via ARTS and Cimini are shown in Figure 5.17. Cimini Jacobians are calculated numerically while ARTS has the option to calculate the Jacobians analytically or numerically. In the top plots of Figure 5.17, the ARTS Jacobians are computed analytically, while those of Cimini are determined numerically. Comparison of these Jacobians shows differences up to 15% for the most transparent channels. If ARTS is parameterized to calculate Jacobians numerically (shown in the bottom left plot of Figure 5.17), the largest difference in Jacobian value is also seen in the most transparent channels, but is now only a 3% difference. The Jacobians determined by the Cimini implementation are more similar to the numerically-determined than analytically-determined ARTS Jacobians. However, in all cases, the calculations are in reasonably good agreement with each other. Figure 5.18 provides a comparison of the mixing ratio profiles retrieved by the two implementations. The figure shows similar values for the two profiles, with a maximum difference of 1.2% near the surface. Above this height, the difference is much smaller, hovering around a 0.2% difference. Due to its similarities with ARTS in its ability to calculate brightness temperatures similar to within the measurement uncertainty as well as the reasonable retrieval of mixing ratio and its associated Jacobians, it is reasonable to use the Cimini implementation for the integrated retrieval.

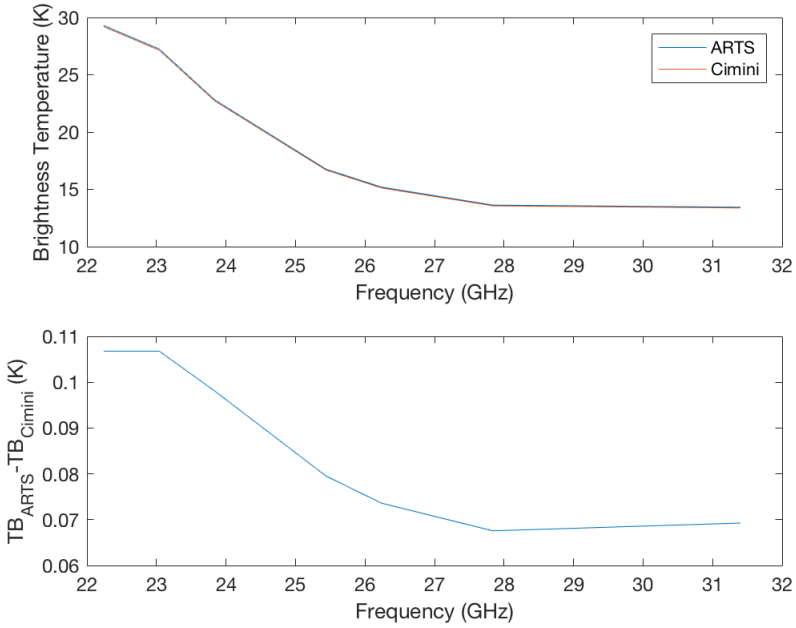

Figure 5.16: Forward model calculations of brightness temperature from US Standard model inputs, using the ARTS and Cimini implementations (top), and the difference between the brightness temperatures calculated via the two implementations (bottom).

5.5 Integrated Retrieval (SLiRadIHuR)

SLiRadIHuR (Swiss Lidar-Radiometer Integrated Humidity Retrieval)[5] is a collection of MATLAB functions developed for carrying out the integrated retrieval presented in this work. The retrieval builds on the individual retrievals of humidity using lidar and microwave radiometer, as described in the previous sections of this chapter.

[5] Although not used here, ACRONYM (Acronym CReatiON for You and Me) is a publicly-available package for generating silly acronyms for all of your projects, based on Natural Language processing. The code is available at https://github.com/bacook17/acronym [12].

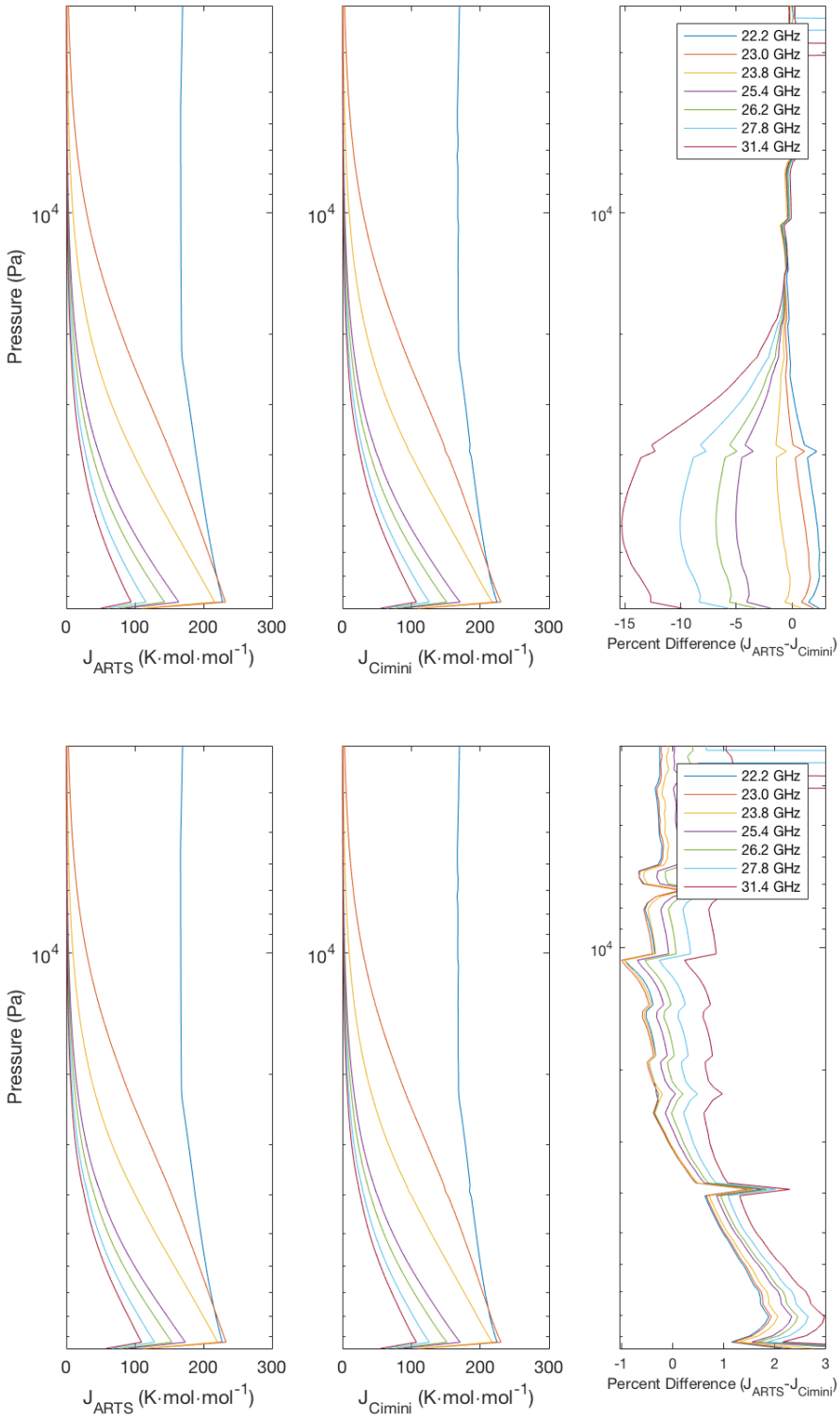

Figure 5.17: Mixing ratio Jacobians calculated via the ARTS and Cimini implementation retrievals. ARTS Jacobians are calculated analytically (top figures) and numerically (bottom figures).

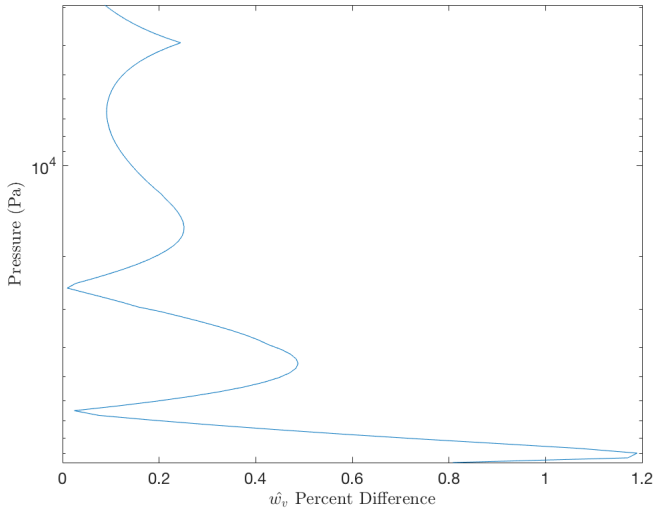

Figure 5.18: Percent difference between the volume mixing ratio retrieval calculated via the ARTS and Cimini forward models.

5.5.1 Measurement state and covariance

For simplicity in constructing a measurement covariance matrix, the measurement state is a 1-dimensional array of radiometric brightness temperatures and lidar signal from the 4 channels:

$$y = [T_{b,1}, ..., T_{b,Nf}, S_{HA,1}, ..., S_{HA,Na}, S_{NA,1}, ..., S_{NA,Na}, S_{HD,1}, ..., S_{HD,Nd}, S_{ND,1}, ..., S_{ND,Nd}] \tag{5.32}$$

where Nf is the number of elements in the brightness temperature measurement grid (7 frequencies), and Na and Nd are the number of elements in the lidar analog and PC measurement grids. The measurement covariance is then comprised of the variance for each element (the same as in the individual lidar radiometer retrievals), with no off-diagonal elements as the elements are assumed to be uncorrelated.

The integrated covariance matrix takes the covariance matrices defined for the lidar (Section 5.3.1) and radiometer (Section 5.4.1) retrievals, and combines them into a single covariance matrix with no off-diagonal elements.

5.5.2 Integrated Forward Model

As shown in the table of the forward model input parameters (Table 5.5), the integrated forward model is similar to the lidar forward model. In addition to the states retrieved by the lidar retrieval (Table 5.2), the water vapor PC channel lidar constant, C_{HD}, is also set as a state to be retrieved. Since it is a lidar constant representing water vapor, the uncertainty is the same as is used for water vapor analog channel lidar constant. This inclusion eliminates the need for the calibration factor, η, thereby removing the need for radiosonde calibration in this retrieval. As the integrated forward model also includes radiometer considerations, temperature and pressure are included as additional *b-parameters* for brightness temperature calculation.

The integrated forward model can then be expressed as:

Radiometer component (Radiative transfer equation):

$$T_B(\nu) = RTE(\nu, w(z), T(z), P(z))$$

Lidar component (Lidar equation for each channel):

$$N'_{HD}(z) = \frac{C_{HD}}{z^2} \cdot w(z) \cdot n_{air}(z) \cdot O_H(z) \cdot \Gamma_H(z, \lambda_H) + B_{HD}(z)$$

$$N_{HD}(z) = \frac{N'_{HD}(z)}{1 + N'_{HD}(z) \cdot \tau_{d,H}}$$

$$N_{HA}(z) = \frac{C_{HA}}{z^2} \cdot w(z) \cdot n_{air}(z) \cdot O_H(z) \cdot \Gamma_H(z, \lambda_H) + B_{HA}(z)$$

$$N'_{ND}(z) = \frac{C_{ND}}{z^2} \cdot w_N \cdot n_N(z) \cdot O_N(z) \cdot \Gamma_N(z, \lambda_N) + B_{ND}(z)$$

$$N_{ND}(z) = \frac{N'_{ND}(z)}{1 + N'_{ND}(z) \cdot \tau_{d,N}}$$

$$N_{NA}(z) = \frac{C_{NA}}{z^2} \cdot w_N \cdot n_{air}(z) \cdot O_N(z) \cdot \Gamma_N(z, \lambda_N) + B_{NA}(z)$$

In the above expression, the green terms are the measurements of radiometric brightness temperatures and lidar signal output by the forward model. The red and blue terms are the state parameters and model *b-parameters*, respectively (listed in Table 5.5). The purple terms are those which contain both state parameters and *b-parameters*, where the overlap is a retrieved

at lower altitudes and parameterized in the forward model for upper altitudes. The oranges are transmission terms, which contain a state parameter (upper altitude extinction), as well as the remaining *b-parameters* (lower altitude extinction, Rayleigh cross section, Angstrom exponent). The radiometer component of the integrated forward model is identical to the radiometer forward model (Table 5.4), while lidar component is similar to the lidar forward model (Table 5.2), but with the replacement of the calibration factor *b-parameter* by the retrieval of the PC water vapor lidar constant.

Integrated Forward Model		
Quantity	State parameters (2m+10)	*a priori* uncertainty, σ_a
Mixing ratio	w [m×1 = $z_0 : z_{top}$]	50% [44]
Overlap	$O(z)$ [m_1×1 = $z_0 : z_{switch}$]	10% [44]
Extinction	$\alpha(z)$ [m_2×1 = $z_{switch} : z_{top}$]	50% [44]
WV analog Lidar Constant (LC)	C_{HA} [1×1]	50% [44]
N_2 analog LC	C_{NA} [1×1]	10% [44]
WV PC LC	C_{HD} **[1×1]**	**50% [44]**
N_2 PC LC	C_{ND} [1×1]	10% [44]
WV PC dead time	$\tau_{d,H}$ [1×1]	0.2% [44]
N_2 PC dead time	$\tau_{d,N}$ [1×1]	0.2% [44]
WV analog background	B_{HA} [1×1]	Measurement standard deviation
N_2 analog background	B_{NA} [1×1]	Measurement standard deviation
WV PC background	B_{HD} [1×1]	Measurement standard deviation
N_2 PC background	B_{ND} [1×1]	Measurement standard deviation
Quantity	Model *b-parameters*	*b-parameter* uncertainty, σ_b
Rayleigh cross section	$\sigma_R(\lambda)$ [1x1]	0.3% [44]
Air density	n_{air} [m×1 = $z_0 : z_{top}$]	1% [44]
~~Calibration factor~~	~~η [1×1]~~	~~5% [44]~~
Angstrom exponent	a [1×1]	10% [44], 50% [23]
Overlap	$O(z)$ [m_2×1 = $z_{switch} : z_{top}$]	0.01% (Complete overlap) [44]
Extinction	$\alpha(z)$ [m_1×1 = $z_0 : z_{switch}$]	50% [44]
Pressure	$P(z)$ **[m×1 =** $z_0 : z_{top}$**]**	**5% [28]**
Temperature	$T(z)$ **[m×1 =** $z_0 : z_{top}$**]**	**5 K [28]**

Table 5.5: The state and model parameters needed for the integrated forward model. The bolded and crossed out quantities show the added and deleted items, compared to the lidar forward model. m is the number of elements in the retrieval grid, an altitude profile ranging from z_0 to z_{top}. m_1 and m_2 are subsets of this retrieval grid, where m_1 is the number of elements from surface up to the handoff for the overlap/extinction retrieval (6 km [23]), while m_2 is the number of elements from handoff to the top of the retrieval.

5.5.3 Execution of SLiRadIHuR

The inversion computation is carried out using Optimal Estimation Method functions included in the Atmlab package released by the ARTS group [17]. As the integrated forward model is nonlinear, it is advantageous to use the Levenberg-Marquardt Method for the inversion, as it can converge to a solution even if the prior estimate of the state is far from the true solution [39]. Using this method, the state vector element is updated iteratively via:

$$x_{i+1} = x_i + [(1+\gamma)S_a^{-1} + K_i^T S_\epsilon^{-1} K_i]^{-1} \cdot [K_i^T S_\epsilon^{-1}(y - F(x_i)) - S_a^{-1}(x_i - x_a)] \tag{5.33}$$

where x_{i+1} is then used to calculate a new fitted spectrum, $F(x_{i+1})$, and Jacobian matrix, K_{i+1}. These terms can then be used to calculate a new cost function. If the new cost is larger than the previous cost, the scaling parameter, γ, is adjusted. In this integrated retrieval, γ_0 is set to 100, with incremental changes by a factor of 10. If instead, the new cost is less than the previous cost, the method tests whether or not the solution has converged. Convergence is achieved if this condition is satisfied:

$$\frac{(x_{i+1} - x_i)^T [S_a^{-1} + K_i^T S_\epsilon^{-1} K_i]^{-1} (x_{i+1} - x_i)}{N_x} < stop \tag{5.34}$$

where N_x normalizes the left side of the expression against the number of elements in the state vector, and *stop* is the convergence criterion [17]. For the purposes of this retrieval, a convergence criterion of 0.1 is employed for converging to the true solution in reasonable time frame. Convergence generally occurs within 15 iterations, with the time of each iteration dependent on the size of the retrieval grid.

5.5.4 Optimizing SLiRadIHuR's performance

Running SLiRadIHuR generally takes a few minutes to execute, depending on how far the *a priori* mixing ratio profile is from the solution. One action to improve its speed was to cache

the Lidar data fetching stage, so that the preliminary processing of these data would not need to be carried out every time SLiRadIHuR is executed. This reduced computation time to about 80% of the original time. The bulk of the processing time, however, comes from iterating through the forward model during the OEM retrieval calculation. Within the forward model itself, the majority of the time is spent calculating the water vapor absorption for the microwave radiometer part of the retrieval. During this calculation, the difference between the channel frequency and absorption line frequency is computed. During the OEM retrieval, these two calculations are each repeated $2 \times N_{iter} \times N_{Jac} \times N_f \times N_{ret} \times N_l$ times, where N_{iter} is the number of OEM iterations (6 is normal), N_f is the number of frequency channels (7 for a water vapor retrieval), N_{ret} is the size of the retrieval grid (202 elements, for example), N_l is the number of absorption lines to be calculated (15), and $N_{Jac} = 21 + 4 \times N_{ret}$ is number of times Jacobians are computed numerically. Using these values gives 210997080 calculations of each of these equations! Since these equations are only dependent on the channel frequency (which is defined at the beginning of the code) and the line frequencies (which are pre-defined constants), these equations were moved from the forward model and into the preliminary forward model setting structure (which is only calculated once, before OEM computation). This way, the calculation would only need to be carried out for $N_f \times N_l$ (105) times for each equation instead of 210997080 times. This simple change reduced the OEM retrieval computation time to approximately 70% of its original timespan.

5.6 Summary

This chapter goes through the elements necessary for OEM retrievals of water vapor mixing ratio via lidar and radiometer measurements. An *a priori* state, provided by the mixing ratio profile from the US Standard Atmosphere Model 1976, is employed. The uncertainties for the mixing ratio, as well as the temperature and pressure profiles used by the forward model, are determined via radiosonde climatological data. In addition to variance, the *a priori* covariance

matrix also requires a correlation length, which is determined by performing least squares fitting across the rows of an autocorrelation matrix of the historic radiosonde profiles. The OEM retrieval using lidar is introduced, in which the forward model developed in Sica & Haefele 2016 [44] is used. A microwave radiometer OEM retrieval is also introduced, where two radiative transfer forward model implementations are considered. Due to its similar performance to the ARTS implementation as well as its ease of use, the Cimini implementation of the radiometer forward model is used hereafter. A novel retrieval method, here called the integrated retrieval, is then introduced, in which the measurement states of the lidar and radiometer as well as their forward models are combined, resulting in a single forward model which takes in information from both instruments in order to retrieve a single mixing ratio profile as well as other useful quantities such lidar constants.

Bibliography

[1] U.S. Standard Atmosphere, 1976, Tech. rep., National Oceanic and Atmospheric Administration, 1976.

[2] Atmospheric radiance and transmittance: FASCOD2, no. 141-144 in Proc. Sixth Conf. on Atmospheric Radiation, Amer. Meteor. Soc., Williamsburg, VA, 1986.

[3] Measurement and Deployment Examples, Radiometer Physics, https://www.radiometer-physics.de/products/microwave-remote-sensing-instruments/radiometers/humidity-and-temperature-profilers/, 2011.

[4] HATPRO Technical Instrument Manual: Description of Instrument Technology, Radiometer Physics, https://www.radiometer-physics.de/products/microwave-remote-sensing-instruments/radiometers/humidity-and-temperature-profilers/, 2013.

[5] Anderson, G., Clough, S., Kneizys, F., Chetwynd, J., and Shettle, E.: AFGL atmospheric constituent profiles (0-120km), Tech. rep., Air Force Geophys. Lab., tech. Rep. TR-86-0110, 1986.

[6] Ansmann, A. and Muller, D.: Lidar: Range-Resolved Optical Remote Sensing of the Atmosphere, chap. Lidar and Atmospheric Aerosol Particles, pp. 803–807, Springer, 2005.

[7] Bleisch, R., Kampfer, N., and Haefele, A.: Retrieval of tropospheric water vapour by using spectra of a 22 GHz radiometer, Atmos. Meas. Tech., 4, 1891, 2011.

[8] Brewer, A.: Evidence for a world circulation provided by the measurements of Helium and water vapour distribution in the Stratosphere, Q. J. R. Meteorol. Soc., 75, 351, 1949.

[9] Bucholtz, A.: Rayleigh-scattering calculations for the terrestrial atmosphere, Applied Optics, 34, 2765, doi:10.1364/ao.34.002765, 1995.

[10] Buehler, S. A., Eriksson, P., Kuhn, T., von Engeln, A., and Verdes, C.: ARTS, the atmospheric radiative transfer simulator, Journal of Quantitative Spectroscopy and Radiative Transfer, 91, 65–93, doi:10.1016/j.jqsrt.2004.05.051, 2005.

[11] Buehler, S. A., Mendrok, J., Eriksson, P., Perrin, A., Larsson, R., and Lemke, O.: ARTS, the Atmospheric Radiative Transfer Simulator - Version 2.2, the planetary toolbox edition, Geoscientific Model Development, 11, 1537–1556, doi:10.5194/gmd-11-1537-2018, 2018.

[12] Cook, B. A.: ACRONYM: Acronym CReatiON for You and Me, pp. 2–4, URL `http://arxiv.org/abs/1903.12180`, 2019.

[13] Crewell, S. and LöHnert, U.: Accuracy of cloud liquid water path from ground-based microwave radiometry 2. Sensor accuracy and synergy, Radio Science, 38, 8042, doi:10.1029/2002RS002634, 2003.

[14] Dinoev, T., Simeonov, V., and Arshinov, Y.: Raman Lidar for Meteorological Observations, RALMO – Part 1: Instrument description, Atmos. Meas. Tech., 6, 1329, 2013.

[15] E., K., Kanamitsu, M., Collins, W., Deaven, D., Gandin, L., Iredell, M., Jenne, R., and Joseph, D.: The NCEP NCAR 40-Year Reanalysis Project, Bulletin of the American Meteorological Society, 77, 437–472, 1996.

[16] Eriksson, P. and Buehler, S.: ARTS Theory, Earth, 2011.

[17] Eriksson, P., Jiménez, C., and Buehler, S. A.: Qpack, a general tool for instrument simulation and retrieval work, Journal of Quantitative Spectroscopy and Radiative Transfer, 91, 47–64, doi:10.1016/j.jqsrt.2004.05.050, 2005.

[18] Farhani, G., Sica, R. J., Godin-Beekmann, S., and Haefele, A.: Optimal estimation method retrievals of stratospheric ozone profiles from a DIAL, Atmospheric Measurement Techniques, 12, 2097–2111, doi:10.5194/amt-12-2097-2019, 2019.

[19] Goody, R. M. and Yung, Y. L.: Atmospheric radiation: Theoretical basis, Oxford University Press, 1989.

[20] Gringorten, I., Salmela, H., Solomon, I., and Sharp, P.: Atmospheric Humidity Atlas - Northern Hemisphere, Air Force Surveys in Geophysics, 186, 66–621, 1966.

[21] Han, Y. and Westwater, E. R.: Analysis and improvement of tipping calibration for ground-based microwave radiometers, IEEE Transactions on Geoscience and Remote Sensing, 38, 1260–1276, doi:10.1109/36.843018, 2000.

[22] Hedin, A. E.: Extension of the MSIS Thermosphere Model into the middle and lower atmosphere, Journal of Geophysical Research: Space Physics, 96, 1159–1172, doi:10.1029/90ja02125, 1991.

[23] Hicks-Jalali, S.: A Tropospheric Water Vapour Climatology and Trends Derived from Vibrational Raman Lidar Measurements over Switzerland, Ph.D. thesis, The University of Western Ontario, 2019.

[24] Hicks-Jalali, S., Sica, R. J., Haefele, A., and Martucci, G.: Calibration of a water vapour Raman lidar using GRUAN-certified radiosondes and a new trajectory method, Atmospheric Measurement Techniques, 12, 3699–3716, doi:10.5194/amt-12-3699-2019, 2019.

[25] Jalali, A., Sica, R. J., and Haefele, A.: A middle latitude Rayleigh-scatter lidar temperature climatology determined using an optimal estimation method, Atmospheric Measurement Techniques Discussions, pp. 1–24, doi:10.5194/amt-2018-117, 2018.

[26] Janssen, M. A.: Atmospheric Remote Sensing by Microwave Radiometry, chap. An Introduction to Passive Microwave Remote Sensing of Atmospheres, John Wiley and Sons, Inc., 1993.

[27] Khanna, J., Bandoro, J., and Sica, R.: New technique for retrieval of atmospheric temperature profiles from Rayleigh-scatter lidar measurements using nonlinear inversion, Appl. Opt., 51, 7945, 2012.

[28] Leblanc, T., Sica, R. J., Van Gijsel, J. A., Haefele, A., Payen, G., and Liberti, G.: Proposed standardized definitions for vertical resolution and uncertainty in the NDACC lidar ozone and temperature algorithms-Part 3: Temperature uncertainty budget, Atmospheric Measurement Techniques, 9, 4079–4101, doi:10.5194/amt-9-4079-2016, 2016.

[29] LöHnert, U. and Crewell, S.: Accuracy of cloud liquid water path from ground-based microwave radiometry 1. Dependency on cloud model statistics, Radio Science, 38, 8041, doi:10.1029/2002RS002654, 2003.

[30] Mahagammulla Gamage, S., Sica, R. J., Martucci, G., and Haefele, A.: Retrieval of Temperature From a Multiple Channel Pure Rotational Raman-Scatter Lidar Using an Optimal Estimation Method, Atmospheric Measurement Techniques Discussions, pp. 1–34, doi:10.5194/amt-2019-107, 2019.

[31] Martucci, G., Voirin, J., Simeonov, V., Renaud, L., and Haefele, A.: A novel automatic calibration system for water vapor Raman LIDAR, EPJ Web of Conferences, 176, 05 008, doi:10.1051/epjconf/201817605008, 2018.

[32] Maschwitz, G., Löhnert, U., Crewell, S., Rose, T., and Turner, D. D.: Investigation of ground-based microwave radiometer calibration techniques at 530 hPa, Atmospheric Measurement Techniques, 6, 2641–2658, doi:10.5194/amt-6-2641-2013, 2013.

[33] Mastenbrook, H. J.: The Variability of Water Vapor in the Stratosphere, Journal of the Atmospheric Sciences, 28, 1455–1501, 1971.

[34] Nicolet, M.: On the molecular scattering in the terrestrial atmosphere: An empirical formula for its calculation in the homosphere, Planetary and Space Science, 32, 1467–1468, 1984.

[35] Povey, A., Grainger, R., and Peters, D.: Estimation of a lidar's overlap function and its calibration by nonlinear regression, Appl. Opt., 51, 5130, 2012.

[36] Povey, A., Grainger, R., and Peters, D.: Retrieval of aerosol backscatter, extinction, and lidar ratio from Raman lidar with optimal estimation, Atmos. Meas. Tech., 7, 757, 2014.

[37] Povey, A. C.: The application of optimal estimation retrieval to lidar observations, Ph.D. thesis, University of Oxford, URL https://ora.ox.ac.uk/objects/ora:8548, 2013.

[38] Rees, D. and Fuller-Rowell, T. J.: The CIRA theoretical thermosphere model, Advances in Space Research, 8, 27–106, doi:10.1016/0273-1177(88)90039-7, 1988.

[39] Rodgers, C.: Inverse Methods for Atmospheric Sounding: Theory and Practice, World Scientific Publishing, London, 2000.

[40] Rosenkranz, P. W.: Water vapor microwave continuum absorption: A comparison of measurements and models, Radio Science, 33, 919–928, doi:10.1029/98RS01182, 1998.

[41] Scholz, T., Ehalt, D., Heidt, L., and Martell, E.: Water Vapor, Molecular Hydrogen, Methane, and Tritium Concentrations Near the Stratopause, Journal of Geophysical Research, 75, 3049–3054, 1970.

[42] Schroeder, J. and Westwater, E.: User Guide to WPL Microwave Radiative Transfer Software, 1991.

[43] Sica, R. and Haefele, A.: Retrieval of temperature from a multiple-channel Rayleigh-scatter lidar using an optimal estimation method, Appl. Opt., 54, 2015.

[44] Sica, R. and Haefele, A.: Retrieval of water vapor mixing ratio from a multiple channel Raman-scatter lidar using an optimal estimation method, Appl. Opt., 55, 763, 2016.

[45] Sissenwine, N., Grantham, D., and Salmela, H.: Midlatitude Humidity to 32 km, Journal of the Atmospheric Sciences, 25, 1129–1140, 1968.

[46] Veselovskii, I., Kolgotin, A., and Griaznov, V.: Inversion with regularization for the retrieval of tropospheric aerosol parameters from multiwavelength lidar sounding, Appl. Opt., 41, 3685, 2002.

[47] Wu, M. F., Geller, M. A., Nash, E. R., and Gelman, M. E.: Global atmospheric circulation statistics-Four year averages, Tech. rep., NASA, nASA technical memo, NASA TM 100690, 1987.

Chapter 6

Synthetic Retrieval of water vapor mixing ratio

Before real measurements are considered, the retrieval is first tested with synthetic measurements, allowing us to test the performance of the forward model and the retrieval in a controlled, idealized environment. The synthetic data is generated by sample atmospheric profiles of temperature, pressure, and humidity, and putting them into the forward model to produce a simulated measurement. Instrument-specific noise is then added to the simulated measurement state. A retrieval is then carried out, with the goal of retrieving the original humidity profile.

The synthetic retrieval is carried out using a radiometer-only forward model, a sonde-calibrated lidar forward model, and a radiometer-calibrated lidar forward model (the integrated forward model). In all cases, the simulated measurement is based on an input atmospheric state from a Payerne radiosonde launch on October 5, 2011 at 22:55 UTC (Figure 5.1). This was a clear night, where lidar and radiometer measurements coincide with a GRUAN-processed radiosonde which was used in testing the radiosonde Trajectory calibration method of Hicks-Jalali et al. 2019. For the first test case, the retrieval grid extends from the surface to 18.5 km, with a grid spacing of 50 m, allowing for a fine scale retrieval without being too computationally consuming. The *a priori* mixing ratio is a smoothed US Standard model profile, with a

variance coming from a 50% standard deviation at all altitudes, which is consistent with what is used in the lidar retrieval of Sica & Haefele 2016. The covariance matrix is constructed from a linear correlation function with a correlation length of 1000 m. Although this correlation length differs from what is determined in Section 5.2.4, the choice of correlation length and function (as will be discussed in Section 6.3.1) does not have a significant effect on the retrieval outcome. Thus, an arbitrary value of 1000 m is considered for these retrievals.

6.1 Radiometer-only retrieval

We first test the performance of the radiometer-only retrieval, in order to determine how well it can retrieve the humidity we provided for the simulated measurement. The simulated radiometer measurement is generated by taking the true atmospheric state quantities and running them through the radiometer forward model (introduced in Section 5.4.2). The true state mixing ratio comes from the radiosonde launch on October 5, 2011, while the input model *b-parameter* temperature and pressure profiles come from the US Standard Atmosphere model. Pressure and temperature *b-parameter* uncertainties are set to 5% and 5 K respectively (from Table 5.4 as suggested in [3]) and no correlation is assumed. The simulated measurement state is output by the forward model, producing 7 frequency-dependent simulated brightness temperatures. Noise is then added to the spectrum by applying a normally-distributed random scalar, with an amplitude equal to the measurement standard deviation, to the simulated brightness temperature. Figure 6.1 shows the simulated brightness temperature spectrum, as well as the simulated spectra with noise on the order of the radiometric resolution added.

The retrieval of mixing ratio is shown in Figure 6.2. The retrieval follows the simulated state (or the *true* state in the case of these synthetic retrievals) well, despite the *a priori* profile being significantly drier than the sonde profile for the bottom 1.5 km. The retrieved profile eventually falls back to the *a priori* profile above 10 km. Although the retrieved state profile follows the sonde humidity profile, it is unable to reproduce its small-scale features because the

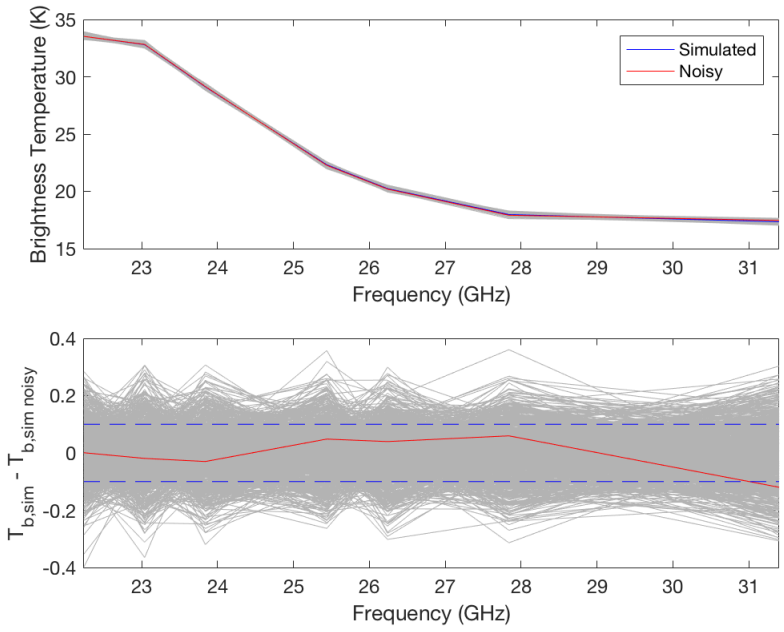

Figure 6.1: (Top) Simulated brightness temperature spectrum and the noise-added simulated spectrum. The grey lines represent 1000 instances of randomly-generated noise-added spectra. (Bottom) Difference between the simulated and noise-added simulated spectrum (red line). The grey lines are the residuals between the simulated spectrum and 1000 randomly generated noisy spectra. The blue dashed lines indicate the measurement standard deviation.

native height resolution for the radiosonde measurement is a few meters, while the radiometric retrieval resolution is a few thousand meters (Figure 6.8). Although the retrieval spacing is set to 50 m, the retrieval is sensitive to changes on the scales of its vertical resolution, which is determined by the width of the derived averaging kernels. A more effective means for comparing the retrieved and radiosonde profiles is to smooth the latter, using the retrieval averaging kernels (Figure 6.7) as a weighting function:

$$x_s = A(x - x_a) + x_a \tag{6.1}$$

where A is the averaging kernel matrix, and x and x_a are the radiosonde and *a priori* mixing ratio profiles, respectively [5]. Using the smoothed radiosonde profile provides a much better comparison with the retrieved profile (Figure 6.2, right plot), where difference between the two profiles is less than 15% at all altitudes, which is in rough agreement with the retrieval uncertainty (Figure 6.9). Additionally, the integrated water vapor determined from the retrieved profile and sonde profile are 16.87 kg/m^2 and 16.44 kg/m^2, a difference of only 2.6%. Figure 6.3 shows the retrieval residuals, the difference between the measurement state and the fitted spectrum (generated by running the retrieved state through the forward model after the solution has converged). In theory, a retrieval which finds the exact solution producing the measurement state would yield residuals equal to zero. In this simulation, random noise on the level of the radiometric resolution (0.1 K) is added. Thus, the retrieval can only produce a fitted measurement which would equal the original measurement to within the noise level. As seen in the figure, although the residual is nonzero, it falls within the defined measurement uncertainty of 0.1 K. These residuals therefore demonstrate the simulation is able to effectively determine a retrieval state producing the measurement state to within the uncertainty.

For the previously mentioned figures, the *b-parameter* pressure and temperature profiles come from US Standard profiles. Figure 6.4 compares retrievals via various pressure and temperature profiles introduced in Section 5.2.2. There is some variation due to the choice of

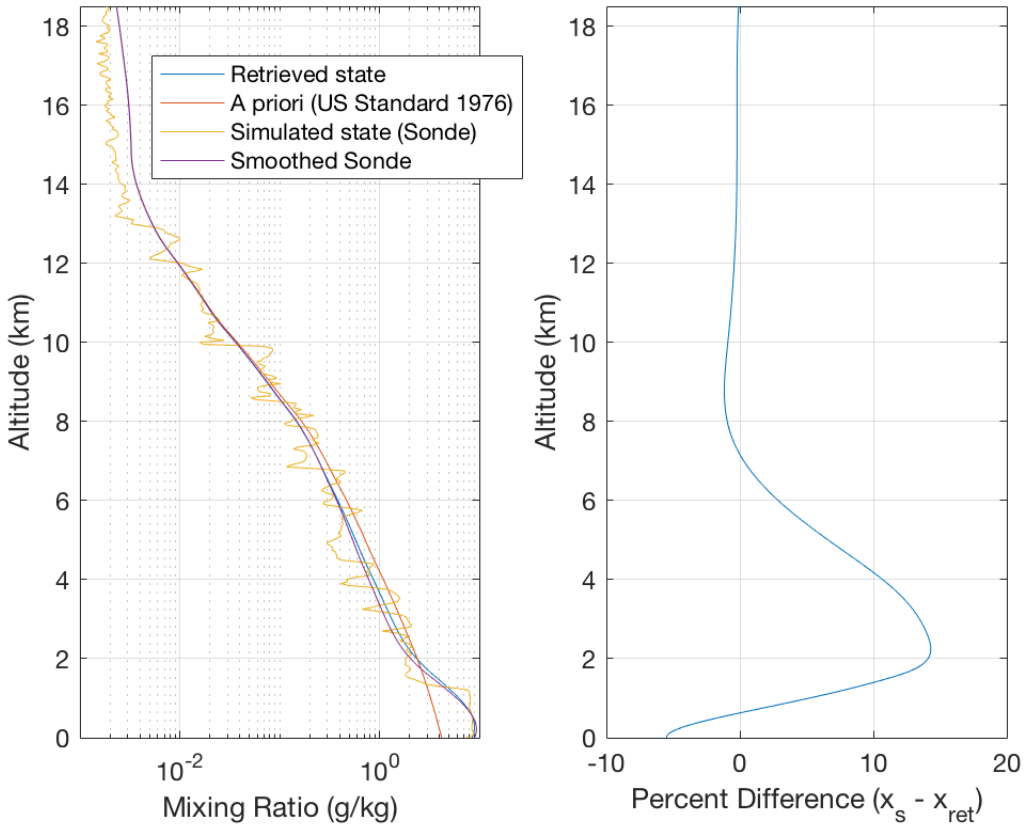

Figure 6.2: (Left) Retrieval of mixing ratio (blue trend), using a synthetic measurement generated by radiosonde atmospheric state inputs (simulated, or true, state in yellow), with the *a priori* state in red. The simulated state (radiosonde) profile which has been smoothed via the retrieval averaging kernels is shown in purple. (Right) Percent difference between the smoothed radiosonde profile and the retrieved profile.

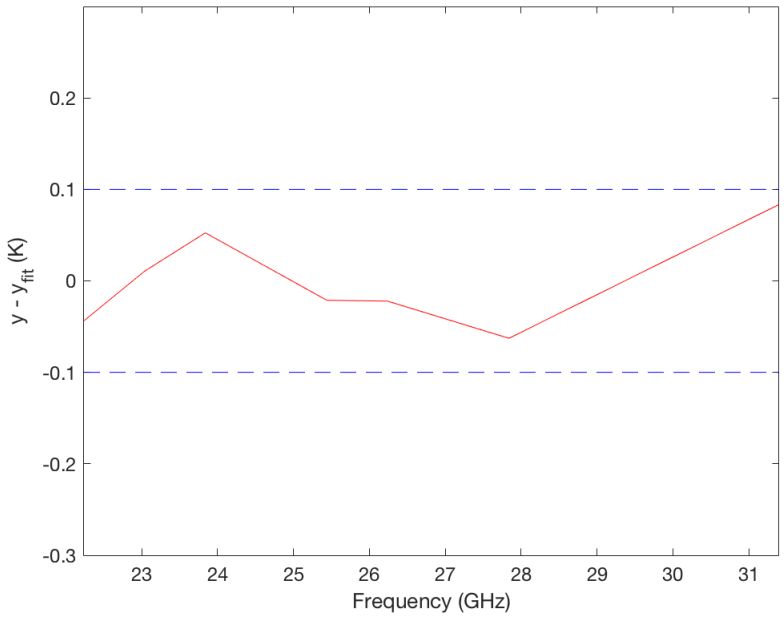

Figure 6.3: Residuals between the measurement and the spectra fitted by the converged retrieval state. The blue dashed lines indicate the measurement uncertainty, which is the HATPRO radiometric resolution.

model, with FASCOD resulting in the largest bias from the true state for the lower troposphere. This bias is due to underestimating temperature in the FASCOD profile, which as shown previously in Figure 5.3, has temperatures more than 5% smaller than sonde or NCEP profiles for the lowest 7 km of the atmosphere. The variability due to profile choice is addressed when determining an uncertainty budget (Figure 6.9).

The numerically-calculated Jacobians for the radiometer retrieval are shown in Figure 6.5. The effect of the smoothness of the *a priori* profile on the computed Jacobians is shown in Figure 6.6. Although the magnitude and general shape of the profiles are the same, we see that using an unsmoothed *a priori* profile generates Jacobians with bumps where the US Standard Model 1976 profile has cusps (See Figure 5.1 for the US Standard profile). The smoothed *a priori* profile, on the other hand, results in smooth Jacobians, since the Jacobians are calculated numerically from the retrieved state in the Cimini implementation.

The averaging kernels for the simulated radiometer retrieval are shown in Figure 6.7. The

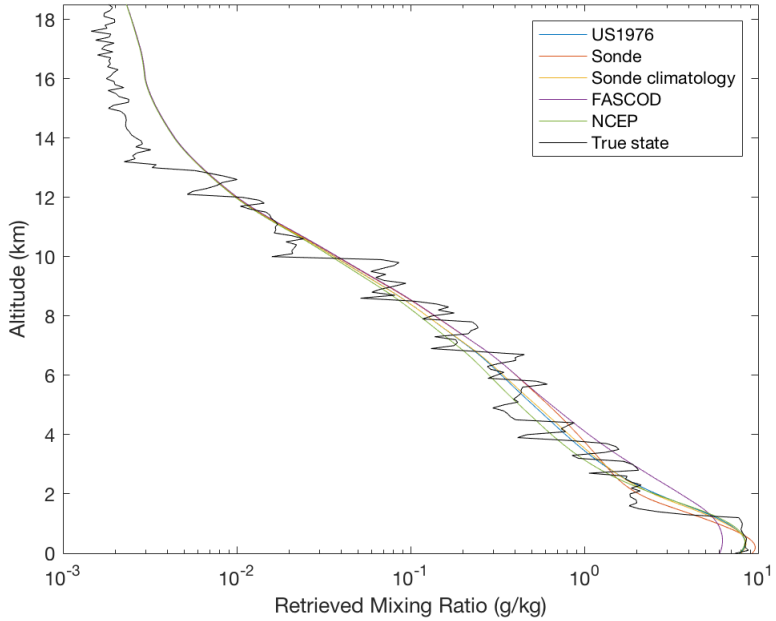

Figure 6.4: Radiometer retrieval of mixing ratio using a simulated (true) measurement state based on a sonde profile (black line). The other lines represent retrievals using different models for the pressure and temperature *b-parameters*.

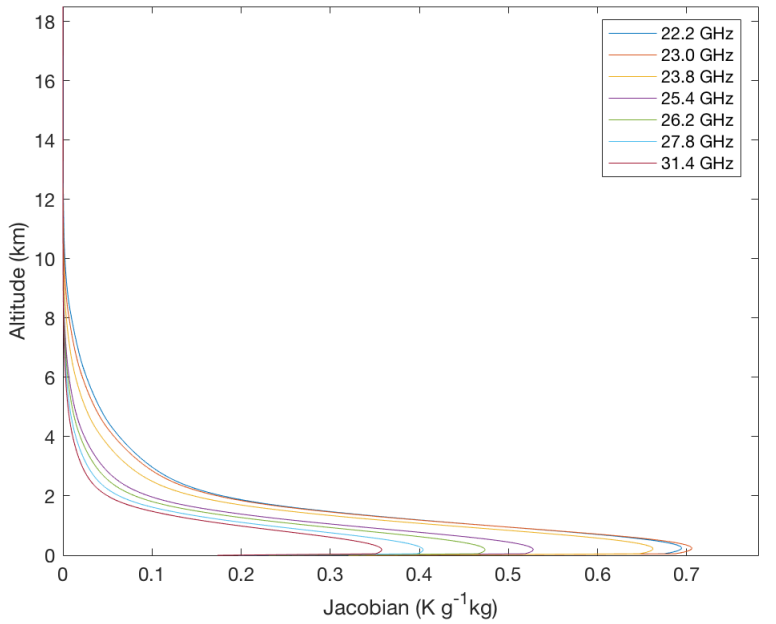

Figure 6.5: Numerically-calculated Jacobians for the radiometric retrieval using a synthetic measurement.

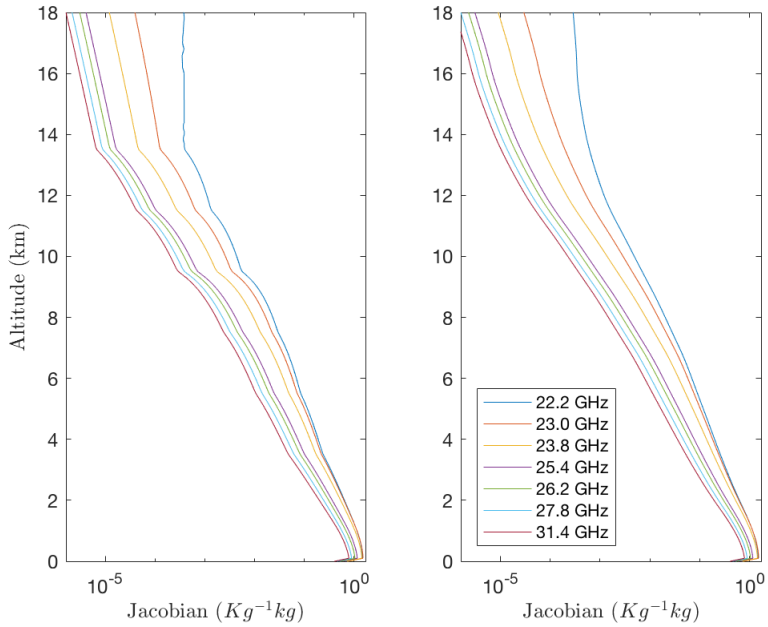

Figure 6.6: Jacobians for the radiometer retrieval, using an unsmoothed (Left) and smoothed (Right) US Standard *a priori* profile.

black line represents the area of the averaging kernel elements, divided by 10. For a perfect retrieval, the averaging kernel matrix would be an identity matrix, in which its unity representing the heights at which the retrieval is accurate [5]. For this retrieval, the averaging kernels are close to unity for the lower portion of the retrieval, falling below a response of 0.9 at 5 km. The averaging kernels are also useful, as their half-widths provide an estimate of the spatial resolution for the retrieval [5]. In this case, the averaging kernels are very wide, producing retrieval vertical resolution that is much coarser than the 50 m grid spacing used for this retrieval (Figure 6.8). The coarseness of the retrieval's resolution explains why the retrieval is unable to account for the variability of the true state radiosonde humidity on scales of 10s of meters, but rather, follows the general trend of the radiosonde on the order of kilometer scale. As discussed above (and shown in Figure 6.2), when the difference in resolution between the true and retrieved states is taken into account, the profiles are displayed to be comparable to within 15%.

Figure 6.9 gives the uncertainty budget for the simulated radiometer retrieval. The sta-

tistical (observational) uncertainty is calculated once a converged retrieval state is found via Equation 5.8, where the retrieval gain (Equation 5.7) and measurement covariance matrices are used. The uncertainty for each *b-parameter* term is calculated *a posteriori* via Equation 5.10. The *b-parameter* covariance matrices are constructed based on the variances for pressure and temperature. Since model profiles are used, the covariance matrices do not have any non-zero off-diagonal elements. The forward model parameter sensitivity for each parameter are computed numerically in the same manner as mentioned in Section 5.3.3. That is, the *b-parameter* profile is perturbed at each retrieval grid level, with the difference between the perturbed and unperturbed forward model calculation at each level forming the Jacobian matrix. The figure shows a total uncertainty ranging from 3 to 15% of the mixing ratio value, with significant contributions from the statistical as well as the b-parameter pressure and temperature uncertainties.

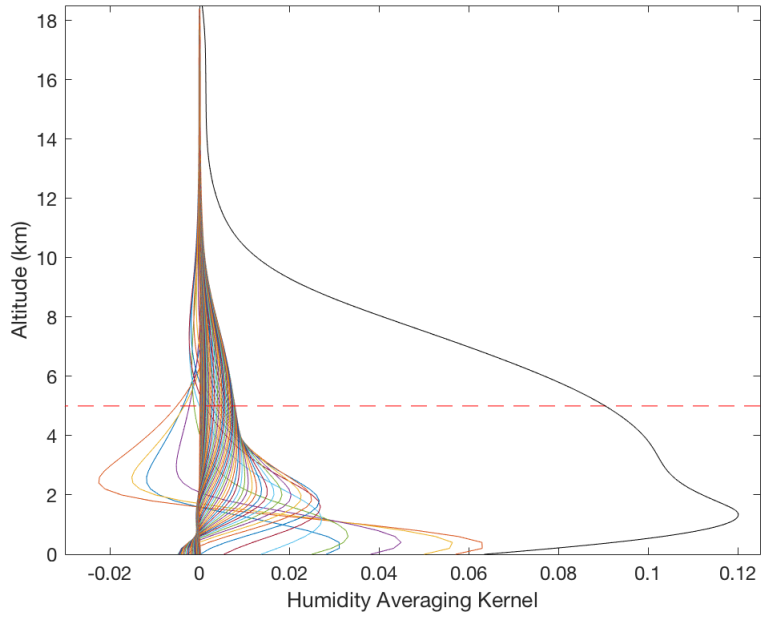

Figure 6.7: Averaging kernels for the simulated radiometer retrieval, showing every fourth kernel. The black line is the area of the averaging kernel at each height (the response function), divided by 10. The dashed red line shows the height below which this response is greater than 90%.

For the uncertainty budget shown in Figure 6.9, the *b-parameter* uncertainties are calculated based on uncorrelated covariance matrices with an input standard deviation of 5% for

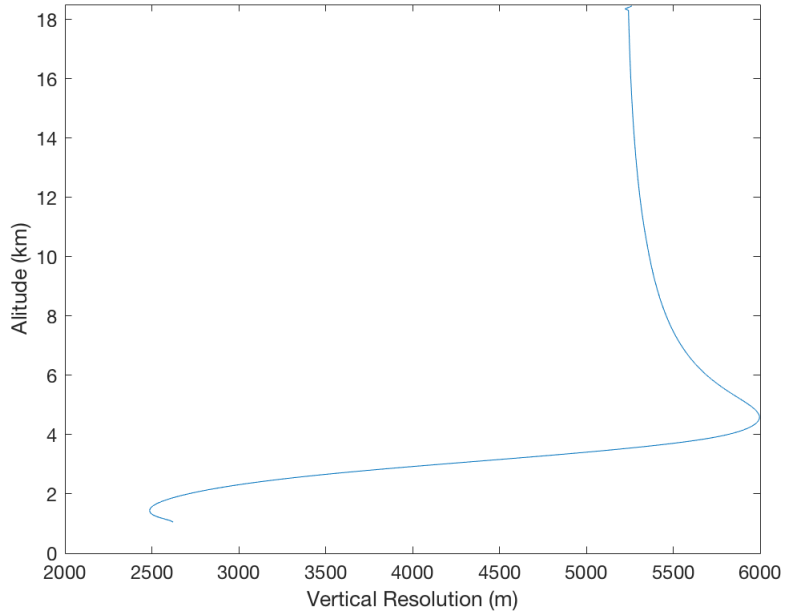

Figure 6.8: Vertical resolution for the simulated radiometer retrieval.

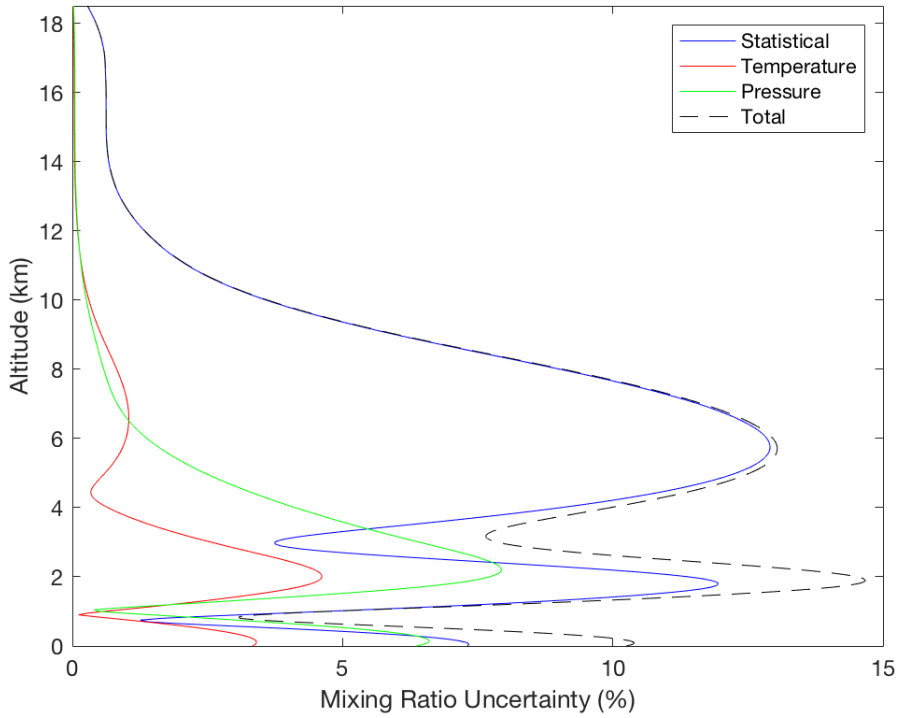

Figure 6.9: Uncertainty budget for the simulated radiometer retrieval. The smoothing error is not included in the total uncertainty here.

pressure and 5 K for temperature. It should be noted that the smoothing error is not included in this figure, such that the total uncertainty is comprised of the statistical, temperature, and pressure uncertainties. It has been argued that since the smoothing error does not follow with Gaussian error propagation, adding it into an uncertainty budget may not be advantageous [7]. As the radiometer is intended for calibrating the high-resolution lidar, the smoothing error is not included in this analysis.

Figure 6.10 examines how the b-parameter uncertainties from Figure 6.9 would vary based on changes to the inputs for S_b, the input covariance matrix used in calculating S_f, the covariance due to the b-parameter contributions (Equation 5.10). As in the case of constructing the *a priori* covariance matrix (originally discussed in Section 5.2.4), S_b requires the variance for the *b-parameters*, as well as a correlation function and a length scale (if the quantities are assumed to be correlated). As shown in the figure, the output *b-parameter* uncertainty is directly related to the input standard deviation. For pressure, increasing the input standard deviation from 1% to 10% would result in the overall *b-parameter* uncertainty at 2500 m to increase, from approximately 2% to 16% (Figure 5.6, top left). Likewise, using an input uncertainty of 10 K instead of 1 K would increase the temperature *b-parameter* uncertainty from 1% to 9.5% (Figure 5.6, top right). Additionally, using a correlated S_b rather than an uncorrelated matrix would significantly increase the *b-parameter* uncertainty, with Gaussian functions slightly larger than tent or exponential functions. For example, if a tent function is used instead of an uncorrelated function, the uncertainty for pressure would increase by a factor of 5 (Figure 5.6, middle right). For correlated covariance matrices, increasing the correlation length also increases the magnitude of the *b-parameter* uncertainty (Figure 5.6, bottom left and right).

This section introduced mixing ratio retrievals of synthetic radiometer measurements, created by inputting radiosonde atmospheric quantities into the radiometer forward model and then adding noise at the level of the radiometric resolution to the simulated brightness temperatures. Although the retrieval resolution is much coarser than the radiosonde resolution, the smoothed radiosonde profile compares with the retrieval to within 15%. The total uncertainty

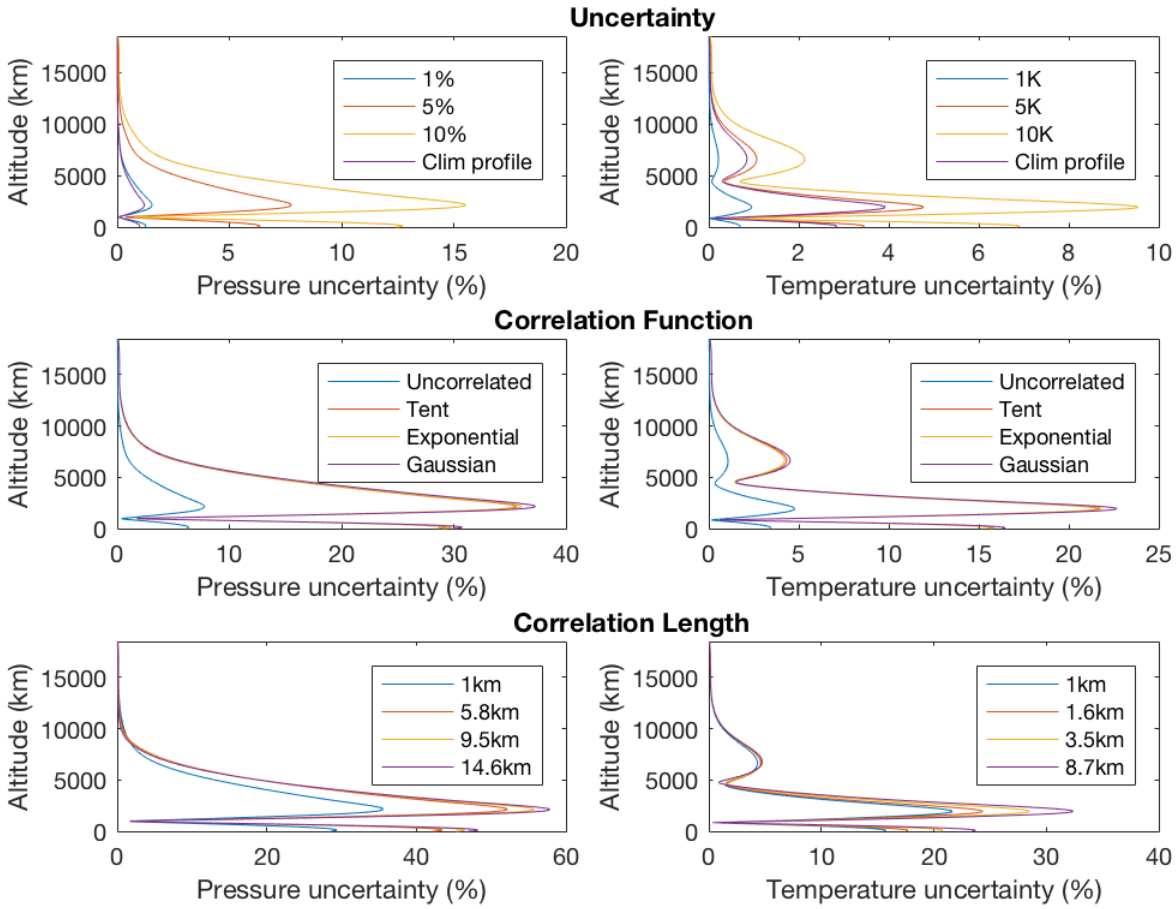

Figure 6.10: The top plots shows how the *b-parameter* uncertainty changes, based on the input uncertainty for the input parameter covariance matrix (S_b in Equation 5.10), for pressure (left) and temperature (right) parameters. The correlation lengths are examples from Table 5.1. *Clim profile* are uncertainty profiles based on the climatological means in Figure 5.6. The middle row shows variability in the error due to the correlation function (with a correlation length of 1 km), and bottom row shows change in error due to correlation length (with a tent correlation function).

in retrieved mixing ratio varies between 3 and 15% below 6 km, when input uncertainties of the pressure and temperature *b-parameters* are 5% and 5 K, respectively. Increasing the input uncertainty and using a correlated covariance matrix for these inputs yield larger output *b-parameter* uncertainties, and therefore a greater total uncertainty.

6.2 Lidar-only retrieval

The lidar retrieval used here is the method developed in Sica & Haefele 2016, with further modifications made by Shannon Hicks-Jalali [2]. As with the radiometer-only retrieval, the only difference from the setup described in Section 5.3 is the use of a synthetic lidar measurement state rather than real measurements. In this case, the true atmospheric state, consisting of a radiosonde mixing ratio profile, is input into the lidar forward model. The outputs are profiles for each of the 4 channels: analog water vapor, PC water vapor, analog nitrogen, and PC nitrogen. Since the PC channels consist of discrete counts, the simulated PC rate is converted to integers, with quantities less than 1 randomly assigned a value of either 0 or 1. Noise is then added to the simulated signal. As the PC counts are assumed to obey Poisson statistics, noise is added to PC counts by calculating random deviates from a Poisson distribution [4]. Noise for the analog counts is applied in the same manner as for the radiometric brightness temperatures, by adding a normally-distributed random scalar, with an amplitude equal to the measurement standard deviation, to the simulated signal. For the analog counts, this standard deviation comes from the piecewise variance of the real measurements taken on October 5, 2011, determined by taking the difference between the measurement and a trend fitted with the 6 adjacent data points [6]. The noise-added simulated measurements are shown in Figure 6.11, with the residuals between the simulated and noisy simulated measurements in Figure 6.12, demonstrating that the noise-added simulated measurements provide reasonable values for lidar signal.

The simulated lidar retrieval of mixing ratio is pictured in Figure 6.13. The retrieval follows the true state quite well until around 8 km, where it eventually falls back to the *a priori* profile.

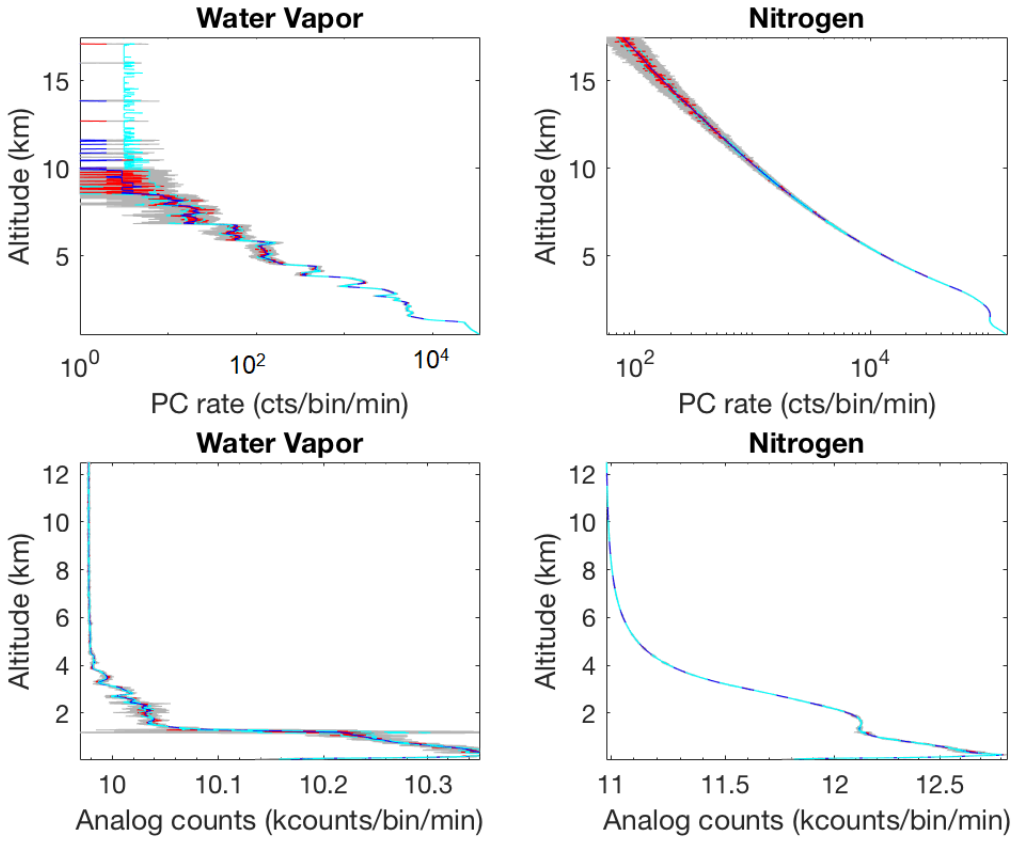

Figure 6.11: Simulated lidar signal. The blue lines represented the simulated lidar measurement, with uncertainty bounds (dashed cyan lines) from the piecewise variance of the real lidar measurements from October 5, 2011. The red lines are the noise-added simulated measurements, with the grey lines showing 1000 possible instances for these noisy profiles.

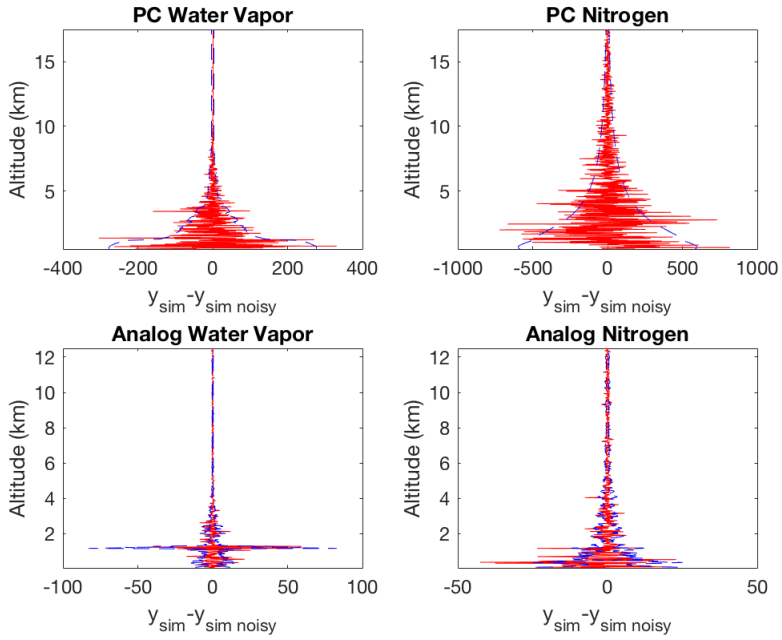

Figure 6.12: Differences between the simulated and noise-added simulated lidar measurements for each lidar channel. The blue dashed line indicates the standard deviation for the analog and PC raw measurements.

The retrieval's regression back toward the *a priori* profile is reflected in the averaging kernel (Figure 6.14), where the averaging kernel response is at unity until 8 km, above which it quickly falls off. An averaging kernel response of at least 0.9 extends up to 9.45 km, below which information is coming from the retrieval rather than the *a priori*. In Figure 6.15, the lowest altitudes show a vertical resolution around 50 m, which is what the grid spacing is set to for the retrieval. However, the resolution gets dramatically coarser above 8 km, with a maximum resolution of 1588 m at the top of the retrieval. The uncertainty budget for the simulated lidar retrieval is shown in Figure 6.16. For the majority of the retrieval, the greatest uncertainties are due to statistical (retrieval observation uncertainty) and calibration factor error. There is also a sharp spike in the statistical uncertainty due to the lack of lidar signal for the lowest 50 m of the retrieval.

This section shows results from retrievals of simulated lidar measurements, in which radiosonde atmospheric state quantities are input into the forward model of Sica & Haefele 2016,

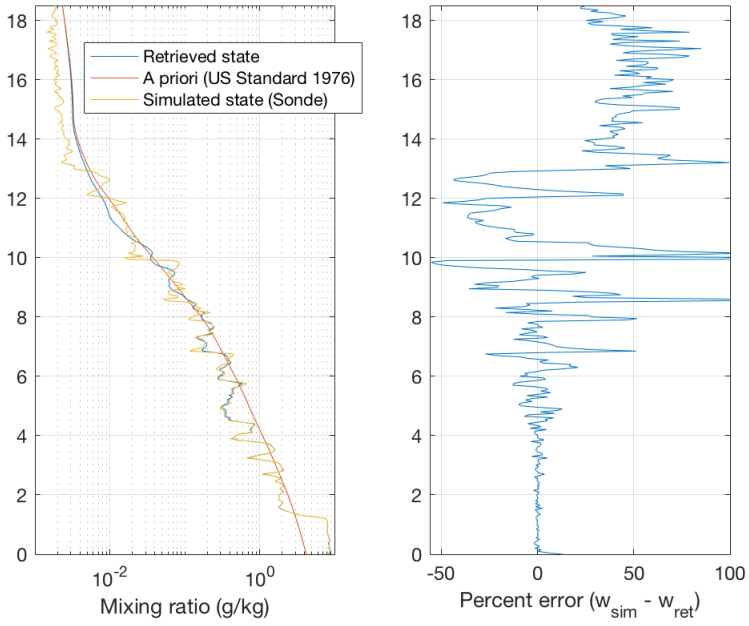

Figure 6.13: Simulated lidar retrieval of mixing ratio. (Left) The retrieved mixing ratio, along with the true (simulated) state and the *a priori* state. (Right) The percent error between the simulated and retrieved states.

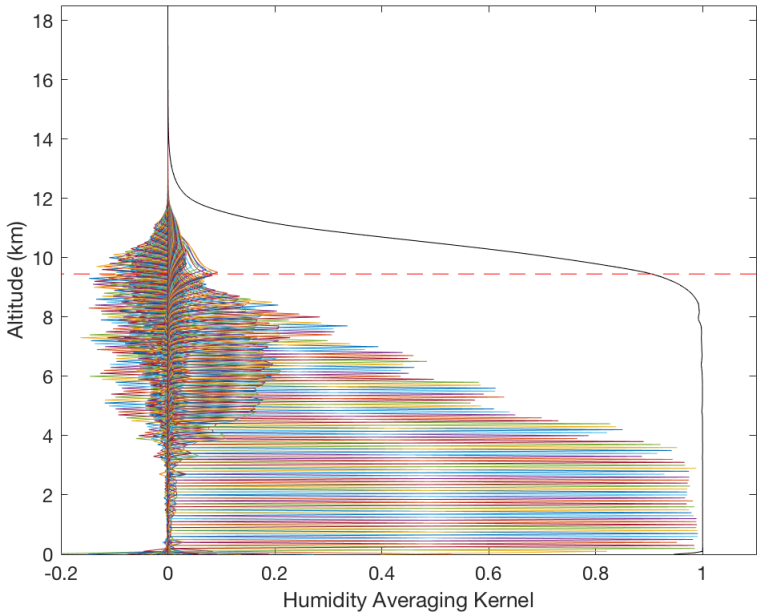

Figure 6.14: Averaging kernel for the simulated lidar retrieval. The black line indicates the response of the averaging kernels, and the dashed red line shows the height below which the response is greater than 90% - 9.45 km here.

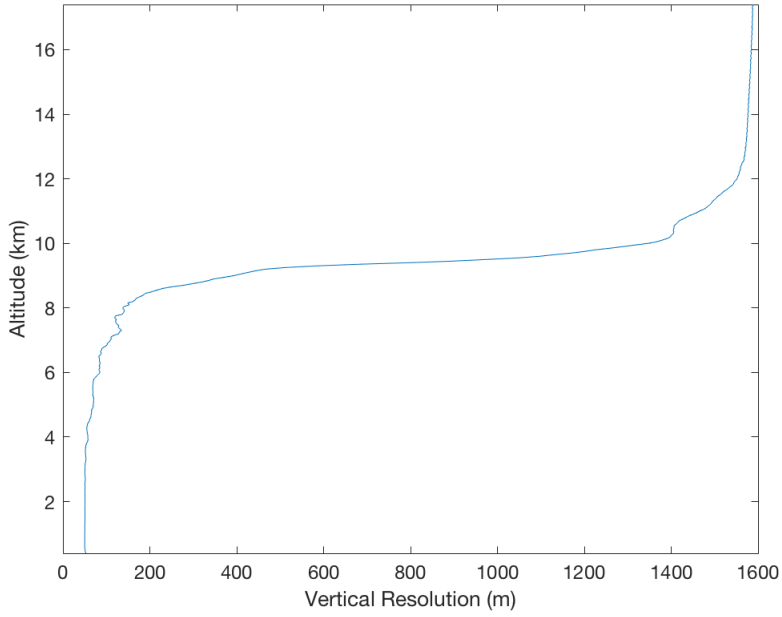

Figure 6.15: Vertical resolution for the lidar retrieval.

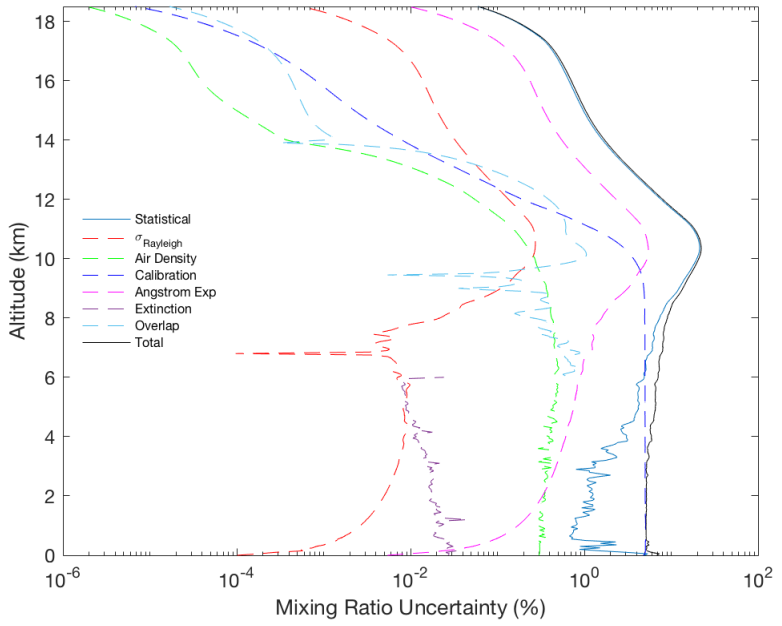

Figure 6.16: Uncertainty budget (including statistical and systematic *b-parameter* errors) for the simulated lidar retrieval.

with Poisson noise and piecewise variance added to the simulated PC and analog signal, respectively. Compared to the radiometer retrieval, the lidar-retrieved mixing ratio has a much finer vertical resolution at approximately 50 m. The retrieved mixing ratio profile is within 15% in the first 6 km, with a total uncertainty which is nearly constant at 5% for the first 4 km, with the primary error contribution from the calibration factor *b-parameter*.

6.3 Integrated retrieval

The retrieval of mixing ratio via the integrated forward model is shown in Figure 6.17. The retrieval is very similar to the lidar retrieval, aside from some divergence around 10 km and near the surface (Figure 6.18). In the integrated retrieval, the radiometer contribution improves the lowest 50 m of retrieval, where lidar measurements cannot be made due to the geometry of the lidar detection system.

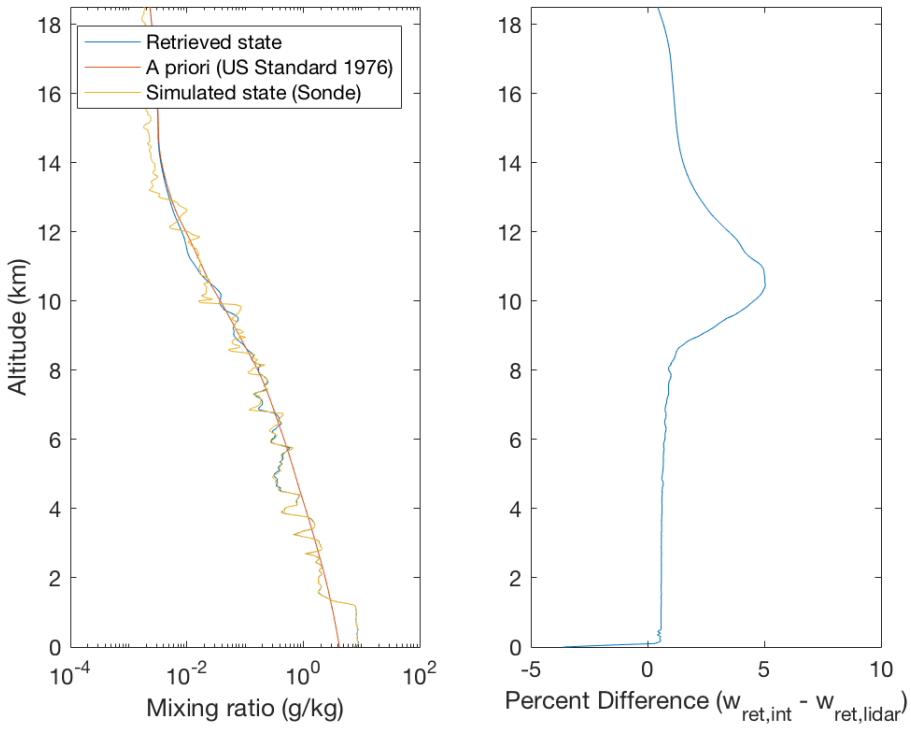

Figure 6.17: (Left) Integrated retrieval of the mixing ratio. (Right) Comparison between the integrated and lidar retrieval of mixing ratio.

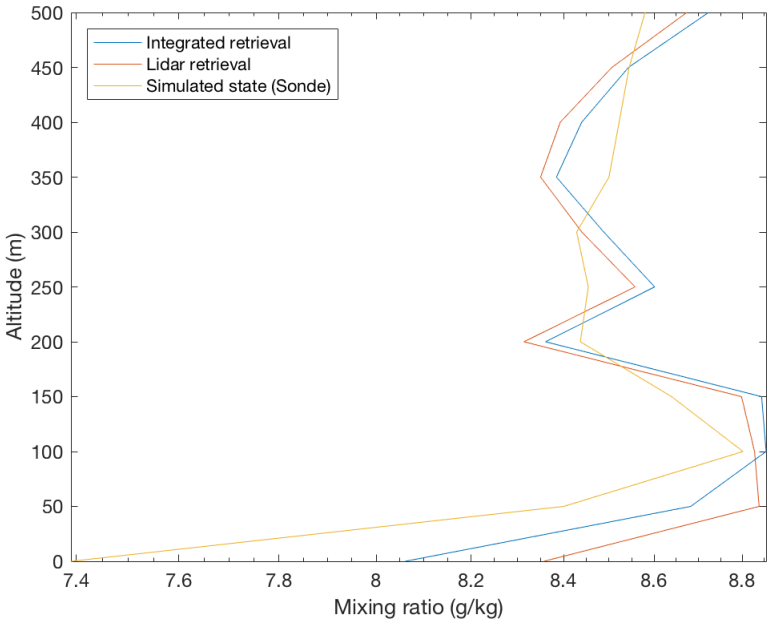

Figure 6.18: The bottom 500 m of the lidar and integrated retrievals, relative to the true state.

As a first order test of its performance, the integrated retrieval is run with the lidar measurement variance set to 10^6 times larger than it would normally be, so that the weight of the lidar measurement would basically be negligible, rendering a radiometer-only retrieval. This is shown in the top portion of Figure 6.19, in which the lidar variance is made prohibitively large. The resulting retrieval reverts back to the radiometer retrieval to within 6%. The same test is carried out, this time replacing the radiometer measurement variance with a value 10^6 times the nominal value. The bottom portion of Figure 6.19, in which the retrieval here resembles the lidar retrieval, but is offset by roughly 10% in the first 7 km. This offset is due to the fact that the lidar retrieval is equipped with the radiosonde-derived calibration factor, providing greater physical significance to the retrieved lidar constants. The integrated retrieval, however, does not have this term included in the forward model, and along with the absence of radiometer measurements, is subject to this roughly scalar offset.

Aside from retrieving a humidity profile, the integrated retrieval also retrieves the channel-specific lidar constants. In addition to the analog water vapor, analog nitrogen, and PC nitrogen channel lidar constants (C_{HA}, C_{NA}, C_{ND}) retrieved by the Lidar retrieval (as shown previously

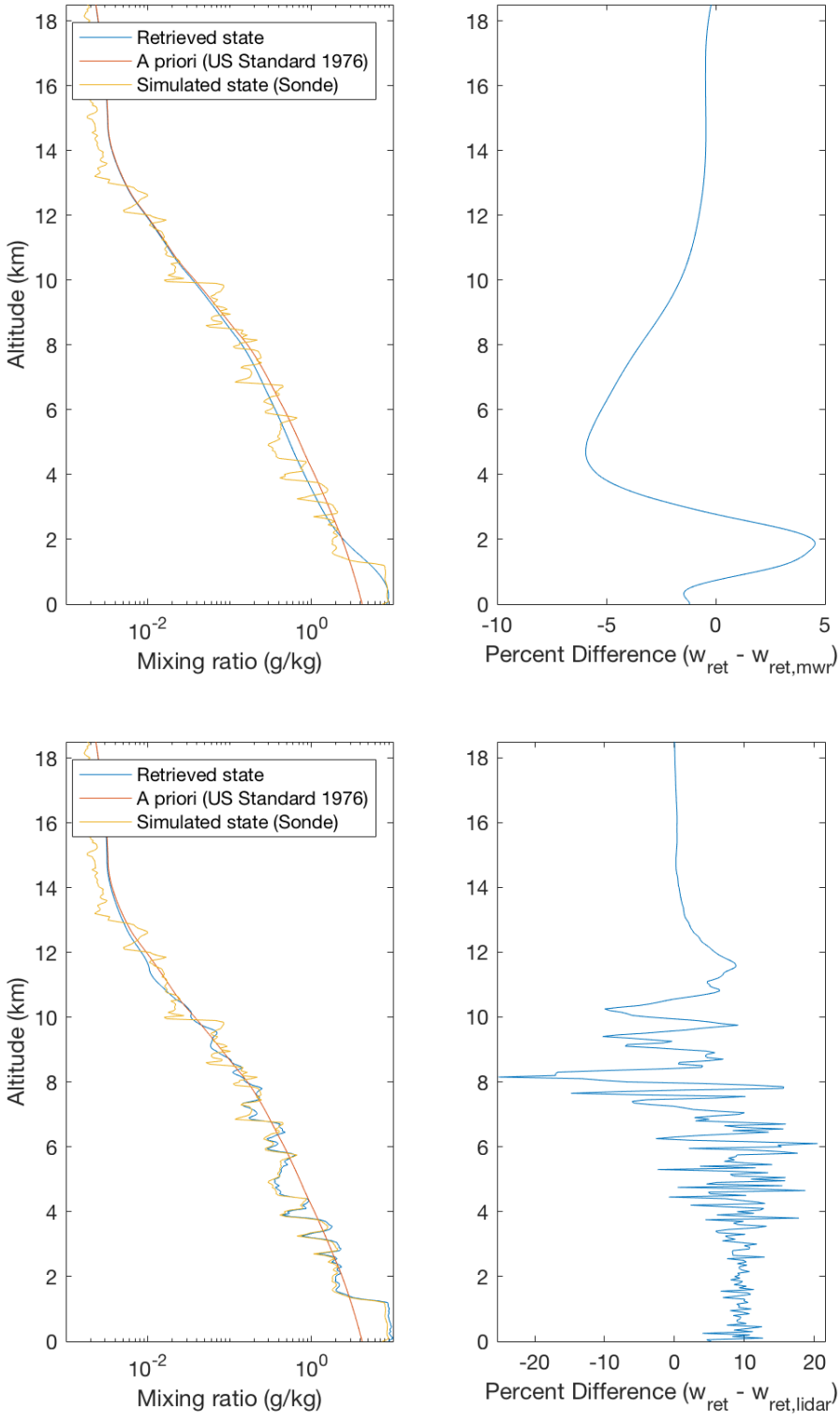

Figure 6.19: Integrated retrieval in which $10^6 \cdot \sigma^2_{y,lidar}$ is used (top left), and the comparison with the radiometer retrieval (top right). Integrated retrieval in which $10^6 \cdot \sigma^2_{y,mwr}$ is used (bottom left), and the comparison with the lidar retrieval (bottom right).

in Table 5.2), the Integrated retrieval also retrieves the PC water vapor lidar constant (C_{HD}, shown previously in Table 5.5). A major advantage of retrieving C_{HD} is the ability to directly determine the calibration factor, $\eta = \frac{C_{HD}}{C_{ND}}$. In order to determine if the lidar constants retrieved are actually significant, and not merely the result of the retrieval falling back to its *a priori* value, the input lidar constant *a priori* value and its covariance are varied and the retrieval is re-executed. For modest changes to *a priori* C_{HD}, there is no effect on the retrieved C_{HD} and thus no change to the calibration factor. A different value for C_{HD} is retrieved only if a much larger or smaller *a priori* C_{HD} value is set. For example, when the *a priori* value for C_{HD} is reduced by a factor of 50, the retrieved calibration factor is consequently reduced by 0.5%. Using a different *a priori* covariance uncertainty has a larger effect, such that a reduction in the *a priori* C_{HD} standard deviation from $0.5C_{HD}$ to $0.1C_{HD}$ decreases the retrieved factor by 5.8%. Thus, changes within a few orders of magnitude on the *a priori* PC water vapor lidar constant have minimal effect on the retrieved lidar constant.

The averaging kernel matrix for the synthetic integrated retrieval is shown in Figure 6.20. It is very similar to the averaging kernels for the lidar retrieval (Figure 6.14), with a response greater than 90% until 9.50 km instead of 9.45 km (a difference of 1 retrieval grid level).

Figure 6.21 shows the vertical resolution from the integrated retrieval. The vertical resolution is virtually identical to the lidar vertical resolution below 12 km (Lidar resolution in Figure 6.15), but gets much coarser above this height. Figure 6.22 gives the uncertainty budget for this retrieval. In the integrated retrieval, the calibration *b-parameter* is removed and parameters for pressure and temperature are added. This demonstrates a notable advantage of the integrated retrieval, as the calibration uncertainty is the largest source of error for much of the lidar budget at approximately 5%. Between 0.5 and 4 km, the temperature and pressure uncertainty are around 0.1% and 0.5% respectively. Even at the lowest altitudes, their combined uncertainty is still smaller than the calibration error.

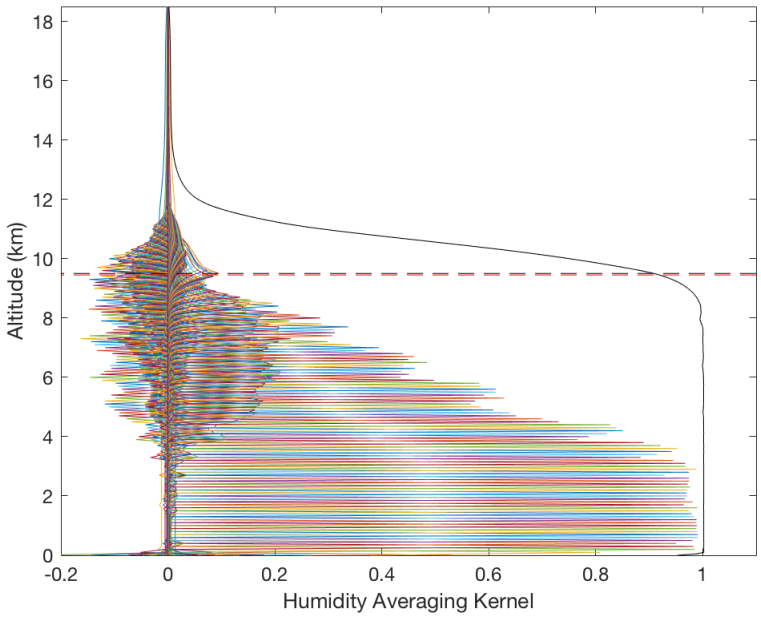

Figure 6.20: Averaging kernels for the integrated retrieval. The black and red dashed lines indicate the height where the response (solid black line) is 0.9 for the integrated (9.5 km) and lidar retrievals (9.45 km), respectively.

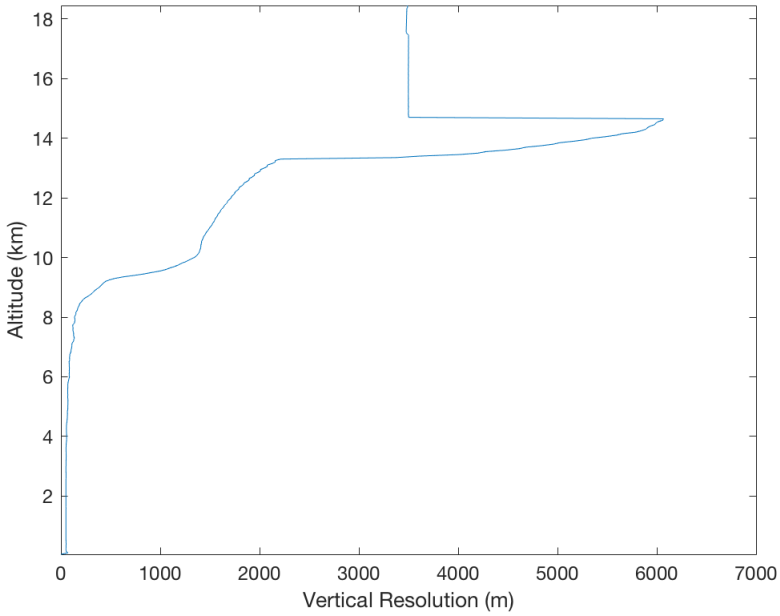

Figure 6.21: Vertical resolution for the synthetic integrated retrieval.

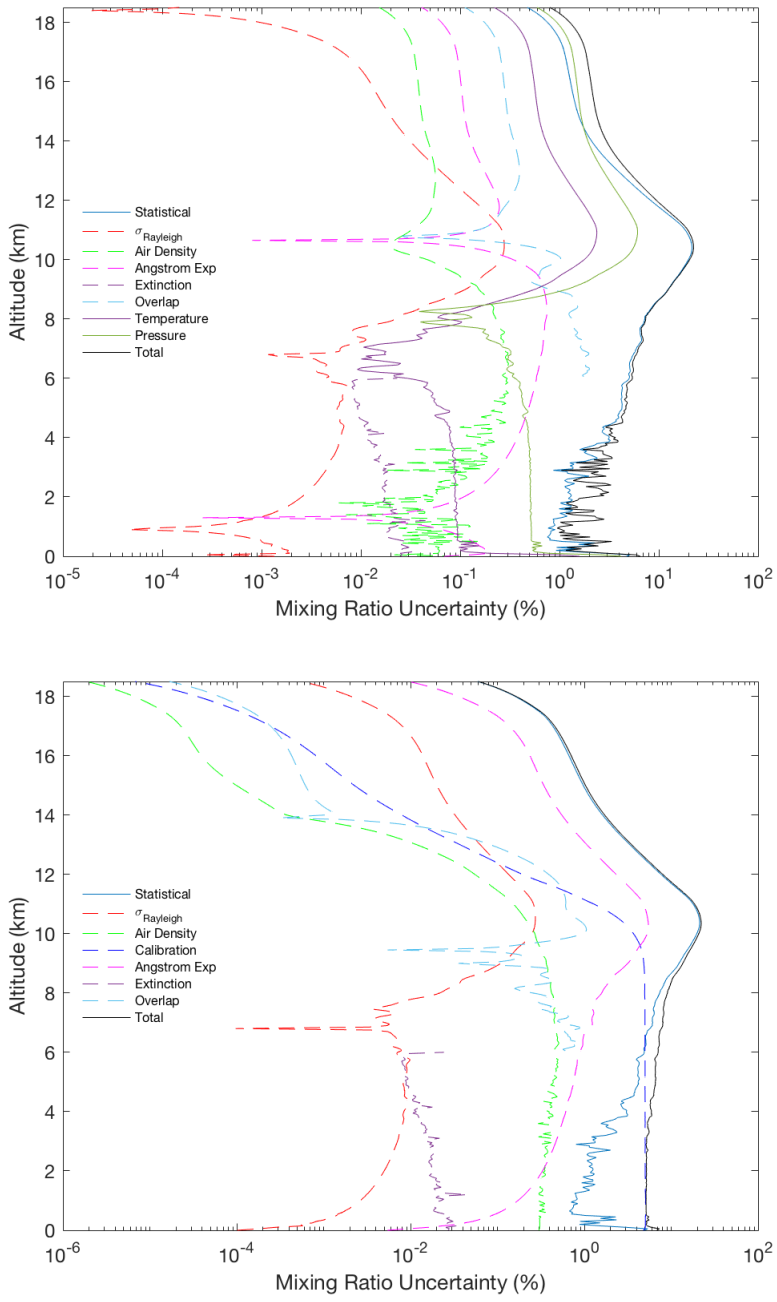

Figure 6.22: Uncertainty budgets for mixing ratio via the synthetic integrated (top) and lidar (bottom) retrieval.

6.3.1 Choice of the *a priori* mixing ratio state

The *a priori* mixing ratio profile

The effect of the choice in *a priori* humidity profile on the retrieved humidity profile is shown in Figure 6.23. In this figure, variations of the *a priori* mixing ratio, including scaled multiples of the US Standard Atmosphere and a constant value, are considered. As the *a priori* state is the starting point, it does not have an effect on the retrieved mixing ratio until about 8 km, where the retrieval has less of a contribution from the measurement, forcing it to fall back to the *a priori* profile. Although the choice of the *a priori* profile does not affect the measurement-based retrieval, it may affect computation time. As shown in Figure 6.24, starting with an *a priori* profile which is significantly different from a reasonable starting point requires the inversion to work longer to converge to a solution, costing additional iterations for the retrieval, which increase the total execution time by 15% for each subsequent iteration after 6. Using an unrealistic profile, such as the constant profile shown in Figure 6.23, actually results in a final measurement cost which is nearly an order of magnitude larger than the other retrievals, due to the profile being considerably larger than the true state profile for the upper range of the retrieval.

The *a priori* mixing ratio covariance matrix

As the *a priori* covariance is involved in the calculation of the cost function and the step size of the retrieval iteration, it plays a larger role in the determination of the retrieved state than the *a priori* profile. To investigate how the *a priori* covariance affects the retrieval, various combinations of inputs for the covariance were tested. The different scenarios, as well as the results are shown in Table 6.1. Cases 1-4 compare the effects of the standard deviation on the retrieval, based on a tent correlation function with a length scale of 1000 m, the correlation conditions for the synthetic measurement retrievals presented earlier in this chapter. Based on the top plot in Figure 6.26 and the left plot of Figure 6.27, the retrieval near the surface

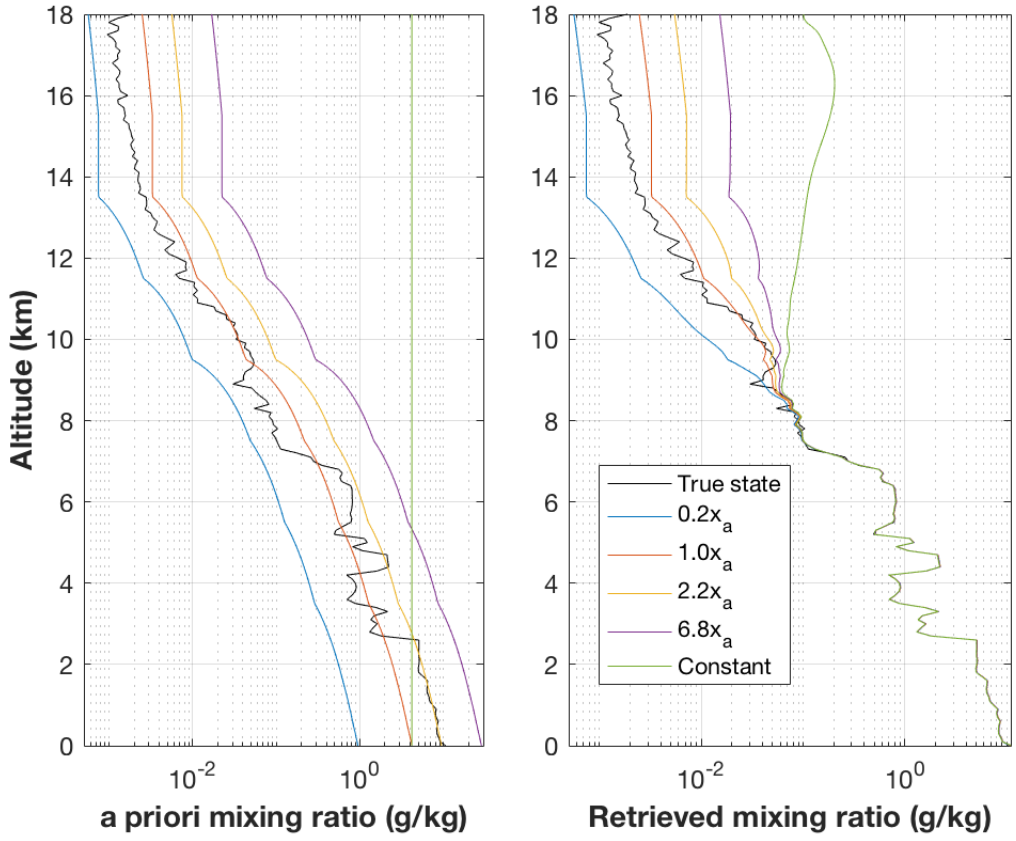

Figure 6.23: (Left) Different *a priori* mixing ratio profiles considered to investigate their effect on the retrieval, compared to the true state (black line). The profiles (blue, yellow, purple lines) are scaled variations of the US Standard Atmosphere model profile [1] (red line), as well as a constant profile (green line), set as the surface value of the US Standard profile. (Right) The retrieved mixing ratio profiles using the *a priori* profiles shown in the left figure.

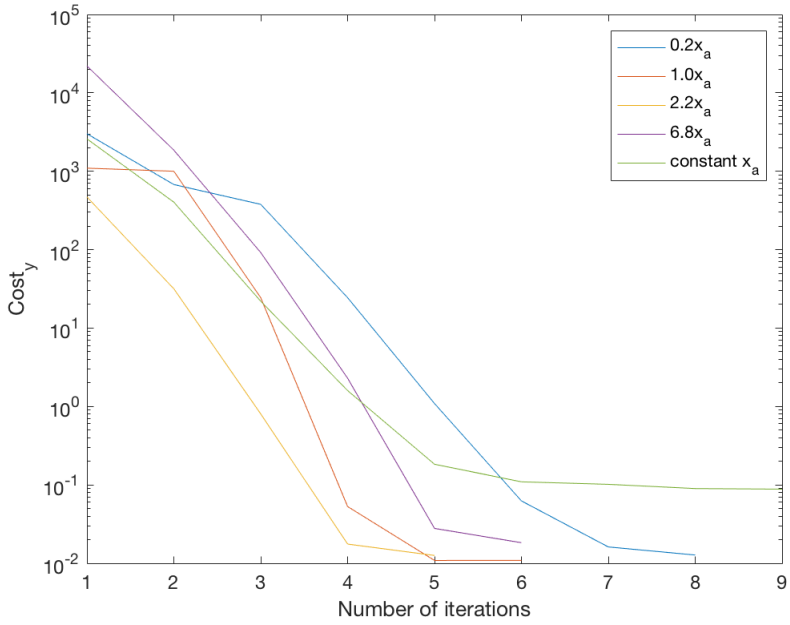

Figure 6.24: Demonstration of how the input of different *a priori* profiles (from Figure 6.23) impact the computation time (number of iterations) as well as the measurement state cost.

more closely resembles the true state when a larger uncertainty is employed. The choice of correlation function does have strong implications for the retrieval. If an uncorrected *a priori* covariance is used, the retrieval is much smaller at the surface than is expected, resulting in a lesser integrated water vapor, with respect to that determined from the coincidental radiosonde. Additionally, although the retrieval with no S_a correlation oscillates about the true state with a greater amplitude than the other cases in the upper retrieval region (middle and right plots of Figure 6.27), it is able to fit more of the variability of the true state. Thus, although the integrated water vapor and calibration factor are more divergent than all of the other cases (aside from the Gaussian case), it does boast smallest measurement cost and highest number of degrees of freedom. Note that most of the cases in this table have measurement costs less than 1. As these retrievals represent synthetic measurements, their associated measurement uncertainties are quite small in order to first gauge how well the Integrated retrieval performed under idealized conditions. According to test cases 1, 5, 6, and 7, Tent and Exponential functions yield similar results, while the Gaussian function leads to a non-sensible inversion, immedi-

ately falling back to the *a priori* state profile. The unusual result for the Gaussian function is due to the fact that the calculation of the measurement cost and the iteration step size use the inverse of S_a rather than S_a itself. As shown in Figure 6.28, while the tent function-based S_a decreases to 0 quickly, the exponential and Gaussian matrices do not decrease to 0, but minima of 2×10^{-9} and 6×10^{-150} respectively. Inverting the latter matrix results in a poorly-conditioned matrix. The effects of correlation length size in shown in the bottom plot of Figure 6.26 and the right plot of Figure 6.27. Case 1 uses a correlation length of 1000 m, while cases 8 and 9 consider shorter lengths. The correlation lengths in cases 10-14 come from the values determined via radiosonde climatological data, as discussed in Section 5.2.4, with the results listed in Table 5.1. Although not as divergent as the uncorrelated S_a retrieval at the surface, a correlation length of 100 m largely underestimates the amount of water vapor at the very bottom of the retrieval, with 1000 m most closely resembling the true state at the surface. Near the top of the retrieval, a larger correlation length is less responsive to the features of the true state, resulting in larger measurement cost and decrease in the number of degrees of freedom.

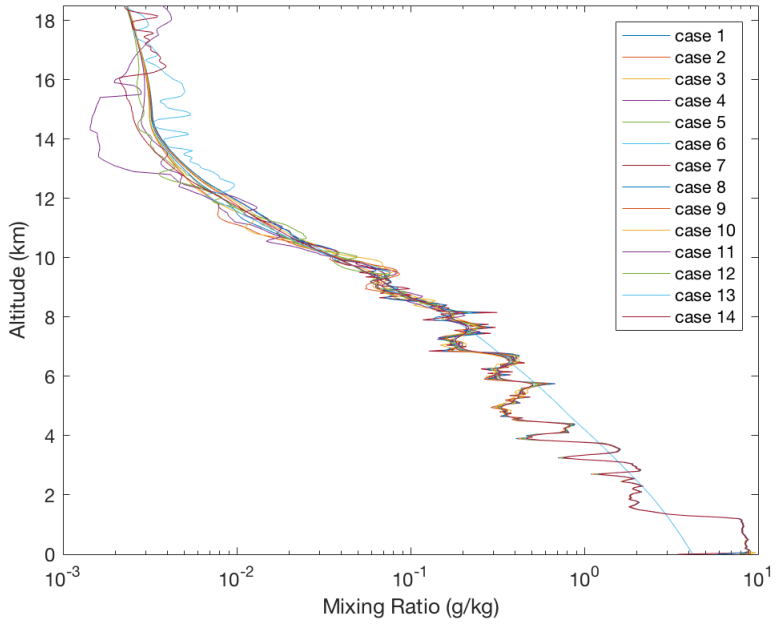

Figure 6.25: Mixing ratio profiles via simulated integrated retrievals using the *a priori* covariance cases listed in Table 6.1.

Effects of S_a on the retrieval								
Case	σ_a	CFUN	l_c (m)	cost$_y$	ΔIWV	$\Delta\eta$	DOF	$A_{0.9}$
1	0.5	Tent	1000	0.727	1.29	0.59	121.7	9.50
2	0.75	Tent	1000	0.710	1.30	0.69	135.6	9.80
3	0.25	Tent	1000	0.800	1.29	0.42	97.0	8.85
4	Clim	Tent	1000	0.714	1.29	0.45	129.5	9.55
1	0.5	Tent	1000	0.727	1.29	0.59	121.7	9.50
5	0.5	Exp	1000	0.707	1.29	0.68	132.6	9.65
6	0.5	Gauss	1000	93.30	37.3	5.28	92.7	18.4
7	0.5	Tent	1*	0.692	1.42	1.69	171.0	8.15
7	0.5	Tent	1*	0.692	1.42	1.69	171.0	8.15
8	0.5	Tent	100	0.698	1.33	1.17	157.4	8.50
9	0.5	Tent	500	0.719	1.29	0.53	132.1	9.50
1	0.5	Tent	1000	0.727	1.29	0.59	121.7	9.50
10	0.5	Tent	1660	0.746	1.30	0.23	110.8	9.70
11	0.5	Tent	3030	0.749	1.29	0.53	103.2	9.60
12	0.5	Tent	3881	0.750	1.29	0.47	100.0	9.80
13	0.5	Tent	6900	0.778	1.28	0.51	90.6	9.80
14	0.5	Tent	9400	0.802	1.28	0.50	84.8	10.15

Table 6.1: The effects of the *a priori* covariance components on retrieval characteristics. Input components include the fractional standard deviation of x_a (σ_a), correlation function (CFUN), and correlation length (l_c, based on some of the values listed in Table 5.1). The retrieval characteristics include the measurement (cost$_y$), percent difference of integrated water vapor (compared to that from the coincidental sonde, ΔIWV), percent difference of calculated calibration factor (compared to the sonde-derived factor, $\Delta\eta$), degrees of freedom (DOF), and the height below which the averaging response is above 0.9 ($A_{0.9}$). σ_a of Clim uses the climatologically-calculated mixing ratio uncertainty profile (Figure 5.6). Correlation lengths of 1* indicate an uncorrelated matrix, with no off-diagonal elements.

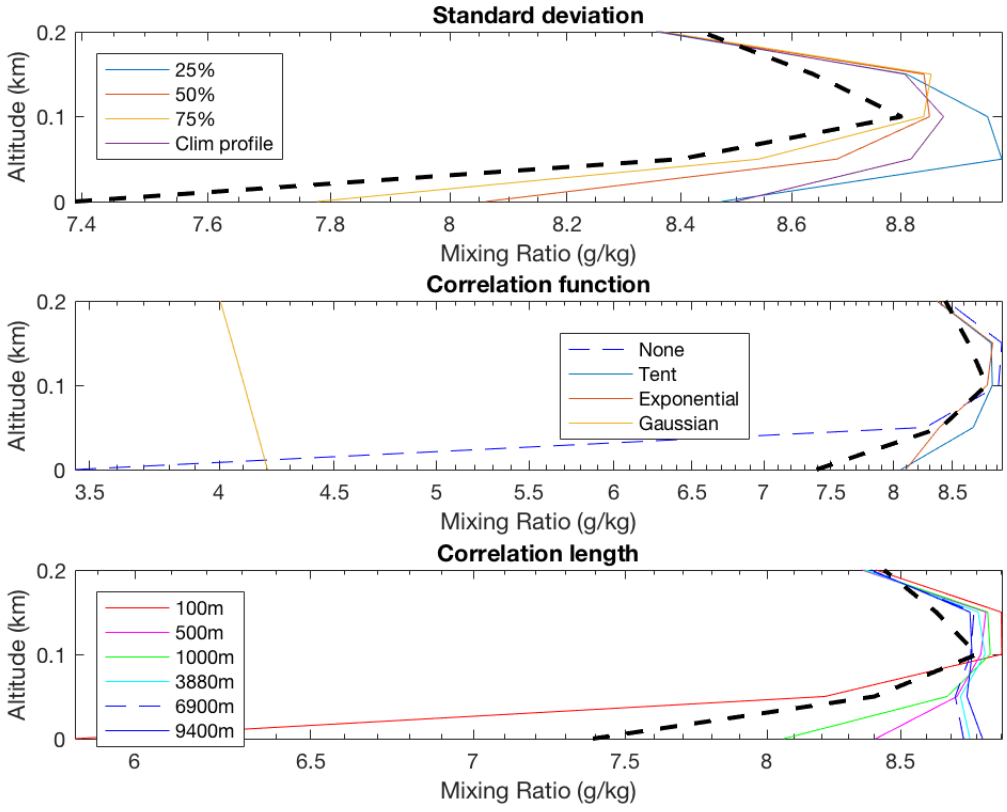

Figure 6.26: The lowest 200 m of the profiles from Figure 6.25, with each subplot focusing on variations of different *a priori* covariance components.The black dashed line in each figure is the true state humidity.

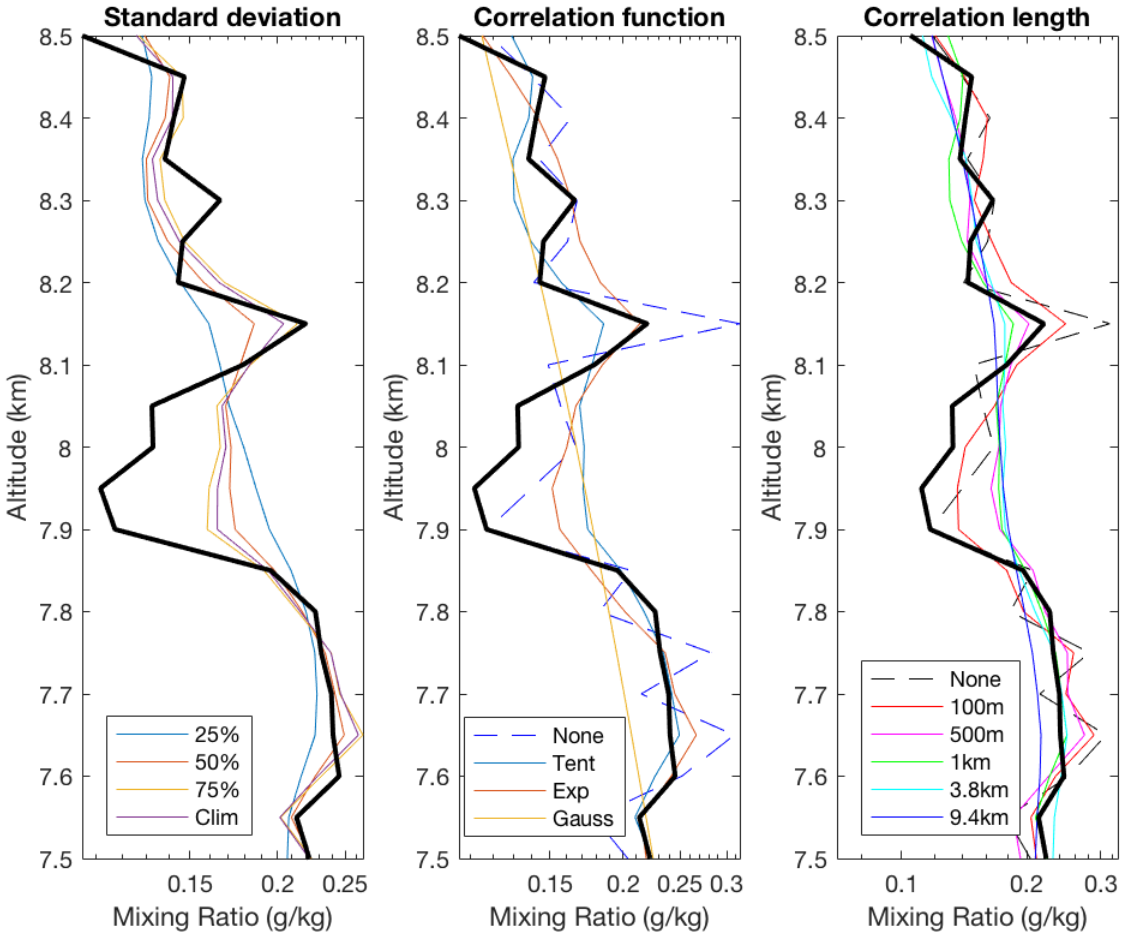

Figure 6.27: The profiles from Figure 6.25 between 7.5-8.5 km, with each subplot focusing on variations of different *a priori* covariance components.The heavy black line in each figure is the true state humidity.

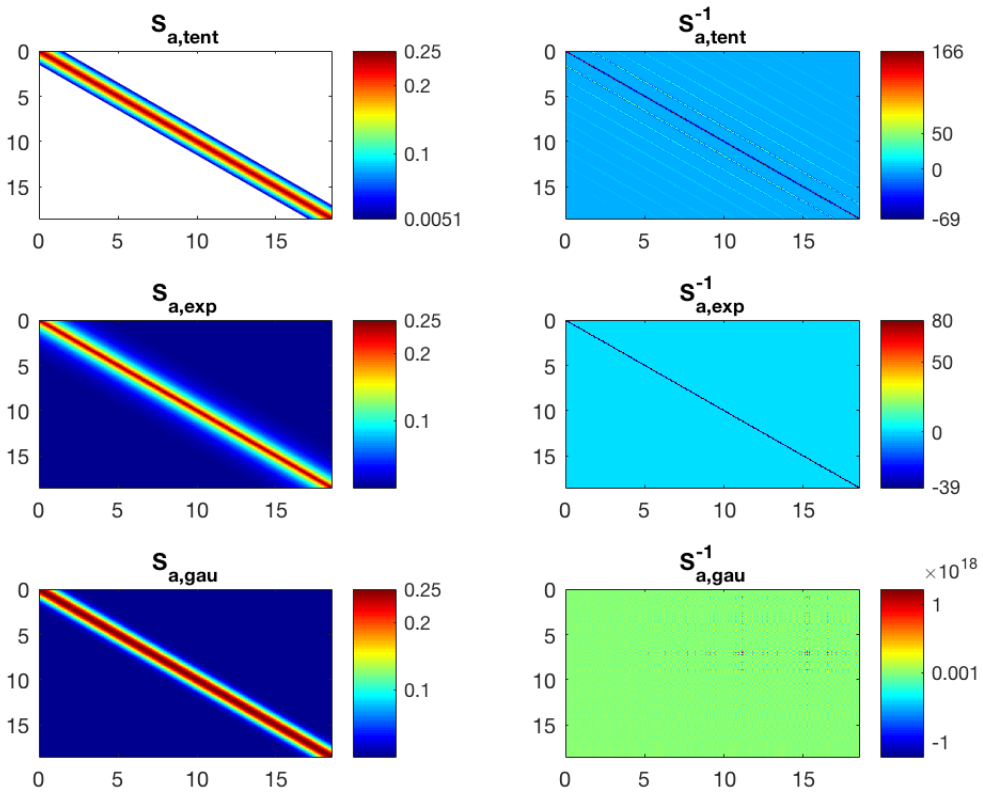

Figure 6.28: Contour plots of covariance matrices (left column) and their inverses (right column). The top, middle, lower panels are covariance matrices constructed using a tent, exponential, and Gaussian correlation function, respectively. All cases use a fractional standard deviation of 0.5 and a correlation length of 1000 m. The white region indicates where the matrix values equal 0. The minimum values for $S_{a,exp}$ and $S_{a,gau}$ are 2.3×10^{-9} and 5.8×10^{-150}, respectively.

6.4 Summary

In this chapter, retrievals using simulated lidar and radiometer measurements were carried out, generated by running radiosonde atmospheric profiles from October 5, 2011 through the lidar and radiometer forward models and adding noise to the simulated measurements. The radiometer retrieval showed promising results, with reasonable residuals and a retrieved mixing ratio profile which is within 15% of the smoothed radiosonde true state profile. The total uncertainty is also within 15% at all altitudes, but is largely dependent on the uncertainties from the pressure and temperature *b-parameters*. These *b-parameters* uncertainties vary based on their covariance matrices, with optimal bounds if they are uncorrelated with standard deviations $\leq$5% for pressure and $\leq$5 K for temperature. The mixing ratio profile from lidar retrieval is of a much finer resolution than the radiometer retrieval, much closer to the native radiosonde resolution. The total uncertainty is approximately 5% for the first 4 km, with the largest contribution from the calibration factor *b-parameter*.

The retrieved mixing ratio profile via the integrated method is within 5% of the profile from the lidar retrieval. It is also able to retrieve a mixing ratio value closer to the true state value for the lowest 100 m of the retrieval than the lidar, as the lidar has no measurements to work with below 50 m. In addition to profile similarities, the integrated and lidar retrievals also have similar mixing ratio averaging kernel matrices, with an integrated retrieval response of 0.9 at a slightly higher altitude than that of the lidar retrieval (9.50 km and 9.45 km, respectively). However, the integrated retrieval does not require a calibration *b-parameter*, resulting in a total uncertainty around 3% for the first 4 km. The integrated retrieval method is therefore shown to retrieve mixing ratio in a simulated environment at least as well as the lidar retrieval, with the additional advantage of a smaller overall uncertainty due to the direct retrieval of a calibration factor (made possible by the radiometer contribution) instead of setting a radiosonde-derived calibration factor as a *b-parameter*.

The retrievals in Sections 6.1-6.3 are carried out using mixing ratio *a priori* covariance matrices constructed by a standard deviation of 50% (employed in Sica & Haefele 2016) and

a tent correlation function with a length of 1000 m (with the correlation function type used in Sica & Haefele 2016, and the length chosen as simple whole number). Alternative values are tested with the integrated retrieval, with results listed in Table 6.1. As a standard deviation of 50% is a reasonably close mean value for the standard deviations determined via radiosonde climatologies (Figure 5.6), there is little difference in the retrieval when the climatology profile is used in place of 50%. Use of significantly larger or smaller mixing ratio standard deviations will have a greater impact on the retrieval. Tent and exponential correlation functions yield similar results, with a Gaussian function producing non-sensible results if an appropriate cutoff threshold is not specified. In terms of correlation length, small values give more degrees of freedom, but tend to differ more from the radiosonde calibration factor and integrated water vapor values. A length of 1660 m, as determined in Section 5.2.4, provides an optimal balance of retrieval traits.

Bibliography

[1] U.S. Standard Atmosphere, 1976, Tech. rep., National Oceanic and Atmospheric Administration, 1976.

[2] Hicks-Jalali, S.: A Tropospheric Water Vapour Climatology and Trends Derived from Vibrational Raman Lidar Measurements over Switzerland, Ph.D. thesis, The University of Western Ontario, 2019.

[3] Leblanc, T., Sica, R. J., Van Gijsel, J. A., Haefele, A., Payen, G., and Liberti, G.: Proposed standardized definitions for vertical resolution and uncertainty in the NDACC lidar ozone and temperature algorithms-Part 3: Temperature uncertainty budget, Atmospheric Measurement Techniques, 9, 4079–4101, doi:10.5194/amt-9-4079-2016, 2016.

[4] Press, W., Teukolsky, S., Vetterling, W., and Flannery, B.: Numerical Recipes in Fortran 77: The Art of Scientific Computing, Cambridge University Press, 2nd edn., 1992.

[5] Rodgers, C.: Inverse Methods for Atmospheric Sounding: Theory and Practice, World Scientific Publishing, London, 2000.

[6] Sica, R. and Haefele, A.: Retrieval of water vapor mixing ratio from a multiple channel Raman-scatter lidar using an optimal estimation method, Appl. Opt., 55, 763, 2016.

[7] von Clarmann, T.: Smoothing error pitfalls, Atmospheric Measurement Techniques, 7, 3023–3034, doi:10.5194/amt-7-3023-2014, 2014.

Chapter 7

Real measurement Retrieval of mixing ratio

After validating the retrievals via synthetic measurements, the retrieval methods can now be tested using real measurements. In this chapter, we use measurements from the HATPRO at times coincidental to clear nighttime GRUAN-corrected soundings, in order to retrieve water vapor mixing ratio. These retrievals are then compared to retrievals using lidar measurements, calibrated against the HATPRO (the integrated method) as well as the GRUAN radiosondes (the lidar method). Retrievals are also carried out for clear daytime observations, with a number of 24-hour cases investigated. For these 24-hour cases, the lidar calibration factors determined for the integrated and lidar methods are monitored, allowing for the investigation of potential diurnal variations in the value of this factor.

7.1 Clear night case

7.1.1 Radiometer-only retrieval

The first case considered is the nighttime observation on October 5, 2011. This date, also used for simulating measurements in Chapter 6, is chosen because it is a clear night, with a

coincidental RS92 radiosonde launch at 22:50 UTC. This radiosonde data has been processed by GRUAN, and a lidar calibration was carried out in Hicks-Jalali et al. 2019 via the Trajectory Method. The radiosonde measurements from this period were also used in generating the simulated state for the synthetic retrieval in the previous chapter.

Figure 7.1 shows the radiometer retrieval of measurements from the 30 minutes following the radiosonde launch at 22:50 UTC. In addition to the OEM retrieval of mixing ratio and the coincidental radiosonde profile, the humidity profile retrieved by the HATPRO is also included in this figure. The HATPRO retrieval is carried out using the built-in quadratic regression algorithm [4] provided with the HATPRO data acquisition software, but it also has the capability to carry out retrievals by linear regression or artificial neural networks [6]. The HATPRO algorithm retrieves absolute humidity rather than mixing ratio, with the instrument manual citing an RMS uncertainty of $0.4 g/m^3$ [1]. One major disadvantage of the neural network approach is the need for a substantial database (such as from radiosondings) in order to train the algorithm [5]. As the HATPRO retrieval is determined partly by surface measurements, it has a surface mixing ratio near that of the radiosonde. However, it retrieves significantly greater humidity from 4-7 km than the other methods shown in the figure. The uncertainties associated with the radiometer retrieval using raw measurements, $T_{b,raw}$, are shown in Figure 7.3. The uncertainty budget determined here is similar to the uncertainty budget ascertained for the synthetic radiometer retrieval (Figure 6.9), with contributions coming primarily from statistical origins and a maximum uncertainty of 14% at a height close to where the averaging kernel response equals 0.9.

The averaging kernel matrix as well as the vertical resolution is shown in Figure 7.2. The averaging kernel matrix does resemble that derived for the synthetic retrieval (Figure 6.7), with a response threshold near 4 km instead of 5 km. With a vertical resolution between 4000 and 5000 m, the radiometer retrieval resolution is much coarser than the radiosonde resolution, which is on the order of a few meters. To account for their differences in vertical resolution, a radiosonde profile smoothed against the averaging kernels of the radiometer retrieval (as was

discussed in Section 6.1) is also shown in Figure 7.1. The OEM retrieval does vary from the smoothed sonde profile, differing by 40% at 250 m and nearly 60% at 3.5 km.

The discrepancy between the OEM retrieval and smoothed sonde profile may be explained by the residuals for the OEM retrieval (Figure 7.1, lower right plot), in which the difference between the brightness temperatures and the fitted measurement exceeds the measurement uncertainty. For the synthetic radiometer retrieval in the previous chapter, it was sufficient to work with the radiometric resolution of 0.1 K provided with the HATPRO instrument documentation as the measurement uncertainty. However, for working with real radiometer measurements, it is more appropriate to use the absolute brightness temperature accuracy instead of the radiometric resolution. This value, which is specified as 0.5 K for the HATPRO K-band channels [1], accounts for uncertainties associated with the instrument's calibration, making it a more realistic representation of real data. Despite the use of a realistic uncertainty, the residuals from the retrieval are still larger than the uncertainty bounds. This difference is even more exaggerated when bias-corrected brightness temperatures are used instead of the uncorrected brightness temperatures. The difference is also reflected in the mixing ratio retrieval, where the OEM retrieval using corrected measurements deviates more from the smoothed sonde profile than the uncorrected measurement retrieval (a difference of 70% opposed to 60% at 3.5 km). As shown in Section 5.4.1, a channel-dependent correction is applied to the raw brightness temperatures in to order to account for biases introduced by instrumental effects. The reason for this exaggeration of the residuals can be seen in the brightness temperature plot (Figure 7.1, upper right plot), where the bias correction actually results in a substantial bump and then a dip in the brightness temperature spectrum at 25.44 GHz and 26.24 GHz, respectively, resulting in unrealistic values which skew the retrieval.

As mentioned in Section 5.4.1 and shown in Figure 5.15, there is a large variability in the 25.44 GHz and 26.24 GHz channels in the 2011 radiometric brightness temperatures, skewing the mean biases for those channels. As a result, using such extreme biases as a correction factor may worsen the outcome of the retrieval. Thus, it is best to consider data from alternative time

periods, in which the bias is smaller and less variable. Referring again to Figure 5.15, prior to mid-2010, there is considerable variation in the bias level across the channels which is not improved through a correction. Late 2010 and early 2011, as well as much of the time between 2014 and 2017, have relatively low levels of bias, which are improved through bias correction. It is therefore advantageous to choose radiometer measurement from these epochs of low bias (Appendix C, which considers more data over an extended time range, investigates this and confirms the same sentiment.)

Additional nights published among the results of Hicks-Jalali et al. 2019 [3] are also considered here, as their spectra are actually improved by applying a bias correction, contrary to October 5, 2011. Two of these nights, February 29, 2012, and April 24, 2013, are plotted in Figure 7.4. These nights have uncertainty budgets, averaging kernel matrices, and vertical resolutions which are comparable to those seen in the October 5, 2011 retrieval. Compared to October 5, 2011, the effects of a bias correction are much more subtle, resulting in modest improvements to the residuals when the correction is applied. This is again is reflected in the retrieved mixing ratio profiles, where now the corrected retrieval more closely resembles the radiosonde over much of the lowest 3 km, for each date. For February 29, the difference between the smoothed sonde profile and the corrected retrieval is less than 16% over the entire profile. For April 23, on the other hand, the OEM retrieval differs from the smoothed sonde profile by only 2% at the surface, but the difference increases above 1 km to a maximum of 24% at 2.9 km. For February 29th, the HATPRO retrieval starts with a surface humidity which is about 1.5 times larger than the sonde profile, rapidly decreasing above. For April 24th, the HATPRO retrieval starts near the sonde surface values, but largely underestimates the humidity for most of the lowermost 1.5 km. In both cases, the HATPRO software retrieval overestimates the humidity in the region between 4 and 7 km.

Two more nights with coincidental GRUAN-corrected sondes are provided in Figure 7.5. Both of these nights are in an epoch where the bias levels are relatively small. However, for January 23, 2014, the correction does improve the residual such that it is within the mea-

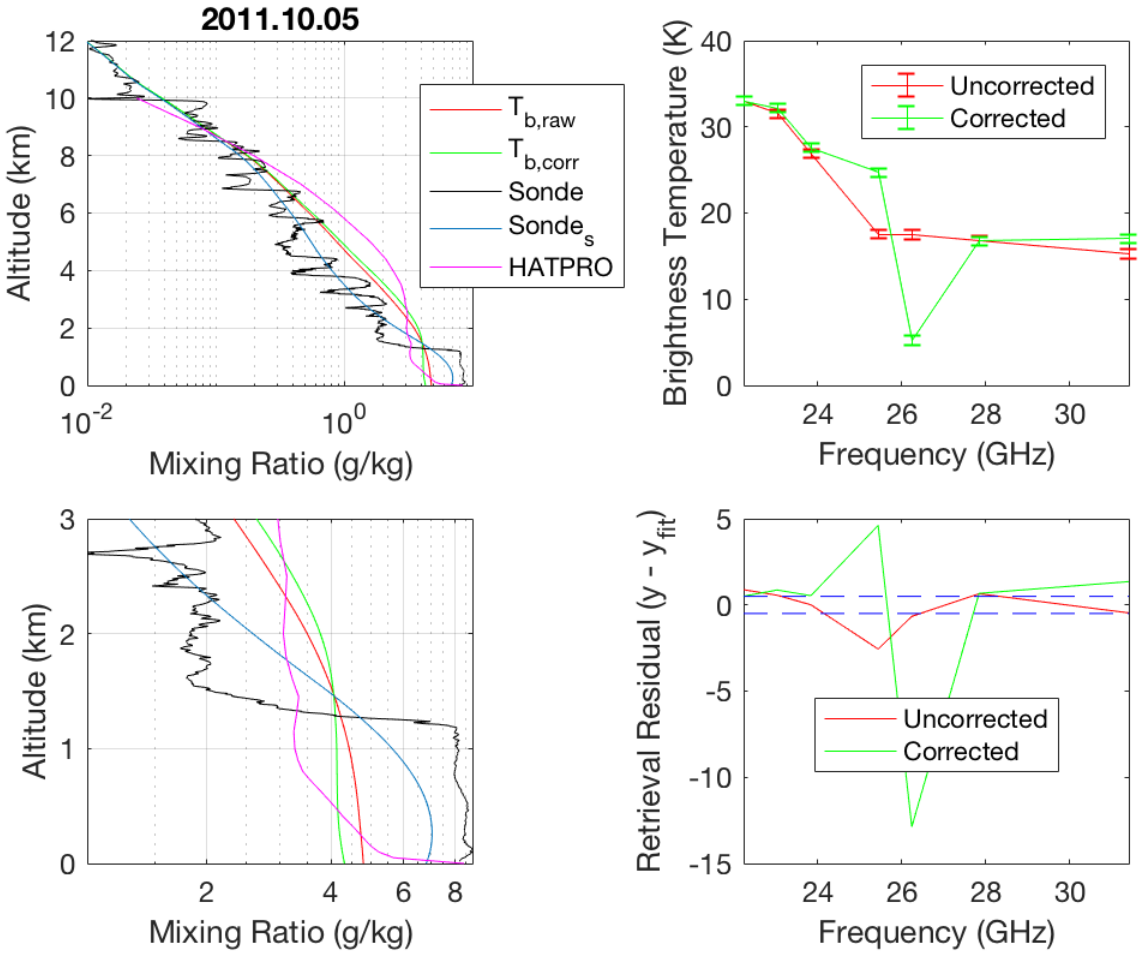

Figure 7.1: Radiometer retrieval of real measurements on October 5, 2011. (Left plots) The retrieved mixing ratio profile (via the raw, $T_{b,raw}$, and corrected, $T_{b,corr}$, brightness temperatures), compared to the coincidental radiosonde profile $Sonde$, the sonde profile smoothed against the radiometer averaging kernels, $Sonde_s$, and the humidity retrieved via the HATPRO software algorithm, $HATPRO$. (Top right) The raw and bias-corrected brightness temperatures and (bottom right) their retrieval residuals.

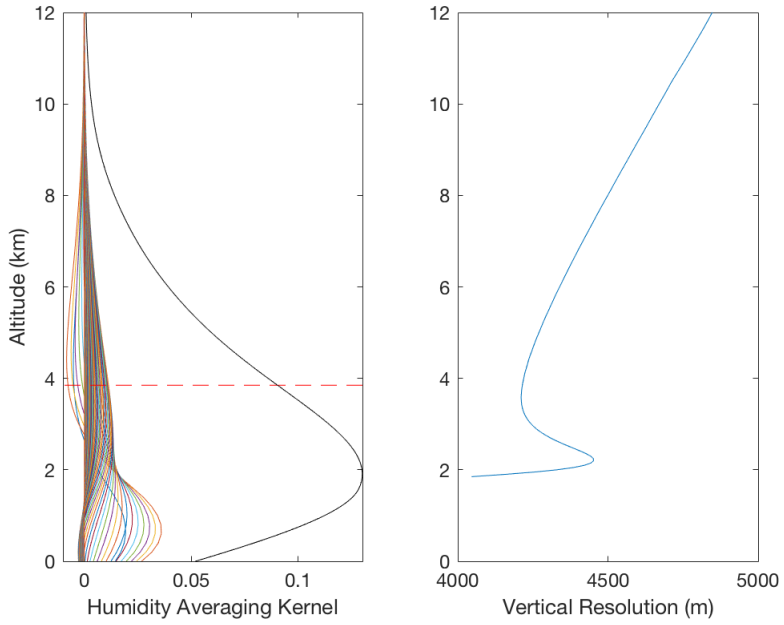

Figure 7.2: Averaging kernel (left) and vertical resolution (right) for the radiometer retrieval of mixing ratio on October 5, 2011. In the left plot, the solid black is the response (divided by 10) and the red dashed line is where the response is 0.9.

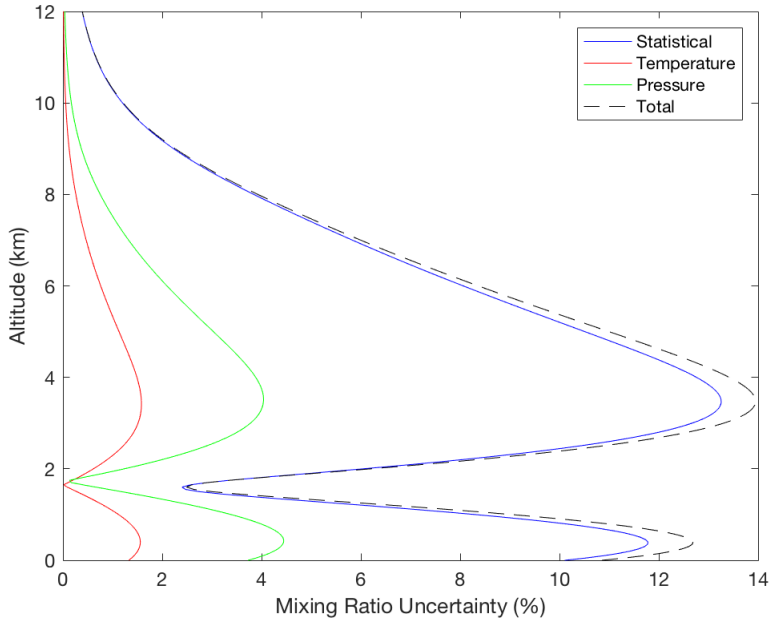

Figure 7.3: Uncertainty budget for the radiometer retrieval of mixing ratio on October 5, 2011.

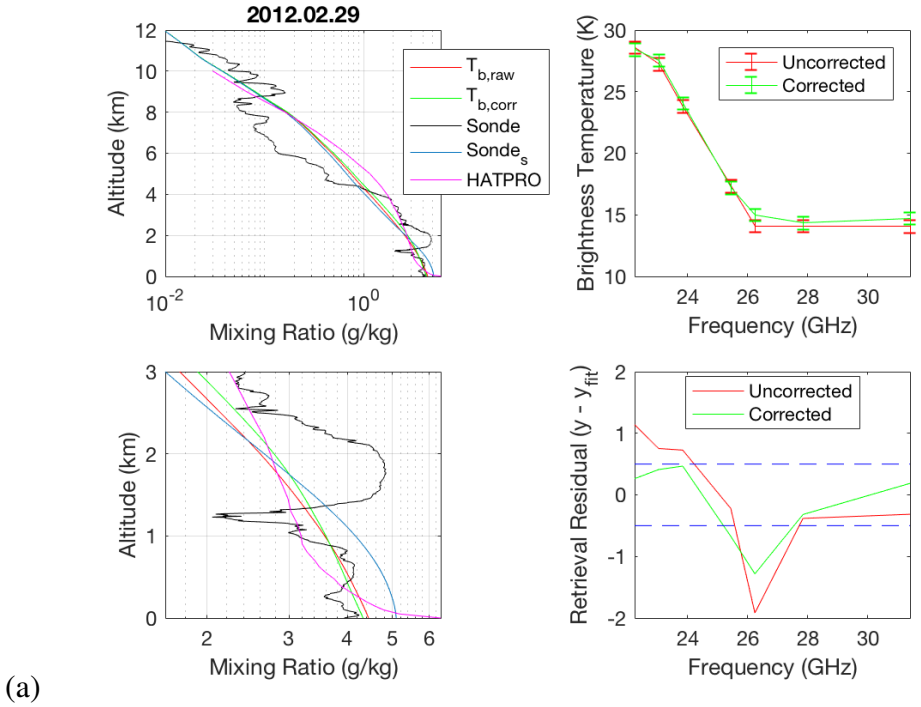

(a)

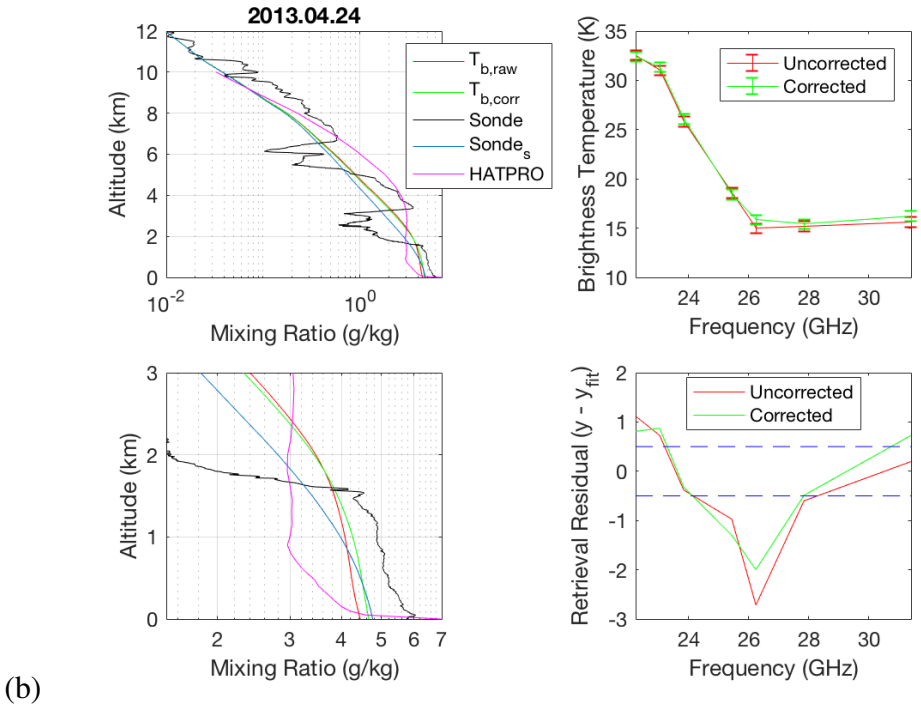

(b)

Figure 7.4: Radiometer retrieval of real measurements on February 29, 2012 (a) and April 24, 2013 (b). For each subfigure, (Left plots) The retrieved mixing ratio profile (via the raw, $T_{b,raw}$, and corrected, $T_{b,corr}$, brightness temperatures), compared to the coincidental radiosonde profile $Sonde$, the sonde profile smoothed against the radiometer averaging kernels, $Sonde_s$, and the humidity retrieved via the HATPRO software algorithm, $HATPRO$. (Top right) The raw and bias-corrected brightness temperatures and (bottom right) their retrieval residuals.

surement uncertainty for all of the K-band channels. The corrected mixing ratio retrieval is approximately 1% smaller than the uncorrected profiles at the lowest altitudes, but provides a better fit over the first 6 km of the humidity retrieval. It is in reasonable agreement with the smoothed sonde profile, with a maximum difference between the profiles of 19% at 3.3 km. This night also has an uncertainty budget, averaging kernel matrix, and vertical resolution which are comparable to those seen in the October 5, 2011 retrieval. July 18, 2014 data show slight improvement of the residuals when a bias correction is incorporated instead of using raw measurements. However, although the residuals do not have the large magnitude seen in the 25.44 and 26.24 GHz channels on October 5, 2011, all of the frequencies aside from 22.24 GHz are greater than 0.5 K. As a result of this poor fit, the retrieved mixing ratios for the corrected and uncorrected, as well as the HATPRO, retrievals exhibit ill-fitting cubic splines. Compared to radiosonde profiles (raw and smoothed), the radiometer-based retrievals grossly underestimate the humidity below 2 km and overestimate the humidity between 3 and 6 km. This date shows that for radiometer retrievals with poorly constrained residuals (5 times the measurement uncertainty in this case), the retrievals yield mixing ratios poorly reflecting the true atmospheric state. The averaging kernels and vertical resolution for this night are shown in Figure 7.6. Compared to those from October 5, 2011, these averaging kernels do not have the bump around 1 km (Figure 7.6), but do have a 0.9 threshold at near 5 km instead of 4 km.

This section shows some initial results of retrievals of real radiometer measurements during clear nights coinciding with GRUAN-corrected radiosondes. The quality of the retrieval can be gauged by the residuals, as well as relative agreement with the coincidental radiosonde. Generally, retrieval residuals which fall completely within the measurement uncertainty bounds result in retrieved mixing ratio profiles that more or less agree with the smoothed radiosonde profile to within the uncertainty of the radiometer retrieval. However, if the residuals are substantial, as in the case of the July 18, 2014 retrievals and the October 5, 2011 retrieval using bias-corrected measurements (where the maximum residuals are more than 10 times larger than the measurement uncertainty), the consequent retrievals deviate greatly from the radiosonde measurement.

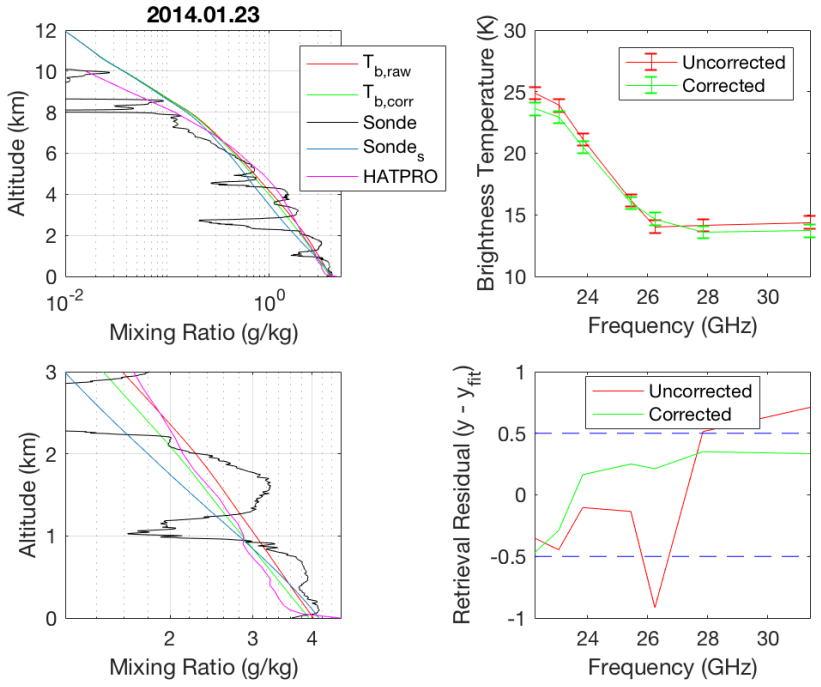

(a)

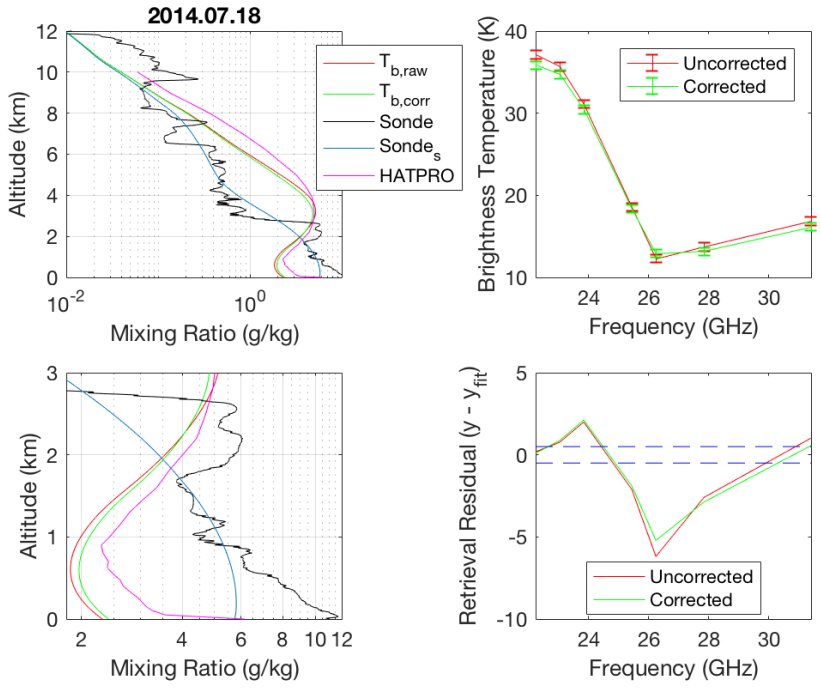

(b)

Figure 7.5: Radiometer retrieval of real measurements on January 23, 2014 (a) and July 18, 2014 (b). For each subfigure, (Left plots) The retrieved mixing ratio profile (via the raw, $T_{b,raw}$, and corrected, $T_{b,corr}$, brightness temperatures), compared to the coincidental radiosonde profile $Sonde$, the sonde profile smoothed against the radiometer averaging kernels, $Sonde_s$, and the humidity retrieved via the HATPRO software algorithm, $HATPRO$. (Top right) The raw and bias-corrected brightness temperatures and (bottom right) their retrieval residuals.

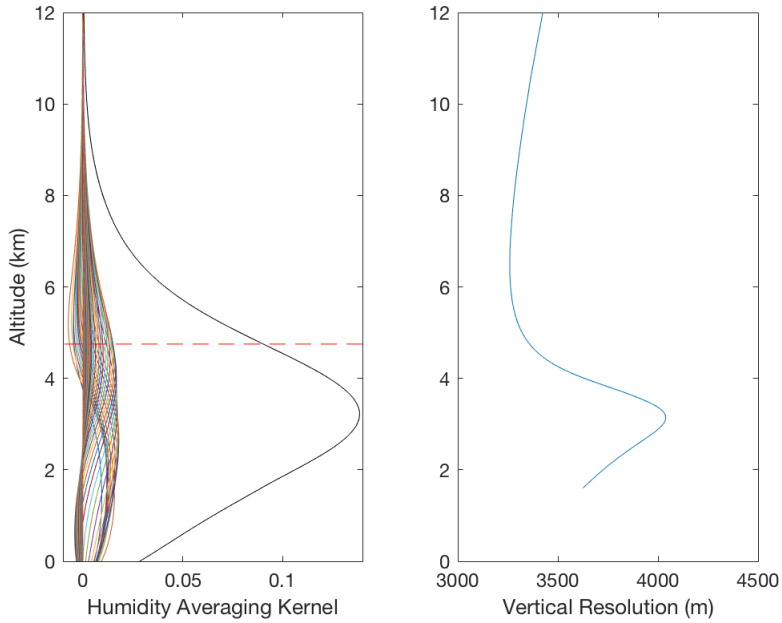

Figure 7.6: Averaging kernel (left) and vertical resolution (right) for the radiometer retrieval of mixing ratio on July 18, 2014. In the left plot, the solid black is the response (divided by 10) and the red dashed line is where the response is 0.9.

Before performing an integrated retrieval, it is therefore important to consider if performing a bias correction for the brightness temperatures improves or hinders the radiometer retrieval.

7.1.2 Integrated retrieval

The 5 clear nights considered in the previous section were also run through the integrated retrieval method. Results from the integrated retrievals for these 5 clear night cases are shown in this section, along with a summary of the results listed in Table 7.1, in which integrated retrievals are compared to radiometer retrievals, as well as lidar retrievals where the calibration factor is assumed based on the radiosonde calibration factor (Table 5.2) or retrieved directly (Table 5.3).

The first of these nights, October 5, 2011, is shown in Figure 7.7, in which the integrated retrieval is compared to both the radiometer and lidar retrievals. The integrated retrieval is nearly identical in shape to the lidar retrieval over the effective range of the retrieval. For this

date, the integrated retrieval in which the uncorrected brightness temperatures used are more closely resembles the lidar-retrieved profile than the bias-corrected retrieval (an insignificant 7.3% vs 7.5% difference between 1 and 6 km), which is reasonable, as the radiometer retrieval for this night has a better fit using raw measurements when compared to the corrected spectrum. The mixing ratio uncertainty for the integrated retrieval is shown in Figure 7.8, which like the synthetic integrated retrieval (Figure 6.22), has a total uncertainty between 2 and 6% for the first 5 km. The integrated retrieval is also compared to the alternate lidar retrieval (so called *Lidar1* in the figure), where the calibration factor is retrieved directly without an external calibration source instead of using one determined by radiosonde calibration. This method is included to demonstrate the importance of calibration to mixing ratio retrievals via lidar. Like the trend in Figure 6.19 (bottom plot, the synthetic integrated retrieval where the radiometric variance is multiplied by 10^6), the shape of the alternative lidar retrieval profile is similar to that of the radiosonde-calibrated lidar retrieval as well as the integrated retrieval, but is offset by a considerable factor, approximately 20% larger than the calibrated lidar retrieval. The retrieved calibration constants have significantly smaller uncertainties than those calculated via the traditional and trajectory radiosonde calibration methods, causing both integrated retrieval calibration constants to fall outside the range of the radiosonde-calibrated factors, with the uncorrected retrieval placed slightly closer. However, both integrated calibration factors are quite close to the factor determined via the solar background method (Section 4.6). The degrees of freedom for the integrated retrieval of humidity are slightly larger than those determined via the lidar retrievals. As a result, the averaging kernels for each method (shown in Figure 7.9) are quite similar, with the lidar averaging kernel dropping below 0.9 at 9.45 km and integrated averaging kernel reaching a value of 0.9 at 9.50 km. The vertical resolution is also comparble between the lidar and integrated retrievals.

The second night considered was February 28, 2012 at 22:57 UTC for 30 minutes. This night is chosen, as it is also a clear night with a coincidental GRUAN-corrected radiosonde at the same time. The retrieved mixing ratio profiles (Figure 7.10) derived from the integrated

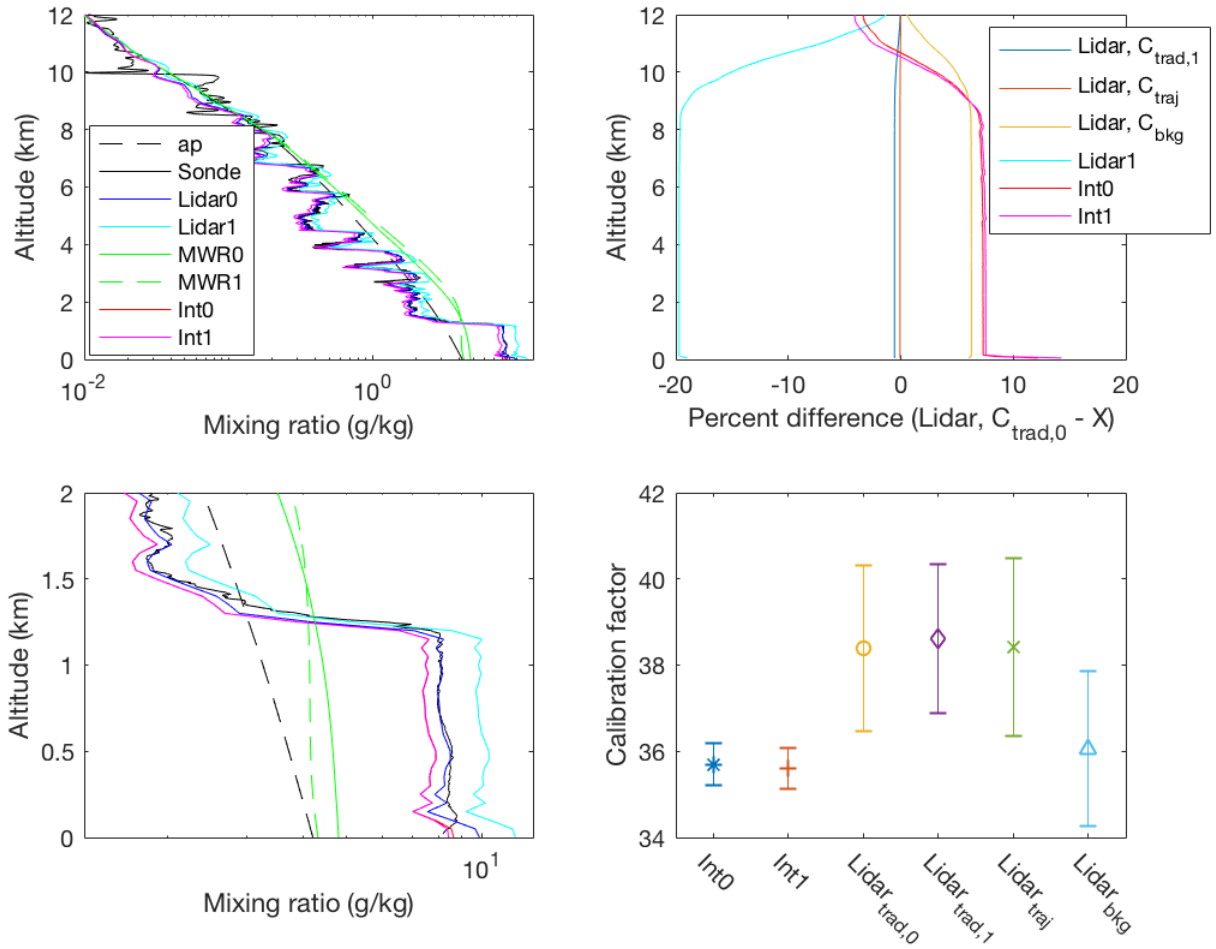

Figure 7.7: Retrievals from October 5, 2011 at 22:55 UTC for 30 minutes. (Left) Mixing ratio retrievals via different retrieval methods up to 12 km (top) and 2 km (bottom). *ap* is the *a priori* profile, from the US Standard Atmosphere and *Sonde* is the radiosonde profile. *Lidar0* is the lidar retrieval where $\eta = C_{trad,0}$, while *Lidar1* retrieves this value. *MWR0* and *Int0* are the radiometer and integrated retrievals, where no bias correction is performed, whereas *MWR1* and *Int1* have the bias correction for brightness temperatures. (Top right) Percent difference in the retrieved mixing ratio, compared to *Lidar0*, where $C_{trad,1}$, C_{traj}, and C_{bkg} are Lidar retrievals using calibration factors determined by the traditional, trajectory, and solar background methods, respectively. (Bottom right) Calibration factors during this observation.

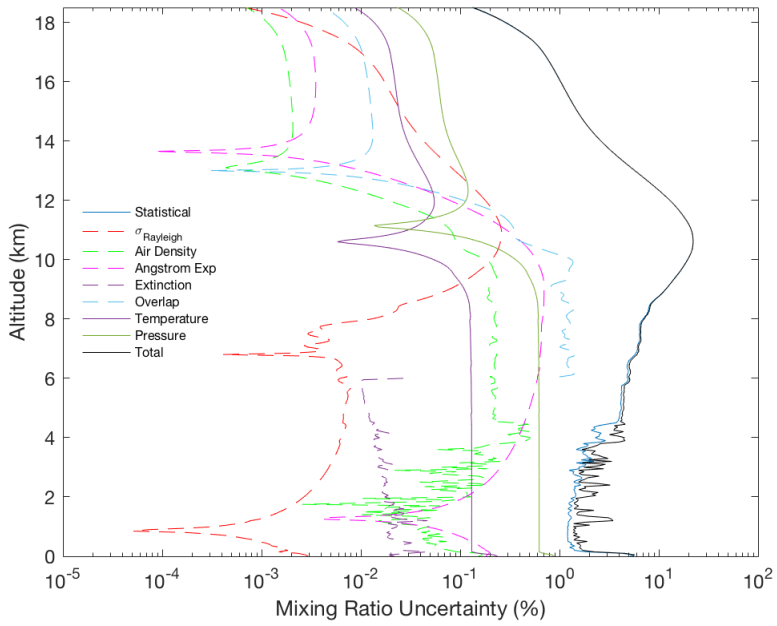

Figure 7.8: Uncertainty budget for the integrated retrieval on October 5, 2011 at 22:55 UTC.

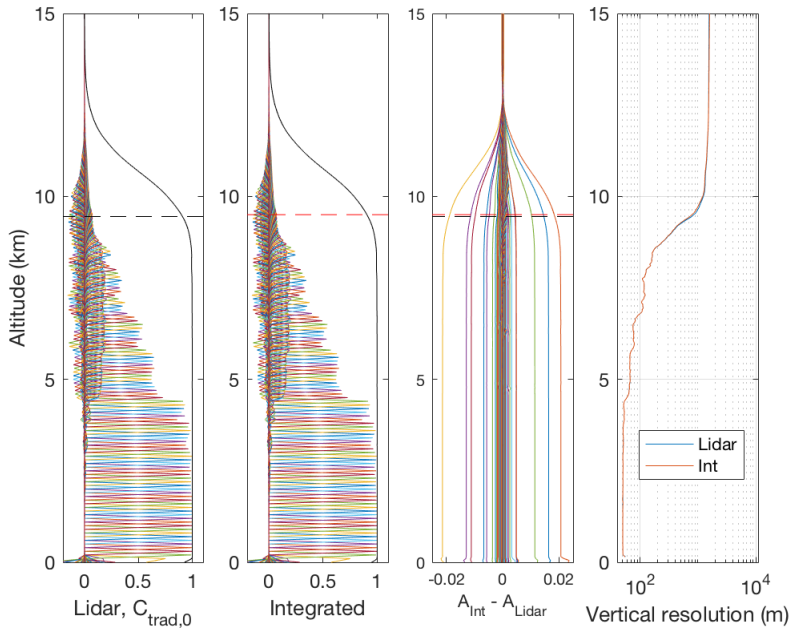

Figure 7.9: Mixing ratio averaging kernels (left 3 plots) and vertical resolution (right plot) on October 5, 2011 at 22:55 UTC for the lidar, *Lidar*0, (left) and integrated (second from the left) retrievals, with the difference between them (third from the left). The horizontal dashed line indicates the height at which the response is 0.9.

retrievals and the lidar retrievals where the calibration factor is not retrieved directly are able to identify the same profile structures, and have magnitudes within 10% of each other. The lidar retrieval where this factor is retrieved (the light blue trend, labeled as *Lidar*1 in these plots) again has a similar shape to the non-radiometer retrievals, but is approximately 55% larger for the first 7 km (Figure 7.10, top right plot). The integrated retrievals, on the other hand, are 3.7% and 2.3% smaller than the traditionally-calibrated lidar retrieval when using uncorrected and corrected brightness temperature measurements, respectively. Both calibration factors retrieved by the integrated retrievals are within the uncertainty bounds of the traditional and trajectory lidar methods, with the corrected integrated retrieval factor slightly closer to the radiosonde-derived calibration factors, relative to the uncorrected integrated retrieval factor (Figure 7.10, bottom right plot). This result is consistent with the radiometer retrievals shown in Figure 7.4, where the bias correction improves the retrieval. Again, the degrees of freedom are slightly larger for the integrated retrievals compared to the lidar retrievals, resulting in averaging kernels (Figure 7.11) which have even smaller residuals than the October 5, 2011 data, where both retrievals reach a kernel value of 0.9 at 9.95 km.

The retrievals for the night of April 23, 2013 are shown in Figure 7.12. Of the 5 nights sampled here, this night has an integrated retrieval of mixing ratio which is closest to the radiosonde as well as the lidar retrieval profile, with a 1.5% difference in the first 5 km when the uncorrected brightness temperatures are used (the difference is 2.8% when the corrected measurements are considered). This small difference in the mixing ratio profile is also reflected in the calibration factor, where the integrated value is within 0.4% of the traditionally-calibrated lidar retrieval of Hicks-Jalali et al. 2019. The calibration factor retrieved by the lidar retrieval (*Lidar1* method) is 41.74, which differs from the Trajectory method factor by merely 0.7%. However, the retrieval uncertainty associated with this factor is 20.87, which is about 36 times larger than the calibration factor uncertainty of the integrated retrieval. As with the prior dates, the degrees of freedom as well as the 0.9 averaging kernel height are slightly higher for the integrated retrieval, with respect to the lidar retrievals (Figure 7.13), causing a response of 0.9

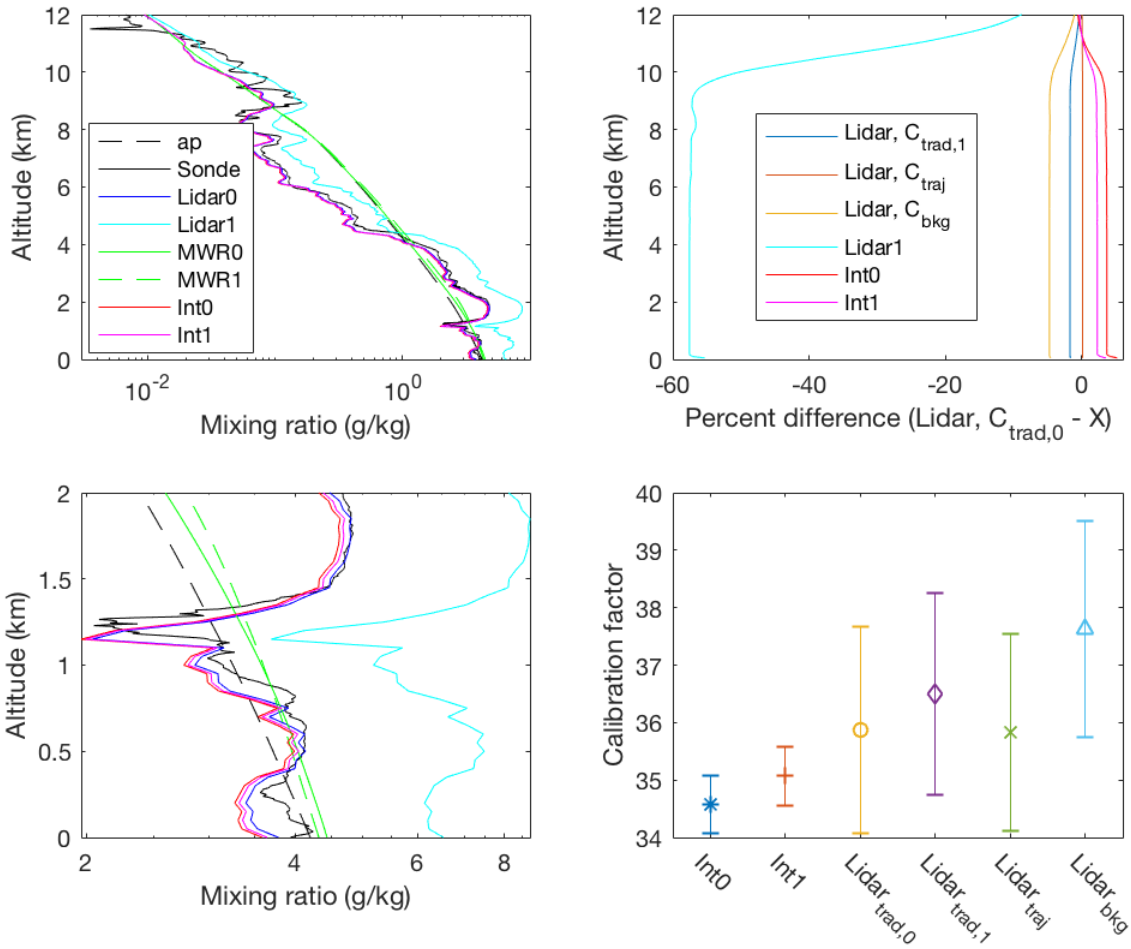

Figure 7.10: Retrievals from February 28, 2012 at 22:57 UTC for 30 minutes. (Left) Mixing ratio retrievals via different retrieval methods up to 12 km (top) and 2 km (bottom). *ap* is the *a priori* profile, from the US Standard Atmosphere and *Sonde* is the radiosonde profile. *Lidar0* is the lidar retrieval where $\eta = C_{trad,0}$, while *Lidar1* retrieves this value. *MWR0* and *Int0* are the radiometer and integrated retrievals, where no bias correction is performed, whereas *MWR1* and *Int1* have the bias correction for brightness temperatures. (Top right) Percent differences in the retrieved mixing ratios, compared to *Lidar0*, where $C_{trad,1}$, C_{traj}, and C_{bkg} are the Lidar retrievals with calibration factors determined by the traditional, trajectory, and solar background calibration methods, respectively. (Bottom right) Calibration factors during this observation.

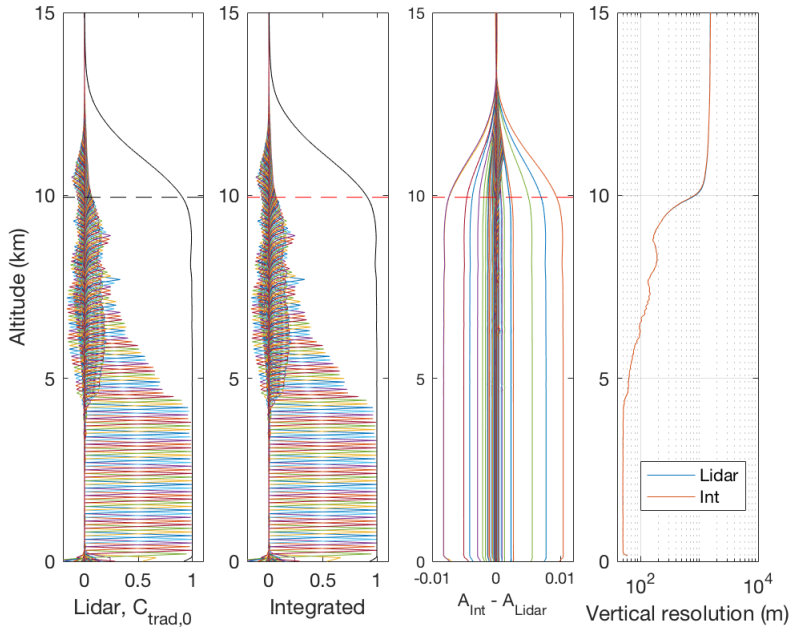

Figure 7.11: Mixing ratio averaging kernels (left 3 plots) and vertical resolution (right plot) on February 28, 2012 at 22:57 UTC for the lidar, *Lidar*0, (left) and integrated (second from the left) retrievals, with the difference between them (third from the left). The horizontal dashed line indicates the height at which the response is 0.9.

to extend slightly higher, reaching a negligibly higher height of 9.30 km as opposed to 9.25 km (an increase of 1 grid point).

For the radiometer retrieval using measurements from January 22, 2014, the use of corrected brightness temperatures vastly improved the outcome of the retrieval, compared to a retrieval via raw measurements. A similar outcome is seen with the integrated retrieval (Figure 7.14), where the difference between the bias-corrected integrated retrieval humidity and the lidar retrieval is only 2.8%, as opposed to 8.0% with the uncorrected integrated retrieval. This is also reflected in the calibration factor, where the corrected factor is within the uncertainty bounds of the radiosonde-derived values, but the uncorrected factor is much larger. For this date, the degrees of freedom are actually slightly lower for the integrated retrieval compared with the lidar retrieval. However, the integrated retrieval averaging kernels (Figure 7.15) reach a value of 0.9 at 7.20 km versus 7.10 km for the lidar retrieval, a difference of 2 retrieval grid points.

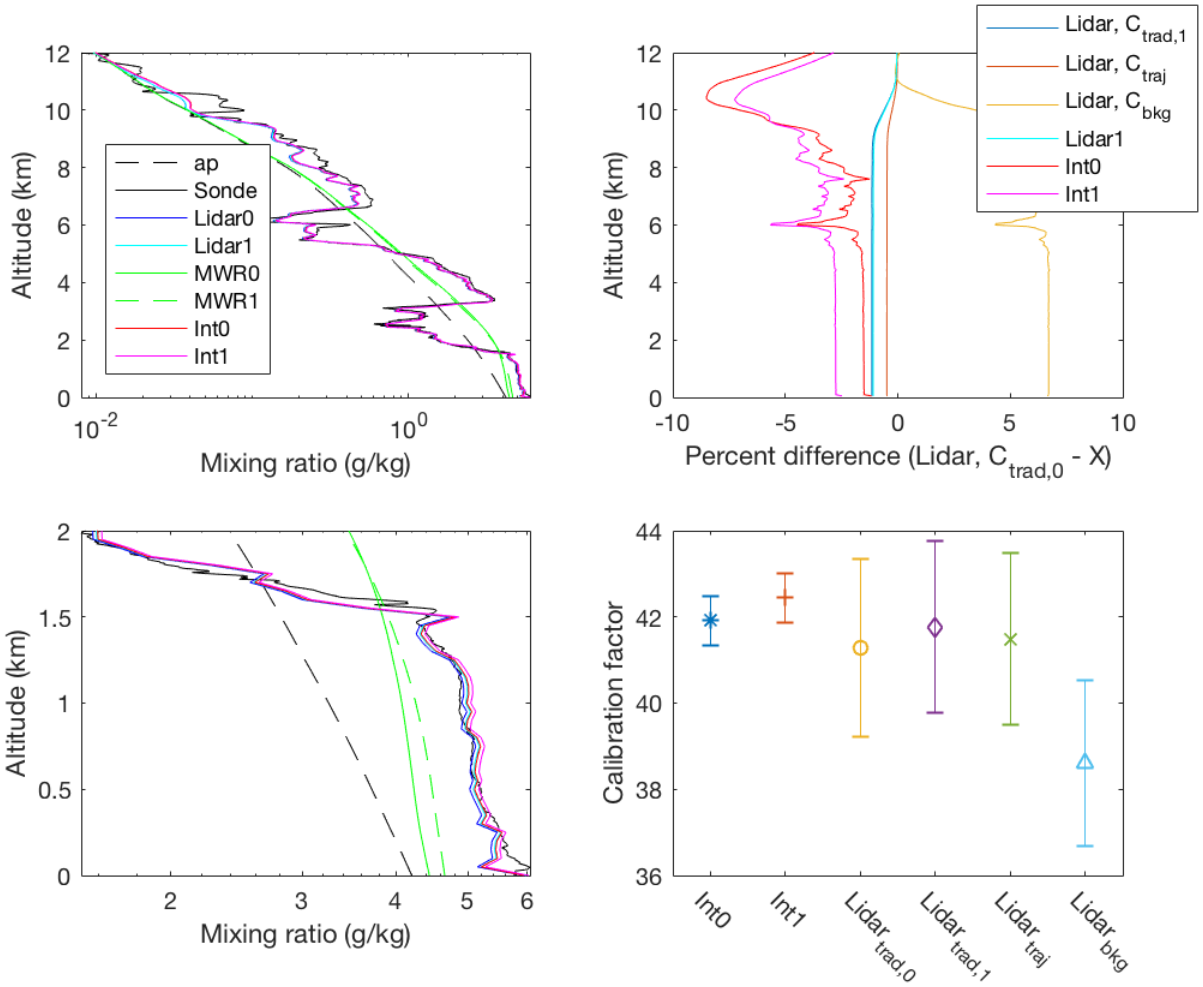

Figure 7.12: Retrievals from April 23, 2013, 22:52 UTC for 30 minutes. (Left) Mixing ratio retrievals via different retrieval methods up to 12 km (top) and 2 km (bottom). *ap* is the *a priori* profile, from the US Standard Atmosphere and *Sonde* is the radiosonde profile. *Lidar0* is the lidar retrieval where $\eta = C_{trad,0}$, while *Lidar1* retrieves this value. *MWR0* and *Int0* are the radiometer and integrated retrievals, where no bias correction is performed, whereas *MWR1* and *Int1* have the bias correction for brightness temperatures. (Top right) Percent differences in retrieved mixing ratio, compared to *Lidar0*, where $C_{trad,1}$, C_{traj}, and C_{bkg} are the Lidar retrievals with calibration factors determined from the traditional, trajectory, and solar background calibration methods, respectively. (Bottom right) Calibration factors during this observation.

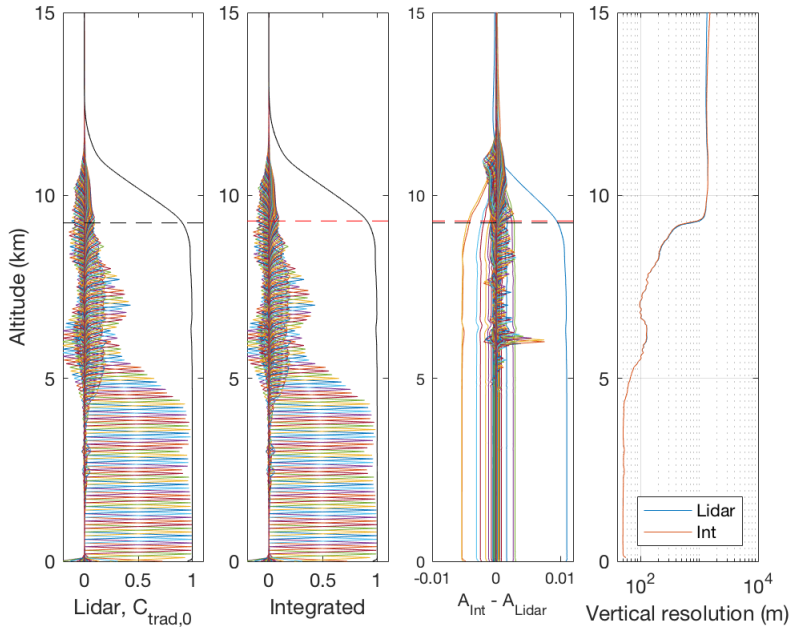

Figure 7.13: Mixing ratio averaging kernels (left 3 plots) and vertical resolution (right plot) on April 23, 2013, 22:52 UTC for the lidar, *Lidar*0, (left) and integrated (second from the left) retrievals, with the difference between them (third from the left). The horizontal dashed line indicates the height at which the response is 0.9.

The night of July 17, 2014 shows the importance of checking the radiometer retrieval outcome before conducting an integrated retrieval. As discussed in Section 7.1.1, the radiometer retrieval for this night boasts an unusual cubic spline shape in the attempt to fit the data, which largely underestimates the humidity below 3 km and overestimates it above 3 km. This effect is translated to the integrated retrieval (Figure 7.16), where although the integrated retrieval's shape is similar to the radiosonde profile and lidar retrieval, it is offset by 39%. Correspondingly, their calibration factors are substantially lower than the radiosonde or Solar background-derived values. This night was unusual, as although conditions were clear, the lidar signal was low. As a result, the lidar retrieval averaging kernels (Figure 7.17) are substantially shorter than those previously displayed, as the signal-to-noise ratio drops off much quicker. However, the noise registered in the integrated retrieval above 3 km inflates its number of degrees of freedom and the averaging kernel response. The integrated retrieval's mixing ratio total uncertainty for this night (Figure 7.18) is also larger than what was determined for the other nights. While

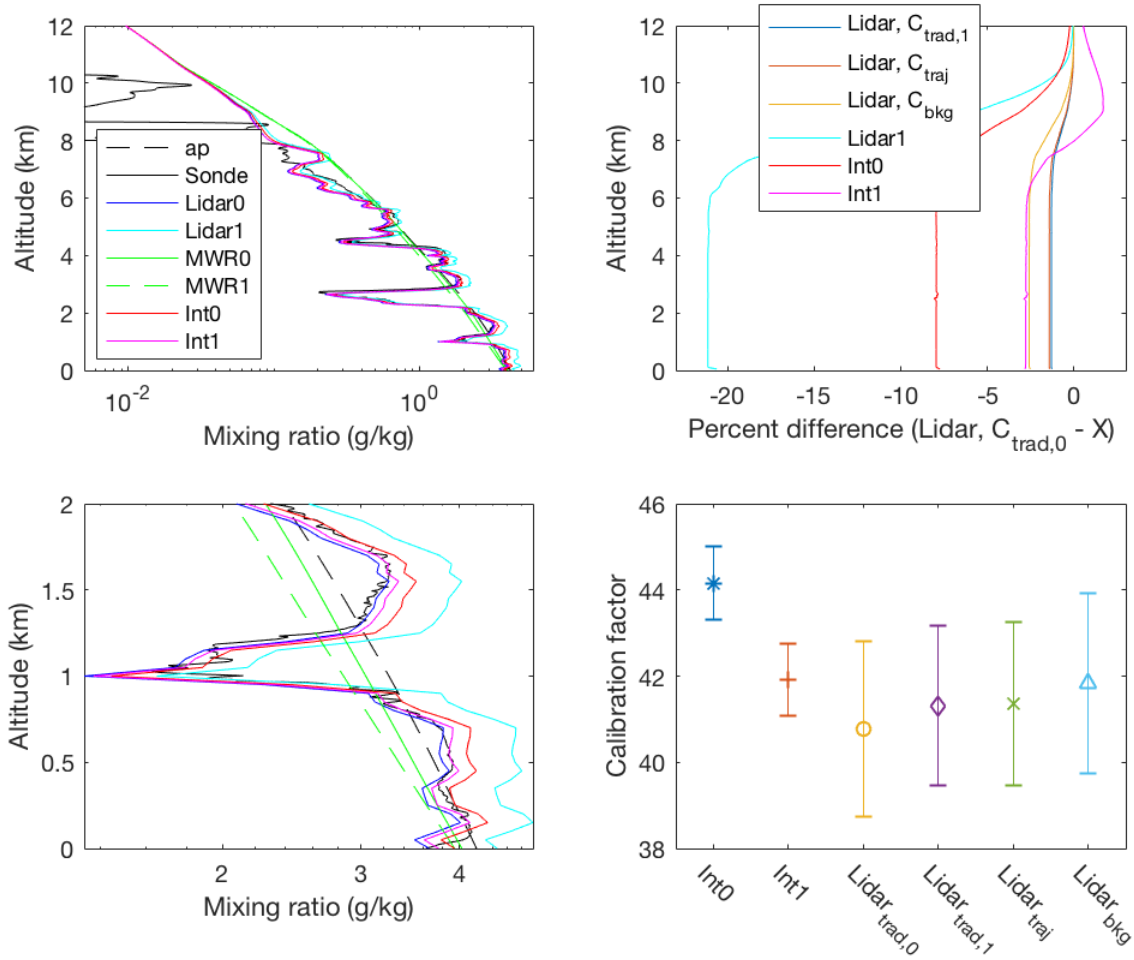

Figure 7.14: Retrievals from January 22, 2014, 22:50 UTC for 30 minutes. (Left) Mixing ratio retrievals via different retrieval methods up to 12 km (top) and 2 km (bottom). *ap* is the *a priori* profile, from the US Standard Atmosphere and *Sonde* is the radiosonde profile. *Lidar0* is the lidar retrieval where $\eta = C_{trad,0}$, while *Lidar1* retrieves this value. *MWR0* and *Int0* are the radiometer and integrated retrievals, where no bias correction is performed, whereas *MWR1* and *Int1* have the bias correction for brightness temperatures. (Top right) Percent differences in retrieved mixing ratio, compared to *Lidar0*, where $C_{trad,1}$, C_{traj}, and C_{bkg} are Lidar retrievals with calibration factors determined from the traditional, trajectory, and solar background methods, respectively. (Bottom right) Calibration factors during this observation.

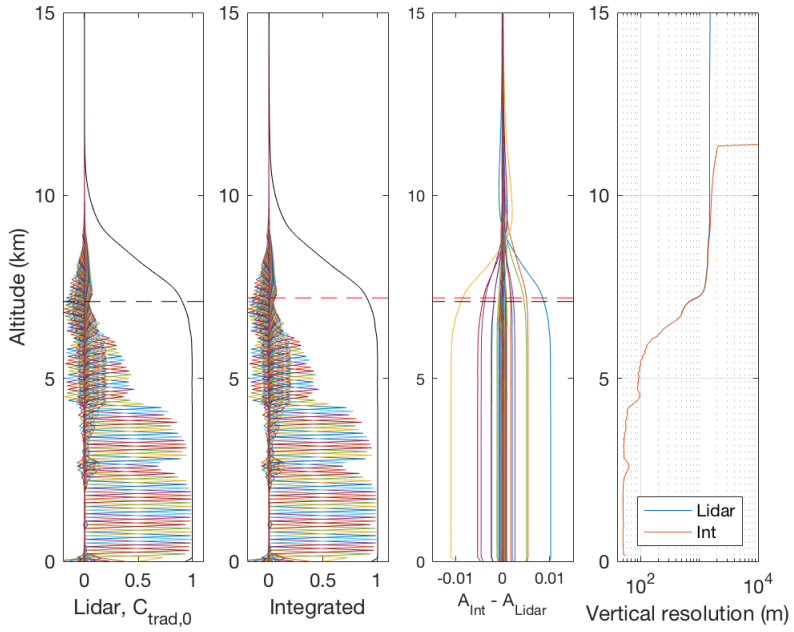

Figure 7.15: Mixing ratio averaging kernels (left 3 plots) and vertical resolution (right plot) on January 22, 2014, 22:50 UTC for the lidar, *Lidar*0, (left) and integrated (second from the left) retrievals, with the difference between them (third from the left). The horizontal dashed line indicates the height at which the response is 0.9.

the total uncertainty for October 5 (Figure 7.8) was between 2 and 6% for the first 5 km, the total uncertainty for July 17th is around 7% at 2 km, increasing to nearly 20% at 5 km. The increased uncertainty for this date seems to be due largely to the Rayleigh cross section.

7.2 Clear Day case

The previous section dealt only with measurements from clear nights. During the day, lidar signal-to-noise ratio is severely reduced due to the large solar background.

As seen in the 14 hour trend (Figure 7.19a, top), there is an significant increase in the lidar count rates around 04:00 UTC as the Sun rises. 30-minute scan average profiles from nighttime measurements (22:50 UTC) and daytime measurements (11:00 UTC) are also displayed (Figure 7.19a, bottom), representing observations near solar midnight and noon for the Payerne site, respectively. Between the night and daytime observations, backgrounds for the analog

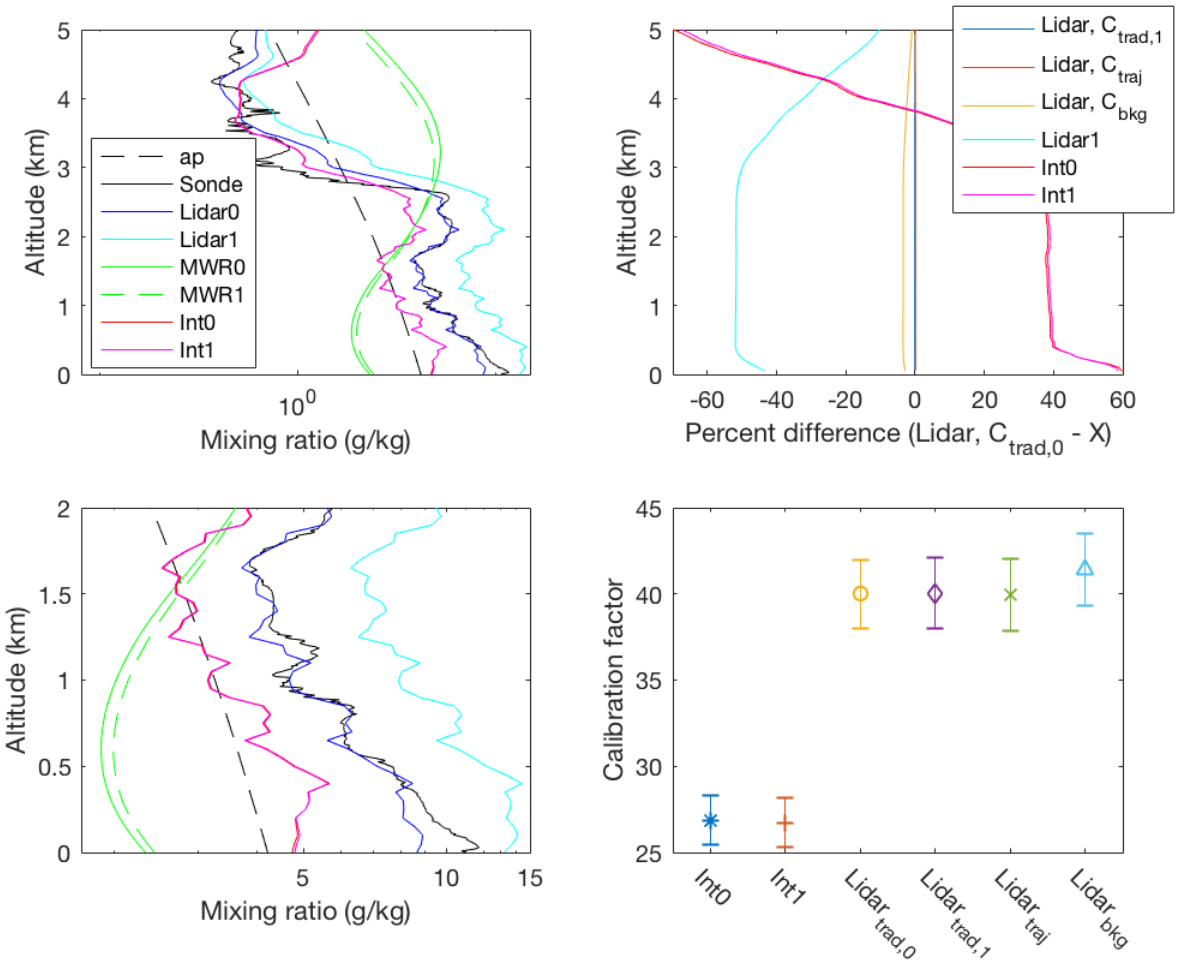

Figure 7.16: Retrievals from July 17, 2014, 22:55 UTC for 30 minutes. (Left) Mixing ratio retrievals via different retrieval methods up to 6 km (top) and 2 km (bottom). *ap* is the *a priori* profile, from the US Standard Atmosphere and *Sonde* is the radiosonde profile. *Lidar0* is the lidar retrieval where $\eta = C_{trad,0}$, while *Lidar1* retrieves this value. *MWR0* and *Int0* are the radiometer and integrated retrievals, where no bias correction is performed, whereas *MWR1* and *Int1* have the bias correction for brightness temperatures. (Top right) Percent differences in retrieved mixing ratio, compared to *Lidar0*, where $C_{trad,1}$, C_{traj}, and C_{bkg} are Lidar retrievals with calibration factors determined from the traditional, trajectory, and solar background methods, respectively. (Bottom right) Calibration factors during this observation.

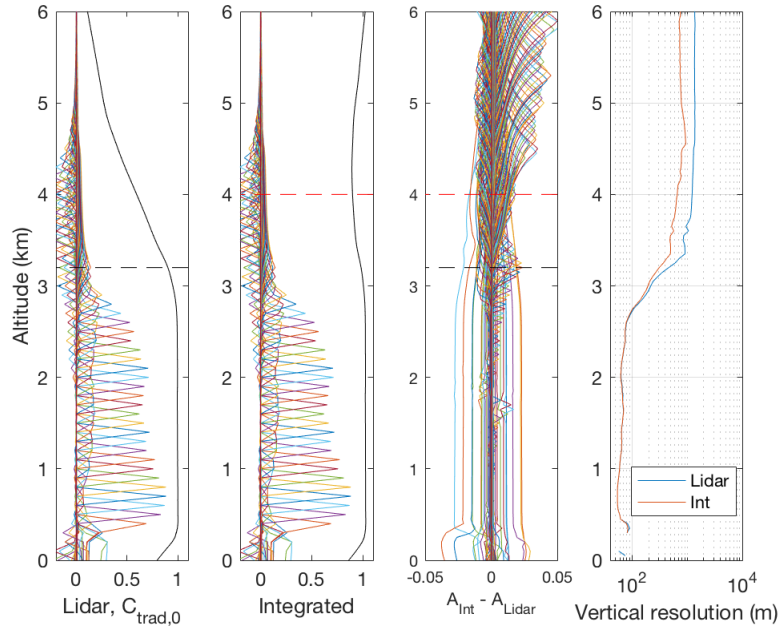

Figure 7.17: Mixing ratio averaging kernels (left 3 plots) and vertical resolution (right plot) on July 17, 2014 at 22:55 UTC for the lidar, *Lidar*0, (left) and integrated (second from the left) retrievals, with the difference between them (third from the left). The horizontal dashed line indicates the height at which the response is 0.9.

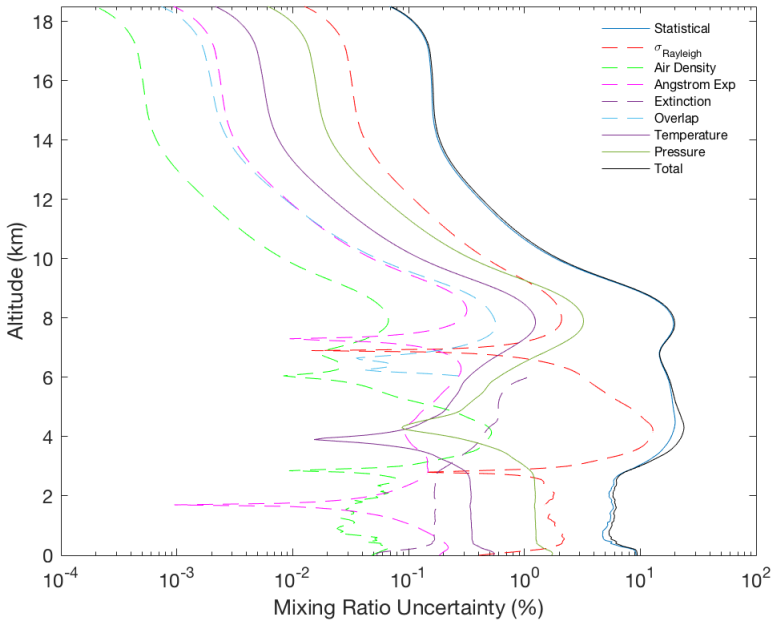

Figure 7.18: Uncertainty budget for the integrated retrieval on July 17, 2014 at 22:55 UTC.

Date	Mode	$Tbcor$?	$\hat{\eta}$?	cost	η	IWV PD	DOF
2011.10.05 22:55	Int	No	-	1.61	35.69±0.49	10.2	126.59
2011.10.05 22:55	Int	Yes	-	1.94	35.6±0.49	10.5	126.62
2011.10.05 22:55	Lidar, $C_{trad,1}$	-	No	1.58	38.61±1.74	2.2	126.47
2011.10.05 22:55	Lidar, C_{traj}	-	No	1.58	38.42±2.07	2.7	126.47
2011.10.05 22:55	Lidar, C_{bkg}	-	No	1.58	36.06	9.0	126.5
2011.10.05 22:55	Lidar1	-	Yes	1.58	46.79±23.4	16.9	126.36
2011.10.05 22:55	MWR	Yes	-	5.18	-	9.2	1.74
2011.10.05 22:55	MWR	Yes	-	109.18	-	8.4	1.73
2012.02.28 22:57	Int	No	-	1.01	34.58±0.5	8.8	125.13
2012.02.28 22:57	Int	Yes	-	1.01	35.07±0.51	7.3	125.11
2012.02.28 22:57	Lidar, $C_{trad,1}$	-	No	1.00	36.5±1.75	3.4	125.07
2012.02.28 22:57	Lidar, C_{traj}	-	No	1.00	35.83±1.72	5.2	125.08
2012.02.28 22:57	Lidar, C_{bkg}	-	No	1.00	37.62	0.3	125.05
2012.02.28 22:57	Lidar1	-	Yes	1.00	64.85±32.43	52.8	124.71
2012.02.28 22:57	MWR	No	-	3.64	-	11.3	1.65
2012.02.28 22:57	MWR	Yes	-	1.57	-	8.1	1.67
2013.04.23 22:52	Int	No	-	1.01	41.92±0.57	2.2	119.28
2013.04.23 22:52	Int	Yes	-	1.00	42.45±0.57	1.0	119.25
2013.04.23 22:52	Lidar, $C_{trad,1}$	-	No	0.99	41.77±2.0	2.6	119.07
2013.04.23 22:52	Lidar, C_{traj}	-	No	0.99	41.49±1.99	3.3	119.07
2013.04.23 22:52	Lidar, C_{bkg}	-	No	0.99	38.61	10.4	119.2
2013.04.23 22:52	Lidar1	-	Yes	0.99	41.74±20.87	2.7	119.07
2013.04.23 22:52	MWR	No	-	6.28	-	1.3	1.72
2013.04.23 22:52	MWR	Yes	-	4.73	-	0.3	1.73
2014.01.22 22:50	Int	No	-	1.13	44.15±0.85	3.5	93.49
2014.01.22 22:50	Int	Yes	-	1.13	41.93±0.84	1.7	93.47
2014.01.22 22:50	Lidar, $C_{trad,1}$	-	No	1.13	41.31±1.86	3.1	93.5
2014.01.22 22:50	Lidar, C_{traj}	-	No	1.13	41.36±1.9	3.0	93.5
2014.01.22 22:50	Lidar, C_{bkg}	-	No	1.13	41.84	1.9	93.5
2014.01.22 22:50	Lidar1	-	Yes	1.13	50.42±25.21	16.6	93.41
2014.01.22 22:50	MWR	No	-	1.12	-	4.6	1.6
2014.01.22 22:50	MWR	Yes	-	0.42	-	2.0	1.57
2014.07.17 22:55	Int	No	-	0.89	26.87±1.43	6.5	41.6
2014.07.17 22:55	Int	Yes	-	0.87	26.72±1.42	10.2	41.33
2014.07.17 22:55	Lidar, $C_{trad,1}$	-	No	0.76	40.05±2.08	0.3	37.39
2014.07.17 22:55	Lidar, C_{traj}	-	No	0.76	39.93±2.08	0.6	37.39
2014.07.17 22:55	Lidar, C_{bkg}	-	No	0.76	41.41 ±	2.9	37.36
2014.07.17 22:55	Lidar1	-	Yes	0.76	68.06±34.06	48.2	37.01
2014.07.17 22:55	MWR	No	-	33.67	-	5.7	1.71
2014.07.17 22:55	MWR	Yes	-	27.25	-	9.3	1.71

Table 7.1: Summary of clear night retrieval results. *Mode* is the type of retrieval (Int=integrated, MWR=radiometer, lidar $C_{trad,1}/C_{traj}/C_{bkg}$ use calibration factors from traditional/trajectory/solar background methods, while Lidar1 retrieves the factor), $Tbcor$? is whether bias-corrected brightness temperatures are used. η and $\hat{\eta}$? are the calibration constant and if the lidar mode retrieves it directly. *IWV PD* is the percent difference between the retrieved and radiosonde humidity profiles. *DOF* is the number of degrees of freedom.

water vapor and nitrogen channels increase by approximately 60% and 5%, respectively. The PC channel backgrounds, on the other hand, are far more sensitive, increasing by a factor of 6.7×10^5 for water vapor and 8.4×10^4 for nitrogen. While the analog signal peaks increase proportionally with the background intensity, the PC signals only increase by a factor of 20 and 1.3 for water vapor and nitrogen channels, respectively, during the day. As a result, the signal-to-noise ratio above the lowest altitude range is greatly reduced, causing daytime retrievals to generally have a maximum height of only 4 km [7]. The brightness temperatures measured by the radiometer, on the other hand, do not experience the diurnal shifts seen in lidar count rates, varying only slightly over the course of the day (Figure 7.19b).

The reduction in range of the retrieval is demonstrated with a comparison of the averaging kernels from night and day observations in Figure 7.20. As previously shown in Figure 7.13, the integrated method retrieves well up to around 9.3 km during the night. However, near solar noon, an averaging kernel response function of 0.9 is encountered at 5.3 km. The daytime vertical resolution begin to degrade at a much lower altitude than that at night. In addition to a reduced retrieval range, there is also an increase in the relative statistical and systematic uncertainties for mixing ratio during the day (Figure 7.21). Although each of the *b-parameter* uncertainties as well as the statistical uncertainties increase, the largest increase is the uncertainty associated with the Rayleigh cross section. It is the smallest source of uncertainty during the nighttime retrieval over much of the range. However, cross section is proportional to background intensity, with much more scattering during the day, causing the Rayleigh cross section uncertainty to grow by a few orders of magnitude and becoming one of the largest contributions around 6 km.

A comparison between the retrieval methods on daytime measurements is shown in Figure 7.22. The integrated profile is within 30% of the radiosonde humidity profile for the first 3 km, but experiences larger variations above that height. As with the previous examples, the integrated and lidar retrievals are the roughly the same shape, but are offset from each other, with the lidar-retrieved profiles being between 20% and 35% smaller than the integrated re-

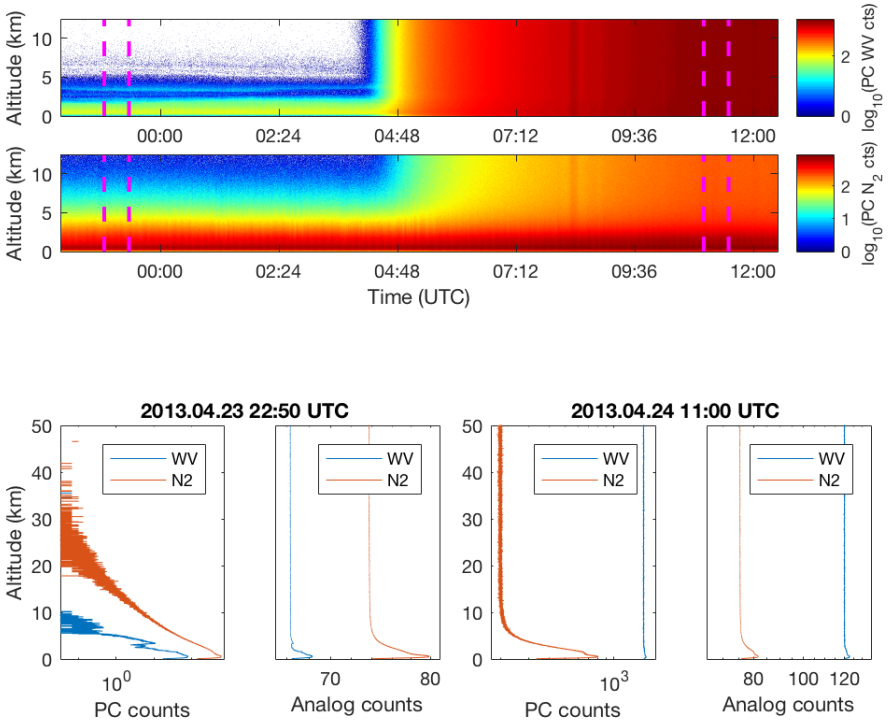

(a)

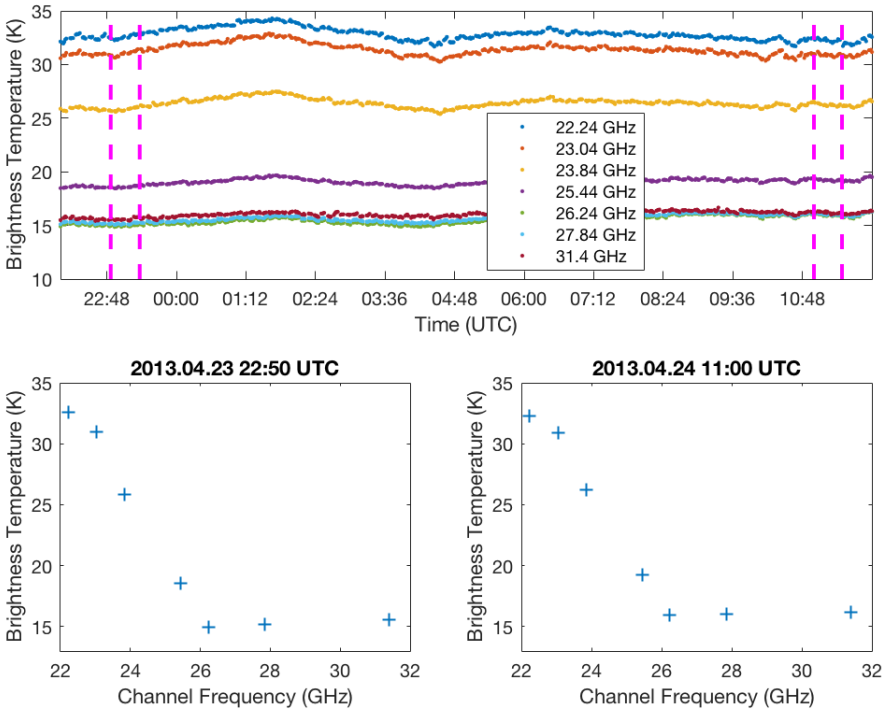

(b)

Figure 7.19: Raw measurements of lidar PC water vapor and nitrogen signal (a) and radiometric brightness temperatures (b) between 2013.04.23 22:00 and 2013.04.24 12:30 UTC. The plots below the time trends provide averaged profiles of the measurements in the 30 minute time periods indicated by the vertical dashed lines.

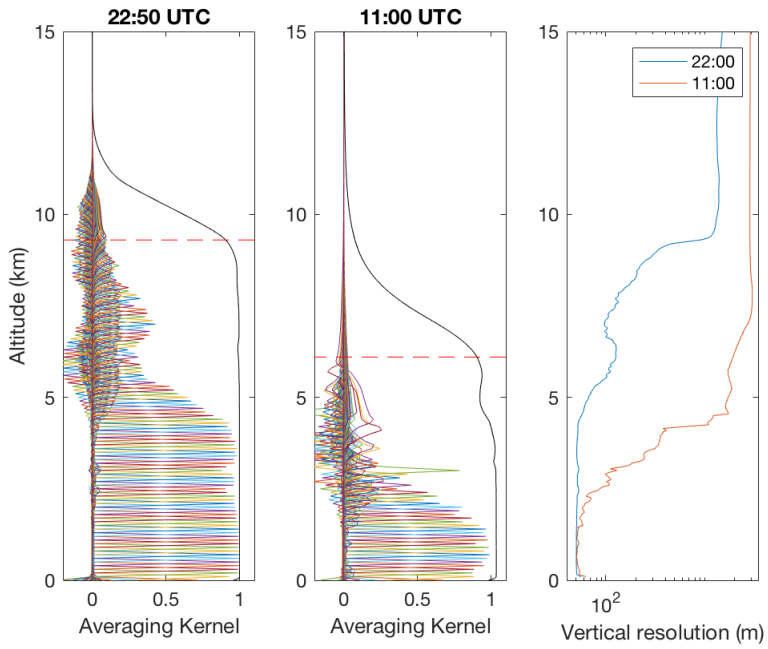

Figure 7.20: Averaging kernels via integrated retrievals at 22:50 on April 23 (left) and 11:00 UTC on April 24 (middle). Vertical resolution for both dates in the right plot.

trieval profile for the lowest 4 km. Above this height, there is a divergence as the integrated retrieval sees a sizable bump in humidity possibly due to sampling a different air mass than the radiosonde, with a maximum difference of approximately 70% at 6 km, above which the profile gradually falls back to the *a priori* profile.

Relative to the retrievals from the previous night (April 24, 2013 at 00:00 UTC, previously shown in Figure 7.12), the radiosonde-calibrated lidar retrievals do not follow the coincidental radiosonde profile, nor the integrated retrieval profile, as closely. This observation is reasonable, as these lidar retrievals use calibration factors determined from coincidence with the nighttime radiosonde instead of the daytime one. Section 7.3.1 examines the differences between nighttime and daytime calibration factors in more detail.

Although the effective range of the integrated retrieval is significantly smaller during the day than at night, it is still noticeably larger than the range for the lidar retrieval. As seen in Figure 7.23, use of the integrated retrieval extends the daytime range by nearly 1 km due to the contributions of the integrated retrieval's averaging kernels in the upper portion of the retrieval.

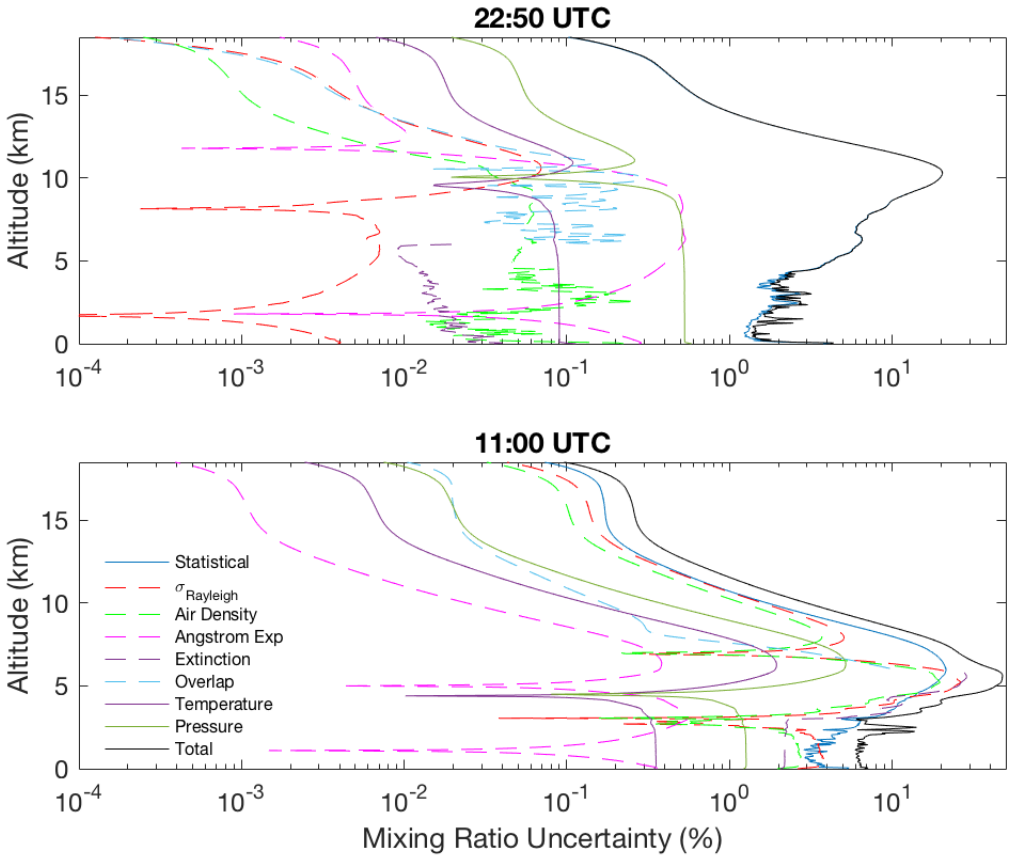

Figure 7.21: Uncertainty percentages via integrated retrievals at 22:50 on April 23 (top) and 11:00 on April 24 (bottom).

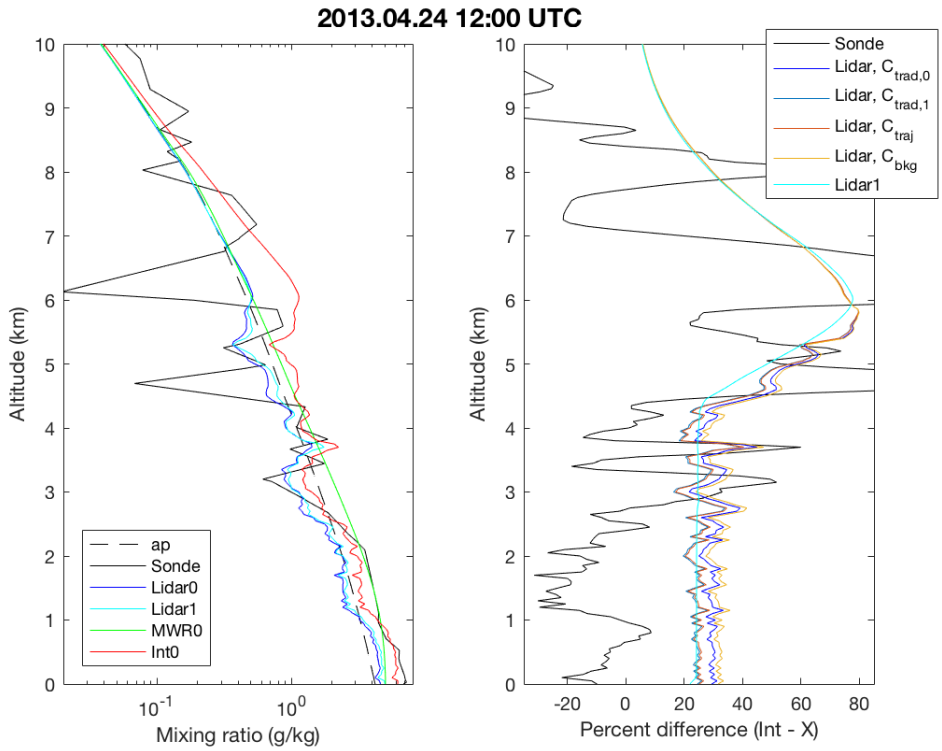

Figure 7.22: Retrievals from April 24, 2013, at 12:00 UTC for 30 minutes. (Left) Mixing ratio retrievals via different retrieval methods up to 10 km. *ap* is the *a priori* profile, from the US Standard Atmosphere and *Sonde* is the radiosonde profile. *Lidar0* is the lidar retrieval where $\eta = C_{trad,0}$, while *Lidar1* retrieves this value. *MWR0* and *Lidar0* are the radiometer and integrated retrievals, where no bias correction is performed. (Right) Percent differences in retrieved mixing ratio, compared to the integrated retrieval, where *Sonde* is a radiosonde profile, and C_{trad}, C_{traj}, and C_{bkg} are Lidar retrievals with calibration factors determined from the traditional, trajectory, and solar background methods, respectively.

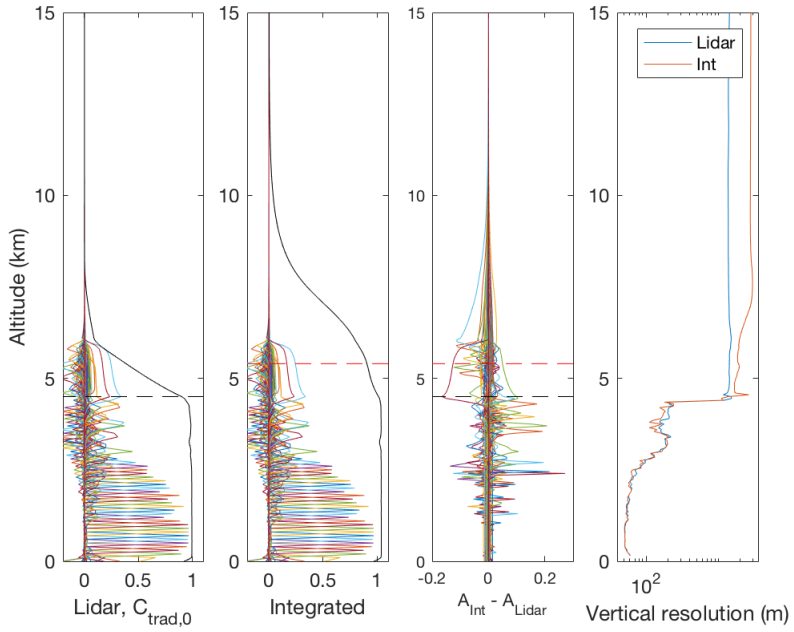

Figure 7.23: Averaging kernels for the *Lidar*0 (left) and integrated (second from the left) retrievals, with the difference between them (third from the left). The horizontal dashed line indicates the height at which the response is 0.9. The vertical resolution for both retrievals is in the right plot.

7.3 Diurnal Variations in the Calibration Constant

For investigating trends over a 24-hour period, we first present measurements from April 24, 2013, as it was a clear date with a GRUAN-corrected radiosonde launch at 22:50 UTC on April 23. Retrievals were run between April 23 at 22:00 UTC and April 25 at 00:30 UTC. Trends of the mixing ratio over this time period are provided in Figure 7.24. The integrated and lidar retrievals are both able to capture similar features, such as the moist layer at 4 km for the first 10 hours. However, they differ in the magnitude of the mixing ratio, where the integrated retrieval is 1.5% larger than the lidar retrieval in the lowest 2 km at 00:00 UTC (Figure 7.12) and 25% larger in the lowest 5 km during the day (Figure 7.22). Due to its much coarser retrieval resolution, the radiometer varies little with time and is not able to identify the moist layer.

Figure 7.25 presents the degrees of freedom for each of the retrievals over the course of

this 24 hour period. As shown in the top plot, the integrated and lidar retrievals are all similar in that they start out with nearly 120 degrees of the freedom at night, rapidly dropping during to around 50 the day. As the brightness temperature measurements do not have the dramatic diurnal cycle seen in lidar counts, the radiometer retrieval is stable, with variation in its number of degrees of freedom of less than 2% over this same period. Since the number of radiometric degrees of freedom is quite low compared to the lidar degrees of freedom, it has only a minor effect for nighttime integrated retrievals. However, during the day when the lidar degrees of freedom fall, the radiometer contributes more proportionally, increasing the total by up to 2 degrees of freedom for this day.

7.3.1 Calibration factor trends

In addition to monitoring humidity profiles over time, running retrievals over 24 hour periods can also gauge possible change in the lidar calibration factor. The radiosonde and Solar background calibrations can only calibrate when radiosondes are present or the Sun is at a particular position. The integrated retrieval presented in this thesis has the distinct advantage of retrieving the channel-dependent lidar constants, allowing for the determination of the calibration factor each time the retrieval is executed.

Monitoring these derived calibration factors over longer periods provides an interesting perspective of diurnal variation of the factor. This trend, shown in Figure 7.26a, is provided for each of the retrieval methods. The retrievals using externally-calibrated factors each have trends that are more or less flat until a new calibration factor is determined. C_{trad} and C_{traj} are based on GRUAN-corrected sondes (in this case, from the beginning of this observation period at 22:52 UTC). The Solar background calibration is carried out when the Sun is at a certain zenith angle. The integrated and Lidar1 retrievals retrieve calibration terms directly, allowing the factor to vary over each retrieval. The *Lidar1* calibration factor does vary with time. However, as there is no calibration in this retrieval, the retrieved factor does not have much physical meaning, providing little in terms of useful information. Additionally, the un-

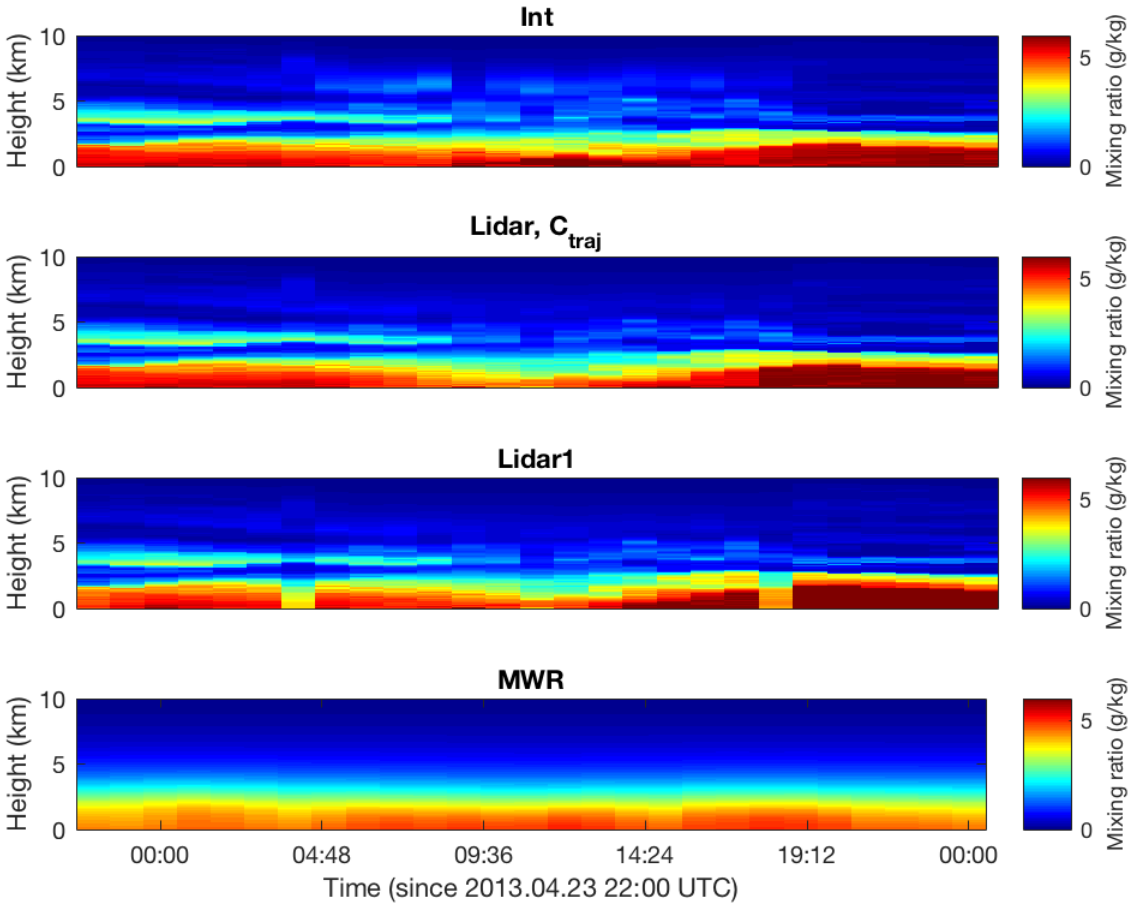

Figure 7.24: Retrieved mixing ratio 24-hour time series. *Int* is the integrated retrieval, *Lidar,* $C_{trad,0}$ is the lidar retrieval where $\eta = C_{trad,0}$, while *Lidar1* retrieves this value. *MWR* is the radiometer retrieval.

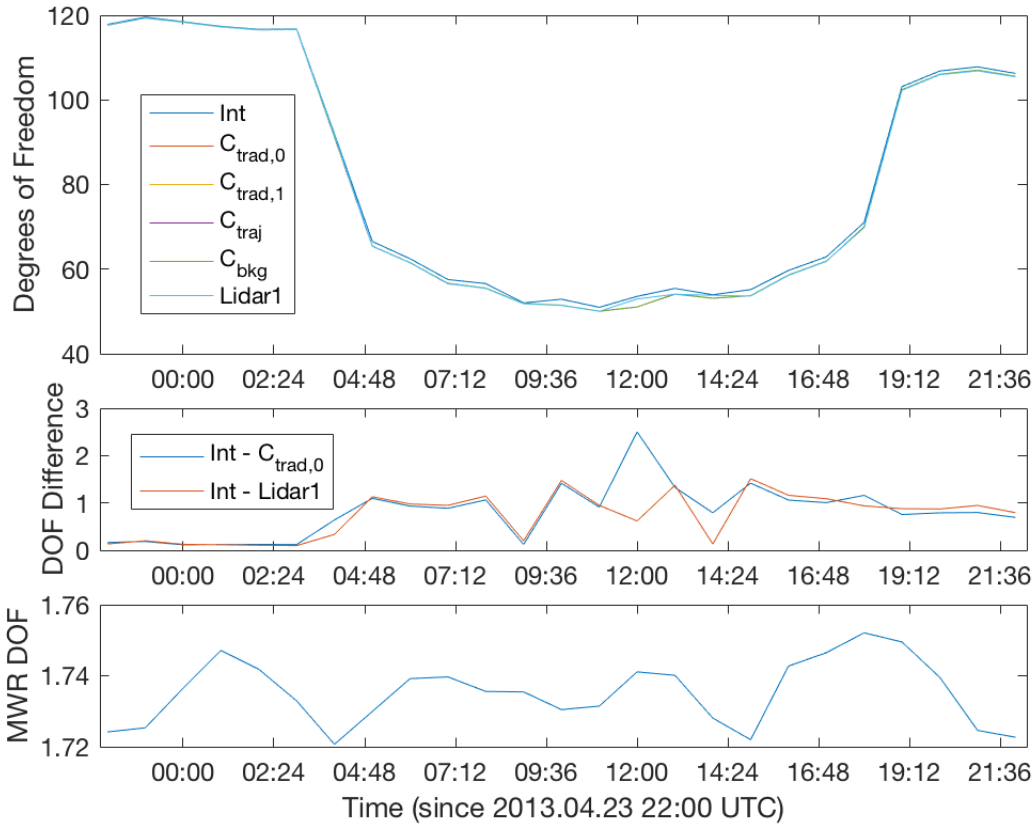

Figure 7.25: Degrees of Freedom as a function of time for April 24, 2013. *Int* and *Lidar1* are the factors retrieved by integrated and lidar retrievals, while C_{trad}, C_{traj}, and C_{bkg} determine this constant via the radiosonde traditional and trajectory methods, and the solar background calibration method, respectively.

certainties associated with the factor for *Lidar1* are substantial, with values around 50% of the retrieved calibration factor, and were not shown in the figure as they would extend well beyond the range of the window. The integrated retrieval, on the other hand, determines a factor that is within the bounds of the GRUAN sonde-determined factor at 22:50 UTC. The trend appears to be correlated with Solar intensity, where the factor begins to increase after 04:00 UTC (coinciding roughly with Civil Twilight), and peaking at 11:00 UTC (coinciding roughly with Solar noon). After peaking at 11:00, the factor drops until 18:00 UTC (just before Civil Twilight again), and again stabilizes over the night.

The importance of using appropriate calibration factors is demonstrated in Figure 7.26b, with the calculation of integrated water vapor for the lidar and integrated retrievals each hour in this period. These values are determined by integrating the retrieved mixing ratio profiles over the entire altitude range. These values are then compared with the integrated water vapor retrieved directly using the HATPRO instrument software retrievals. During the first few hours of night, the integrated water vapor from these 3 sources, as well as that from the coincidental GRUAN-corrected sonde, are all within good agreement. However, as day approaches, the lidar retrieval's integrated water vapor drops, reaching a minimum value at 11:00 UTC and increasing until 18:00 UTC. During the day, the integrated water vapor does not drop for the HATPRO and integrated retrievals, as well as a radiosounding at 12:00 UTC. In fact, the integrated retrieval is well within the uncertainty of the HATPRO retrieval, following many of its small-scale variations.

Similar trends were also plotted for a date in late summer, August 21, 2010, in Figure 7.27. Due to cloudy conditions early on the 21st and later on the 22nd, this sample starts at 10:00 UTC on the August 21, and extends until 10:00 UTC on August 22. As with the previous day, the retrieval experiences a peak calibration factor at 11:00 UTC before dropping until 18:00 UTC. The Solar background calibration is updated at 13:00 UTC, at which point it is in agreement with the factor. This agreement is also seen in Figure 7.27b, where the integrated, lidar, and HATPRO retrievals all agree to within their uncertainties at 13:00 UTC. However, the

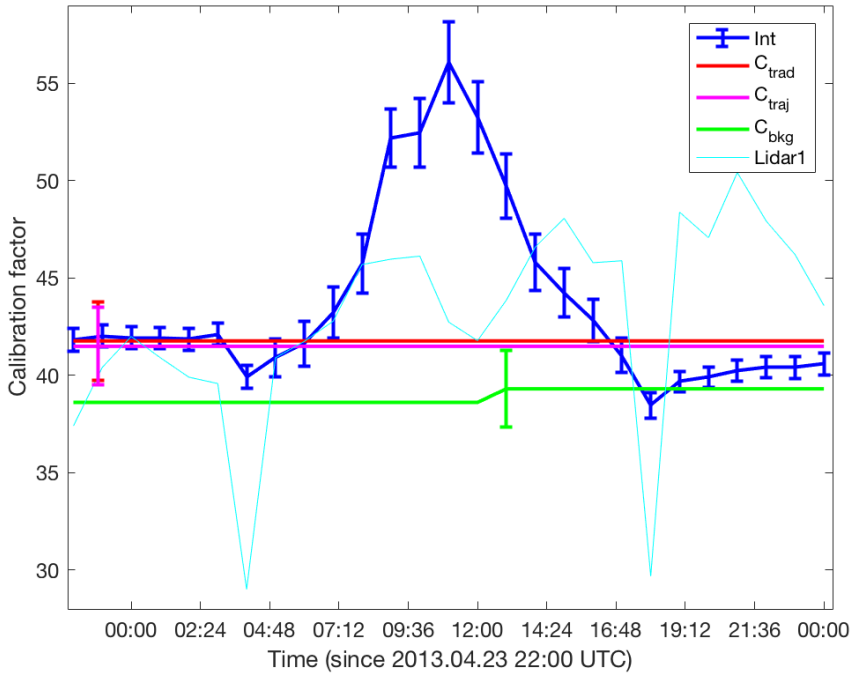

(a)

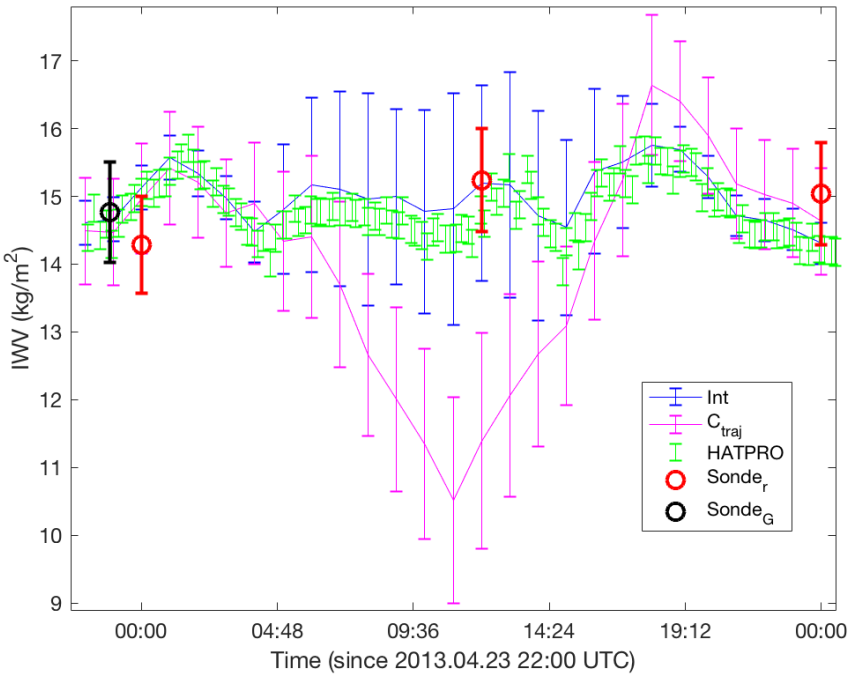

(b)

Figure 7.26: (a) Calibration factor as a function of time. *Int* and *Lidar1* are the factors retrieved by integrated and lidar retrievals, while C_{trad}, C_{traj}, and C_{bkg} determine this constant via the radiosonde traditional and trajectory methods, and the solar background calibration method, respectively. (b) integrated water vapor trends, where *HATPRO* are values retrieved via the HATPRO software. The black, $Sonde_G$, and red, $Sonde_r$, circles are values from GRUAN-corrected and routine radiosonde, respectively.

lidar integrated water vapor value diverges from the HATPRO value later in the day, coinciding with a greater difference from the retrieval's calibration factor, until the factors are again in agreement at 06:00 UTC on August 22.

The two previous dates, in late April and late August, have similar day lengths at approximately 14 hours. To test for possible seasonal effects on the calibration factor diurnal cycle, dates from winter and early summer are also included. A date in winter, with clear-sky observations from February 28, 2012 at 20:00 UTC until March 1 at 00:00 UTC, is given in Figure 7.28. Aside from being a winter date with a relatively short day of approximately 11 hours, it also coincides with a GRUAN-corrected sonde calibration at 22:57 UTC on February 28, 2012. From this time until daybreak, the method-retrieved calibration factor is in reasonable agreement with the Trajectory method's factor. This agreement is also reflected in the integrated water vapor. Although the value fluctuates over the night, the lidar retrieval is still comparable to the and HATPRO retrievals. However, we again see a decrease in the detected lidar's integrated water vapor, relative to the other methods during the day, possibly due to its calibration factor not being representative of the actual daytime calibration factor value. It is also worth noting that for this date, the retrieval's calibration factor does not begin to increase until 06:00 UTC, with a peak at 12:00 UTC (closest to Solar noon for Payerne at this time of year), and then decreasing until 17:00 UTC. Overall, this peak is narrower than the April and August dates, as well as shorter. Relative to the nighttime baseline calibration value, the daytime peak value is an increase of approximately 10% while the April and August dates peak is about 28% larger than their nighttime values.

An example of a summer date is provided in Figure 7.29, representing measurements between June 24, 2010 at 00:00 UTC and 04:00 UTC on June 25, 2010. The integrated retrieval's calibration begins to increase after 03:00, peaking at 11:00, then decreasing until 19:00 UTC, a total time of 16 hours (compared to 11 hours for the February date and 14 hours for the April and August dates). The change in the calibration factor is also larger for this June date, increasing by nearly 39%.

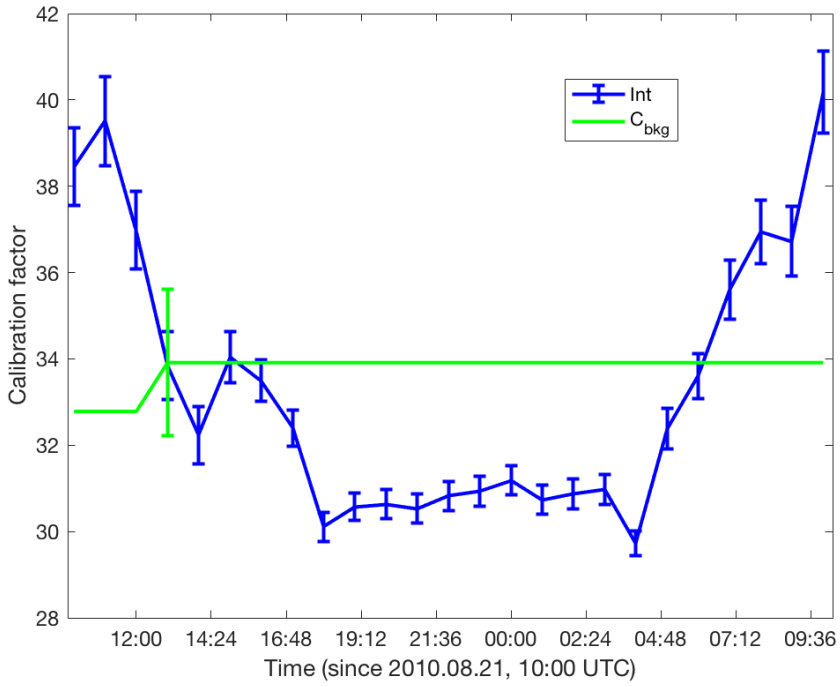

(a)

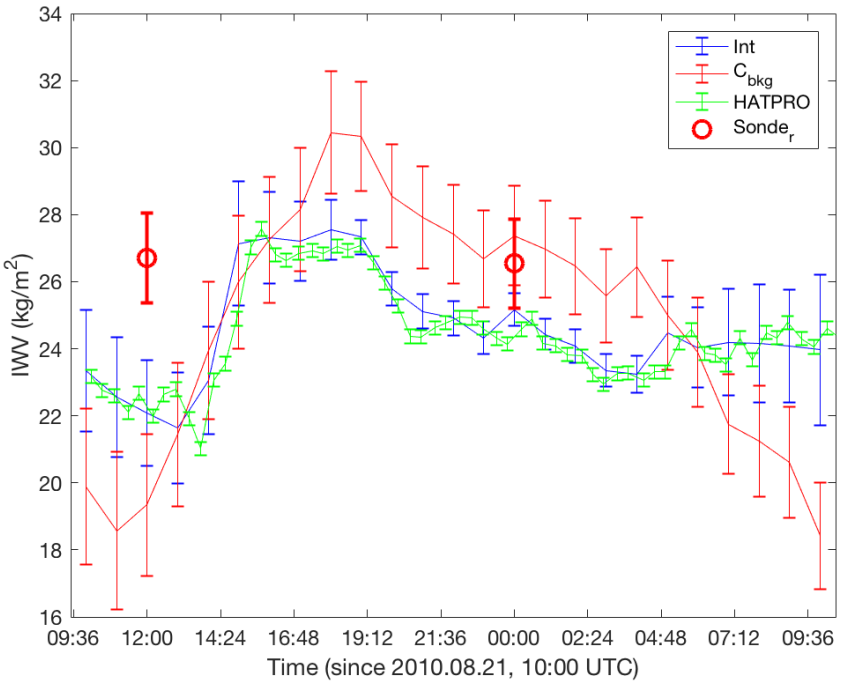

(b)

Figure 7.27: (a) Calibration factor as a function of time for August 21, 2010. *Int* is the factor retrieved by the retrieval, while C_{bkg} determines this constant via the radiosonde traditional method, and the solar background calibration method, respectively. (b) water vapor trends, where *HATPRO* are values retrieved via the HATPRO software. The red circles are values from routine radiosonde.

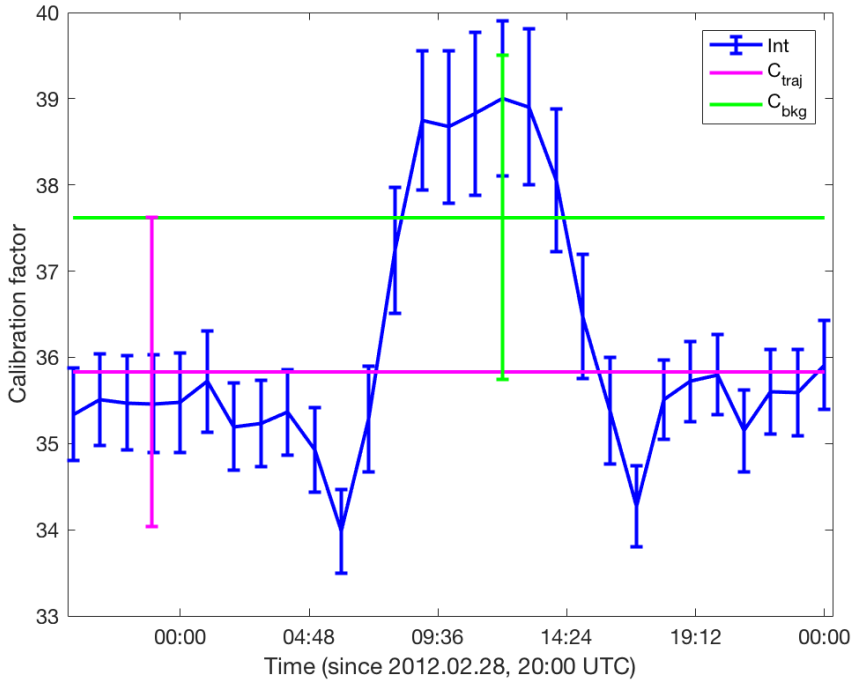

(a)

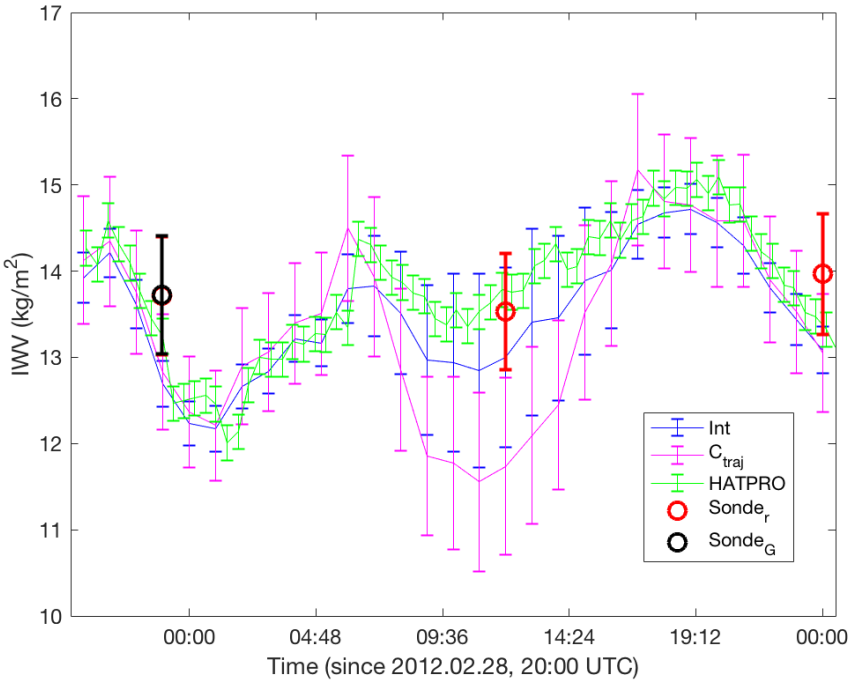

(b)

Figure 7.28: (a) Calibration factor as a function of time for February 29, 2012. *Int* is the factor retrieved by the retrieval, while C_{traj} and C_{bkg} determine this constant via the radiosonde trajectory and Solar background methods. (b) Integrated water vapor trends, where *HATPRO* are values retrieved via the HATPRO software. The black, $Sonde_G$, and red, $Sonde_r$, circles are values from GRUAN-corrected and routine radiosonde, respectively.

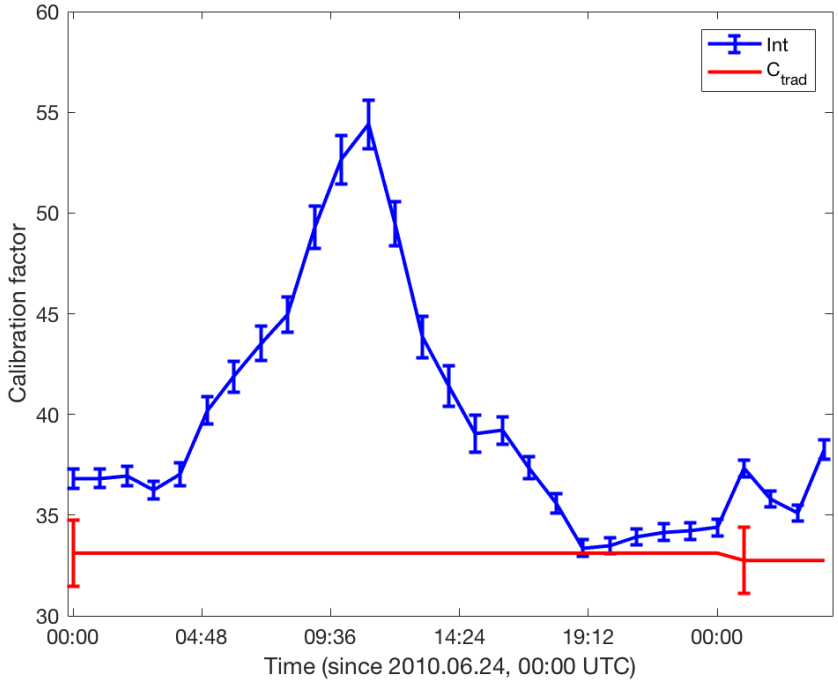

(a)

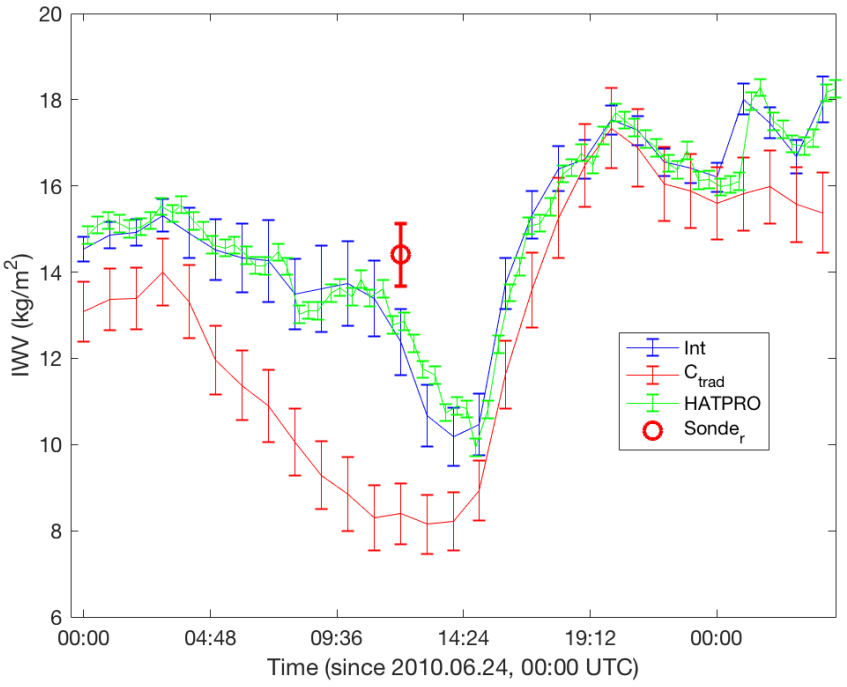

(b)

Figure 7.29: (a) Calibration factor as a function of time for June 24, 2010. *Int* and *Lidar1* are the factors retrieved by and lidar retrievals, while C_{trad} determines this constant via the traditional radiosonde method. (b) Integrated water vapor trends, where *HATPRO* are values retrieved via the HATPRO software. The red circle, $Sonde_r$, is from the routine radiosonde.

Trends in the retrieval's calibration factor do not always have the same characteristics seen in the previous 4 dates. Raw lidar signal from a 24-hour window on January 13, 2015 is shown in Figure 7.30. Starting at 00:00 UTC, the signal-to-noise ratio is stable, as are the count rates for the different channels. During the day, the signal-to-noise ratio drops to its daytime value, and remains stable until evening. The sharp dips starting at 16:00 UTC in the signal-to-noise ratio as well as the nitrogen and Rayleigh count rates indicate clouds, where there is brief cloud cover, followed by thicker clouds moving in around 19:00 UTC. Profiles of retrieved mixing ratio (Figure 7.31) indicate concentrations of atmospheric water vapor were very low at 00:00 UTC, with moist air gradually moving in as clouds began to form in the early evening. Thus, despite the apparently clear conditions seen on this date prior to 16:30 UTC, the integrated water vapor over this time is markedly different than the trends seen for the other 24-hour cases. For previous cases shown in this section, the integrated water vapor determined by the integrated and HATPRO retrievals, as well as the radiosonde, varies little for the time periods in question. In Figure 7.32b however, the integrated water vapor is determined to be around 3 kg/m^2 at 00:00 UTC, and increasing nearly monotonically by more than a factor 3 to approximately 10 kg/m^2 at 15:00 UTC. The calibration factors from January 13, 2015 are shown in Figure 7.32a. Contrary to the trends observed on the other dates, the calibration factor here decreases by approximately 20% (a larger change than seen during the February date) between 00:00 and 15:00 UTC, with no apparent indication of a diurnal cycle observed.

7.4 Relation between Calibration Factor and Background

As demonstrated in Section 7.1.2, the calibration factors derived by the Integrated retrieval at times coinciding with nighttime GRUAN soundings agree with those determined by the radiosonde-derived Trajectory method to within 10% when the radiometer retrieval is of sufficient quality, with associated uncertainties which are a factor of 2 or 3 times smaller (listed in Table 7.1) due to the larger relative systematic uncertainties in calibrating to the radiosonde

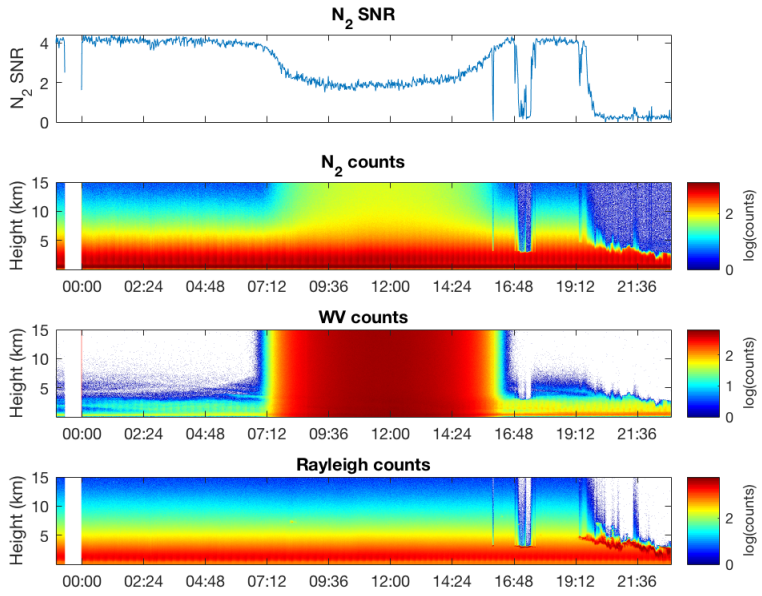

Figure 7.30: RALMO measurements over a 24-hour period on January 13, 2015. The top plot shows the nitrogen channel signal-to-noise ratio at 12 km. The additional plots show the PC nitrogen, water vapor, and Rayleigh-scatter channel counts.

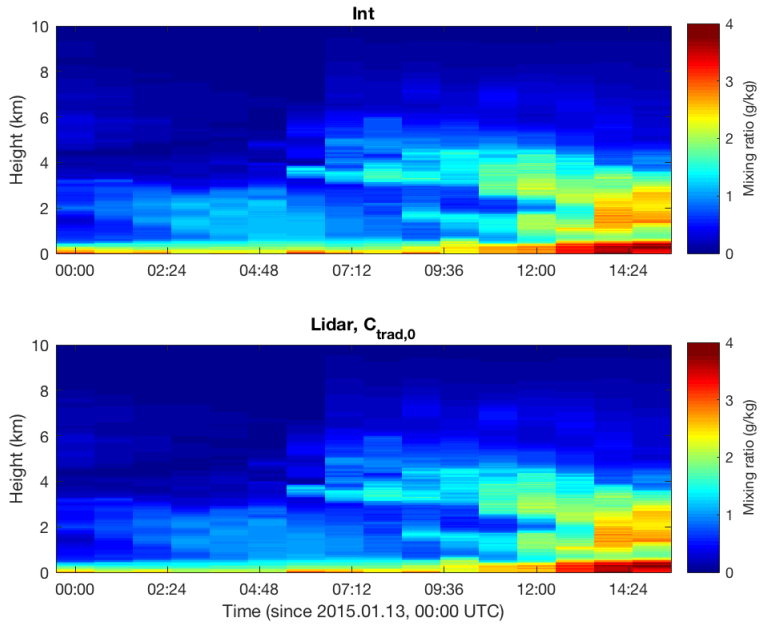

Figure 7.31: Mixing ratio trends for January 13, 2015 between 00:00 and 15:00 UTC, via the (top) and sonde-calibrated lidar (bottom) retrievals.

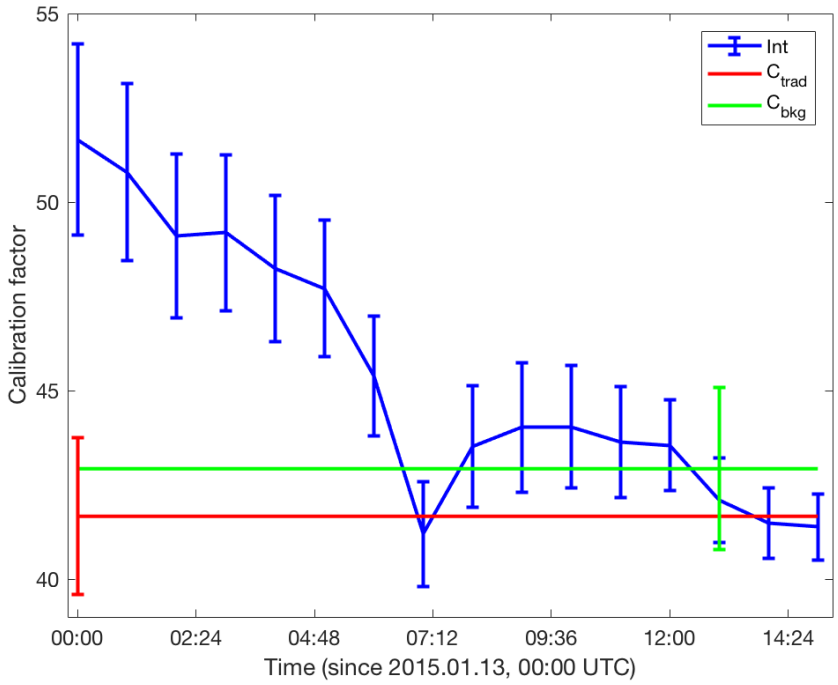

(a)

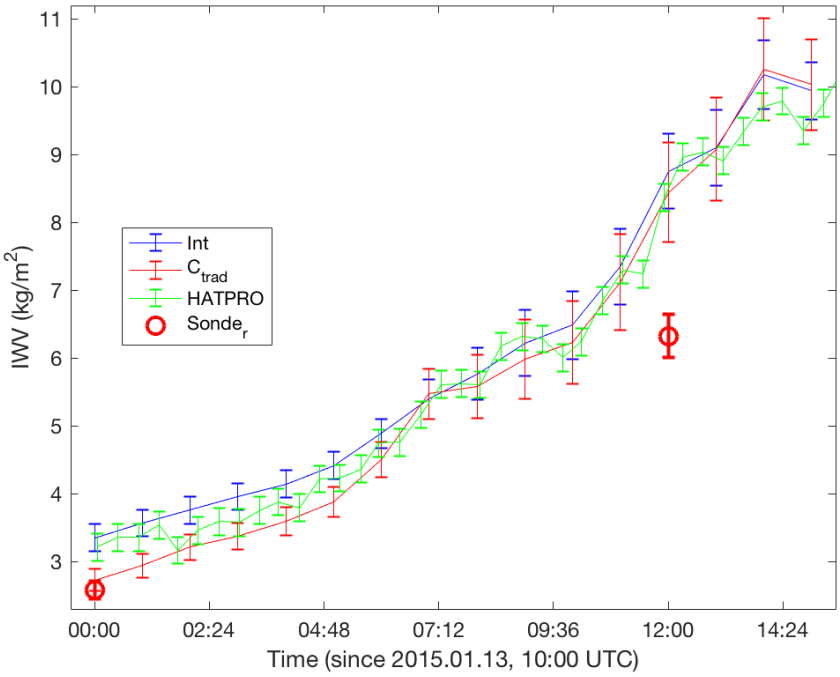

(b)

Figure 7.32: (a) Calibration factor as a function of time for January 13, 2015. *Int* and *Lidar1* are the factors retrieved by and lidar retrievals, while C_{trad} and C_{bkg} determine this constant via the traditional radiosonde and background calibration method, respectively. (b) Integrated water vapor trends, where *HATPRO* are values retrieved via the HATPRO software. The red circles, Sonde$_r$, are values from routine radiosondes.

than the radiometer. However, as mentioned in Section 7.3.1, this agreement is no longer apparent during daytime observations, if the nighttime calibration factor is still used for the Lidar retrieval. In fact, for 4 of the 5 dates shown in this section, the Integrated retrieval determines a calibration factor which clearly increases dramatically during the daytime. The fifth case, January 13, 2015 (Figure 7.32), does not share the same calibration factor characteristics of the other dates. From the relatively small number of dates investigated thus far, it is still undetermined how anomalous cases such as January 13, 2015 actually are.

The calibration factor is a treated as a scalar for the mixing ratio. Thus, using a larger calibration factor yields a larger relative mixing ratio. If this value is determined from nighttime measurements and held constant over the day, it can result in a daytime mixing ratio profile which underestimates the amount of water vapor, as portrayed in the 24-hour trend for April 24, 2013 (Figure 7.26). Consequently, use of a constant calibration factor determined during the night could be valid for the entirety of that night as well as possibly the following nights, but the findings from this work indicate it is not advisable for daytime retrievals.

What terms in the retrieval would cause changes in the calibration factor anyway? As shown in the long-term trend (Figure 5.12), the baseline factors show a generally increasing trend over time, from approximately 30 at the beginning of 2009 to 48 by late 2018. This gradual increase over time is commonly seen, and is likely due to differential aging of the water vapor and nitrogen channel detection systems [8][9].

However, as such calibrations can only be made during radiosonde launches or when the Sun is at a particular zenith angle, it is difficult for these methods to monitor short-term changes in the calibration factor. Based on the 24-hour trends of the Integrated retrievals, it is evident that there is often a relation between such short-term changes and the background sky light. Aside from the unusual case on January 13, 2015, the calibration factor is greatest around Solar noon for the cases presented in Section 7.3.1. The factor increases and decreases in value with respect to the Solar zenith angle, and the relative change in the factor between the nighttime baseline and daytime peak varies depending on season with a larger relative range during sum-

mer. As shown in Figure 7.33, the retrieved and observed backgrounds follow a trend similar to the calibration factors, with small, stable backgrounds during the night, a sharp increase in the morning, and a peak around Solar noon. Taking the calibration factors and separating the background counts from daytime and nighttime observations for each date, one ascertains a collection of trends as depicted in Figures 7.34 and 7.35. For each date shown, there is no discernible change in the nighttime calibration factor with respect to the nightly background for either nitrogen or water vapor channels. Thus, nighttime (baseline) calibration factors appear not to have a detectable dependence on the background value, but rather only exhibit long-term increases due to other factors. However, these plots do show there is indeed a strong linear relation between the value of the daytime background count rate and the calibration factor. Validation of RALMO in Brocard et al. 2013 found a bias in the lidar humidity values, causing underestimation of the integrated water vapor [2]. Although they contend it is due to an overestimation from the radiosonde, perhaps it could actually be due to the means of processing and handling daytime background counts (such as not accounting for variability in the individual laser shots being averaged across lidar scans correctly).

7.5 Summary

This chapter provides the first real results for the integrated retrieval method. When testing the radiometer retrieval on clear nights with coincidental GRUAN-corrected radiosonde launches, it was observed that performing a bias correction on the raw brightness temperature measurements may improve or harm the retrieval, depending on how far the measurement is from the mean bias correcting factor. The quality of the retrieval can be assessed by the size of the retrieval residuals, with respect to measurement noise, as well as closeness of the retrieved mixing ratio profile to the smoothed GRUAN-corrected radiosonde profile. For 3 of the clear night cases considered (2012.02.29, 2013.04.24, 2014.01.23) the retrieval was improved when bias-corrected measurements were incorporated, while one case (2011.10.05) saw better results

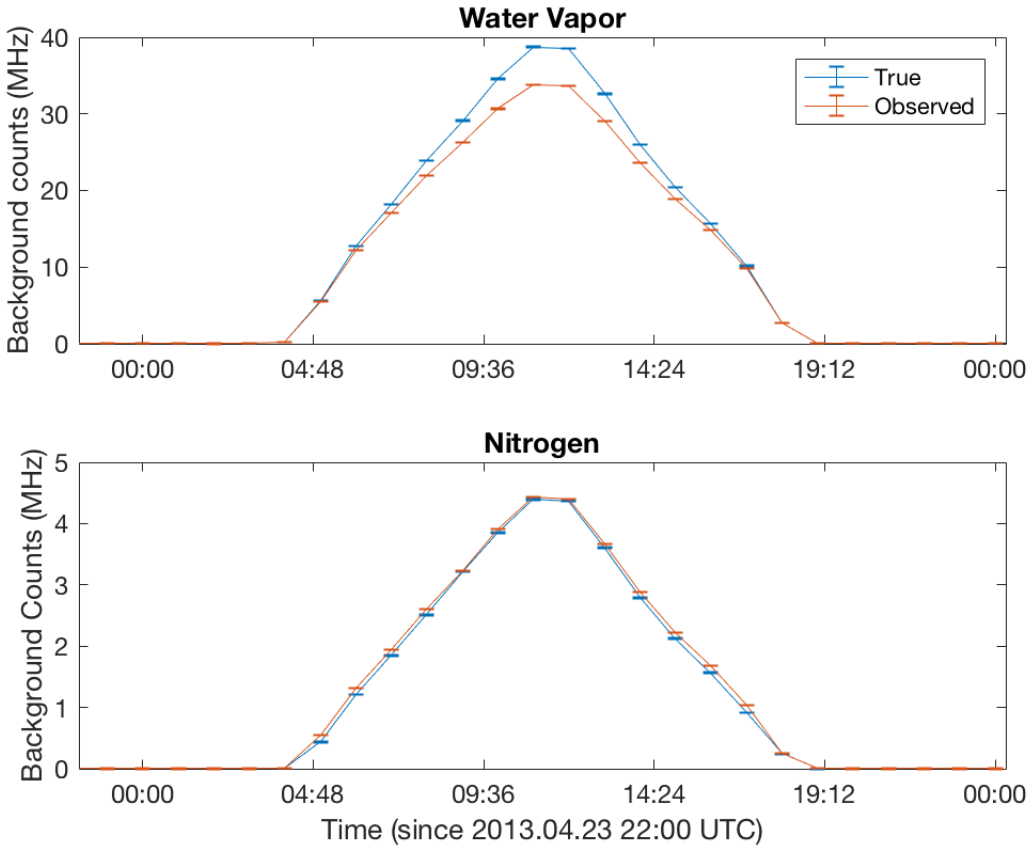

Figure 7.33: Background count values from April 24, 2013 for the PC Water Vapor (top) and Nitrogen (bottom) channels. The blue trend is the true background, the retrieved value, and the red trend is the background observed in the lidar measurement.

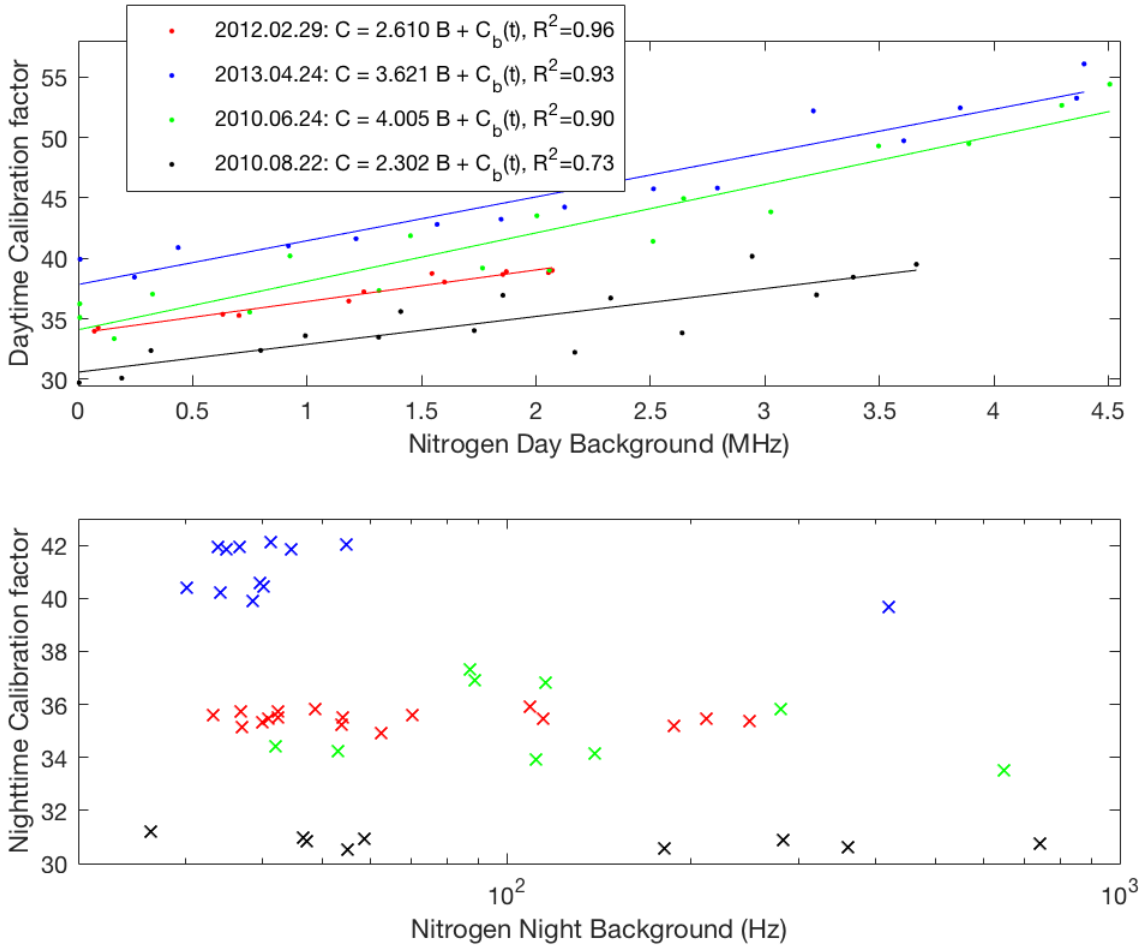

Figure 7.34: Relation between the Integrated method calibration factor and the background for the PC nitrogen channel for 4 of the 24-hour observation periods, for daytime (top) and nighttime (bottom) observations. The points indicate the individual data points, while the trends in the top plot represent the fitted functions (expressed in the legend), where B is the background value, $C_b(t)$ is the nighttime baseline calibration factor as a function of time in years, and R^2 is the coefficient of determination.

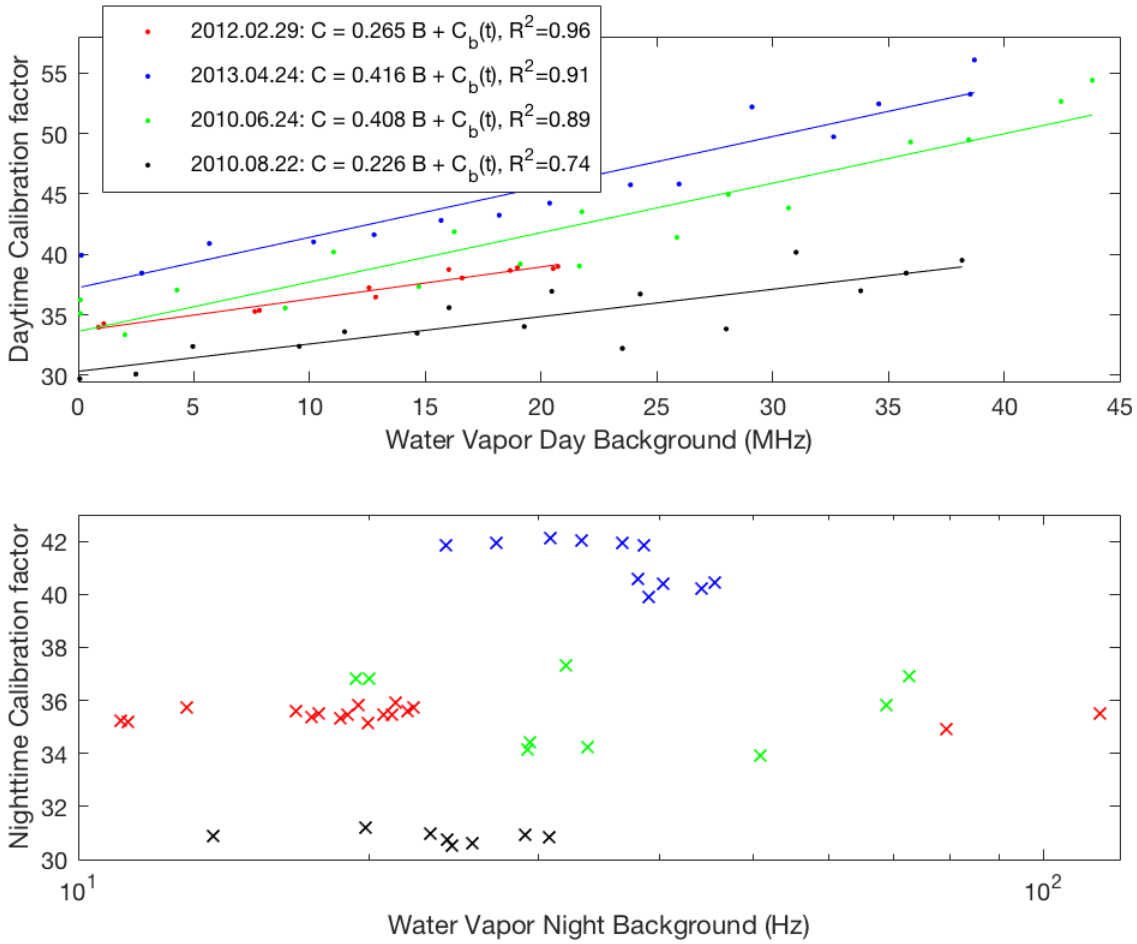

Figure 7.35: Relation between the Integrated method calibration factor and the daytime background for the PC water vapor channel for 4 of the 24-hour observation periods, for daytime (top) and nighttime (bottom) observations. The points indicate the individual data points, while the trends in the top plot represent the fitted functions (expressed in the legend), where B is the background value, $C_b(t)$ is the nighttime baseline calibration factor as a function of time in years, and R^2 is the coefficient of determination.

when the uncorrected measurements were used. This latter exception is due to the data being in a calibration epoch where a few of the mean channel-dependent biases are extreme (as seen previously in Figure 5.15) and not representative of the measurements from this date. For the observations of July 17, 2014, the bias correction factor is small, resulting in large residuals and ill-fitting radiometer retrievals.

When the radiometer retrieval is of sufficient quality, the integrated retrieval utilizing the better brightness temperature measurement (either uncorrected or corrected) produces a mixing ratio profile which is within 10% of the radiosonde-calibrated lidar retrieval. Additionally, the calibration factors are also generally comparable within their uncertainties. The exception is the night of July 17, 2014, where the ill-fitting radiometer retrieval causes the integrated retrieval to differ from the lidar retrieval and radiosonde profiles by approximately 40% below 3 km, with calibration factors differing by about 40% as well. The results of these 30-minute nighttime retrievals are listed in Table 7.1.

Integrated retrievals are then carried out for 5 longer term periods of clear conditions at different times throughout the year. Although the integrated retrieval retrieves calibration factors which agree well with the radiosonde-determined factors during nighttime observations, the 24-hour factors retrieved show diurnal variation related to the Solar intensity. The next chapter will look more closely into the relation between the calibration factor and the Solar background. One of these dates, January 13, 2015, does not have the diurnal trend in calibration factor seen by the other dates. Although it was clear, there was a large increase in detected water vapor over the course of the day, masking the potential effects of Solar intensity on the calibration factor. In investigating a possible cause for the diurnal variation in calibration factor, is was considered that diurnal changes in sky light may be responsible for the observed effect. Taking the daytime calibration factors for each of these time periods, and relating them to the daytime background shows there is indeed a linear relation between these quantities.

Bibliography

[1] HATPRO Technical Instrument Manual: Description of Instrument Technology, Radiometer Physics, https://www.radiometer-physics.de/products/microwave-remote-sensing-instruments/radiometers/humidity-and-temperature-profilers/, 2013.

[2] Brocard, E., Jeannet, P., Begert, M., Levrat, G., Philipona, R., Romanens, G., and Scherrer, S. C.: Upper air temperature trends above Switzerland 1959-2011, Journal of Geophysical Research Atmospheres, 118, 4303–4317, doi:10.1002/jgrd.50438, 2013.

[3] Hicks-Jalali, S., Sica, R. J., Haefele, A., and Martucci, G.: Calibration of a water vapour Raman lidar using GRUAN-certified radiosondes and a new trajectory method, Atmospheric Measurement Techniques, 12, 3699–3716, doi:10.5194/amt-12-3699-2019, 2019.

[4] LöHnert, U. and Crewell, S.: Accuracy of cloud liquid water path from ground-based microwave radiometry 1. Dependency on cloud model statistics, Radio Science, 38, 8041, doi:10.1029/2002RS002654, 2003.

[5] Navas-Guzmán, F., Kämpfer, N., and Haefele, A.: Validation of brightness and physical temperature from two scanning microwave radiometers in the 60 GHz O2 band using radiosonde measurements, Atmospheric Measurement Techniques, 9, 4587–4600, doi:10.5194/amt-9-4587-2016, 2016.

[6] Rose, T. and Czekala, H.: RPG-HATPRO Operating Manual, Radiometer Physics, 8.04 edn., https://www.radiometer-physics.de/products/microwave-remote-sensing-instruments/radiometers/humidity-and-temperature-profilers/, 2009.

[7] Sica, R. and Haefele, A.: Retrieval of water vapor mixing ratio from a multiple channel Raman-scatter lidar using an optimal estimation method, Appl. Opt., 55, 763, 2016.

[8] Simeonov, V., Larcheveque, G., and Quaglia, P.: Influence of the photomultiplier tube spatial uniformity on lidar signals, Appl. Opt., 38, 5186, 1999.

[9] Simeonov, V., Fastig, S., and Haefele, A.: Instrumental correction of the uneven PMT aging effect on the calibration constant of a water vapor Raman lidar, Proc. of SPIE, 9246, 2014.

Chapter 8

Summary and Conclusions

8.1 Summary of Results

This thesis has demonstrated the successful implementation of an integrated forward model, using lidar and microwave radiometer measurements, to retrieve water vapor mixing ratio profiles in the troposphere from a Raman-scattering lidar.

Chapter 5 introduces the integrated retrieval and details its development. The *a priori* mixing ratio, as well as the parameter pressure and temperature profiles are provided by the US Standard Model Atmosphere. As long as any cusps in the profile are smoothed, the choice of *a priori* profile does not affect the retrieval over its effective range, until the retrieval begins to falls back toward the *a priori* due to lack of signal (Figure 6.23). The retrieval has a stronger dependence on the choice of inputs for the *a priori* covariance matrix, which requires a variance, correlation length, and correlation function for the *a priori* state. Uncertainty in mixing ratio, as well as pressure and temperature can be estimated via long-term records from radiosondes (Figure 5.6), while the correlation length and function can be determined by performing a least squares fit on an autocorrelation matrix for each atmospheric state quantity (Figures 5.7 and 5.8). Section 6.3.1 explains that, as long as the variance used is appropriate, the choice of a correlation length or function will not have a tremendous effect on the outcome

of the retrieval. However, it is advised not to use a Gaussian correlation function unless a lower limit cutoff is defined, as the extremely minuscule off-diagonal elements would yield a poorly-conditioned matrix when inverted. Use of a Tent or Exponential correlation function are instead recommended. The forward model is comprised of two existing forward models, the lidar equation model of Sica & Haefele [7], and a radiative transfer model characterizing the microwave radiometer measurements. For the latter model, 2 implementations were considered: the Cimini (a MATLAB adaptation of the model of Schroeder & Westwater [6]) and the ARTS (Atmospheric Radiative Transfer Simulator [2]) models. When testing with the same atmospheric inputs, both models produced comparable simulated brightness temperature measurements (Figure 5.16) and retrieval Jacobians (Figure 5.17). As a result, it was deemed acceptable to use the Cimini implementation, which is advantageous in its relative simplicity relative to the ARTS implementation.

Chapter 6 tests the performance of the newly-developed Integrated forward model retrieval, in which synthetic lidar and radiometer measurements are generated by running radiosonde-measured atmospheric quantities through the combined forward model. The simulated measurements are then perturbed by a certain noise level, and inserted into the retrieval as the measurement state. The advantage of this approach is the ability to determine how well the method is able to retrieve the original radiosonde humidity "true state". The radiometer-only retrieval is able to retrieve the radiosonde's humidity, but due to its coarse retrieval resolution, is not able to catch smaller-scale variations of humidity in the profile. Both the Lidar-only and Integrated retrievals are able to retrieve the true state to a comparable degree (Figure 6.17), while the Integrated retrieval has a lesser total uncertainty in the lowest 5 km (averaging 3% uncertainty, compared to 5% for the Lidar retrieval. Figure 6.22).

Chapter 7 looks at retrievals using real measurements from the MeteoSwiss instrumentation in Payerne. Contrary to the simulated retrievals, real measurements are not always simple. Particularly evident for the radiometer retrieval of mixing ratio, in which only 7 measurements of brightness temperature are used, the outcome of the retrieval is highly dependent on the

effect of the bias correction. Depending on the difference between the measurement and the epoch mean measurement, a bias correction performed on the brightness temperatures may be beneficial or detrimental to the radiometric retrieval. A closer look (in Appendix C) reveals that radiometer brightness temperature bias varies significantly across the calibration epochs (Figure 5.15). As a result, it is best to run radiometer retrievals for dates (ideally from times of relatively small bias and few outliers) and consider these dates only if the retrieval and its residuals are reasonable. For such reasonable radiometer retrievals (examples of such clear night radiometer observations coinciding with GRUAN-corrected radiosondes are shown in Section 7.1.1), the integrated retrievals of humidity agree with the Lidar retrievals to within 5% up to the effective height of the retrieval (Section 7.1.2). An agreement between the calibration factors retrieved by the Integrated method and those determined externally is also evident in these case (Table 7.1). When compared to nighttime observations, daytime observations have lidar measurements of much lesser signal-to-noise ratio, resulting in a lesser effective range for the Integrated method, as well as greater uncertainty. However, when daytime Integrated retrievals are compared to Lidar retrievals, the integrated retrieval has noticeably more degrees of freedom (generally 1-2 more, due to the contribution of the radiometer to the retrieval, Figure 7.25), resulting in greater relative effective range (increased by nearly 1 km in April 23, 2013, Figure 7.23). It is then shown that there is a direct relation between the daytime calibration and the background intensity during the day.

8.2 Significance of this work

As mentioned in Chapter 1, other retrievals using measurements from lidar and microwave radiometer have been carried previously [1][3][8]. Compared to these works, one of the major advantages of this thesis and its use of raw lidar data is the reduced dependence on intermediate processing of the lidar data. Our Integrated method shows that the retrieval of a water vapor mixing ratio profile from raw radiometer and lidar data is possible, yielding a product which

is improved over retrievals from the instruments individually. Since radiosonde observations generally perform on a much less continuous timescale than either lidar or radiometer, it is not possible to monitor changes in the calibration factor on a short term basis via radiosonde calibration methods. As our method also performs retrievals from raw data directly, we are able to determine lidar calibration factors without the need for radiosonde-based calibration.

8.3 Future Work

8.3.1 Integrated Retrieval

Although the results here are quite interesting, there is still much to investigate for this integrated retrieval. Suggestions for the next steps are as follows.

1. The first step is to run through more clear dates at different times of the year and over the course of RALMO's lifetime in order to obtain more 24-hour trends of the calibration factor. Analyzing more dates would allow for the extrapolation of a stronger empirical relation between the relative and absolute diurnal change in the calibration factor and the Sun's position and year.

2. For this work, the radiometer forward model consisted of 1 state parameter (water vapor mixing ratio) and 2 *b-parameters* (temperature and pressure). To be more consistent with the lidar forward model, it may be worthwhile to look into additional retrieval parameters, such as absorption model, calibration, and instrumental (such as the HATPRO center frequencies and band passes, which are actually not known precisely [4]) considerations, giving a more comprehensive characterization of the uncertainties associated with the radiometer.

3. It would also be beneficial to update the code so it can handle more recent data. Lidar data from 2016 onward is collected using a new data acquisition system. This should be a straightforward undertaking, and would make much more data available for analysis. The most

recent radiometer data from 2018 onward has the additional benefit of having an improved bias correction, reducing the need to check whether or not the bias correction is actually helpful to the retrieval. Additionally, further optimization of the code should be attempted to carry out the retrievals more efficiently.

4. So far, only clear conditions have been studied, which were confirmed to be clear by on-site Ceilometer measurements. It would be advantageous to adapt the retrieval code so that cloudy cases can be handled appropriately. Such an update would include the ability to determine (eventually automatically) whether or not it is cloudy via use of the HATPRO's liquid water content estimate, the elastic channels from RALMO, or potential integration with a collocated ceilometer, as to provide essential information such as cloud thickness and base height required for the radiometer forward model. Kalman filtering may be useful to this end, with more explanation given in the thesis of Marc Schneebeli [5].

5. Once recent data and cloudy conditions can be handled without trouble, the next logical step would be to automate as much of the procedure as possible so it could be used on an operational basis. Automation would also facilitate the development of a climatological record for monitoring daytime calibration factor trends.

6. Aside from the handling and initial processing of raw data, changes to the retrieval itself should be minimal. Thus, once an operational Integrated retrieval mechanism is in place for Payerne, it can be applied at other sites globally with a collocated radiometer and Raman Water Vapor Lidar, such as Table Mountain, Mauna Loa, and Atmospheric Radiation Measurement facility.

8.3.2 Purple Crow Lidar

Although not covered in this thesis, the Purple Crow Lidar is a powerful instrument, with a large power-aperture product capable of detecting water vapor into the stratosphere (a detailed description of the instrument is provided in Appendix A). Although it is a powerful instrument, there are no routine collocated instruments available for calibration. The addition of a microwave radiometer to this site would allow for an integrated retrieval of the water vapor mixing ratio, with a potential to retrieve calibrated profiles extending even higher than those derived using RALMO measurements. Such efforts would have the profound benefit of providing accurate retrievals of UTLS water vapor, products which are highly valuable in the atmospheric community currently. However, before attempting an integrated retrieval, I have some recommendations for efforts which should be carried out for the Purple Crow Lidar system:

1. After the validation campaign with ALVICE in 2012 (See Section A.3.2 for more details on the campaign), it was suggested that the Purple Crow Lidar might be affected by fluorescence. Although fluorescence is generally less of a concern in the visible than ultraviolet region, it would still be of use to carry out such a test. See Appendix B for discussion on Fluorescence.

2. An OEM retrieval of water vapor has not yet been performed on the Raman Lidar measurements from the Purple Crow Lidar. Although there has not been a reliable microwave radiometer located at the site, the ALVICE campaign did launch a number of radiosondes. It would therefore be possible to take the radiosonde-calibrated lidar retrieval method of Sica & Haefele 2016 (originally set up for RALMO) and adapt it for execution on the Purple Crow Lidar data during this campaign.

3. Prior to the ALVICE campaign, there is a dataset comprising more than 10 years of lidar

water vapor measurements at the Purple Crow Lidar. If a reasonable means of calibration can be determined (See Section A.3 for some of the previous calibration efforts), OEM retrievals of these older measurements can also be carried out, along with the determination of climatological trend analysis.

4. For the future sake of Purple Crow Lidar analyses, it would be advantageous to consider permanent, complementary instruments on site for potential validation of the lidar measurements.

Bibliography

[1] Barrera-Verdejo, M., Crewell, S., Löhnert, U., Orlandi, E., and Di Girolamo, P.: Ground-based lidar and microwave radiometry synergy for high vertical resolution absolute humidity profiling, Atmospheric Measurement Techniques, 9, 4013–4028, doi:10.5194/amt-9-4013-2016, 2016.

[2] Eriksson, P., Jiménez, C., and Buehler, S. A.: Qpack, a general tool for instrument simulation and retrieval work, Journal of Quantitative Spectroscopy and Radiative Transfer, 91, 47–64, doi:10.1016/j.jqsrt.2004.05.050, 2005.

[3] Foth, A. and Pospichal, B.: Optimal estimation of water vapour profiles using a combination of Raman lidar and microwave radiometer, Atmospheric Measurement Techniques, 10, 3325–3344, doi:10.5194/amt-10-3325-2017, 2017.

[4] Löhnert, U. and Maier, O.: Operational profiling of temperature using ground-based microwave radiometry at Payerne: Prospects and challenges, Atmospheric Measurement Techniques, 5, 1121–1134, doi:10.5194/amt-5-1121-2012, 2012.

[5] Schneebeli, M.: Advancements in Ground-Based Microwave Remote Sensing of the Troposphere - Calibration, Data Retrieval and Applications, Ph.D. thesis, Universitat Bern, URL http://publications.iap.unibe.ch/pub-detail.php?lang=en&id=3246, 2009.

[6] Schroeder, J. and Westwater, E.: User Guide to WPL Microwave Radiative Transfer Software, 1991.

[7] Sica, R. and Haefele, A.: Retrieval of water vapor mixing ratio from a multiple channel Raman-scatter lidar using an optimal estimation method, Appl. Opt., 55, 763, 2016.

[8] Turner, D. D. and Blumberg, W. G.: Improvements to the AERIoe thermodynamic profile

retrieval algorithm, IEEE Journal of Selected Topics in Applied Earth Observations and Remote Sensing, 12, 1339–1354, doi:10.1109/JSTARS.2018.2874968, 2019.

Bibliography

[1] U.S. Standard Atmosphere, 1976, Tech. rep., National Oceanic and Atmospheric Administration, 1976.

[2] Photomultiplier Handbook, Tech. rep., Burle Technologies, Inc., 1980.

[3] Atmospheric radiance and transmittance: FASCOD2, no. 141-144 in Proc. Sixth Conf. on Atmospheric Radiation, Amer. Meteor. Soc., Williamsburg, VA, 1986.

[4] Multichannel Scaler/Averager Model SR430, Stanford Research Systems, 2007.

[5] Licel Transient Recorder and Ethernet-Controller Programming Manual, Tech. rep., Licel GmbH, 2010.

[6] Licel TR20-160 Lidar Transient Recorder Manual, Tech. rep., Licel GmbH, 2010.

[7] SRS-C34 Digital Radiosonde, Meteolabor AG, Wetzikon, Switzerland, 2010.

[8] Measurement and Deployment Examples, Radiometer Physics, https://www.radiometer-physics.de/products/microwave-remote-sensing-instruments/radiometers/humidity-and-temperature-profilers/, 2011.

[9] TR20-160 Licel transient recorder Manual, Licel GmbH, 2011.

[10] HATPRO Technical Instrument Manual: Description of Instrument Technology, Radiometer Physics, https://www.radiometer-physics.de/products/microwave-remote-sensing-instruments/radiometers/humidity-and-temperature-profilers/, 2013.

[11] Vaisala Radiosonde RS92 Data Sheet, Tech. rep., Vaisala, URL `www.vaisala.com`, 2013.

[12] Radiosondes: Backbone of GRUAN, https://www.gruan.org/instruments/radiosondes/, 2019.

[13] Adam, M.: Notes on temperature-dependent lidar equations, J. Atm. & Oceanic Tech., 26, 1021, 2009.

[14] Ahrens, C.: Meteorology Today: an introduction to weather, climate, and the environment, Brooks/Cole Publishing, Pacific Grove, CA, 2000.

[15] Algara-Siller, M.: Purple Crow Lidar calibration of the water vapour mixing ratios in the lowest atmosphere, Master's thesis, University of Western Ontario, 2004.

[16] Anderson, G., Clough, S., Kneizys, F., Chetwynd, J., and Shettle, E.: AFGL atmospheric constituent profiles (0-120km), Tech. rep., Air Force Geophys. Lab., tech. Rep. TR-86-0110, 1986.

[17] Anderson, J., Wilmouth, D., and Smith, J.: UV Dosage Levels in Summer: Increased Risk of Ozone Loss from Convectively Injected Water Vapor, Science, 337, 835, 2012.

[18] Andrews, D.: An Introduction to Atmospheric Physics, Cambridge University Press, 2nd edn., 2010.

[19] Andrews, D., Holton, J., and Leovy, C.: Middle Atmosphere Dynamics, Academic Press, 1987.

[20] Ansmann, A. and Muller, D.: Lidar: Range-Resolved Optical Remote Sensing of the Atmosphere, chap. Lidar and Atmospheric Aerosol Particles, pp. 803–807, Springer, 2005.

[21] Argall, S. and Sica, R.: Encyclopedia of Imaging Science and Technology, chap. LIDAR, John Wiley & Sons, Inc., 2002.

[22] Argall, S., Vassiliev, O., and Sica, R.: Lidar Measurements taken with a large- aperture liquid mirror: 2. Sodium resonance-fluorescence system, Appl. Opt., 39, 2393, 2000.

[23] Argall, S., Sica, R., and Bryant, C.: Calibration of the Purple Crow Lidar vibrational Raman water-vapour mixing ratio and temperature measurements, Can. J. Phys., 85, 119, 2007.

[24] Avila, G., Fernandez, J., and Mate, B.: Ro-vibrational Raman cross sections of water vapor in OH stretching region, J. Mol. Spectrosc., 196, 77, 1999.

[25] Avila, G., Fernandez, J., and Tejeda, G.: The Raman spectra and cross-sections of H2O, D2O, and HDO in the OH/OD stretching regions, J. Mol. Spectrosc., 228, 38, 2004.

[26] Baray, J. L., Courcoux, Y., Keckhut, P., Portafaix, T., Tulet, P., Cammas, J. P., Hauchecorne, A., Godin Beekmann, S., De Mazière, M., Hermans, C., Desmet, F., Sellegri, K., Colomb, A., Ramonet, M., Sciare, J., Vuillemin, C., Hoareau, C., Dionisi, D., Duflot, V., Vérèmes, H., Porteneuve, J., Gabarrot, F., Gaudo, T., Metzger, J. M., Payen, G., Leclair De Bellevue, J., Barthe, C., Posny, F., Ricaud, P., Abchiche, A., and Delmas, R.: Maïdo observatory: A new high-altitude station facility at Reunion Island (21 S, 55 E) for long-term atmospheric remote sensing and in situ measurements, Atmospheric Measurement Techniques, 6, 2865–2877, doi:10.5194/amt-6-2865-2013, 2013.

[27] Barrera-Verdejo, M., Crewell, S., Löhnert, U., Orlandi, E., and Di Girolamo, P.: Ground-based lidar and microwave radiometry synergy for high vertical resolution absolute humidity profiling, Atmospheric Measurement Techniques, 9, 4013–4028, doi: 10.5194/amt-9-4013-2016, 2016.

[28] Berks, A., Bernstein, L., and Robertson, D.: MODTRAN: A moderate resolution model for LOWTRAN 7, Tech. rep., Spectral Sciences, Inc., Burlington, MA, 1989.

[29] Bevis, M., Businger, S., Herring, T. A., Rocken, C., Anthes, R. A., and Ware, R. H.: GPS meteorology: remote sensing of atmospheric water vapor using the global positioning system, Journal of Geophysical Research, 97, 787–801, 1992.

[30] Bleisch, R., Kampfer, N., and Haefele, A.: Retrieval of tropospheric water vapour by using spectra of a 22 GHz radiometer, Atmos. Meas. Tech., 4, 1891, 2011.

[31] Borra, E., Content, R., and Girard, L.: Liquid Mirrors: Optical shop tests and contributions to the technology, ApJ, 398, 829, 1992.

[32] Borra, E. F.: The liquid-mirror telescope as a viable astronomical tool, Journal of the Royal Astronomical Society of Canada, 76, 245–256, 1982.

[33] Brewer, A.: Evidence for a world circulation provided by the measurements of Helium and water vapour distribution in the Stratosphere, Q. J. R. Meteorol. Soc., 75, 351, 1949.

[34] Bribes, J., Gaufres, R., and Monan, M.: Raman band contours for water water vapour as a function of temperature, Appl. Physics Lett., 28, 336, 1976.

[35] Brocard, E., Jeannet, P., Begert, M., Levrat, G., Philipona, R., Romanens, G., and Scherrer, S. C.: Upper air temperature trends above Switzerland 1959-2011, Journal of Geophysical Research Atmospheres, 118, 4303–4317, doi:10.1002/jgrd.50438, 2013.

[36] Bryant, C.: First measurements of the upper tropospheric and lower stratospheric water vapour mixing ratios using the Purple Crow Lidar raman-scatter lidar, Master's thesis, University of Western Ontario, 1999.

[37] Brydegaard, M., Guan, Z., and Weelenreuther, M.: Insect monitoring with fluorescence lidar techniques: feasibility study, Appl. Opt., 48, 5668, 2009.

[38] Bucholtz, A.: Rayleigh-scattering calculations for the terrestrial atmosphere, Applied Optics, 34, 2765, doi:10.1364/ao.34.002765, 1995.

[39] Buehler, S. A., Eriksson, P., Kuhn, T., von Engeln, A., and Verdes, C.: ARTS, the atmospheric radiative transfer simulator, Journal of Quantitative Spectroscopy and Radiative Transfer, 91, 65–93, doi:10.1016/j.jqsrt.2004.05.051, 2005.

[40] Buehler, S. A., Mendrok, J., Eriksson, P., Perrin, A., Larsson, R., and Lemke, O.: ARTS, the Atmospheric Radiative Transfer Simulator - Version 2.2, the planetary toolbox edition, Geoscientific Model Development, 11, 1537–1556, doi:10.5194/gmd-11-1537-2018, 2018.

[41] Cairo, F., Congeduti, F., and Poli, M.: A survey of the signal induced noise in photomultiplier detection of wide dynamics luminous signals, Rev. of Sci. Instruments, 67, 3274, 1996.

[42] Carleer, M. R., Boone, C. D., Walker, K. A., Bernath, P. F., Strong, K., Sica, R. J., Rand all, C. E., Vömel, H., Kar, J., Höpfner, M., Milz, M., von Clarmann, T., Kivi, R., Valverde-Canossa, J., Sioris, C. E., Izawa, M. R. M., Dupuy, E., McElroy, C. T., Drummond, J. R., Nowlan, C. R., Zou, J., Nichitiu, F., Lossow, S., Urban, J., Murtagh, D., and Dufour, D. G.: Validation of water vapour profiles from the Atmospheric Chemistry Experiment (ACE), Atmospheric Chemistry & Physics Discussions, 8, 4499–4559, 2008.

[43] Chollet, L.: Balloon fabrics made of Goldbeater's skins, Tech. rep., Technical Section of Aeronautics (S. T. Ae.), 1922.

[44] Clemesha, R., Kent, G., and Wright, R.: Laser Probing the Lower Atmosphere, Nature, 209, 184, 1966.

[45] Collis, R. and Ligda, M.: Laser Radar Echoes from the Clear Atmosphere, Nature, 203, 1964.

[46] Cook, B. A.: ACRONYM: Acronym CReatiON for You and Me, pp. 2–4, URL `http://arxiv.org/abs/1903.12180`, 2019.

[47] Cooney, J.: Measurements on the Raman Component of Laser Atmospheric Backscatter, Appl. Physics Lett., 12, 40, 1968.

[48] Cooney, J.: Remote Measurements of Atmospheric Water Vapor Profiles Using the Raman Component of Laser Backscatter, J. Appl. Met., 9, 182, 1970.

[49] Crewell, S. and LöHnert, U.: Accuracy of cloud liquid water path from ground-based microwave radiometry 2. Sensor accuracy and synergy, Radio Science, 38, 8042, doi: 10.1029/2002RS002634, 2003.

[50] Crewell, S. and Lohnert, U.: Accuracy of Boundary Layer Temperature Profiles Retrieved With Multifrequency Multiangle Microwave Radiometry, IEEE Transactions on Geoscience and Remote Sensing, 45, 2195–2201, doi:10.1109/tgrs.2006.888434, URL https://doi.org/10.1109/tgrs.2006.888434, 2007.

[51] Dakin, J. and King, A.: Limitations of a single optical fiber fluorimeter system due to background fluorescence, IEEE Proc., 131, 273, 1984.

[52] Davis, S.: Fourier transfer spectrometry, Academic Press, 2001.

[53] Dinoev, T., Simeonov, V., and Arshinov, Y.: Raman Lidar for Meteorological Observations, RALMO – Part 1: Instrument description, Atmos. Meas. Tech., 6, 1329, 2013.

[54] Dinoev, T., Hafele, A., Martucci, G., Simeonov, V. B., Calpini, B., Serikov, I., Bobrovnikov, S., and Leuenbergerd, D.: Raman lidar in operational meteorology, p. 18, doi:10.1117/12.2501987, 2018.

[55] Dionisi, D., Keckhut, P., and Courcoux, Y.: Water vapor observations up to the lower stratosphere through the Raman lidar during the Maïdo Lidar Calibration Campaign, Atmos. Meas. Tech., 8, 1425, 2015.

[56] Dirksen, R. J., Sommer, M., Immler, F. J., Hurst, D. F., Kivi, R., and Vömel, H.: Reference quality upper-air measurements: GRUAN data processing for the Vaisala RS92 radiosonde, Atmospheric Measurement Techniques, 7, 4463–4490, doi:10.5194/amt-7-4463-2014, 2014.

[57] Dobson, G.: Origin and distribution of the polyatomic molecules in the atmosphere, Proc. Royal Soc. London, 236, 187, 1956.

[58] Donovan, D., Whiteway, J., and Carswell, A.: Correction for nonlinear photon-counting effects in lidar systems, Appl. Opt., 32, 6742, 1993.

[59] Doucet, P., Sica, R., and Argall, S.: LIDAR Measurements of Lofted Stratospheric Layers from Biomass Burning, in: 37th COSPAR Scientific Assembly, vol. 37, p. 741, 2008.

[60] E., K., Kanamitsu, M., Collins, W., Deaven, D., Gandin, L., Iredell, M., Jenne, R., and Joseph, D.: The NCEP NCAR 40-Year Reanalysis Project, Bulletin of the American Meteorological Society, 77, 437–472, 1996.

[61] Ehret, G., Hoinka, K., and Stein, J.: Low stratospheric water vapor measured by an airborne DIAL, J. Geophys. Res., 104, 31,351, 1999.

[62] Elterman, L.: The measurement of stratospheric density distribution with the searchlight technique, J. Geophys. Res, 56, 1951.

[63] England, M., Ferrare, R., Melfi, S., Whiteman, D., and Clark, T.: Atmospheric Water Vapor Measurements: Comparison of Microwave Radiometry and Lidar, J. Geophys. Res., 97, 899, 1992.

[64] Eriksson, P. and Buehler, S.: ARTS Theory, Earth, 2011.

[65] Eriksson, P., Jiménez, C., and Buehler, S. A.: Qpack, a general tool for instrument simulation and retrieval work, Journal of Quantitative Spectroscopy and Radiative Transfer, 91, 47–64, doi:10.1016/j.jqsrt.2004.05.050, 2005.

[66] Farhani, G.: Improved techniques for atmospheric ozone retrievals from lidar measurements using the Optimal Estimation Method and Machine Learning, Ph.D. thesis, University of Western Ontario, 2018.

[67] Farhani, G., Sica, R. J., Godin-Beekmann, S., and Haefele, A.: Optimal estimation method retrievals of stratospheric ozone profiles from a DIAL, Atmospheric Measurement Techniques, 12, 2097–2111, doi:10.5194/amt-12-2097-2019, 2019.

[68] Fiocco, G. and Smullins, L.: Detection of Scattering Layers in the Upper Atmosphere (60–140 km) by Optical Radar, Nature, 199, 1963.

[69] Foth, A. and Pospichal, B.: Optimal estimation of water vapour profiles using a combination of Raman lidar and microwave radiometer, Atmospheric Measurement Techniques, 10, 3325–3344, doi:10.5194/amt-10-3325-2017, 2017.

[70] Gelbwachs, J. and Birnbaum, M.: Fluorescence of Atmospheric Aerosols and Lidar Implications, Appl. Opt., 12, 2442, 1973.

[71] Goody, R. M. and Yung, Y. L.: Atmospheric radiation: Theoretical basis, Oxford University Press, 1989.

[72] Gringorten, I., Salmela, H., Solomon, I., and Sharp, P.: Atmospheric Humidity Atlas - Northern Hemisphere, Air Force Surveys in Geophysics, 186, 66–621, 1966.

[73] Guldner, J. and Spankuch, D.: Remote Sensing of the Thermodynamic State of the Atmospheric Boundary Layer by Ground-Based Microwave Radiometry, J. Atm. & Oceanic Tech., 18, 926, 2001.

[74] Han, Y. and Westwater, E. R.: Analysis and improvement of tipping calibration for ground-based microwave radiometers, IEEE Transactions on Geoscience and Remote Sensing, 38, 1260–1276, doi:10.1109/36.843018, 2000.

[75] Han, Y., Snider, J. B., Westwater, E. R., Melfi, S. H., and Ferrare, R. A.: Observations of water vapor by ground-based microwave radiometers and Raman lidar, Journal of Geophysical Research, 99, 18 695, doi:10.1029/94jd01487, 1994.

[76] Harms, J.: Lidar return signals for coaxial and noncoaxial systems with central obstruction, Appl. Opt., 18, 1559, 1979.

[77] Hedin, A. E.: Extension of the MSIS Thermosphere Model into the middle and lower atmosphere, Journal of Geophysical Research: Space Physics, 96, 1159–1172, doi:10.1029/90ja02125, 1991.

[78] Held, I. M. and Soden, B. J.: Water Vapor Feedback and Global Warming, Annual Review of Energy and the Environment, 25, 441–475, doi:10.1146/annurev.energy.25.1.441, URL https://doi.org/10.1146/annurev.energy.25.1.441, 2000.

[79] Hicks, S.: The Automation and Characterization of the Zaber Motorized Mount and an Update on the Status of the Purple Crow Lidar, Master's thesis, University of Western Ontario, 2015.

[80] Hicks-Jalali, S.: A Tropospheric Water Vapour Climatology and Trends Derived from Vibrational Raman Lidar Measurements over Switzerland, Ph.D. thesis, The University of Western Ontario, 2019.

[81] Hicks-Jalali, S., Sica, R., Haefele, A., and Martucci, G.: A Calibration of the MeteoSwiss RAman Lidar for Meteorological Observations (RALMO)Water Vapour Mixing Ratio Measurements using a Radiosonde Trajectory Method, EPJ Web of Conferences, 176, 08 015, doi:10.1051/epjconf/201817608015, URL https://doi.org/10.1051/epjconf/201817608015, 2018.

[82] Hicks-Jalali, S., Sica, R. J., Haefele, A., and Martucci, G.: Calibration of a water vapour Raman lidar using GRUAN-certified radiosondes and a new trajectory method, Atmospheric Measurement Techniques, 12, 3699–3716, doi:10.5194/amt-12-3699-2019, 2019.

[83] Hogg, D., Guiraud, F., Snider, J., Decker, M., and Westwater, E.: A Steerable Dual-

Channel Microwave Radiometer for Measurement of Water Vapor and Liquid in the Troposphere, J. Climate & Appl. Met., 22, 789, 1983.

[84] Hogg, D. C., Guiraud, F. O., and Decker, M. T.: Measurement of excess radio transmission length on earth-space paths, Astronomy and Astrophysics, 95, 304–307, 1981.

[85] Holton, J., Haynes, P., and McIntyre, M.: Stratosphere-troposphere exchange, Revs. Geophys., 33, 405, 1995.

[86] Immler, F., Engelbart, D., and Schrems, O.: Fluorescence from atmospheric aerosol detected by a lidar indicates biogenic particles in the lowermost stratosphere, Atmos. Chem. Phys., 5, 345, 2005.

[87] Inaba, H.: Detection of atoms and molecules by Raman scattering and resonance fluorescence, Springer-Verlag, 1976.

[88] Inaba, H. and Kobayasi, T.: Laser-Raman Radar: Laser-Raman scattering methods for remote detection and analysis of atmospheric pollution, Opto-electronics, 4, 101, 1972.

[89] Jalali, A., Sica, R. J., and Haefele, A.: A middle latitude Rayleigh-scatter lidar temperature climatology determined using an optimal estimation method, Atmospheric Measurement Techniques Discussions, pp. 1–24, doi:10.5194/amt-2018-117, 2018.

[90] Janssen, M. A.: Atmospheric Remote Sensing by Microwave Radiometry, chap. An Introduction to Passive Microwave Remote Sensing of Atmospheres, John Wiley and Sons, Inc., 1993.

[91] Jeannet, P.: Swiss Contribution to the Global Climate Observing Systems 2001, Tech. rep., MeteoSwiss, 2001.

[92] Jiang, J. H., Su, H., Zhai, C., Wu, L., Minschwaner, K., Molod, A., and Tompkins, A.: An assessment of upper troposphere and lower stratosphere water vapor in MERRA,

MERRA2, and ECMWF reanalyses using Aura MLS observations, Journal of Geophysical Research: Atmosphere, 120, 11 468–11 485, 2015.

[93] Kampfer, N., ed.: Monitoring Atmospheric Water Vapour: Ground-Based Remote Sensing and In-situ Methods, vol. 10, Springer Science, 2013.

[94] Kampfer, N., Nedoluha, G., Haefele, A., and DeWachter, E.: Monitoring Atmospheric Water Vapour: Ground-Based Remote Sensing and In-situ Methods, chap. 5: Microwave Radiometry, Springer Science, 2013.

[95] Kent, G. and Wright, R.: A Review of Laser Radar Measurements of Atmospheric Properties, J. Atm. & Terrest. Phys., 32, 917, 1970.

[96] Khanna, J., Bandoro, J., and Sica, R.: New technique for retrieval of atmospheric temperature profiles from Rayleigh-scatter lidar measurements using nonlinear inversion, Appl. Opt., 51, 7945, 2012.

[97] Kovalev, V. and Eichinger, W.: Elastic Lidar: Theory, Practice, and Analysis Methods, John Wiley & Sons, Inc., 2004.

[98] Leblanc, T. and McDermid, I.: Accuracy of raman liar water vapour calibration and its applicability to long-term measurements, Appl. Opt., 47, 5592, 2008.

[99] Leblanc, T., Walsh, T., and McDermid, I.: Measurements of Humidity in the Atmosphere and Validation Experiments (MOHAVE)-2009: overview of campaign operations and results, Atmos. Meas. Tech., 4, 2579, 2011.

[100] Leblanc, T., McDermid, I., and Walsh, T.: Ground-based water vapor raman lidar measurements up to the upper troposphere and lower stratosphere for long-term monitoring, Atmos. Meas. Tech., 5, 17, 2012.

[101] Leblanc, T., Trickl, T., and Vogelmann, H.: Monitoring Atmospheric Water Vapour:

Ground-Based Remote Sensing and In-situ Methods, chap. 7: Lidar, Springer Science, 2013.

[102] Leblanc, T., Sica, R. J., Van Gijsel, J. A., Haefele, A., Payen, G., and Liberti, G.: Proposed standardized definitions for vertical resolution and uncertainty in the NDACC lidar ozone and temperature algorithms-Part 3: Temperature uncertainty budget, Atmospheric Measurement Techniques, 9, 4079–4101, doi:10.5194/amt-9-4079-2016, 2016.

[103] LöHnert, U. and Crewell, S.: Accuracy of cloud liquid water path from ground-based microwave radiometry 1. Dependency on cloud model statistics, Radio Science, 38, 8041, doi:10.1029/2002RS002654, 2003.

[104] Löhnert, U. and Maier, O.: Operational profiling of temperature using ground-based microwave radiometry at Payerne: Prospects and challenges, Atmospheric Measurement Techniques, 5, 1121–1134, doi:10.5194/amt-5-1121-2012, 2012.

[105] Löhnert, U., Crewell, S., and Simmer, C.: An integrated approach toward retrieving physically consistent profiles of temperature, humidity, and cloud liquid water, Journal of Applied Meteorology, 43, 1295–1307, doi:10.1175/1520-0450(2004)043⟨1295:AIATRP⟩2.0.CO;2, 2004.

[106] Mahagammulla Gamage, S., Sica, R. J., Martucci, G., and Haefele, A.: Retrieval of Temperature From a Multiple Channel Pure Rotational Raman-Scatter Lidar Using an Optimal Estimation Method, Atmospheric Measurement Techniques Discussions, pp. 1–34, doi:10.5194/amt-2019-107, 2019.

[107] Marenco, A., Thouret, V., NéDéLec, P., Smit, H., Helten, M., Kley, D., Karcher, F., Simon, P., Law, K., Pyle, J., Poschmann, G., von Wrede, R., Hume, C., and Cook, T.: Measurement of ozone and water vapor by Airbus in-service aircraft: The MOZAIC airborne program, An overview, Journal of Geophysical Research, 103, 25,631–25,642, doi:10.1029/98JD00977, 1998.

[108] Martucci, G., Voirin, J., Simeonov, V., Renaud, L., and Haefele, A.: A novel automatic calibration system for water vapor Raman LIDAR, EPJ Web of Conferences, 176, 05 008, doi:10.1051/epjconf/201817605008, 2018.

[109] Maschwitz, G., Löhnert, U., Crewell, S., Rose, T., and Turner, D. D.: Investigation of ground-based microwave radiometer calibration techniques at 530 hPa, Atmospheric Measurement Techniques, 6, 2641–2658, doi:10.5194/amt-6-2641-2013, 2013.

[110] Mastenbrook, H. J.: The Variability of Water Vapor in the Stratosphere, Journal of the Atmospheric Sciences, 28, 1455–1501, 1971.

[111] McCullough, E.: A new technique for interpreting depolarization measurements using the CRL atmospheric lidar in the Canadian High Arctic, Ph.D. thesis, University of Western Ontario, 2015.

[112] Measures, R.: Laser Remote Sensing: Fundamentals and Applications, Krieger Publishing Company, 1984.

[113] Melfi, S.: Remote Measurements of the Atmosphere using Raman Scatteing, Appl. Opt., 11, 1605, 1972.

[114] Melfi, S., Lawrence, J., and McCormick, M.: Observation of Raman Scattering by Water Vapor in the Atmosphere, Appl. Physics Lett., 15, 295, 1969.

[115] Mielke, B.: Analog & photon counting, Tech. rep., Licel GmbH.

[116] Miloshevich, L., Vomel, H., and Whiteman, D.: Accuracy assessment and correction of Vaisala RS92 radiosonde water vapour measurements, J. Geophys. Res., 114, 11 305, 2009.

[117] Mu, T., Chen, S., and Zhang, Y.: Classification of edible oils using 532 nm laser-induced fluorescence combined with support vector machine, Anal. Methods, 5, 6960, 2013.

[118] Murphy, D. and Koop, T.: Review of the vapour pressures of ice and supercooled water for atmospheric applications, Q. J. R. Meteorol. Soc., 131, 1539, 2005.

[119] Navas-Guzmán, F., Kämpfer, N., and Haefele, A.: Validation of brightness and physical temperature from two scanning microwave radiometers in the 60 GHz O2 band using radiosonde measurements, Atmospheric Measurement Techniques, 9, 4587–4600, doi: 10.5194/amt-9-4587-2016, 2016.

[120] Newsom, R., Turner, D., and Mielke, B.: Simultaneous analog and photon counting detection for Raman lidar, Appl. Opt., 48, 20, 2009.

[121] Nicolet, M.: On the molecular scattering in the terrestrial atmosphere: An empirical formula for its calculation in the homosphere, Planetary and Space Science, 32, 1467–1468, 1984.

[122] North and Erukhimova: Atmospheric Thermodynamics: Elementary Physics and Chemistry, Cambridge University Press, 2009.

[123] Parker: Concise Encyclopedia of Science & Technology, McGraw Hill, 1984.

[124] Penney, C. and Lapp, M.: Raman-scattering cross sections for water vapor, J. Opt. Soc. Am., 66, 422, 1976.

[125] Penney, C., Goldman, L., and Lapp, M.: Raman Scattering Cross Sections, Nature Physical Science, 235, 110, 1972.

[126] Petty, D. and Turner, D.: Combined analog-to-digital and photon counting detection utilized for continuous Raman lidar measurements, in: 23rd International Laser Radar Conference, Nara, Japan, 2006.

[127] Pinnick, R., Hill, S., and Pan, Y.: Fluorescence spectra of atmospheric aerosol at Adelphi, Maryland, USA: measurement and classification of single particles containing organic carbon, Atmos. Environ., 38, 1657, 2004.

[128] Pourney, J., Renault, D., and Orszag, A.: Raman-lidar humidity sounding of the atmospheric boundary layer, Appl. Opt., 18, 1141, 1979.

[129] Povey, A., Grainger, R., and Peters, D.: Estimation of a lidar's overlap function and its calibration by nonlinear regression, Appl. Opt., 51, 5130, 2012.

[130] Povey, A., Grainger, R., and Peters, D.: Retrieval of aerosol backscatter, extinction, and lidar ratio from Raman lidar with optimal estimation, Atmos. Meas. Tech., 7, 757, 2014.

[131] Povey, A. C.: The application of optimal estimation retrieval to lidar observations, Ph.D. thesis, University of Oxford, URL https://ora.ox.ac.uk/objects/ora:8548, 2013.

[132] Press, W., Teukolsky, S., Vetterling, W., and Flannery, B.: Numerical Recipes in Fortran 77: The Art of Scientific Computing, Cambridge University Press, 2nd edn., 1992.

[133] Racette, P. E., Westwater, E. R., Han, Y., Gasiewski, A. J., Klein, M., Cimini, D., Jones, D. C., Manning, W., Kim, E. J., Wang, J. R., Leuski, V., and Kiedron, P.: Measurement of Low Amounts of Precipitable Water Vapor Using Ground-Based Millimeter-wave Radiometry, Journal of Atmospheric and Oceanic Technology, 22, 317–337, doi: 10.1175/JTECH1711.1, 2005.

[134] Rees, D. and Fuller-Rowell, T. J.: The CIRA theoretical thermosphere model, Advances in Space Research, 8, 27–106, doi:10.1016/0273-1177(88)90039-7, 1988.

[135] Renault, D., Pourny, J., and Capitini, R.: Daytime Raman-lidar measurements of water vapor, Opt. Lett., 5, 233, 1980.

[136] Rodgers, C.: Inverse Methods for Atmospheric Sounding: Theory and Practice, World Scientific Publishing, London, 2000.

[137] Rose, T. and Czekala, H.: RPG-HATPRO Operating Manual, Radiometer

Physics, 8.04 edn., https://www.radiometer-physics.de/products/microwave-remote-sensing-instruments/radiometers/humidity-and-temperature-profilers/, 2009.

[138] Rose, T., Crewell, S., Löhnert, U., and Simmer, C.: A network suitable microwave radiometer for operational monitoring of the cloudy atmosphere, Atmospheric Research, 75, 183–200, doi:10.1016/j.atmosres.2004.12.005, 2005.

[139] Rosenkranz, P. W.: Water vapor microwave continuum absorption: A comparison of measurements and models, Radio Science, 33, 919–928, doi:10.1029/98RS01182, 1998.

[140] Russell, A. T. and Sica, R. J.: Observations of high-frequency temporal gravity wave spectra in the middle upper stratosphere, Journal of Geophysical Research, 106, 11,849–11,858, doi:10.1029/2000JD900644, 2001.

[141] Sakai, T., Nagai, T., and Nakazato, M.: Comparisons of Raman Lidar Measurements of Tropospheric Water Vapor Profiles with Radiosondes, Hygrometers on the Meteorological Observation Tower, and GPS at Tsukuba, Japan, J. Atm. & Oceanic Tech., 24, 1407, 2007.

[142] Schmidt, G. A., Ruedy, R. A., Miller, R. L., and Lacis, A. A.: Attribution of the present-day total greenhouse effect, Journal of Geophysical Research Atmospheres, 115, 1–6, doi:10.1029/2010JD014287, 2010.

[143] Schneebeli, M.: Advancements in Ground-Based Microwave Remote Sensing of the Troposphere - Calibration, Data Retrieval and Applications, Ph.D. thesis, Universitat Bern, URL http://publications.iap.unibe.ch/pub-detail.php?lang=en&id=3246, 2009.

[144] Scholz, T., Ehalt, D., Heidt, L., and Martell, E.: Water Vapor, Molecular Hydrogen, Methane, and Tritium Concentrations Near the Stratopause, Journal of Geophysical Research, 75, 3049–3054, 1970.

[145] Schroeder, J. and Westwater, E.: User Guide to WPL Microwave Radiative Transfer Software, 1991.

[146] Seidel, D. J., Sun, B., Pettey, M., and Reale, A.: Global radiosonde balloon drift statistics, Journal of Geophysical Research: Atmospheres, 116, doi:10.1029/2010JD014891, URL https://agupubs.onlinelibrary.wiley.com/doi/abs/10.1029/2010JD014891, 2011.

[147] Sherlock, V., Garnier, A., and Hauchecorne, A.: Implementation and validation of a Raman lidar measurement of middle and upper tropospheric water vapour, Appl. Opt., 38, 5838, 1999.

[148] Sherlock, V., Hauchecorne, A., and Lenoble, J.: Methodology for the independent calibration of Raman backscatter water-vapor lidar systems, Applied Optics, 38, 5816, doi:10.1364/ao.38.005816, 1999.

[149] Sherwood, S., Roca, R., Weckwert, T., and Andronova, N.: Tropospheric Water Vapor, Convection, and Climate, Reviews of Geophysics, 48, 2010.

[150] Sica, R. and Haefele, A.: Retrieval of temperature from a multiple-channel Rayleigh-scatter lidar using an optimal estimation method, Appl. Opt., 54, 2015.

[151] Sica, R. and Haefele, A.: Retrieval of water vapor mixing ratio from a multiple channel Raman-scatter lidar using an optimal estimation method, Appl. Opt., 55, 763, 2016.

[152] Sica, R., Sargoytchev, S., and Argall, S.: Lidar measurements taken with a large-aperture liquid mirror. 1: Rayleigh-scatter system, Appl. Opt., 34, 6925, 1995.

[153] Sica, R. J., Thayaparan, T., Argall, P. S., Russell, A. T., and Hocking, W. K.: Modulation of upper mesospheric temperature inversions due to tidal-gravity Wave interactions, Journal of Atmospheric and Solar-Terrestrial Physics, 64, 915–922, doi:10.1016/S1364-6826(02)00046-9, 2002.

[154] Sica, R. J., Argall, P. S., Bandoro, J., Iserhienrhien, B., Khanna, J., McCullough, E. M., Olofson, K. F., and Wing, R.: The New and Improved Purple Crow Lidar, in: AGU Fall Meeting Abstracts, vol. 2010, pp. A11A–0027, 2010.

[155] Simeonov, V., Larcheveque, G., and Quaglia, P.: Influence of the photomultiplier tube spatial uniformity on lidar signals, Appl. Opt., 38, 5186, 1999.

[156] Simeonov, V., Fastig, S., and Haefele, A.: Instrumental correction of the uneven PMT aging effect on the calibration constant of a water vapor Raman lidar, Proc. of SPIE, 9246, 2014.

[157] Sissenwine, N., Grantham, D., and Salmela, H.: Midlatitude Humidity to 32 km, Journal of the Atmospheric Sciences, 25, 1129–1140, 1968.

[158] Soden, B. J., Jackson, D. L., Ramaswamy, V., Schwarzkopf, M. D., and Huang, X.: The Radiative Signature of Upper Tropospheric Moistening, Science, 310, 841–844, doi:10.1126/science.1115602, URL https://science.sciencemag.org/content/310/5749/841, 2005.

[159] Solheim, F. and Godwin, J. R.: Passive ground-based remote sensing of atmospheric temperature, water vapor, and cloud liquid water profiles by a frequency synthesized microwave radiometerPassive bodengebundene atmosphärische Fernerkundung von Temperatur-, Wasserdampf- und Wolkenwasserprofilen mit eine frequenzsynthetisierten Mikrowellen-Radiometer, Meteorologische Zeitschrift, 7, 370–376, doi:10.1127/metz/7/1998/370, 1998.

[160] Solomon, S., Rosenlof, K. H., Portmann, R. W., Daniel, J. S., Davis, S. M., Sanford, T. J., and Plattner, G.-K.: Contributions of Stratospheric Water Vapor to Decadal Changes in the Rate of Global Warming, Science, 327, 1219–1223, doi:10.1126/science.1182488, URL https://science.sciencemag.org/content/327/5970/1219, 2010.

[161] Stelmaszczyk, K., Dell'Aglio, M., and Chudzynski, S.: nalytical function for lidar geometrical compression form-factor calculations, Appl. Opt., 44, 1323, 2005.

[162] Stocker, T. and Qin, D., eds.: Climate Change 2013: The Physical Science Basis (IPCC Report 2013), Cambridge University Press, 2013.

[163] Strauch, R., Derr, V., and Cupp, R.: Atmospheric Water Vapor Measurement by Raman Lidar, Remote Sensing of Environment, 2, 101, 1972.

[164] Synge, E.: A method of investigating the higher atmosphere, Phil. Mag., 9, 1014, 1930.

[165] Thayer, G. D.: An improved equation for the radio refractive index of air, Radio Science, 9, 803–807, doi:10.1029/RS009i010p00803, 1974.

[166] Thayer, J., Nielsen, N., and Warren, R.: Rayleigh lidar system for middle atmosphere research in the arctic, Opt. Eng., 36, 2045, 1997.

[167] Trenberth, K. E.: Atmospheric Moisture Residence Times and Cycling: Implications for Rainfall Rates and Climate Change, Climate Change, 39, 667–694, 1998.

[168] Trickl, T., Cooper, O. R., Eisele, H., James, P., Mücke, R., and Stohl, A.: Intercontinental transport and its influence on the ozone concentrations over central Europe: Three case studies, Journal of Geophysical Research (Atmospheres), 108, 8530, doi: 10.1029/2002JD002735, 2003.

[169] Turner, D. D. and Blumberg, W. G.: Improvements to the AERIoe thermodynamic profile retrieval algorithm, IEEE Journal of Selected Topics in Applied Earth Observations and Remote Sensing, 12, 1339–1354, doi:10.1109/JSTARS.2018.2874968, 2019.

[170] Tuve, M., Johnson, E., and Wulf, O.: A New Experimental Method for Study of the Upper Atmosphere, J. Geophys. Res., 40, 1935.

[171] VanKerkhove, J.: Characterizing the Purple Crow Lidar Raman channels to investigate potential sources of wet bias, Master's thesis, University of Western Ontario, 2015.

[172] Vaughan, G., Wareing, D., and Thomas, L.: Humidity measurements in the free troposphere using Raman backscatter, Q. J. R. Meteorol. Soc., 114, 1471, 1988.

[173] Venable, D., Whiteman, D., and Calhoun, M.: Lamp mapping technique for independent determination of the water vapour mixing ratio calibration factor for a Raman lidar system, Appl. Opt., 50, 2011.

[174] Veselovskii, I., Kolgotin, A., and Griaznov, V.: Inversion with regularization for the retrieval of tropospheric aerosol parameters from multiwavelength lidar sounding, Appl. Opt., 41, 3685, 2002.

[175] Vogelmann, H. and Trickl, T.: Wide-range sounding of free-tropospheric water vapor with a differential-absorption lidar (DIAL) at a high-altitude station, Appl. Opt., 47, 2116–2132, doi:10.1364/AO.47.002116, URL http://ao.osa.org/abstract.cfm?URI=ao-47-12-2116, 2008.

[176] Voirin, J.: Water Vapor Calibration of the Raman LIDAR for meteorological Observation Master Internship Report, Tech. rep., MeteoSwiss, 2017.

[177] Vomel, H. and Jeannet, P.: Monitoring Atmospheric Water Vapour: Ground-Based Remote Sensing and In-situ Methods, chap. 3: Balloon-Borne Frostpoint Hygrometry, Springer Science, 2013.

[178] Vömel, H., Fujiwara, M., Shiotani, M., Hasebe, F., Oltmans, S. J., and Barnes, J. E.: The behavior of the Snow White chilled-mirror hygrometer in extremely dry conditions, Journal of Atmospheric and Oceanic Technology, 20, 1560–1567, doi:10.1175/1520-0426(2003)020⟨1560:TBOTSW⟩2.0.CO;2, 2003.

[179] Vomel, H., David, D., and Smith, K.: Accuracy of tropospheric and stratospheric water vapour measurements by the cryogenic frost point hygrometer: Instrumental details and observations, J. Geophys. Res., 112, 8305, 2007.

[180] von Clarmann, T.: Smoothing error pitfalls, Atmospheric Measurement Techniques, 7, 3023–3034, doi:10.5194/amt-7-3023-2014, 2014.

[181] Walker, M., Venable, D., and Whiteman, D.: Gluing for Raman Lidar systems using the lamp mapping technique, Appl. Opt., 53, 8535, 2014.

[182] Wallace and Hobbs: Atmospheric Science: an introductory survey, Academic Press, New York, 2006.

[183] Wandinger, U. and Ansmann, A.: Experimental determination of the lidar overlap profile with Raman lidar, Appl. Opt., 41, 511, 2002.

[184] Weitkamp, C., ed.: Lidar: Range-Resolved Optical Remote Sensing of the Atmosphere, Springer Science, 2005.

[185] Whiteman, D.: Examination of the traditional raman lidar technique, II: Evaluating the ratios for water vapour and aerosols, Appl. Opt., 42, 2593, 2003.

[186] Whiteman, D.: Examination of the Traditional Raman lidar technique. I. Evaluating the temperature- dependent lidar equations, Appl. Opt., 42, 2003.

[187] Whiteman, D., Melfi, S., and Ferrare, R.: Raman lidar system for the measurement of water vapor and aerosols in the Earth's atmosphere, Appl. Opt., 31, 3068, 1992.

[188] Whiteman, D., Cadrirola, M., and Venable, D.: Correction technique for Raman water vapor lidar signal-dependent bias and suitability for water vapor trend monitoring in the upper troposphere, Atmos. Meas. Tech., 5, 2893, 2012.

[189] Whiteman, D. N., Veselovskii, I., Cadirola, M., Rush, K., Comer, J., Potter, J. R., and Tola, R.: Demonstration measurements of water vapor, cirrus clouds, and carbon dioxide using a high-performance raman lidar, Journal of Atmospheric and Oceanic Technology, 24, 1377–1388, doi:10.1175/JTECH2058.1, 2007.

[190] Whiteman, D. N., Rush, K., Rabenhorst, S., Welch, W., Cadirola, M., McIntire, G., Russo, F., Adam, M., Venable, D., Connell, R., Veselovskii, I., Forno, R., Mielke, B., Stein, B., Leblanc, T., McDermid, S., and Vömel, H.: Airborne and ground-based measurements using a high-performance raman lidar, Journal of Atmospheric and Oceanic Technology, 27, 1781–1801, doi:10.1175/2010JTECHA1391.1, 2010.

[191] Whiteman, D. N., Venable, D., and Landulfo, E.: Comments on "Accuracy of Raman lidar water vapor calibration and its applicability to long-term measurements", Applied Optics, 50, 2170–2176, doi:10.1364/AO.50.002170, 2011.

[192] Wing, R.: Multi-sensor calibration and validation of the UWO-PCL water vapour lidar, Master's thesis, University of Western Ontario, 2012.

[193] Wu, M. F., Geller, M. A., Nash, E. R., and Gelman, M. E.: Global atmospheric circulation statistics-Four year averages, Tech. rep., NASA, nASA technical memo, NASA TM 100690, 1987.

Appendix A

Practical Lidar Applications: the Purple Crow Lidar

This appendix provides a detailed overview of the Purple Crow Lidar (PCL) system. In addition to a description of the instrumental components, data acquisition, processing, and calibration, it also includes some instrumental upgrades, as well as some processing and calibration updates which have been carried out since starting my graduate program in this research group. Although the PCL was not used in fulfilling the goals of this thesis, this appendix may be relevant for understanding how lidar systems are operated, maintained, and calibrated, as well as how the measurements are processed and analyzed. This appendix may also serve as a guide for those who wish to work with this system in the future.

A.1 The Purple Crow Lidar - Instrument Overview

A.1.1 History of PCL

PCL was built in 1992 at the Delaware observatory (42.52° N, 81.23° W, 225 m elevation), located near the community of Delaware, approximately 20km southwest of London, Ontario. When observations began in 1993, it consisted of Rayleigh-scatter and Sodium-resonance-

fluorescence lidars, capable of measuring atmospheric temperature and density fluctuations from the upper Stratosphere into the thermosphere [31]. The Sodium-resonance-fluorescence system was able to measure temperature and sodium density between 83-100 km [8], with measurements of density fluctuations used to observe gravity wave spectra [27] [32]. In 1999, two detectors were added to the system for monitoring Raman-backscatter of nitrogen and water vapor. These detectors are used in determining water vapor mixing ratio profiles into the lower Stratosphere [13][9]. Analysis of the attenuation from the mechanical chopper used by the Rayleigh system allows for the computation of the lidar ratio, and consequently aerosol measurements, including stratospheric aerosols originating from the 2008 Kasatochi eruption [16].

Due to unsuitable conditions, the components of the PCL were moved to its current location, approximately 9km north of the University of Western Ontario campus, in the summer of 2010. This site, referred to as the Echo Base observatory (43.07° N, 81.34° W, 280 m elevation), is closer to the university and is on the premises of the Environmental Sciences Western Field Station. The move also provided an opportunity to upgrade the system. The transmitter was replaced with a powerful experimental laser (nominally operating at 2.5 times the power of the previous laser) [33]. A new geothermal cooling system was installed to ensure stability of the laser temperature as well as a new beam expander [47]. Counting electronics were also upgraded, improving the height resolution of measurements [33]. The detector for the Sodium system was removed to make way for a second Rayleigh system detector (referred as the ”Low Rayleigh” channel) for testing the linearity of the original Rayleigh detector (referred to as the ”High Rayleigh” channel) and as means of gauging alignment of the system [47]. Table A.1 lists the changes made for the Echo Base observatory.

A.1.2 PCL Instrumentation

This section describes the components specific to the PCL system. Although all atmospheric lidars are unique, this section provides an overview of the components found in most of these

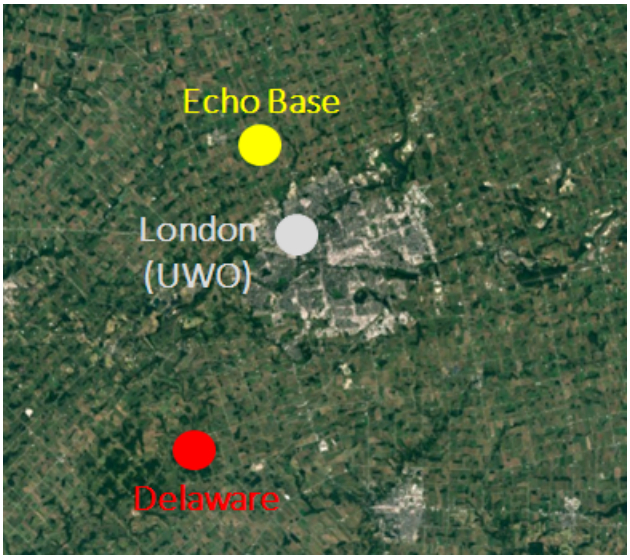

Figure A.1: Map of the former PCL observatory location (Delaware) and the current location (Echo Base), with respect to the UWO campus.

Observatory	Delaware	Echo Base
Coordinates	42.52°N, 81.23°W	43.07°N, 81.34°W
Elevation	225 m	280 m
Laser Power	12 W	30 W
Power-aperture product	66 W/m^2	160 W/m^2
High Rayleigh height resolution	24 m	7.5 m
Nitrogen res	250 m	7.5 m
Water Vapour res	250 m	24 m
Low Rayleigh res	—	24 m

Table A.1: Comparison between the old system (Delaware) and new system (Echo Base) at PCL. (Adapted from [36].)

systems.

Laser Transmitter

As lasers can be designed with low beam divergence, narrow spectral width, and short, intense pulses, they are advantageous over white light for atmospheric ranging [7]. PCL uses an Nd:YAG (Neodymium: Yttrium-Aluminum-Garnet) solid state laser, custom manufactured by Litron Lasers Ltd. A nonlinear potassium titanyl phosphate ($KTiOPO_4$) crystal doubles the frequency, from a fundamental 1064 nm to a 532 nm second harmonic [47]. In general, 532 nm Nd:YAG lasers are less popular than UV lasers for water vapour measurements, since the Raman cross section is smaller at longer wavelengths and detector efficiency is usually lower [40]. However, backscatter induced by UV light is much more susceptible to fluorescence. Originally utilizing a laser with an output of 600 mJ/pulse at a 20 Hz repetition rate (12 W power), the new Litron laser produces more than 1 J/pulse at 30 Hz (30 W power) [31][47].

Beam Path

The laser beam, exiting its housing with a 12 mm diameter and divergence exceeding 0.5 mrad, passes through a beam expander which expands the diameter to 60 mm and reduces the divergence to 17 μrad [47]. The beam is then directed into the sky through a series of mirrors (Figure A.3). In order to receive the maximum possible signal, the laser beam should be co-aligned with the rotational axis of the telescope's receiver [7]. In the case of PCL, the final mirror directing the beam vertically into the sky is motorized, so that beam alignment can be controlled by a computer.

Receiver

The receiver plays a big role in determining the measurement capabilities of a lidar. The maximum measurement range is proportional to the power-aperture product, the product of laser power and receiver area [20]. However, large, custom-built mirrors are profoundly ex-

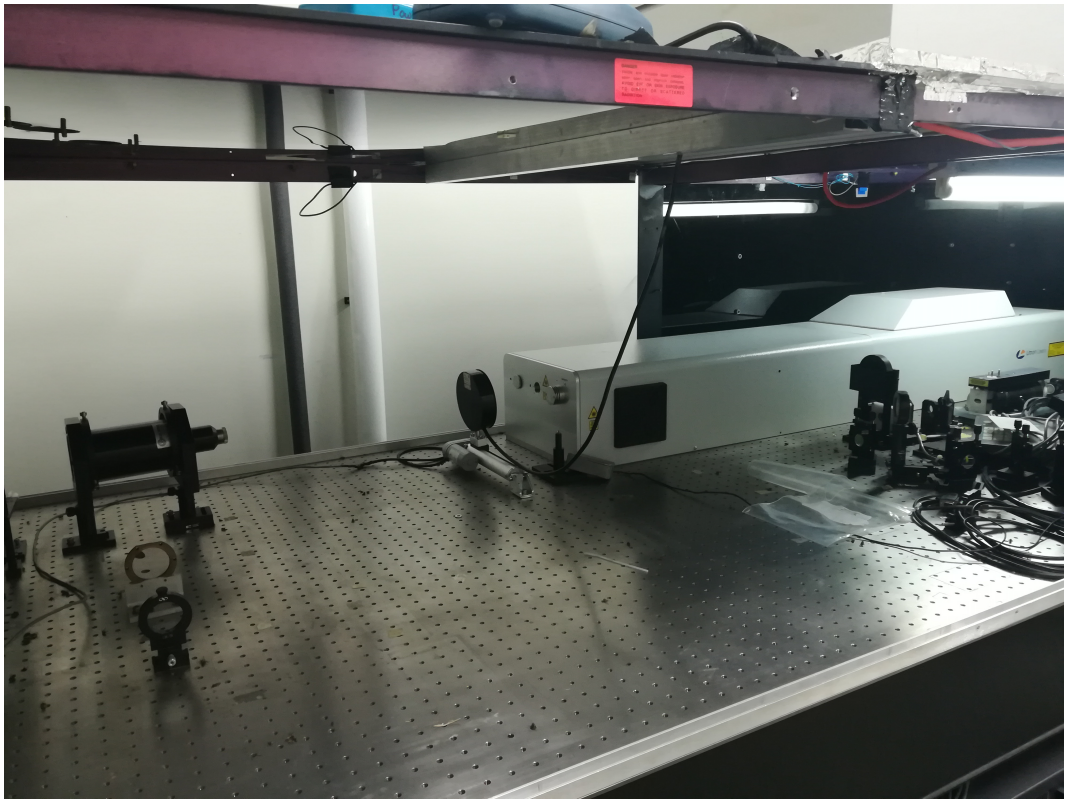

Figure A.2: Image of the *Litron* Nd:YAG laser at PCL (the white box), with a power meter and beam expander to the left. The optics to the right of the laser are components from a previous laser system.

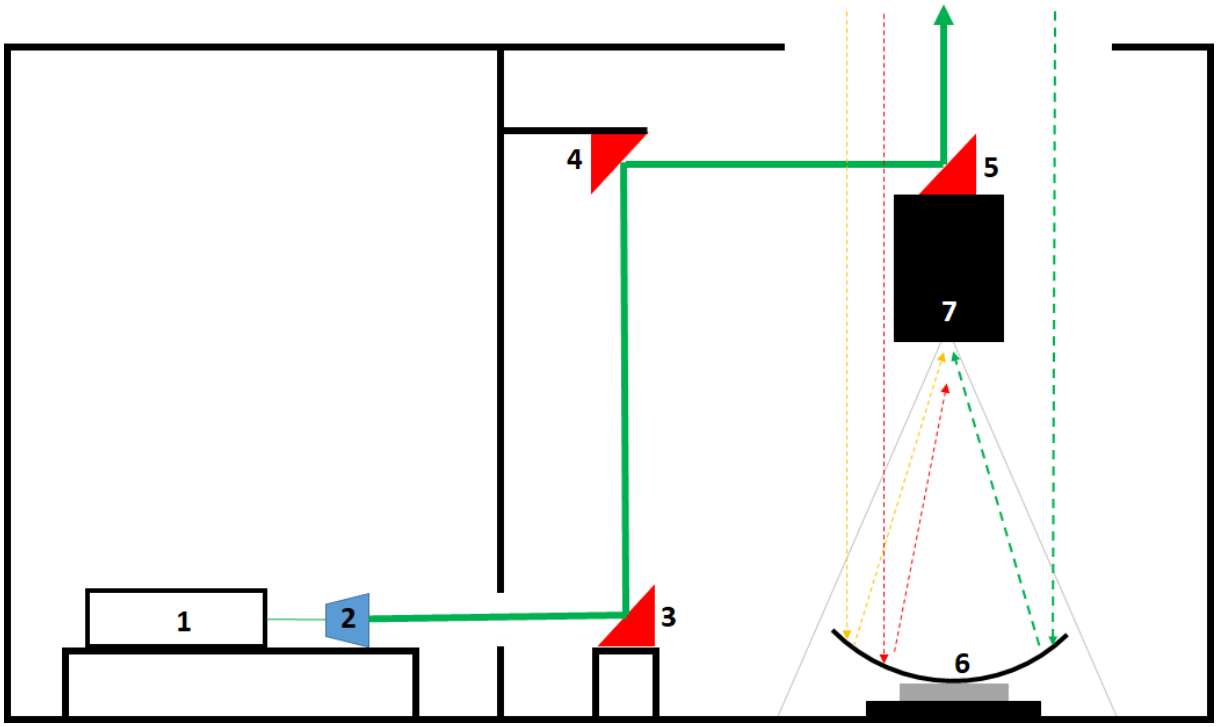

Figure A.3: Diagram of the transmitter-receiver sysytem for the PCL. After leaving the laser housing (1), the beam is expanded (2), and directed by mirrors (3,4,5) skyward. The final mirror (5) is motorized and can be adjusted to optimize alignment. Backscatter is collected by the receiver (6) and focused through a pinhole aperture into a box containing detectors (7).

pensive, especially considering the maintenance and costs of re-coating. The team at UWO therefore sought an alternate approach to building a large aperture receiver. A team at Laval University originally investigated using liquid mirrors as astronomical telescopes in the 1980s. In a rotating liquid, the summation of the gravitational and centrifugal components yields a parabolic fluid surface [12]. If a reflective liquid (such as mercury) is placed in a uniformly rotating container, the liquid would spread out and conform to a parabolic shape, rendering a liquid mirror telescope. In addition, the container's rotational speed would determine the telescope's focal length, by considering gravitational and centrifugal accelerations:

$$L = \frac{g}{2\omega^2} \tag{A.1}$$

where ω is the mirror's angular velocity, and g is gravitational acceleration [11]. As a result, the PCL is unique among atmospheric lidars, not only for employing a liquid mirror telescope, but also having a receiver with a diameter of 2.65 m, making it one of the largest telescopes actively used among atmospheric lidars [31].

Aside from the relatively low initial cost of the mirror (costing approximately $32,000 USD in 1992 [11]), a major advantage of a liquid mercury mirror is the ease of cleaning its surface. Cleaning involves stopping the mirror, and using a partially-weighted plastic tube to skim debris, such as insect matter and dust, from the mirror surface. The debris is collected and wiped up with industrial wipes, with any remaining material sucked up using a vacuum pump. Once the mirror is pristine, it can immediately be spun up, and used for operation as soon as its rotation stabilizes.

Despite the low installation costs and ease of cleaning, it can be challenging to for the mirror to maintain a stable rotation rate. For the PCL's 2.6 m diameter receiver, the ideal rotation period is 6.350 s. To get the mirror spinning smoothly, the roughly 100 kg mirror container must rest on a high-quality air bearing, fed by a reliable supply of dry and particulate-free air. The air is supplied by an oil-free compressor, stored in a pressure tank, and then passed

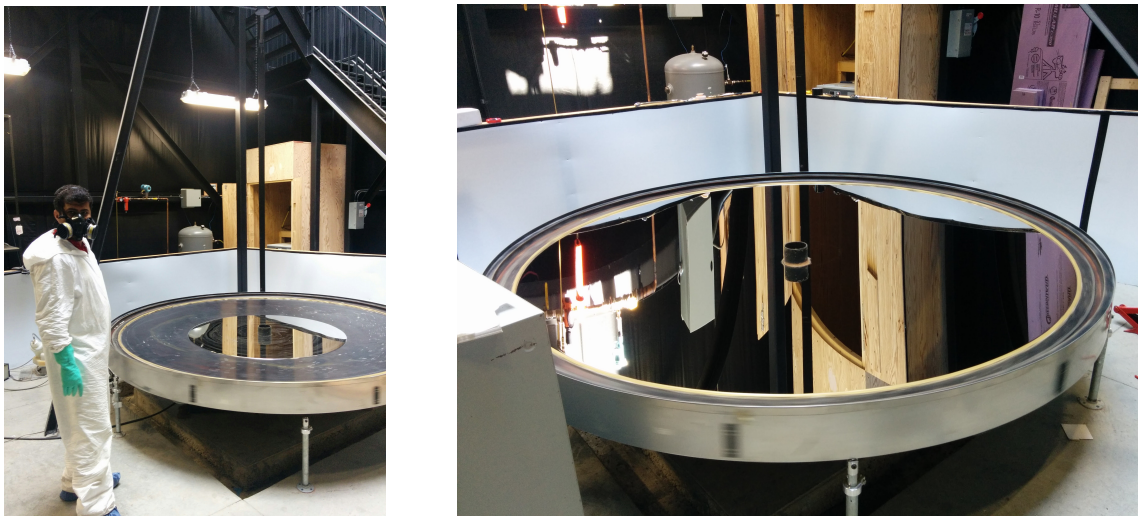

Figure A.4: Left: PCL alumnus Ali Jalali in protective gear spinning up the mirror after cleaning. Right: Mirror spinning smoothly.

through a series of desiccant and particulate filters as well as a pressure regulator before being sent to the bearing [47]. Failure of one or more components in this system may jeopardize the quality of the air bearing and cause it to seize. Measures to combat this threat are mentioned in Section A.1.4. Even if there are no issues with the air bearing, the mirror should rotate with a tolerance within 0.005 s in order to kept the mirror in focus. This is addressed by measuring the rotation period and implementing a feedback control which can remotely speed up or slow the motor based on the measured period.

Signal Filtering

After backscatter is collected in the receiver, it is focused, directed toward its intended channel detector, and filtered. Filters are necessary for blocking spurious light and reducing background light, thereby increasing the signal-to-noise ratio. Generally, filtering is accomplished via interference filters, which block virtually all light aside from a narrow band around the specific Rayleigh or Raman Stokes wavelength. In some systems, a grating polychromator is used. A grating is can be advantageous to use, as it does not have a coating that will degrade over time, nor is there a gradual shift of the peak wavelength over time [15]. Intense backscatter from lower altitudes, particularly in Rayleigh systems, can cause instrumental issues (see Sec-

tion A.2.2). Such effects can be reduced or even eliminated by installing a mechanical chopper in the beam path, to block returns from the lowest altitudes. [31]

Figure A.6 shows a schematic of the signal filtering for the PCL detection system (contained in the detector box, item 7 in Figure A.3). Backscattered signal enters through a pinhole aperture and is collimated. Light less than 541 nm is transmitted through a beam splitter and sent through a chopper, which is generally set to block intense returns below 25 km. The Rayleigh backscatter then passes through a 5% mirror before being filtered via interference filter and detected by PMT. The Raman signal is channeled by a 630 nm beam splitter, sending nitrogen and water vapor backscatter to their respective PMTs.

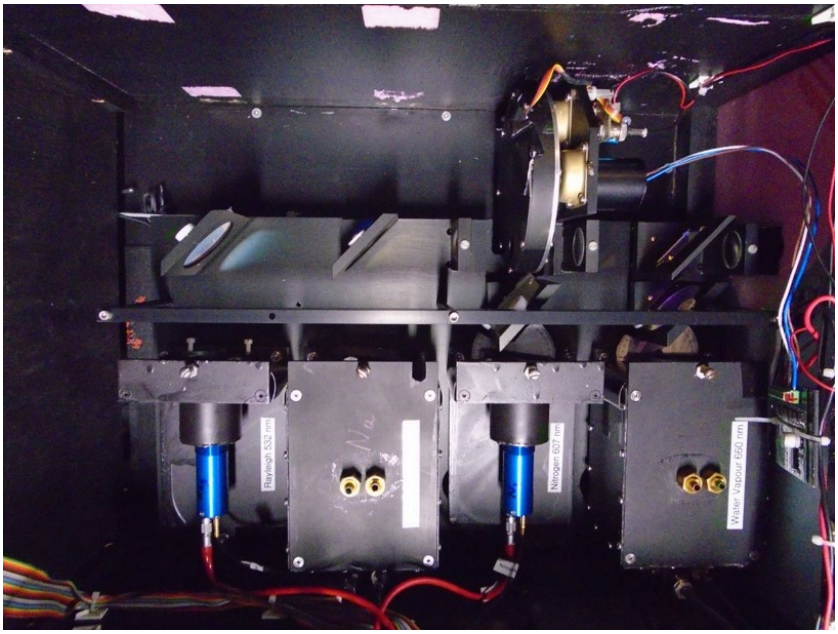

Figure A.5: Image of the detector box.

Comparison between PCL and RALMO

Table A.2 compares some of the important properties between the RALMO (described in Section 3.1.1) and PCL lidar systems. A much larger primary receiver and more powerful laser gives PCL an impressively large power-aperture product, allowing it to detect signal much higher up than RALMO. Due to its UV laser and narrowband filtering, RALMO can operate in

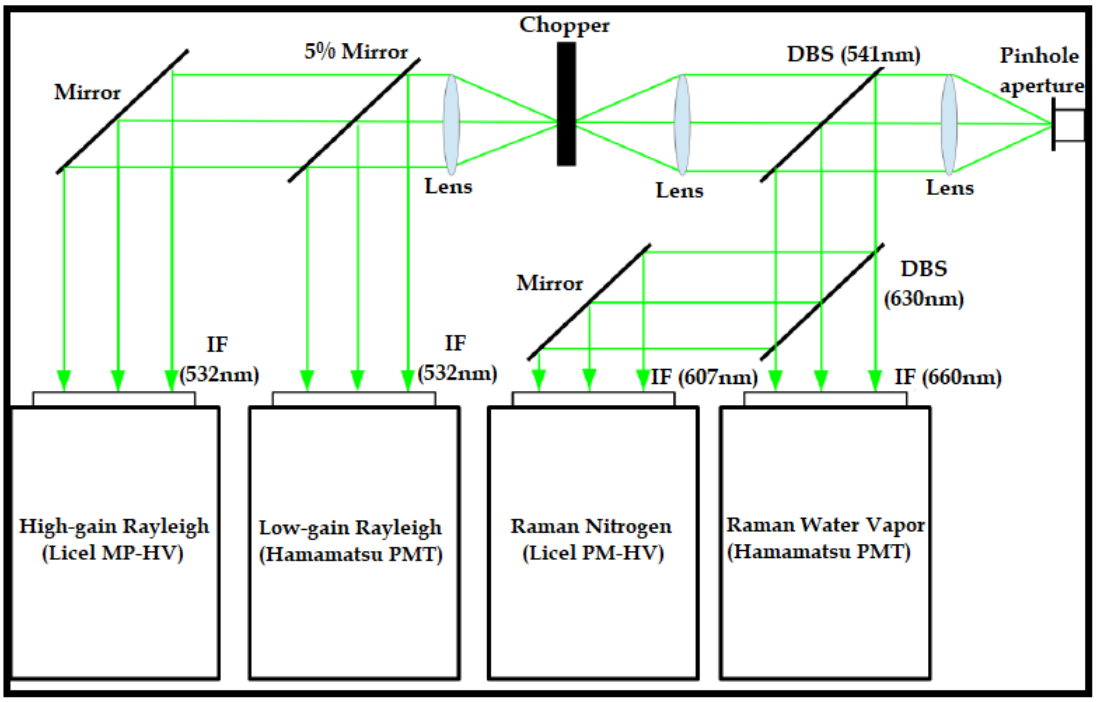

Figure A.6: Schematic of the detector box. (DBS=Dichroic BeamSplitter, IF=Interference Filter, PM=PhotoMultiplier) Adapted from [36]

daytime as well as nighttime. Additionally, the RALMO system is set up to run continuously, with uptime of approximately 50%. PCL, on the other hand, only operates on a few clear nights each month. Furthermore, as Payerne is a weather station, RALMO has the advantage of being collocated with other humidity-monitoring instruments (including a HATPRO radiometer - Section 3.2.1). Although this thesis used RALMO in order to carry out an integrated lidar-radiometer retrieval, further work may include a similar integrated retrievals using PCL if a radiometer were assembled at the Echo Base observatory.

A.1.3 Data Acquisition

PMTs

In lidar systems, backscatter is usually detected by photomultiplier tubes (PMTs). PMTs are vacuum tubes containing a photocathode at one end. When a photon reaches the photo-

Lidar	RALMO	PCL (Echo Base)
Coordinates	46.81° N, 6.95° E	43.07°N, 81.34°W
Elevation	491 m	281 m
Aperture size	0.3 m^2	5.5 m^2
Laser power	9 W	30 W
Power-aperture product	2.7 W/m^2	160 W/m^2
Laser wavelength	355 nm	532 nm
Signal filtering	polychromator	interference filter
Operation times	Day/Night	Clear Nights
Autonomous?	Yes	No
Collocated Instruments?	Yes	No

Table A.2: Comparison between RALMO and PCL systems.

cathode, electrons are ejected, which cascade along a series of dynodes, causing the ejecting of more electrons and secondary cascading. At the end of tube, the last electrons reach the anode, producing a current pulse in the load resistor. The number of electrons released by the intermediate dynodes is related to the gain, the ratio between the anode and cathode current, with an amplification in the current generally ranging from 10^3 to 10^8 [1]. Since the photocathode has a low work function, thermal electrons are emitted at room temperature, producing a small dark current [20].

Transient Recorders

Signal detected by the PMTs is then sent to the transient recorders, which amplify and digitize the signal, and then sum or average it in successive time bins. The counts in these time bins are equal to counts in altitude bins, based on the pulse relay time:

$$t_i = 2 \cdot \frac{z_i}{c} \tag{A.2}$$

At PCL, the low-level Rayleigh and water vapour channels use transient recorders manufactured by Stanford Research Systems, while the high-level Rayleigh and nitrogen channels use transient recorders from Licel GmbH.

Counting Modes: Photon counting (PC)

In the photon-counting detection mode, a signal pulse above the preset discriminator level is counted as one photocount (Figure A.8). However, if the count rates are greater than the transient recorder's detection rate, such that signal pulses are overlapping, the system will not be able to distinguish between the pulses, and it would still be counted as one photocount. As a result, this technique works well for low count rates, where the interval between incoming pulses is greater than the discriminator's resolution. However, at high count rates, non-linearity corrections are required (see Section A.2.1).

Counting Modes: Analog

Licel transient recorders also have the capacity to use an analog detection mode in parallel with PC detection, where the signal is measured as a voltage instead of discrete pulses. The signal is recorded using an analog-to-digital converter in binary code, in which each of the 2^{24} bits correspond to a specific voltage, with a maximum value set by the user. Although this mode is less sensitive and has a greater uncertainty at low count rates, the response is linear for high count rates and does not require a correction [4].

A.1.4 System Upgrades

Since my arrival to UWO in 2013, there have been a few noteworthy improvements to the PCL system.

Automation of the alignment process

Prior to each operation run, the alignment of the lidar must be fine-tuned by adjusting the position of the final mirror directing the laser beam skyward. As this procedure takes up valuable observing time, some work has been devoted to automating the alignment process [18], however it has yet to be incorporated into routine operation.

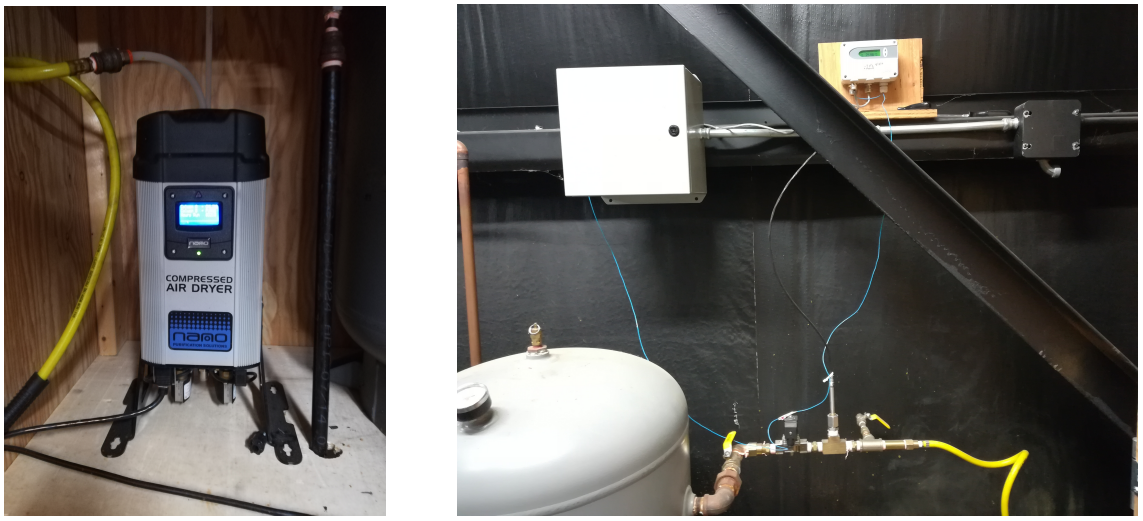

Figure A.7: Left: Air Dryer for bearing air supply. Right: Moisture fail-safe, including a dew monitor and solenoid valve.

Air bearing system

As the air bearing is crucial for a smoothly rotating liquid mercury mirror, it is of utmost importance to ensure its air supply is clean. If not, the bearing may seize, which requires the disassembly of the mirror and detector box systems in order to service the bearing. Re-assembly then requires re-leveling of the container and re-alignment of the detector box, which is highly labor-intensive. To limit the possibility of bearing seizure, a new air dryer as well as a new dewpoint meter and electronic solenoid valve were added to the air line. If the air dryer, which nominally dries the air to a dewpoint of -70°C, fails and the dewpoint meter registers a dewpoint above -25°C, it will trigger the electronic valve to shut. This effectively acts as a fail-safe for the air supply line, shutting off the air supply and halting the mirror before moist air can reach the bearing. Additionally, portions of hose were replaced with brass piping to prevent the possibility moisture seeping into the air line. A partially climate-controlled shed was built by Brian Dalrymple and Frank Van Sas from UWO physics department's machine shop to house the compressor and air dryer to insulate them from extreme temperatures experienced in the mirror room.

White Light calibration

It is important to monitor the performance of the optics and detectors in the data acquisition system, as their efficiency may degrade over time. One way to monitor instrument changes over time and provide a means of internal calibration is by using a white light calibration.

A 50 W Quartz Tungsten Halogen white light was originally mounted in 2012, during a validation campaign (See Section A.3.2 for more on the ALVICE campaign). This was re-mounted in 2017, attached to the detector box tripod, directed toward the mirror. It can now be turned on from the control room, and is set up so that signal from the white light runs is saved in the same manner as the routine operation data acquisition files, making it easy to integrate these calibration counts into the data processing.

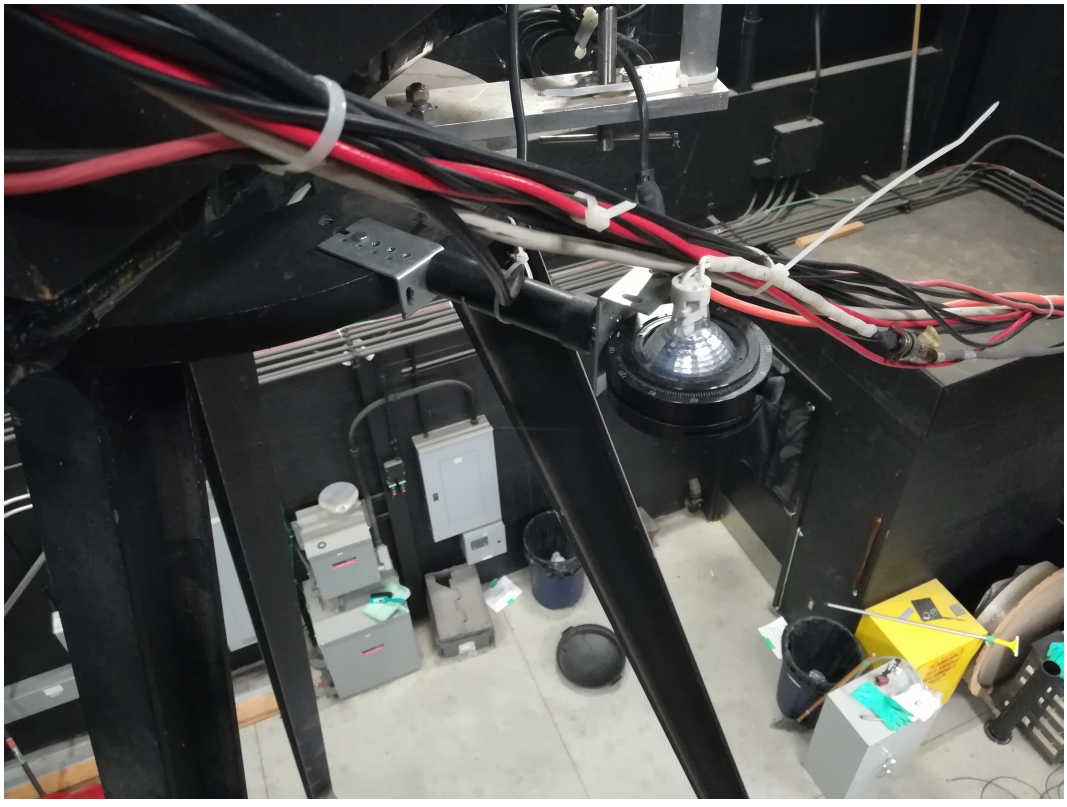

Figure A.8: The white light calibration lamp, mounted to the top of the tripod and directed downward toward the mirror.

A.2 Processing of Raman Lidar measurements

A.2.1 Low-level processing

As seen in equation 2.14, the determination of WVMR via Raman lidar requires nitrogen and water vapour count profiles. However, this equation requires corrected count profiles. This section discusses the process of correcting the raw count profiles, accounting for instrumental effects.

For the PCL system, signal from the low-gain Rayleigh and Raman water vapor channels (See Figure A.6) is collected and binned by 2 Stanford Research Systems SR430 Multichannel Scaler/Averagers [2] via the PC counting mode, at a height resolution of 24 m. The high-gain Rayleigh and Raman nitrogen channels send counts through a newer Licel TR20-160 Transient Recorder [5], which includes analog and PC counting modes at a vertical resolution of 7.5 m. The height-dependent signal backscatter is summed up into 1 minute scans (or 1800 laser shots).

This section will follow the processing of counts from June 4, 2012, as this was clear night with a long observation time. Examples of the raw PC counts for each of the channels are shown in Figure A.9. Note that the intense Rayleigh signal in the lower atmosphere is blocked by a mechanical chopper set around 20 km. Also note how much the water vapor signal varies over time.

Count conversion

One of the first steps in processing is to convert the transient recorder's photo count into a physical unit. In the Licel transient recorder, PC counts are expressed in terms of counts per bin per laser shot. The PC counts can be converted to MHz (adapted from [24]):

$$counts\ [\text{MHz}] = \text{Raw counts} \cdot \frac{c}{2 \times 10^6 \times f \times \Delta z \times \Delta t} \tag{A.3}$$

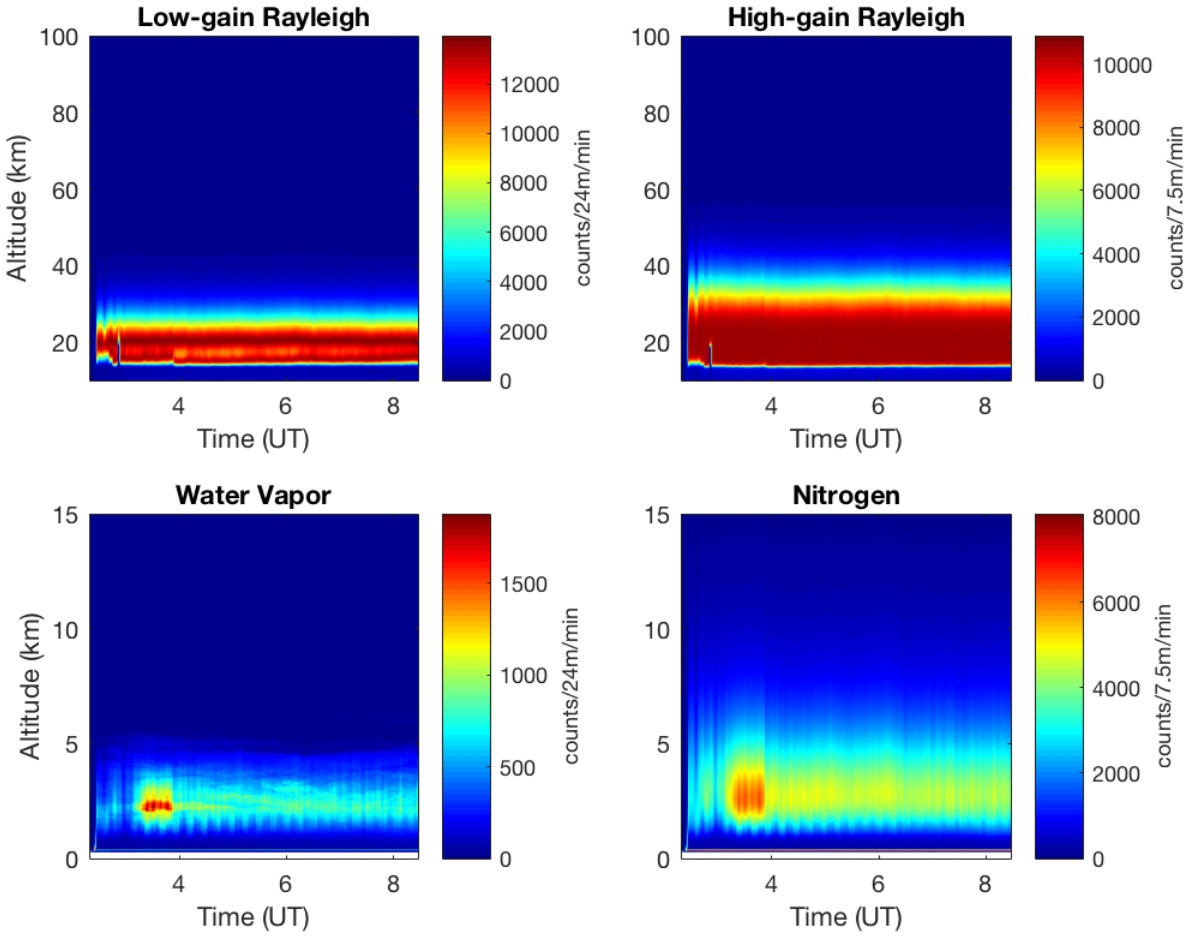

Figure A.9: Raw PC counts for each of the channels in PCL on June 4, 2012.

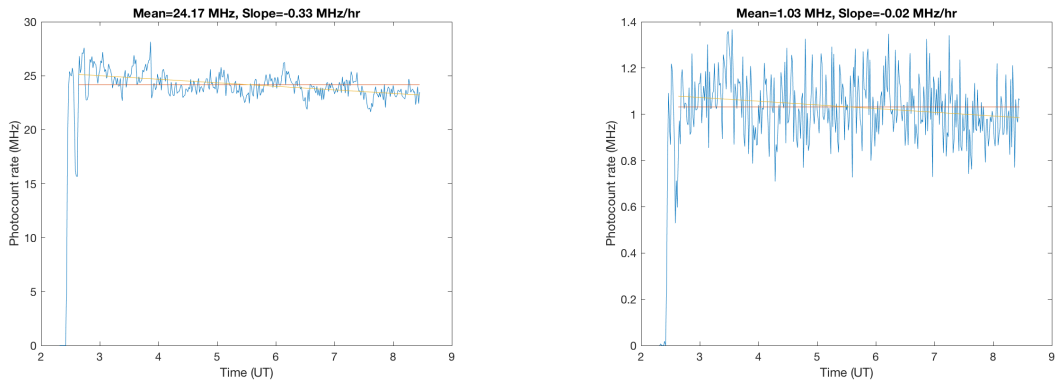

Figure A.10: High-gain Rayleigh PC counts at 40 km (left) and Nitrogen PC counts at 15 km (right) as a function of scan.

where c is the speed of light, f is the laser's repetition rate, Δz is the initial altitude resolution (7.5 m for Licel, 24 m for Stanford), and Δt is the initial time resolution (time for each scan is 1800 laser shots, or 1 minute).

The analog signal can be converted to a voltage by:

$$counts\ [\text{mV}] = \text{raw counts} \times \frac{range}{2^{ADCbits} - 1} \tag{A.4}$$

where *range* is the transient recorder's maximum range setting and, and $2^{ADCbits} - 1$ is the maximum bit value [3].

Scan Filtering

Although water vapor can be highly variable over the course of a night, the Rayleigh and Raman nitrogen signals should not change much on such timescales. As seen in Figure A.9, the first few scans show very low count rates in all the channels. Figure A.10 more clearly shows a dramatic jump in the count rates at specific altitudes for the High-gain Rayleigh and Nitrogen channels. Possibly due to instrumental effects such as tuning the motorized mirror's alignment, these first few scans are not representative of the true atmosphere and must be removed before proceeding with data processing.

Removal of these bad scans is an essential quality control measure during the low-level data

processing. This can be accomplished by plotting the count rates for each scan. For nitrogen counts, the trend should be log-linear, such that count rate decreases smoothly with altitude. Scans with abnormally large background counts, from bright sources such as the Moon, should also be removed [6]. Unless there is no signal or an egregious artifact or no signal at all, all water vapor counts can be considered good, as its signal is so tenuous.

Aside from the time consuming task of manually checking each scan, the criteria for determining whether a scan is good or bad is subjective. In Figure A.11, left plot is clearly a good count profile, while the middle plot is bad. The rightmost plot, although it has the same shape as the good scan, has a lower signal level - possibly due to a dip in the laser power. Other considerations include dealing with thin clouds, which may cause the signal to dip at certain altitudes. The inclusion of these scans in the processing that follows without their proper characterization may adversely affect the calculation of the WVMR.

One possible solution is the use of machine learning to automate this process, where a training set of examples of good, bad, and in-between scans is created, on which the computer can be trained to classify new scans. Initial testing of supervised and unsupervised methods has already been performed on approximately 2000 scans of PCL Rayleigh and Nitrogen channel counts, with accuracy scores in excess of 90% [17].

Additionally, the lowest few 100 meters of the profile are generally removed due primarily to a large geometric overlap, though strong PMT electronic ringing may also be a concern for analog measurements at these lowest altitudes [24].

Channel Delay

Due to differences in the recording mechanisms of the data acquisition electronics, the channel altitude profiles may be slightly offset. The offset can be estimated by triggering a diagnostic spike via a function generator and shifting the height profiles so that the spikes line up [24]. The delay was tested for the Licel transient recorders at PCL by summer research student, Sean Hartery, in 2013. The delay between the PC and analog modes of the nitrogen

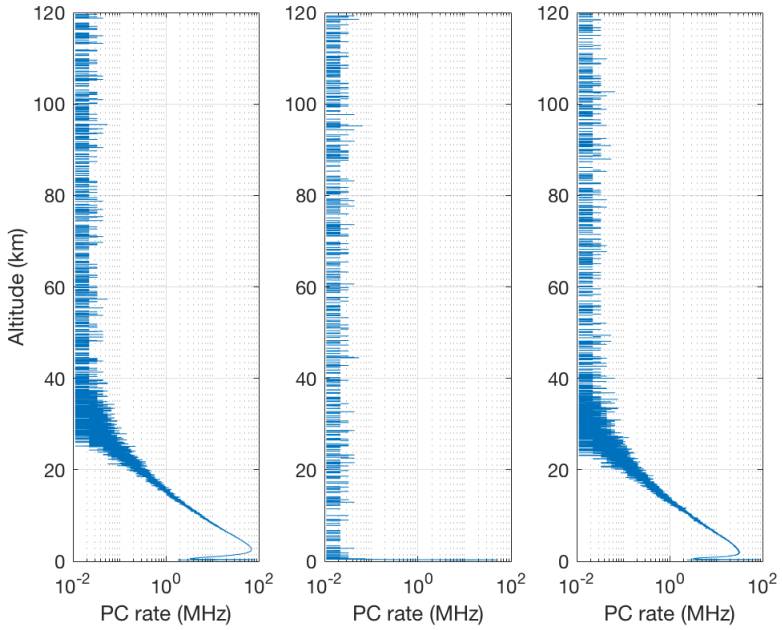

Figure A.11: Raw PC counts for each of the channels in PCL on June 4, 2012.

channel is 68.1±0.5 m, while the Rayleigh channel delay is 73.6±0.4 m [36]. At the Howard University Raman Lidar (HURL), based in Beltsville, Maryland, the analog and PC channels were offset by 3 bins (22.5 m), while the ALVICE scanning lidar channels were offset by 7 bins (52.5 m) [39].

Background

Determination and subtraction of the background counts for the PCL data channels is mentioned in my Master's thesis (See Section 1.4.2 [36]), along with a discussion of handling pecularities in the background values (See Section 3.1.3 of [36]).

Analog Processing: Transient Recorder Warm-Up

As with most instruments, the Licel transient recorder needs time to warm up before it can be used in data acquisition. As the system takes time to thermally stabilize, dark analog background counts taken immediately after turning the unit on may be lower than those measured after the recorder has stabilized. In the case of the HURL, the dark analog signal from the

nitrogen and water vapour channels would both take approximately 1 hour to reach a stable level [39]. In the case of PCL, the Nitrogen analog signal takes approximately 50 minutes to warm up, and the effect is negligible for the High-gain Rayleigh channel [36]. Thus, to avoid incorrect analog dark counts in the first few scans, a scaling correction can be applied, or one can simply ensure the transient recorder has been running for at least 1 hour before use.

PC Processing: Dead time Correction

Many transient recording systems, including the Licel instruments, are non-paralyzable, making the correction less computationally consuming [25].

The effects of a deadtime correction on the raw signal from June 4, 2012 is shown in Figure A.12. In this case, the water vapor and nitrogen signals show increases of approximately 1.7% and 28% respectively. This correction also assumes the manufacturer's deadtime of 4 ns [25]. Recent developments have allowed for the retrieval of the dead time value [29][30].

The effects of pulse pileup can also be gauged empirically by directly comparing the measured PC count rates to the *true* count rates. This eliminates the need for using the aforementioned equations involving a fixed deadtime value. For Licel systems, or other systems with dual PC and analog capabilities, the PC and analog channels can be compared such that PC comprises the measured count rates, with analog comprising the scaled, true count rates as analog is not susceptible to pulse pileup. For systems without analog channels, the empirical test can be carried out by comparing the unattenuated PC signal with neutral density-filtered (attenuated) PC signal [31][13][41]. In this case, the unattenuated signal still represents the measured/observed count rate, while the attenuated signal would be the true count rate, since the count rate is now much lower and less vulnerable to saturation. If saturation is evident, the relation between observed and true counts will be nonlinear, and should be approximated by either the paralyzable or non-paralyzable dead time expression. At PCL, a dead time correction curve is made by using a function generator to pulse a sawtooth wave function through an LED placed in front of the PMT assembly. Measurements are taken first in this setup, and then

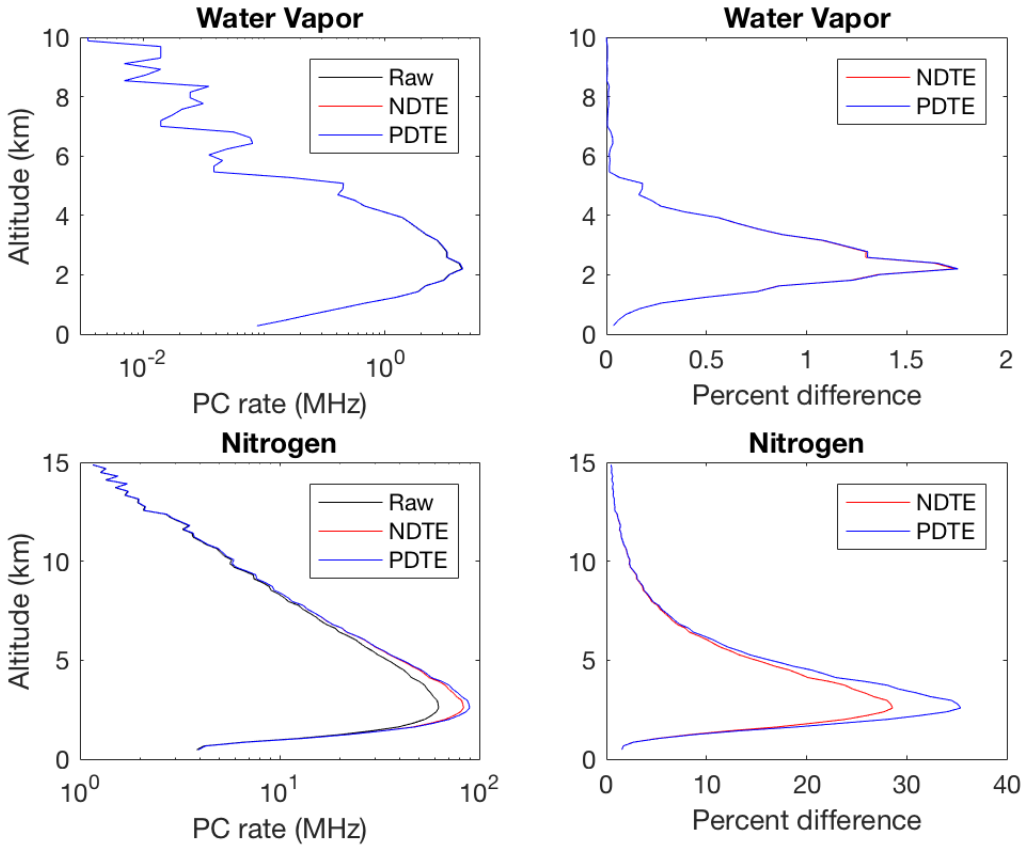

Figure A.12: Change in the nitrogen and water vapor raw PC signal after applying NDTE (non-paralyzable, Equation 2.25) and PDTE (paralyzable, Equation 2.25) deadtime corrections, assuming a deadtime of 4 ns for both channels.

with a neutral density filter (11 % transmittance) placed between the LED and PMT. A plot of scaled, neutral density-filtered data versus unfiltered data is plotted and fitted with a 5th-order polynomial [31][13]. Thus, the empirical approach provides a method to determine whether the system is paralyzable or non-paralyzable, as well as an estimate of the system's dead time.

Channel merging

The traditional method of calculating WVMR for PCL only includes PC modes of detection for the nitrogen and water vapor channels, and therefore does not employ any channel merging. However, this is something that can be incorporated into the traditional WVMR processing in the future.

Coadding

Coadding is the process of summing counts spatially and/or temporally. Summing white noise averages to 0 and does not increase signal, while summing signal does. Since much of the background is white noise, coadding improves the signal-to-noise ratio at the cost of reducing the resolution. Additionally, coadding decreases the statistical uncertainty at the expense of resolution.

A.2.2 Additional Instrumental Considerations

Signal-Induced Noise

Subjecting a PMT to an intense light source may generate signal-induced noise, in which weak returns are dwarfed by noise induced from the strong, close-range signal. It is caused by charge remaining between the dynodes, in which the photocathode electrons are trapped in a long-lasting metastable decay state [14]. The effects are evident at the higher altitudes of water vapour retrievals, and are more pronounced in glass-bulb PMTs, making metal-channel PMTs a better choice [15]. Signal-induced noise can be addressed by blocking the most intense

returns from the lowest altitudes, by either mechanical blocking the light (via a chopper), or by electronic gating (switching the detector off when the brightest returns are expected to arrive) [7][14][35].

Fluorescence

Fluorescence can be an issue for lidar systems, particularly those operating in UV ranges. Appendix B provides an overview of fluorescence in lidar systems.

A.2.3 Calculating WVMR (Traditional method)

This section will discuss the more commonly used means by which the lidar community determines atmospheric water vapour. Now the corrected counts for the nitrogen and water vapor, N_N and N_H, can be added to the WVMR:

$$w = \mathbf{C} \cdot \frac{M_H}{M_{dry}} \cdot \frac{n_N}{n_{dry}} \cdot \frac{N_H}{N_N} \tag{A.5}$$

where $\mathbf{C} = \frac{\xi_N}{\xi_H} \cdot \frac{\sigma_N}{\sigma_H} \cdot \frac{\Gamma_N}{\Gamma_H} \cdot \frac{O_N}{O_H} \cdot \frac{F_N}{F_H}$ are the terms that still need to be accounted for. The following subsections look at these parameters, where the subscript X denotes the terms for either the nitrogen or water vapour channel.

Raman backscattering cross section

The determination of the Raman backscattering cross sections for water vapor and nitrogen at the PCL Raman wavelengths is discussed in Section 3.3.2 in my Masters project [36].

Instrument Efficiency

In the case of PCL, the light path ultimately going into the water vapour channel detector is as follows: the beam first leaves the laser and is directed through three mirrors into the sky. The backscatter is then collected in the primary mirror, focused through a lens, reflected off

a dichroic beam splitter, transmitted through a second beam splitter, transmitted through an interference filter, and sent through the PMT. The instrument efficiency for the water vapour channel would then be:

$$\xi_H(\lambda = 660\,\text{nm}) = 3R_m \cdot R_{pm} \cdot T_{lens} \cdot R_{dbs1} \cdot T_{dbs2}(660\,\text{nm}) \cdot T_{Hif}(660\,\text{nm}) \cdot \Phi_H(660\,\text{nm}) \quad \text{(A.6)}$$

where R_m are the reflectance through the initial mirrors, R_{pm} is the primary mirror reflectance, T_{lens} is the transmittance through the focusing lens, R_{dbs1} is the first beam splitter's reflectance at , T_{dbs2} is the second beam splitter's transmittance, T_{Hif} is the interference filter for the water vapour channel, and Φ_H is quantum efficiency of the water vapour channel's PMT. The efficiency for the nitrogen channel is then:

$$\xi_N(\lambda = 607\,\text{nm}) = 3R_m \cdot R_{pm} \cdot T_{lens} \cdot R_{dbs1} \cdot R_{dbs2}(607\,\text{nm}) \cdot R_m \cdot T_{Nif}(607\,\text{nm}) \cdot \Phi_N(607\,\text{nm}) \quad \text{(A.7)}$$

where R_{dbs2} is the second beam splitter's reflectance, T_{Nif} is the interference filter for the nitrogen channel, and Φ_N is the nitrogen's channel PMT quantum efficiency. Assuming the first 4 terms are not strongly wavelength-dependent, the instrument efficiency ratio used in the WVMR is:

$$\frac{\xi_H}{\xi_N} = \frac{1}{R_m} \cdot \frac{T_{dbs2}(660\,\text{nm})}{R_{dbs2}(607\,\text{nm})} \cdot \frac{T_{Hif}(660\,\text{nm})}{T_{Nif}(607\,\text{nm})} \cdot \frac{\Phi_H(660\,\text{nm})}{\Phi_N(607\,\text{nm})} \quad \text{(A.8)}$$

For the PCL, the transmittance for the Raman channel interference filters was measured directly on multiple occasions. Measurements were first made in 2013 by former PCL researcher Steve Argall, and in 2014 by me, using a Shimadzu UV-VIS-NIR UV-3600 spectrometer at the UWO Engineering Common Lab (managed by Dr. Paul Charpentier). In 2017, I made a simple set up using a calibrated lamp and a spectrometer loaned from the UWO Meteor Lab (managed by Dr. Margaret Campbell-Brown and Dr. Peter Brown) to measure these optical properties independently (See Figure A.13). The measurements from these 3 tests are shown in Figure A.14. As seen in this figure, there are numerous changes in the shape, bandwidth, and

position of the spectra over the subsequent measurements (the central wavelength for the nitrogen shifted from 604.4 nm in 2013 to 610.9 nm in 2019. Although it is possible that the optical coating could have degraded over time, imprecise positioning of the filter stand is more probable, as the central wavelength and bandwidth are strongly dependent on the angle of incidence [36].

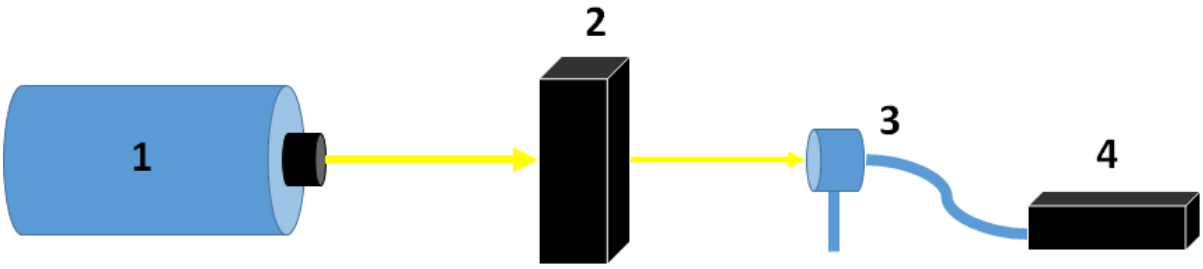

Figure A.13: Schematic of set up for measuring interference filter spectra. An Ocean Optics HL-2000-CAL Halogen calibrated lamp (1) is directed toward a stand holding the interference filter (2), with the transmitted light traveling through a fiber optic (3) to an Ocean Optics USB4000 spectrometer (4).

Since we are only concerned with the instrument efficiency ratio for the WVMR, we only need to find the ratios for the terms instead of the efficiencies for each instrument. For instance, if we wanted to determine the interference filter ratio, $\frac{T_{Hif}(660\,\text{nm})}{T_{Nif}(607\,\text{nm})}$, we could shine a stable light source through the interference filters and detectors, measuring the output signal. The filters could then be swapped and the new output signal measured [37]. The filter efficiency ratio would then be $\frac{T_H}{T_N} = \sqrt{\frac{S_0}{S_1}}$, where S_0 is the output signal from the initial configuration, and S_1 is the signal when the filters are swapped. The same can be done for other components, such as the PMTs.

However, both of these approaches are time consuming, potentially taking up valuable observing time. Properties can be monitored and calibrated more regularly if a white light calibration is carried out.

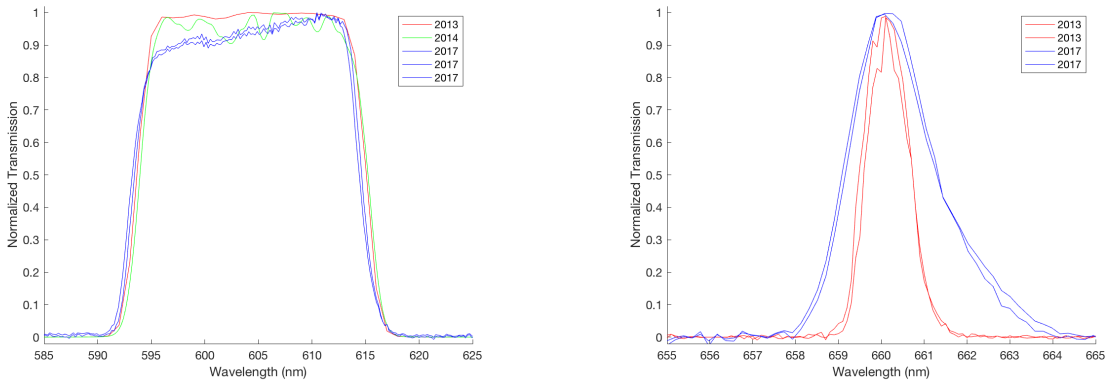

Figure A.14: Spectrum of the interference filter used for the Nitrogen (left) and water vapor (right) channels.

Temperature Dependence Function

This analysis was carried out for PCL, using radiosondes for temperature profiles, giving a correction with a maximum value of 4.3 % at the lowest altitude [6]. However, these estimates were made using the manufacturer's specifications for the interference transmission, which may no longer be accurate. An updated determination of the temperature correction (using in-house interference filter measurements) is discussed in my Master's thesis (Section 3.3.2 of [36]).

Atmospheric Transmission

The overall transmissions at 607 nm and 660 nm differ by approximately 5% due to the λ^{-4} dependence of Rayleigh scattering [42].

For the PCL, as well as other lidars [28][40], the atmospheric transmission is calculated using the model conditions provided in MODTRAN. Developed by Spectral Sciences, Inc. and the US Air Force, MODTRAN (MODerate resolution atmospheric TRANsmission) is a program modelling atmospheric radiative transfer processes between infrared and ultraviolet wavelengths [10]. For PCL water vapour analysis, MODTRAN 3 is used to determine the transmissions for the Raman wavelengths, assuming a rural aerosol model with 23 km visibility [13][9] (Figure A.15).

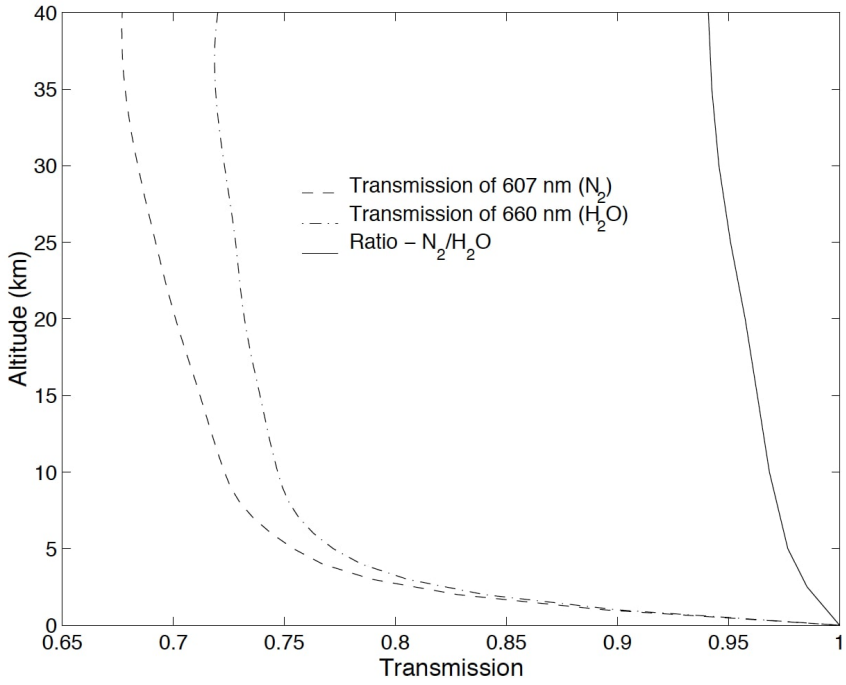

Figure A.15: Sample of the atmospheric transmission at 607 nm and 660 nm using MODTRAN [13]

.

Geometric Overlap

Geometric overlap calculations were carried out for the PCL using the Stelmaszczyk et al. 2005 [34]. approach. However, due to the uncertainties of some telescope and laser beam properties, it was difficult to constrain the overlap function (see Section 3.4 of [36]).

A.2.4 Uncertainty Budget

Statistical uncertainty

The PC counts are expected to obey Poisson statistics, so their statistical uncertainty is simply the count rate:

$$\sigma_N = \sqrt{N} \tag{A.9}$$

These uncertainties increase with altitude, being negligible at the lowest altitudes and in excess of 30% at the top of the retrieval. [23] However, calculation of the uncertainty associated

with the analog data requires knowledge of the individual data points' sum of the squares [42]. Calculating analog statistical uncertainties are further complicated during the merging process.

Systematic uncertainty

Estimates of the major sources of uncertainties for the traditional WVMR retrieval are listed below [19][1][43].

Processing uncertainties

1. Dead time correction: Up to 10 % at the lowest altitudes, < 1 % elsewhere
2. Cross section: 5-12 % (10 % using experimental data, [26])
3. Differential transmission for 2 Raman wavelengths: < 1 %
4. Overlap function: up to 10 % at lowest altitudes
5. Temperature-dependence function: > 1 % (depending on filter transmission curve)
6. Fluorescence: 0-10 % depending on system (can occasionally be much larger)

Calibration uncertainties

Ia. Radiosonde sensor: 3 % in lower atmosphere, up to 50 % in lower stratosphere

Ib. Radiosonde position: 3-30 % (depending on how far sonde has drifted)

IIa. Microwave radiometer: 3-5 %

IIb. Scaling to radiometer units: 3-15 %

IIIa. Lamp: 5-10 %

IIIb. Transfer of calibration source to lidar profile: 0.5-2 %

[1] p. 126, Table 7.2

A.3 Calibration

Calibration is a crucial consideration for any observational system, with Raman water vapor lidars being no exception. PCL is at a particular disadvantage, as the site does not have any permanent co-located instruments capable of measuring water vapor.

A.3.1 Overview of calibration efforts

When the Raman data channels were first installed at PCL in 1999, Atmospheric Environment Service (later renamed Meteorological Service of Canada, a division of Environment and Climate Change Canada) loaned out a microwave radiometer for the Delaware site [13]. Lidar water vapor mixing ratio profiles can be converted to total column measurements, and compared to the column measured by the radiometer. Unfortunately, the radiometer could not produce stable data, so a proper comparison could not be carried out [13].

Another attempt at calibration involved the use of routine radiosonde launches from White Lake, Michigan (DTX, 42.70° N, 83.46° W, 329 m elevation) and Buffalo International Airport (BUF, 42.93° N, 78.73° W, 215 m elevation) [6][9]. Located 160 km west of PCL and 200 km east respectively, these are the closest routine sonde launch sites, and are roughly at the same latitude. As air masses over Southwestern Ontario tend to move eastward, using the White Lake sonde at 0 UT and the Buffalo sonde at 12 UT may give reasonably comparable measurements, if in the same air mass. Comparisons of sonde and scaled lidar measurements from selected nights between 2000 and 2003 show an average agreement of 12% [9]. However, the high spatial-temporal variability of atmospheric water vapor makes this method impractical as a regular means of calibration.

Another possibility considered for PCL was the use of a GPS receiver for estimating integrated water vapor (IWV). However, after consultation with a local distributor, it was deemed a network of multiple receivers would be required for this objective - which is not feasible for the PCL group currently.

A.3.2 ALVICE validation campaign

Lidar sites without immediate access to permanent co-located instruments, such as PCL, can be calibrated during validation campaigns. One major campaign was MOHAVE (Measurements Of Humidity in the Atmosphere and Validation Experiments) 2009. Based at JPL's Table Mountain Facility in Southern California in October 2009, many instruments including 3 Raman lidars, 2 microwave radiometers, and dozens of radiosondes and frost-point hygrometers converged to validate water vapour measurements [22]. Two of the lidars, ALVICE (Atmospheric Laboratory for Validation, Inter-agency Collaboration and Education) and STROZ (STRatospheric OZone), are mobile units commissioned by NASA GSFC, and are taken to different lidar sites to participate in campaigns. In late spring of 2012, PCL took part in a comparison campaign with the ALVICE mobile laboratory in the late spring of 2012. As PCL had recently been established at the Echo Base site, the campaign provided an excellent opportunity to calibrate the upgraded system.

ALVICE description

ALVICE (Atmospheric Laboratory for Validation, Interagency Collaboration and Education) is a mobile laboratory operated by NASA-Goddard Space Flight Center comprised of multiple instruments, including a Raman lidar. The lidar, originally developed for airborne observations, consists of a 0.6 m Dall-Kirkham telescope and a Nd:YAG frequency-tripled laser (354.7 nm) with a power of 17.5 W [44]. Like PCL, it operates at nighttime only, and can measure water vapor profiles from 3-20 km [45]. Since ALVICE is a mobile unit, it is ideal for intercomparisons, and has been employed for previous campaigns including MOHAVE-II [45] and MOHAVE-2009 [22].

Campaign overview

The campaign took place from May 23 to June 10, 2012, when ALVICE was set up next to the PCL, culminating in over 50 hours of measurements from the two lidars. During this time, 3

CFHs and 18 RS92 radiosondes were also launched from Echo Base [47].

White Light calibration

ALVICE uses a stabilized calibration lamp for performing internal calibration of its receiver and detector system [43]. The white light calibration technique used by Leblanc and McDermid [21] considers a lamp in a fixed location. As a lamp at a fixed position cannot give a comprehensive picture of the system's optical efficiency, a scanning lamp for mapping the receiver surface has been incorporated for the Howard University Raman Lidar, as well as ALVICE [38][46].

A calibrated lamp was also set up to monitor instrumental efficiency for PCL. During the campaign, approximately 3 hours of white light calibration observations were made [47].

A.4 PCL White Light calibration

White light internal calibration is one of the possible means for providing a partial calibration for the PCL, an instrument without any collocated instruments for comparison. After the conclusion of the campaign in 2012, the same lamp was set up and white light scans resumed briefly in 2017. These white light calibration measurements are shown in Figures A.16 and A.17. The variability of the measurements is substantial, as shown with the large uncertainty. However, a single trend can be placed to connect the data sets, and fits within the uncertainties for most of the data, with a coefficient of determination of 0.76 and 0.85 for the nitrogen and water vapor trends respectively.

The primary motivation for the performing this calibration is to monitor changes in the instrument efficiency. For the WVMR, this is the ratio of the water vapor channel efficiency to the nitrogen channel efficiency. This channel efficiency ratio is shown in Figures A.18 and A.20. Aside from the latter dates of the 2017 data set, the series trend represents the data

reasonably well, giving an empirical correction of (R^2=0.78):

$$(\frac{\xi_H}{\xi_N})_{cal} = 2.277 \times 10^{-6} \cdot t - 1.4313 \tag{A.10}$$

where t is the serial date (the number of days since January 0, 0000).

Although it is possible to determine a time-dependent correction for the instrument efficiency, it must be approached with caution. As shown in the related figures, the uncertainties are quite large, giving a large range of permissible trends. Additionally, an instrumental effect has caused an altitude-varying signal in the water vapor channel when subjected to white light in the 2017 data. This phenomenon should be investigated further.

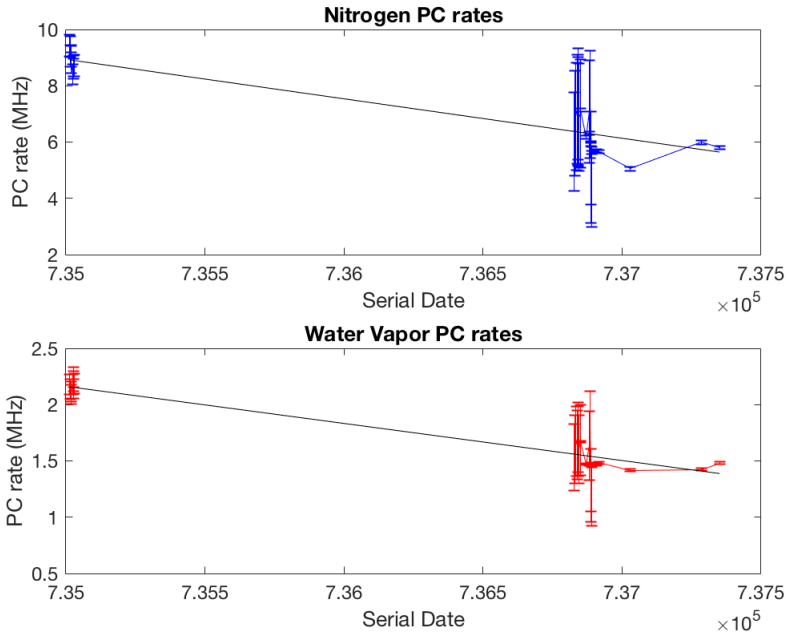

Figure A.16: Scaled PC rates from white light calibration runs for the nitrogen and water vapor channels, over a time span from 2012 (serial date 735000) to 2018 (serial date 737000).

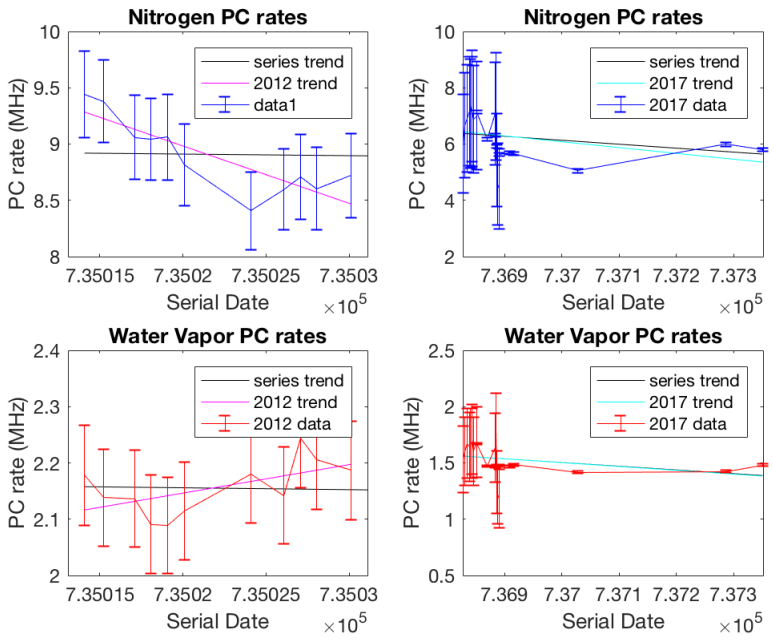

Figure A.17: A zoomed-in version of Figure A.16 for the 2012 runs (left figures) and 2017-2018 runs (right figures). The black series trend in each of the figures is the trend for the entire series of runs, while the magenta and cyan lines are the trends for the 2012 and 2017 data, respectively.

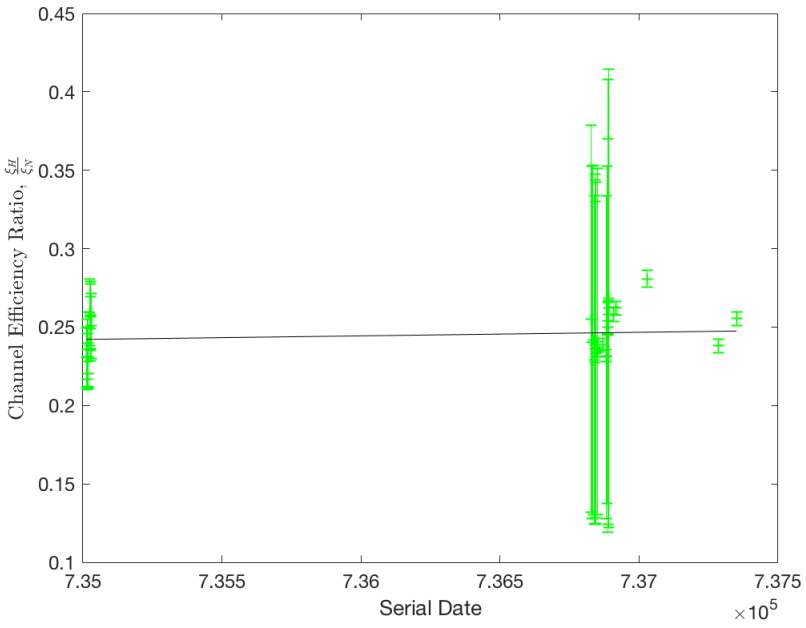

Figure A.18: Ratio of water vapor to nitrogen channel white light calibration counts, over a time span from 2012 (serial date 735000) to 2018 (serial date 737000).

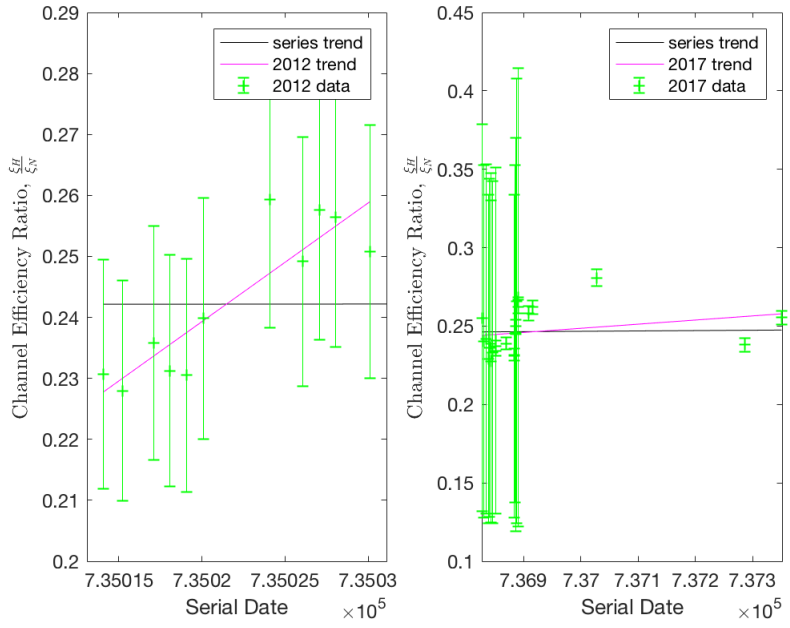

Figure A.19: A zoomed-in version of Figure A.18 for the 2012 runs (left figures) and 2017-2018 runs (right figures). The black series trend in each of the figures is the trend for the entire series of runs, while the magenta and cyan lines are the trends for the 2012 and 2017 data, respectively.

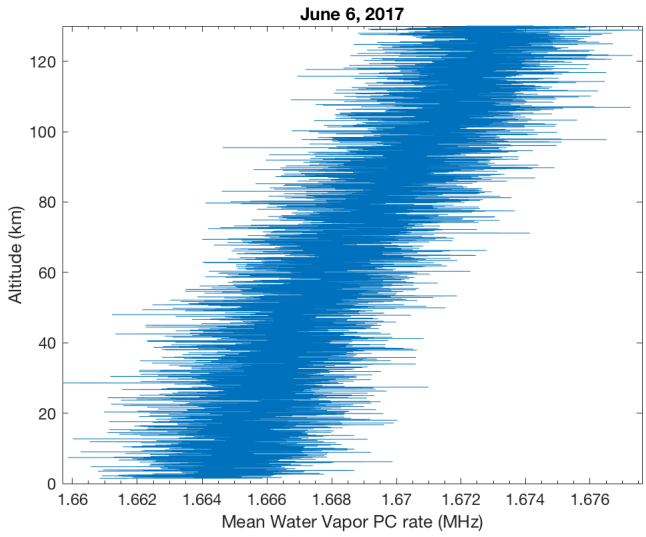

Figure A.20: White light calibration counts for the water vapor PC channel on June 6, 2017, showing an unexplained height-varying signal.

Bibliography

[1] Photomultiplier Handbook, Tech. rep., Burle Technologies, Inc., 1980.

[2] Multichannel Scaler/Averager Model SR430, Stanford Research Systems, 2007.

[3] Licel Transient Recorder and Ethernet-Controller Programming Manual, Tech. rep., Licel GmbH, 2010.

[4] Licel TR20-160 Lidar Transient Recorder Manual, Tech. rep., Licel GmbH, 2010.

[5] TR20-160 Licel transient recorder Manual, Licel GmbH, 2011.

[6] Algara-Siller, M.: Purple Crow Lidar calibration of the water vapour mixing ratios in the lowest atmosphere, Master's thesis, University of Western Ontario, 2004.

[7] Argall, S. and Sica, R.: Encyclopedia of Imaging Science and Technology, chap. LIDAR, John Wiley & Sons, Inc., 2002.

[8] Argall, S., Vassiliev, O., and Sica, R.: Lidar Measurements taken with a large- aperture liquid mirror: 2. Sodium resonance-fluorescence system, Appl. Opt., 39, 2393, 2000.

[9] Argall, S., Sica, R., and Bryant, C.: Calibration of the Purple Crow Lidar vibrational Raman water-vapour mixing ratio and temperature measurements, Can. J. Phys., 85, 119, 2007.

[10] Berks, A., Bernstein, L., and Robertson, D.: MODTRAN: A moderate resolution model for LOWTRAN 7, Tech. rep., Spectral Sciences, Inc., Burlington, MA, 1989.

[11] Borra, E., Content, R., and Girard, L.: Liquid Mirrors: Optical shop tests and contributions to the technology, ApJ, 398, 829, 1992.

[12] Borra, E. F.: The liquid-mirror telescope as a viable astronomical tool, Journal of the Royal Astronomical Society of Canada, 76, 245–256, 1982.

[13] Bryant, C.: First measurements of the upper tropospheric and lower stratospheric water vapour mixing ratios using the Purple Crow Lidar raman-scatter lidar, Master's thesis, University of Western Ontario, 1999.

[14] Cairo, F., Congeduti, F., and Poli, M.: A survey of the signal induced noise in photomultiplier detection of wide dynamics luminous signals, Rev. of Sci. Instruments, 67, 3274, 1996.

[15] Dinoev, T., Simeonov, V., and Arshinov, Y.: Raman Lidar for Meteorological Observations, RALMO – Part 1: Instrument description, Atmos. Meas. Tech., 6, 1329, 2013.

[16] Doucet, P., Sica, R., and Argall, S.: LIDAR Measurements of Lofted Stratospheric Layers from Biomass Burning, in: 37th COSPAR Scientific Assembly, vol. 37, p. 741, 2008.

[17] Farhani, G.: Improved techniques for atmospheric ozone retrievals from lidar measurements using the Optimal Estimation Method and Machine Learning, Ph.D. thesis, University of Western Ontario, 2018.

[18] Hicks, S.: The Automation and Characterization of the Zaber Motorized Mount and an Update on the Status of the Purple Crow Lidar, Master's thesis, University of Western Ontario, 2015.

[19] Kampfer, N., ed.: Monitoring Atmospheric Water Vapour: Ground-Based Remote Sensing and In-situ Methods, vol. 10, Springer Science, 2013.

[20] Kovalev, V. and Eichinger, W.: Elastic Lidar: Theory, Practice, and Analysis Methods, John Wiley & Sons, Inc., 2004.

[21] Leblanc, T. and McDermid, I.: Accuracy of raman liar water vapour calibration and its applicability to long-term measurements, Appl. Opt., 47, 5592, 2008.

[22] Leblanc, T., Walsh, T., and McDermid, I.: Measurements of Humidity in the Atmosphere

and Validation Experiments (MOHAVE)-2009: overview of campaign operations and results, Atmos. Meas. Tech., 4, 2579, 2011.

[23] Leblanc, T., Trickl, T., and Vogelmann, H.: Monitoring Atmospheric Water Vapour: Ground-Based Remote Sensing and In-situ Methods, chap. 7: Lidar, Springer Science, 2013.

[24] McCullough, E.: A new technique for interpreting depolarization measurements using the CRL atmospheric lidar in the Canadian High Arctic, Ph.D. thesis, University of Western Ontario, 2015.

[25] Mielke, B.: Analog & photon counting, Tech. rep., Licel GmbH.

[26] Penney, C. and Lapp, M.: Raman-scattering cross sections for water vapor, J. Opt. Soc. Am., 66, 422, 1976.

[27] Russell, A. T. and Sica, R. J.: Observations of high-frequency temporal gravity wave spectra in the middle upper stratosphere, Journal of Geophysical Research, 106, 11,849–11,858, doi:10.1029/2000JD900644, 2001.

[28] Sherlock, V., Garnier, A., and Hauchecorne, A.: Implementation and validation of a Raman lidar measurement of middle and upper tropospheric water vapour, Appl. Opt., 38, 5838, 1999.

[29] Sica, R. and Haefele, A.: Retrieval of temperature from a multiple-channel Rayleigh-scatter lidar using an optimal estimation method, Appl. Opt., 54, 2015.

[30] Sica, R. and Haefele, A.: Retrieval of water vapor mixing ratio from a multiple channel Raman-scatter lidar using an optimal estimation method, Appl. Opt., 55, 763, 2016.

[31] Sica, R., Sargoytchev, S., and Argall, S.: Lidar measurements taken with a large-aperture liquid mirror. 1: Rayleigh-scatter system, Appl. Opt., 34, 6925, 1995.

[32] Sica, R. J., Thayaparan, T., Argall, P. S., Russell, A. T., and Hocking, W. K.: Modulation of upper mesospheric temperature inversions due to tidal-gravity Wave interactions, Journal of Atmospheric and Solar-Terrestrial Physics, 64, 915–922, doi:10.1016/S1364-6826(02)00046-9, 2002.

[33] Sica, R. J., Argall, P. S., Bandoro, J., Iserhienrhien, B., Khanna, J., McCullough, E. M., Olofson, K. F., and Wing, R.: The New and Improved Purple Crow Lidar, in: AGU Fall Meeting Abstracts, vol. 2010, pp. A11A–0027, 2010.

[34] Stelmaszczyk, K., Dell'Aglio, M., and Chudzynski, S.: nalytical function for lidar geometrical compression form-factor calculations, Appl. Opt., 44, 1323, 2005.

[35] Thayer, J., Nielsen, N., and Warren, R.: Rayleigh lidar system for middle atmosphere research in the arctic, Opt. Eng., 36, 2045, 1997.

[36] VanKerkhove, J.: Characterizing the Purple Crow Lidar Raman channels to investigate potential sources of wet bias, Master's thesis, University of Western Ontario, 2015.

[37] Vaughan, G., Wareing, D., and Thomas, L.: Humidity measurements in the free troposphere using Raman backscatter, Q. J. R. Meteorol. Soc., 114, 1471, 1988.

[38] Venable, D., Whiteman, D., and Calhoun, M.: Lamp mapping technique for independent determination of the water vapour mixing ratio calibration factor for a Raman lidar system, Appl. Opt., 50, 2011.

[39] Walker, M., Venable, D., and Whiteman, D.: Gluing for Raman Lidar systems using the lamp mapping technique, Appl. Opt., 53, 8535, 2014.

[40] Whiteman, D.: Examination of the traditional raman lidar technique, II: Evaluating the ratios for water vapour and aerosols, Appl. Opt., 42, 2593, 2003.

[41] Whiteman, D.: Examination of the Traditional Raman lidar technique. I. Evaluating the temperature- dependent lidar equations, Appl. Opt., 42, 2003.

[42] Whiteman, D., Melfi, S., and Ferrare, R.: Raman lidar system for the measurement of water vapor and aerosols in the Earth's atmosphere, Appl. Opt., 31, 3068, 1992.

[43] Whiteman, D., Cadrirola, M., and Venable, D.: Correction technique for Raman water vapor lidar signal-dependent bias and suitability for water vapor trend monitoring in the upper troposphere, Atmos. Meas. Tech., 5, 2893, 2012.

[44] Whiteman, D. N., Veselovskii, I., Cadirola, M., Rush, K., Comer, J., Potter, J. R., and Tola, R.: Demonstration measurements of water vapor, cirrus clouds, and carbon dioxide using a high-performance raman lidar, Journal of Atmospheric and Oceanic Technology, 24, 1377–1388, doi:10.1175/JTECH2058.1, 2007.

[45] Whiteman, D. N., Rush, K., Rabenhorst, S., Welch, W., Cadirola, M., McIntire, G., Russo, F., Adam, M., Venable, D., Connell, R., Veselovskii, I., Forno, R., Mielke, B., Stein, B., Leblanc, T., McDermid, S., and Vömel, H.: Airborne and ground-based measurements using a high-performance raman lidar, Journal of Atmospheric and Oceanic Technology, 27, 1781–1801, doi:10.1175/2010JTECHA1391.1, 2010.

[46] Whiteman, D. N., Venable, D., and Landulfo, E.: Comments on "Accuracy of Raman lidar water vapor calibration and its applicability to long-term measurements", Applied Optics, 50, 2170–2176, doi:10.1364/AO.50.002170, 2011.

[47] Wing, R.: Multi-sensor calibration and validation of the UWO-PCL water vapour lidar, Master's thesis, University of Western Ontario, 2012.

Appendix B

Fluorescence in Raman-scattering Lidars

Wet bias, or excess observations of water vapour, has been observed frequently in the lidar community literature. In many instances, this wet bias is due to fluorescence, where light is re-emitted within the system or externally, originating from instrumental or atmospheric sources.

Wet bias has been observed due to fluorescence in fiber optics cables bringing light from the focal point to the detectors [3][10]. Airborne aerosols and bio-aerosols such as pollen, dust, spores, and bacteria have also been shown to fluoresce, resulting in wet-biased signal [6][9][7]. Fluorescence can even be induced by swarms of certain insects, such as damselflies [1], causing wet-biased lidar returns during the MOHAVE campaign [11]. The magnitude of the wet bias can vary tremendously, from a few percent of the total WVMR to orders of magnitude larger, with the greatest effects often seen in the lower stratosphere [11].

As fluorescence is much more common in the ultraviolet, wet biases associated with fluorescence are much more of a concern for UV lidars than lidars operating at visible wavelengths [12]. However, fluorescence is still possible for visible lidars, as some materials such as certain types of vegetable oils actually fluoresce at the nitrogen and water vapour Raman wavelengths when excited by 532 nm laser pulses [8].

Fluorescence can be monitored by observing "dead bands"- wavelengths offset from the Raman peaks where signal should not be found, to ensure spurious light is not being recorded

[2]. It can also be detected by replacing the water vapour channel's interference filter with another filter centered at another wavelength (i.e. replacing a 0.98 nm bandwidth UV water vapour filter centred at 407 nm, with 10 nm bandpass cavity filter centered at 432 nm) [5].

Once detected, fluorescence can sometimes be mitigated by introducing instrument changes. The best way to limit such effects is by avoiding contamination by blocking elastic returns as early as possible and using proper optics [4]. In the case of [10], fluorescence was reduced by a factor of 10 after old fiber optic cables were replaced by newer, OH-rich cables. Lidar layouts involving separate optical paths for the transmitted and received light, elimination of fiber optic cables by placing the detectors next to the focal point, and transmitting the beam through an open hatch instead of a window, are all design changes that can reduce instrument-induced fluorescence [12]. For fluorescence of an external origin, the fluorescent effects can be modelled and used to apply a correction to the WVMR [11].

Bibliography

[1] Brydegaard, M., Guan, Z., and Weelenreuther, M.: Insect monitoring with fluorescence lidar techniques: feasibility study, Appl. Opt., 48, 5668, 2009.

[2] Cooney, J.: Remote Measurements of Atmospheric Water Vapor Profiles Using the Raman Component of Laser Backscatter, J. Appl. Met., 9, 182, 1970.

[3] Dakin, J. and King, A.: Limitations of a single optical fiber fluorimeter system due to background fluorescence, IEEE Proc., 131, 273, 1984.

[4] Dinoev, T., Simeonov, V., and Arshinov, Y.: Raman Lidar for Meteorological Observations, RALMO – Part 1: Instrument description, Atmos. Meas. Tech., 6, 1329, 2013.

[5] Dionisi, D., Keckhut, P., and Courcoux, Y.: Water vapor observations up to the lower stratosphere through the Raman lidar during the Maïdo Lidar Calibration Campaign, Atmos. Meas. Tech., 8, 1425, 2015.

[6] Gelbwachs, J. and Birnbaum, M.: Fluorescence of Atmospheric Aerosols and Lidar Implications, Appl. Opt., 12, 2442, 1973.

[7] Immler, F., Engelbart, D., and Schrems, O.: Fluorescence from atmospheric aerosol detected by a lidar indicates biogenic particles in the lowermost stratosphere, Atmos. Chem. Phys., 5, 345, 2005.

[8] Mu, T., Chen, S., and Zhang, Y.: Classification of edible oils using 532 nm laser-induced fluorescence combined with support vector machine, Anal. Methods, 5, 6960, 2013.

[9] Pinnick, R., Hill, S., and Pan, Y.: Fluorescence spectra of atmospheric aerosol at Adelphi, Maryland, USA: measurement and classification of single particles containing organic carbon, Atmos. Environ., 38, 1657, 2004.

[10] Sherlock, V., Garnier, A., and Hauchecorne, A.: Implementation and validation of a Raman lidar measurement of middle and upper tropospheric water vapour, Appl. Opt., 38, 5838, 1999.

[11] Whiteman, D., Cadrirola, M., and Venable, D.: Correction technique for Raman water vapor lidar signal-dependent bias and suitability for water vapor trend monitoring in the upper troposphere, Atmos. Meas. Tech., 5, 2893, 2012.

[12] Wing, R.: Multi-sensor calibration and validation of the UWO-PCL water vapour lidar, Master's thesis, University of Western Ontario, 2012.

Appendix C

Investigating the effects of the Brightness Temperature bias correction

The use of bias-corrected brightness temperatures was first discussed in Section 5.4.1, with the bias values over the observational history of the Payerne HATPRO instrument shown in Figure 5.15. In addition to the radiometric retrievals discussed in Section 7.1.1, retrievals were also carried out for 120 other clear nights between 2009 and 2015 to more effectively gauge the effects of brightness temperature bias correction on radiometer retrievals.

Figure C.1 shows the retrieval residuals for each channel over the course of the 125 nights shown. Visually comparison of the residuals via uncorrected and corrected brightness temperatures shows no obvious change between the two figures. In both cases, the residuals in the first epoch are relatively small, where retrievals between 2012 and 2015 have large negative residuals for the 25.44 GHz 27.84 GHz channels. No data was used in the epoch from May to September 2013, and only 2 dates from the April-November 2011 were included, due to the substantial bias variability during this time (as seen in the 25.44 GHz and 26.24 GHz channels, in Figure 5.15).

An alternative look at this data is provided in Table C.1. For each observational calibration epoch, the percentage of dates with residuals less than the measurement uncertainty of 0.5 K

are listed for each frequency. The first epoch considered here, spanning from September 2009 until April 2011, shows that aside from 22.24 GHz and 31.4 GHZ, the majority of dates have residual values within the measurement uncertainty. And since the biases for this epoch are small, there is little difference between the corrected and uncorrected data. There are only 2 dates in the range from April to November 2011, with a bias correction removing all but 2 frequency residuals. The epoch from November 2011 to May 2013 shows that aside from 25.44 GHz and 26.24 GHz, the other 5 channels have more than 50% of residuals within 0. K. However, applying a bias correction for these data worsens the retrieval for all channels except 31.4 GHz, in which a slight improvement is seen. For the uncorrected data from final epoch considered here, the transparent frequencies have better agreement than the opaque channels, where only a small percentage of the residuals are actually less than 0.5 K. Applying a bias correction does help to an extent in this case, significantly improving the residual for the 2 largest frequencies.

The effects of the bias correction is also reflected in the retrieval measurement cost. Figure C.2 compares the cost functions determined via retrievals using uncorrected and corrected brightness temperatures. The earliest epoch shows a relatively small difference in the cost between the uncorrected and corrected measurements, and small difference that does exist indicates an overall improvement for the majority of the dates. The epoch from April to November 2011 shows a profoundly higher cost when the bias correction is applied (which is not displayed in the lower plot of Figure C.2, as it is well outside the frame). The epoch spanning from 2011 to 2013 does see some dates with very large costs. However, applying a bias correction does reduce many of these larger costs (the larger differences, in excess of +20, are not displayed in the lower plot of Figure C.2). Despite the cost reduction for a few of these dates, the majority of dates had relatively small costs initially, which were increased when a bias correction was applied. The results from the final epoch are similar to the previous epoch, but only the nights in January 2015 adversely impacted by a bias correction.

Results from this section confirms that it is safest to data from epochs in which the cor-

rection bias is small. For the data after April 2011, one should carefully inspect the data on an individual date basis in order to gauge whether or not bias correction is beneficial to the retrieval.

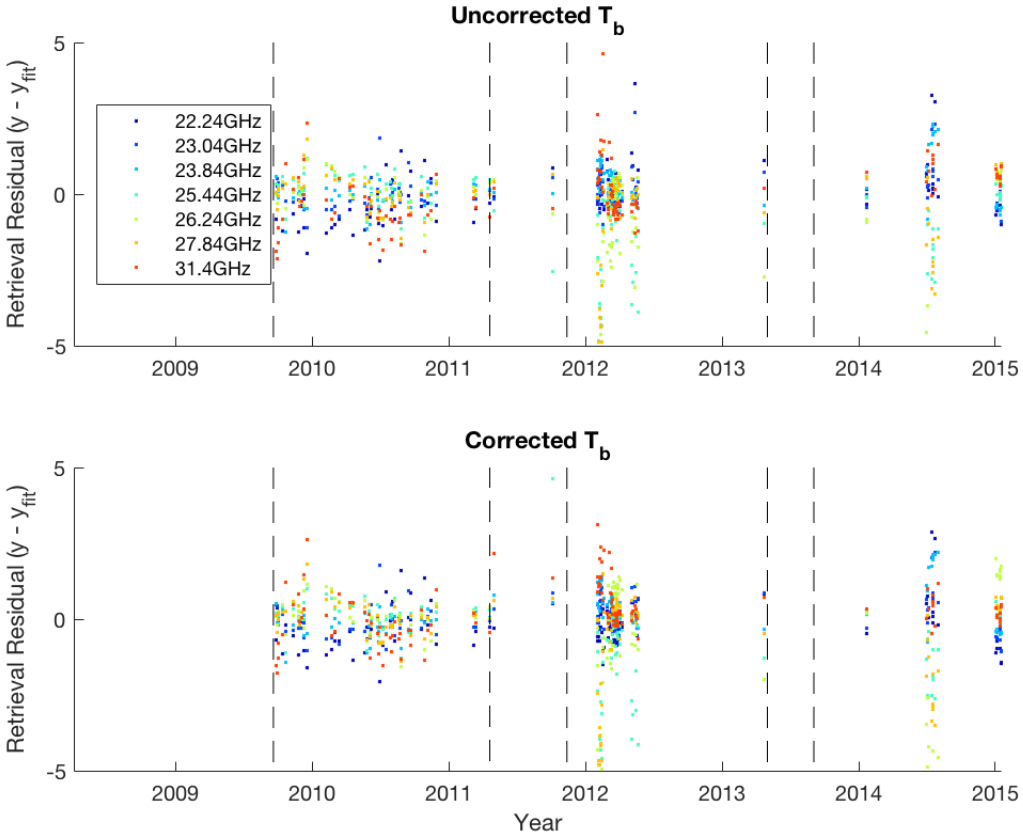

Figure C.1: (Top) Retrieval residuals using uncorrected brightness temperatures, for each channel over the course of the nights considered. (Bottom) Retrieval residuals using bias-corrected brightness temperatures. The vertical dashed lines indicate the calibration epochs defined for determining the bias correction value. In both plots, the vertical axis is in degrees Kelvin.

The effects of bias correction on residual								
Epoch	Bias correction	22.24 GHz	23.04 GHz	23.84 GHz	25.44 GHz	26.24 GHz	27.84 GHz	31.4 GHz
2009-04.2011	No	48.94	72.34	89.36	63.83	65.96	70.21	34.04
2009-04.2011	Yes	47.92	77.08	85.42	**77.08**	**70.83**	68.75	**47.92**
Apr-Nov 2011	No	50	50	100	0	50	50	100
Apr-Nov 2011	Yes	50	50	0	0	0	0	0
11.2011-05.2013	No	73.58	79.25	69.81	43.4	33.96	62.26	52.83
11.2011-05.2013	Yes	49.06	73.58	66.04	30.19	16.98	60.38	**54.72**
09.2013-2016	No	59.09	50	40.91	50	18.18	4.55	27.27
09.2013-2016	Yes	59.09	36.36	**45.45**	50	9.09	**40.91**	**72.73**

Table C.1: Table of the percentages of dates for each epoch in which the channel-dependent residual is within the measurement uncertainty of 0.5 K. Bolded values show improvement when using bias-corrected data rather than uncorrected data.

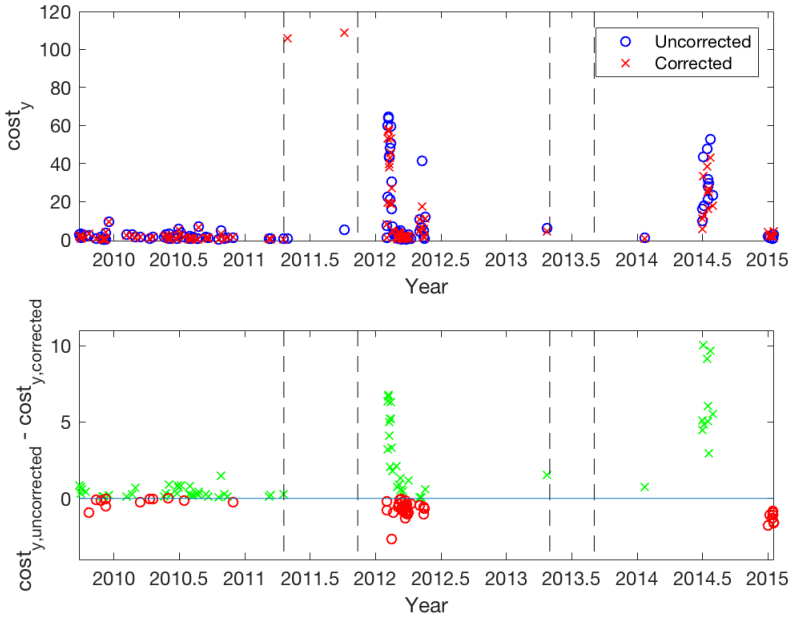

Figure C.2: (Top) Measurement cost from the retrieval for each date due uncorrected (blue circles) and corrected (red x's) brightness temperatures. (Bottom) The difference between the uncorrected and corrected costs. Green x's indicate positive differences (an improvement when bias-corrected values are used), while red circles indicate negative differences (a worsened retrieval when bias-corrected values are used). The vertical dashed lines represent the calibration epochs defined for determining the bias correction value.

Curriculum Vitae

Name:	Jeffrey VanKerkhove
Post-Secondary Education and Degrees:	University of Western Ontario London, ON 2015 - 2019 (Ph.D.)
	University of Western Ontario London, ON 2013 - 2015 (M.Sc.)
	University of Rochester Rochester, NY 2009 - 2013 (B.Sc.)
Related Work Experience:	Research/Teaching Assistant University of Western Ontario 2013 - 2019

Publications:

VanKerkhove, J., Haefele, A., & Sica, R. J., *Improved retrieval of atmospheric water vapor mixing ratio using an integrated lidar-microwave radiometer forward model* (in prep)

VanKerkhove, J. (2018) Integrating Computer Programming into Introductory Physics Courses, *Teaching Innovations Projects*, 8(1). https://doi.org/10.5206/tips.v8i1.6221

VanKerkhove, J., Sica, R. J., Wing, R., & Argall, P. S., *Investigating potential wet bias in the Purple Crow Lidar water vapor measurements*, EPJ Web of Conferences 176, 05026, 2018. (ILRC 28) http://doi.org/10.1051/epjconf/201817605026